Chemical Vapor Deposition of Metastable Germanium Based Semiconductors for Optoelectronic Applications

by

Charutha Lasitha Senaratne

A Dissertation Presented in Partial Fulfillment
of the Requirements for the Degree
Doctor of Philosophy

Approved July 2016 by the
Graduate Supervisory Committee:

John Kouvetakis, Chair
Andrew Chizmeshya
José Menéndez

ARIZONA STATE UNIVERSITY

August 2016

ABSTRACT

Optoelectronic and microelectronic applications of germanium-based materials have received considerable research interest in recent years. A novel method for Ge on Si heteroepitaxy required for such applications was developed via molecular epitaxy of Ge_5H_{12}. Next, $As(GeH_3)_3$, $As(SiH_3)_3$, SbD_3, $S(GeH_3)_2$ and $S(SiH_3)_2$ molecular sources were utilized in degenerate *n*-type doping of Ge. The epitaxial Ge films produced in this work incorporate donor atoms at concentrations above the thermodynamic equilibrium limits. The donors are nearly fully activated, and led to films with lowest resistivity values thus far reported.

Band engineering of Ge was achieved by alloying with Sn. Epitaxy of the alloy layers was conducted on virtual Ge substrates, and made use of the germanium hydrides Ge_2H_6 and Ge_3H_8, and the Sn source SnD_4. These films exhibit stronger emission than equivalent material deposited directly on Si, and the contributions from the direct and indirect edges can be separated. The indirect-direct crossover composition for $Ge_{1-y}Sn_y$ alloys was determined by photoluminescence (PL). By *n*-type doping of the $Ge_{1-y}Sn_y$ alloys via $P(GeH_3)_3$, $P(SiH_3)_3$ and $As(SiH_3)_3$, it was possible to enhance photoexcited emission by more than an order-of-magnitude.

The above techniques for deposition of direct gap $Ge_{1-y}Sn_y$ alloys and doping of Ge were combined with *p*-type doping methods for $Ge_{1-y}Sn_y$ using B_2H_6 to fabricate *pin* heterostructure diodes with active layer compositions up to y=0.137. These represent the first direct gap light emitting diodes made from group IV materials. The effect of the single defected *n*-*i* interface in a *n*-Ge/*i*-$Ge_{1-y}Sn_y$/*p*-$Ge_{1-z}Sn_z$ architecture on electroluminescence

(EL) was studied. This led to lattice engineering of the *n*-type contact layer to produce diodes of *n*-$Ge_{1-x}Sn_x$/*i*-$Ge_{1-y}Sn_y$/*p*-$Ge_{1-z}Sn_z$ architecture which are devoid of interface defects and therefore exhibit more efficient EL than the previous design. Finally, *n*-$Ge_{1-y}Sn_y$/*p*-$Ge_{1-z}Sn_z$ *pn* junction devices were synthesized with varying composition and doping parameters to investigate the effect of these properties on EL.

ACKNOWLEDGMENTS

I would chiefly like to thank my advisor, Prof. John Kouvetakis, without whose guidance, instruction and enthusiasm this work would not have been possible. Similarly, the knowledge and support provided by my committee members Prof. José Menéndez and Prof. Andrew Chizmeshya was essential in bringing this effort to completion.

I would also like offer my gratitude to Dr. Gordon Grzybowski and Dr. Richard Beeler for the training they provided at the initial stages of this research. The collaborative effort of my colleagues Dr. Chi Xu, Dr. James Gallagher, Patrick Sims, Dr. Liying Jiang, Ruben Favaro, and Patrick Wallace contributed directly and indirectly to many components of this research, and I am sincerely grateful for their support.

Many facilities provided by the LeRoy Eyring Center for Solid State Science at Arizona State University were essential for this research. I would like to especially thank Barry Wilkens for assistance with ion beam analysis, and Prof. Lynda Williams for providing SIMS training. The John M. Cowley Center for High Resolution Electron Microscopy and Ira A. Fulton Center for Solid State Electronics Research also provided equipment and instruments used in this work.

I am also grateful for the Air Force Office of Scientific Research for funding that enabled this work.

Finally, I am forever grateful to my family who, though a world away, were a constant source of support and strength throughout the demanding process of completing my graduate studies.

TABLE OF CONTENTS

Page

CHAPTER Page

CHAPTER Page

CHAPTER Page

CHAPTER Page

CHAPTER Page

LIST OF TABLES

Table Page

LIST OF FIGURES

Figure Page

Figure Page

Figure Page

Figure Page

Figure Page

CHAPTER ONE

Introduction and Background

1. Introduction

The microelectronics revolution has had a massive effect on modern society. Technologies developed in the past 60-70 year have dramatically changed the way we interact with each other, and the way we interact with our environment. Innovations in this field have been dependent on the ability to manipulate various types of semiconductor materials that have come to be used in modern electronic devices. Despite the wide range of materials that can be used, one in particular has come to dominate mainstream electronic technology due to its abundance, ease of use, and suitable physical, chemical, and electronic properties. This material is Si, which forms the basis for manufacturing a vast majority of the commercially available electronic devices.

Si based technologies have long been able to achieve exponential performance gains with time, as exemplified by Moore's law.[1,2] This has been a result of technology advances that enabled rapid miniaturization of transistor sizes. However the latest generation of Si devices are fast approaching the physical limits of device scaling. Therefore, various techniques have been successfully investigated to maintain increase in device performance while circumventing the need for smaller devices. Examples include the use of strained Si[3] and high κ dielectrics.[4]

A novel aspect of this drive for higher performance is the use of alternate semiconductor materials in device fabrication. One of the 'new' materials which has been widely studied for this purpose is Ge.[5] While the use of Ge as a semiconductor predates the use of Si -with

the first transistor[6] and integrated circuit[7] being made using Ge- it was eventually replaced with Si due to the latter material's more favorable properties. However, the ability to use Ge in combination with Si for strain engineering, as well as the superior carrier mobilities and optical properties of Ge, have resulted in a resurgence of interest in Ge based materials in microelectronics. An example is the use of silicon-germanium alloys for fabricating devices containing strained Si.[3] In the photonics arena, Ge on Si photodetectors have become common in recent years.[8] Another potential application area for Ge is in Si integrated lasers.[9] Lasing from Ge has been experimentally demonstrated,[10,11] but these devices require high threshold currents, and utilize complementary metal-oxide-semiconductor (CMOS) incompatible fabrication methods which employ high temperatures to induce tensile strain in the Ge active material. Due to such drawbacks, significant improvements are necessary before they can be used in practical applications.

In order to obtain the desired optical properties for lasing and to expand the ability to manipulate strain to enhance device performance, next generation optoelectronic and electronic devices require greater flexibility in band gap and lattice engineering than can be obtained only from the combination of Si and Ge. In this context, germanium-tin (GeSn) alloys have been receiving increasing interest as a means of extending the capabilities of the group IV semiconductor system. The state-of-the-art for this materials system prior to the contributions arising from the work described in this thesis is briefly described below.

2. Germanium-tin

2.1. Properties and Potential Applications

Substitution of Sn atoms in place of Ge in the elemental Ge matrix will give the GeSn alloy which shares with Ge the diamond cubic crystal structure. The Ge rich alloy is only

thermodynamically stable up to Sn content of 1.1%, with the maximum solubility being observed at around 400°C.[12] In the compositionally opposite extreme, the solubility of Ge in Sn is even less, at 0.6%.[12] Furthermore, the semiconducting diamond cubic structure of Sn (α-Sn) is only stable up to 13°C.[12] Therefore, thermodynamically stable combinations represent only a small fraction of the composition space –and in turn optical and physical properties– accessible with GeSn alloys. In consequence, it is not straightforward to use this alloy system for expanding the properties of the group IV semiconductors, as is the case for the fully miscible silicon-germanium (SiGe) alloys. However, theoretical considerations have shown that GeSn alloys with metastable compositions will have properties of great interest from the perspective of semiconductor device design.

The first and most intuitive property is the change of the lattice constant. The α-Sn allotrope has a lattice constant of 6.4892 Å,[13] compared to the 5.6571 Å of Ge.[14] It is therefore possible to achieve materials with lattice constants between these two extremes by an alloying process. One technological significance of such materials lies in the fact that they can be used as stressors for Ge channel material in device applications. The use of SiGe for creating strained Si sets a precedent for this type of process. Applying tensile strain to Si in transistors has paved the way for major increases in carrier mobility.[3,15] Strained Ge has the property of possessing even faster carrier transport capabilities. Furthermore, it has been suggested that Ge alloyed with Sn has higher carrier mobilities than Ge itself, which raises the possibility of fabricating transistors based on GeSn.[16–19]

The second aspect of GeSn alloys which is of technological interest is their use in bandgap engineering of Ge. Two features of the change in band structure upon alloying with Sn are

of particular importance. Firstly the band gap is reduced, causing a redshift of the wavelengths that can be used for emission and detection purposes.[20,21] This in turn allows the fabrication of GeSn based detectors that can cover the entire telecommunication bandwidth and beyond, even into the mid-infrared region. Such detectors, being composed of entirely group IV materials, can be integrated into existing Si platforms. At wavelength of several microns, GeSn based devices become potential candidates for use in infrared (IR) cameras and sensors which can be used for spectroscopic analyses. These may even be combined with Si to fabricate lab-on-chip devices to be used in environmental analysis.[22] Secondly, upon alloying with Sn, the reduction of the direct gap located at the Γ point is greater than the reduction of the indirect gap at the L point, the latter being the fundamental band gap of elemental Ge. Therefore, when sufficient amount of Sn is incorporated into the Ge lattice, a direct gap semiconductor can be synthesized. The most potent use of such a direct gap material would be the manufacture of lasers.[23,24] A laser made of GeSn can be directly integrated with prevalent Si microelectronics. Therefore it would be a major milestone in achieving optical on-chip communication, leading the way to faster and more energy efficient electronic devices.

2.2. History of Materials Synthesis and Elucidation of Fundamental Physical Properties

Due to the range of extremely beneficial applications, growth of GeSn alloys with Sn compositions beyond the thermodynamic solubility limit has been a topic of interest to researches for a number of years. The first experimental work with a bearing to this area is the growth of α-Sn on InSb and CdTe substrates using molecular beam epitaxy (MBE) during the 1980's.[25] This work showed that the problems posed by the thermodynamic instability of the Sn allotrope of interest can be successfully circumvented by using growth

conditions which maintained low temperature, far from equilibrium conditions. At about the same time, Goodman speculated on the possibility of obtaining direct gap materials based on GeSn alloys.[26] More detailed theoretical investigation of the band structure of GeSn was later conducted by Jenkins and Dow.[27] Shortly thereafter, successful experimental synthesis of GeSn crystalline films using MBE techniques was demonstrated by several authors.[28–32]

In subsequent work, the indirect and direct transition energies were determined experimentally, and it was evident that the actual values deviate strongly from earlier theoretical predictions.[33] These results led to a more thorough investigation of the optical properties of GeSn. Experimental studies were conducted by studying GeSn films using Fourier transform infrared interferometry,[34,35] spectroscopic ellipsometry,[36] photoreflectance spectroscopy[37] and photoluminescence spectroscopy.[38–40] Theoretical calculations based on density functional theory[41,42] and empirical pseudopotential methods[43,44] agreed well with these experimental results, leading to an emerging consensus in literature that the indirect-direct crossover composition for the $Ge_{1-y}Sn_y$ alloy system (y_c) was in the range of y=0.06-0.13. This composition regime is much more amenable to experimental realization than the earlier prediction of y_c=0.20,[27] and increased hope that the practical demonstration of a direct gap group IV semiconductor material was within reach.

Furthermore, the crystal quality of the films produced by the various techniques has also improved overtime. Much of the early work mentioned above made use of MBE techniques, and several groups have continued their development in recent years.[38,45–48]

However, greater progress has been achieved in synthesis of device quality GeSn materials after the introduction of ultra-high vacuum chemical vapor deposition (UHV-CVD) methods at Arizona State University (ASU).[49,50] Several groups have since employed different chemical vapor deposition (CVD) techniques such as atmospheric pressure CVD (APCVD),[51] reduced pressure CVD (RPCVD)[52,53] and even metal organic CVD (MOCVD)[54] for the growth of GeSn alloys with great success, as will be discussed in greater detail below. The major milestones achieved using both techniques have also been summarized in recent reviews.[55,56] Alternate deposition techniques such as solid phase epitaxy[57] and magnetron sputtering[58] have also been investigated. Overall, tremendous progress has been made in demonstrating the potential viability of this novel semiconductor material in practical applications.

2.3. Progress in Device Implementation

Several researchers have investigated the possibility of using GeSn in advanced Ge *p*-channel metal-oxide-semiconductor field-effect transistors (MOSFETs). One focus in this area has been on using GeSn as source/drain stressors to impart compressive strain on the active Ge channel. Proof-of-concept devices have been reported in literature, which demonstrate the viability of this design concept.[59,60] As an alternative method of using GeSn alloys to obtain the same benefit, relaxed GeSn has been used as substrates to produce tensile strained Ge epilayers.[59] When used in devices, this material has increased hole and electron mobilities, in contrast to the compressively strained case, where the mobility enhancement is only observed for holes.

In addition to their use in stress implementation, GeSn alloys have themselves been used as channel materials for MOSFETs. Increased carrier mobility resulting from the modified band structure of the alloy in comparison to Ge results in improved performance, as has been demonstrated for pMOSFETs fabricated using GeSn as channel material.[17,51,61] In addition, the reduced band gap offers additional pathway for using GeSn in next-generation microelectronic devices, by increasing the band-to-band tunneling probability. This makes GeSn a promising material for fabrication of tunneling field-effect transistors (TFETs), which are being considered as an alternative to MOSFETs due to their superior power efficiency. Several groups have demonstrated experimental TFETs fabricated from GeSn, making this materials system a candidate worthy of consideration for practically implementing TFET technology.[62–64] Finally, research on interface engineering for gate stack formation[65,66] and metal contact formation to GeSn materials[67] has also been ongoing.

In parallel with the development of GeSn based transistors, prototype light detection and emission devices have also been developed by several groups. The first to report such a device were Mathews and coworkers, who reported photoresponse from *pin* heterostructure photodiodes fabricated on Si platforms.[20] Electroluminescence (EL) from devices with the same architecture were reported by Roucka *et al*.[21] These results show the feasibility of using this type of detector in the telecommunications arena for covering the entire band range.[20,68] While the reduction of band gap required for this purpose can be achieved with an alloy with as little as 2% Sn, other applications such as IR sensors has spurred the development of prototype devices incorporating increasing amounts of Sn, which push the operable wavelengths further into the mid-IR region. MBE techniques have been used by Kasper's group to fabricate devices in which the active components have up

to 4% Sn.[45,69,70] Tseng *et al.* have reported a light emitting diode (LED) comprising of y=0.08 $Ge_{1-y}Sn_y$ alloy, also grown using MBE techniques.[48,71] More recently Du and coworkers to demonstrated EL from a y=0.08 device grown using CVD techniques.[72] All of the above devices use a *pin* architecture in which the light emission occurs from an intrinsic alloy sandwiched between *p*- and *n*- type doped Ge layers which act as electrical contacts. Gupta *et al.* were the first to demonstrate EL from a *pn* device with a GeSn component. In this case, emission was obtained from the *p*-GeSn layer which was deposited on an *n*-Ge substrate which completed the device.[73]

3. Outline of Current Work

Many milestones in GeSn research were achieved at ASU. These include the abovementioned demonstration of the first working GeSn LED,[21] and measurement of photoluminescence (PL) from GeSn alloy films grown directly on Si.[74] The materials that allowed these achievements were deposited Si(100) wafers using UHV-CVD techniques. The key to the success of these methods was the use of a new class of precursors that are highly reactive at low temperatures. The initial stage of development of these techniques was first reported by Taraci *et al.* who used digermane (Ge_2H_6) as the precursor containing Ge and phenyldeuterostannane ($PhSnD_3$) for delivery of Sn.[49] Bauer *et al.* subsequently replaced the carbon containing $PhSnD_3$ with the fully inorganic source deuterostannane (SnD_4).[50] Higher reactivity Ge precursors in the form of trigermane (Ge_3H_8) and tetragermane (Ge_4H_{10}) were introduced by Grzybowski *et al.* in order to further enhance the low temperature compatibility of this method.[75] While these methods have been successful in producing a wide range of GeSn alloys suitable for optical studies and device fabrication, obtaining highly crystalline material at and beyond the indirect-direct

composition proved challenging. One major limitation was the use of Si substrates. The large lattice mismatch between the alloy and the substrate produces a high density of defects, and the rapidly decreasing thermal stability of $Ge_{1-y}Sn_y$ alloys as they near y_c limits the applicability of thermal treatments used on lower composition alloys to improve crystal quality.

3.1. Growth of High Sn Content Alloys on Ge Buffered Si Substrates

In order to overcome this limitation, the work described in this thesis applied the above UHV-CVD techniques for deposition of GeSn on Ge buffered Si substrates, also known as virtual Ge substrates. Such substrates were first used for the growth of GeSn films because they allow the integration of the alloys with Si, while providing a more compatible growth platform.[76] The cost effectiveness and mechanical robustness compared to Ge wafers also make them a popular option as a substrate for GeSn deposition. The work described here made use of high quality virtual Ge substrates produced using the methods first described by Xu *et al*.[77] As an extension of this, the use of Ge_5H_{12} as a potential route for improving the deposition of Ge on Si was investigated, and will be described in Chapter 3.

3.2. Measurement of Photoluminescence from GeSn Alloys

The GeSn alloy films grown on the new Ge/Si(100) substrates were found to possess a level of exceptional crystallinity suitable for observation of room temperature PL without the need for additional thermal treatment. The growth of these films will be described in Chapter 5. The PL intensity from these films was high enough to allow the unambiguous determination of the indirect gap emission in $Ge_{1-y}Sn_y$ alloys with compositions up to y=0.06. Combining the indirect gap energies obtained from the above measurements with

direct gap emission observed from alloys with compositions up to y=0.11, it was possible to determine the y_c using PL techniques for the first time.

3.3. Development of Low Temperature Hydride Chemistries for the Doping of Ge and GeSn

The advances made in PL studies of GeSn by growing the alloys on virtual Ge substrates suggests that similar improvements in device performance can be made by applying the same strategy for GeSn LEDs and photodetectors. However, the synthesis of *pin* structures using CVD techniques requires dopant sources compatible with the chemistry of the reactive hydride precursors used for the growths. The use of group V germyl compounds with the formula $M(GeH_3)_3$ (M = P, As, Sb) for the doping of GeSn alloys has been pioneered at ASU.[78–80] In this work, systematic studies on doping of Ge using these precursors was carried out with the aim of understanding the full capabilities of this class of compounds. In addition, the compounds trisilylarsine ($As(SiH_3)_3$) and stibine (SbD_3) were introduced for the first time for the doping of Ge. Doping of Ge using S was also investigated. These results are presented in Chapter 4. These high reactivity doping agents were also used for the doping of GeSn alloys grown on Ge buffered Si substrates, as described in Chapter 6. The study of these doped materials using PL advanced earlier work which show substantial enhancement in emission intensity when GeSn is *n*-type doped. The materials created in this work were later shown to exhibit room temperature lasing, as described in Reference 81.

3.4. Optical Devices from GeSn Alloys

Such advances in growth of GeSn alloys with superior optical properties and the doping of these materials allowed the fabrication of efficient $Ge_{1-y}Sn_y$ LEDs with $y \geq y_c$ for the first

time. Initial prototypes consisted of an *n*-Ge/*i*-$Ge_{1-y}Sn_y$/*p*-$Ge_{1-z}Sn_z$ ($z<y$) design. The impact of directness of the band gap and the defect distribution within the diode stack on the emission properties of these devices were described.[82] An *n*-$Ge_{1-x}Sn_x$/*i*-$Ge_{1-y}Sn_y$/*p*-$Ge_{1-z}Sn_z$ design leading to enhanced light emission was also investigated,[83] as were the first *pn* diode structures comprising entirely of direct gap group IV materials.[84] The synthesis of GeSn alloys and devices required for these advances are described in Chapter 7.

4. Conclusion

This work discusses the progress made in developing synthetic techniques for GeSn alloys that allowed experimental demonstration of direct gap group IV materials as the active components of LEDs. These advances are an important first step in the realization of device architectures based on GeSn that can be used to implement a Si integrated laser.

At the time of writing, many of the results discussed above have been independently confirmed. PL studies were conducted by Al-Kabi *et al.* on $Ge_{1-y}Sn_y$ alloys with compositions up to y=0.12, and the indirect-direct transition determined by these authors is in good agreement with our results.[85] Low temperature PL of alloys with $y\approx0.12$ have further confirmed the direct nature of these materials.[86] A major milestone which vindicates the effort directed towards the search for a direct gap GeSn alloy was the optically pumped GeSn laser reported in 2015 by Wirths *et al.*[23] Progress has also been made in fabricating electrically injected light emitting devices based on GeSn alloys. Very recently, Yu *et al.* have demonstrated light emission from a double heterostructure diode with a Sn content of y=0.10.[87] Pham *et al.* have shown photodetectors containing alloys of the same composition, corresponding to a detector cutoff of 2.6 μm.[88] Stange *et al.* have investigated

GeSn multi quantum well LEDs with y=0.08.[89] Furthermore, Esaki diode behavior for devices containing y=0.11 alloys was reported by Schulte-Braucks and coworkers, confirming the possibility of fabricating diode structures using entirely direct gap group IV materials.[90]

The advances made in the doping of Ge described in this work can potentially have a significant impact on future microelectronic devices, in addition to photonic analogs. While *in situ* doping techniques developed here have yet to be used in the electronics arena, they represent an important pathway through with Ge based *p* and *n* MOSFET devices can be fabricated. Coupled with strain engineering capabilities afforded by GeSn, the outlook for fabricating high performance transistors based on Ge in the near future is promising. Even greater performance enhancements may be possible by using GeSn alloys for such microelectronic devices. Therefore the work described here in synthesizing doped alloy materials has a high degree of technological significance.

In conclusion, the GeSn alloys system has reached a level of maturity that clearly demonstrates its potential in next generation microelectronic and optoelectronic devices. Further research in this arena can be expected to continue unabated, in order to further develop the technologies necessary for practical applications. The improvement in device performance resulting from integration of GeSn alloys in mainstream products is to be eagerly anticipated.

CHAPTER TWO

Synthesis of CVD Precursors for Deposition of Intrinsic and Doped Ge and GeSn

1. Introduction

This chapter describes the synthetic procedures employed for the preparation of various precursors used throughout this work. These compounds exhibit high reactivity, enabling CVD at low temperatures. They are also fully inorganic, eliminating the introduction of carbon impurities into the deposition environment. The methods described below were used to synthesize these compounds with semiconductor grade purity, and in gram scale quantities required for CVD processes. All synthetic procedures were carried out using Schlenk techniques in order to ensure that the products did not come into contact with oxygen or moisture. It must be stressed that many of the chemicals described herein are pyrophoric, and requisite precautions must be taken when attempting these syntheses in order to ensure the safety of the operators.

2. Synthesis of Trigermane and Tetragermane

The deposition of Ge and GeSn films described in the subsequent chapters requires gram quantities of trigermane and tetragermane precursors of semiconductor grade purity. The synthetic techniques suitable for this purpose was first described by Grzybowski *et al.*[91] The products are obtained via the thermolysis of digermane, which occurs in a heated Pyrex tube through which a continuous flow of the reactant diluted in H_2 is maintained. The reactions which result in the desired products are as follows:

$$Ge_2H_6 + Ge_2H_6 \Rightarrow GeH_4 + Ge_3H_8 \qquad (2.1)$$

$$Ge_2H_6 + Ge_3H_8 \Rightarrow GeH_4 + Ge_4H_{10} \qquad (2.2)$$

This same experimental setup was used for producing the required precursors in this work. The methodology was slightly modified to enhance the efficiency of the process.

During a typical reaction, 6-7 g of Ge_2H_6 is used as the starting material, which is purchased as a 30% mixture in H_2 from Air Liquide Advanced Materials. The reaction is done in a controlled manner by condensing the Ge_2H_6 into a bubbler in which it is kept at a temperature of -30°C and flowing H_2 through the liquid at a rate of 125 mL/min. The H_2 acts as a carrier gas for transporting the Ge_2H_6 to the reaction zone, which is a piece of Pyrex tubing 2.5 cm in diameter and ≈25 cm long, heated to 250°C using a resistance furnace. The Pyrex tubing is lightly packed with Pyrex wool in order to increase the catalytic surface area available for the reaction. The condensable exhaust gases are then collected in two serially connected traps held at -196°C. The pressure within the system is kept at 1 atm by means of a mercury relief valve through which the uncondensed H_2 flows out.

The collected gases are then separated using trap-to-trap distillation. The Ge_4H_{10} can be collected in a -25°C trap and the Ge_3H_8 in a -78°C trap. The unreacted Ge_2H_6 and the GeH_4 byproduct are collected in -110°C and -196°C traps, respectively. The purity of the products of interest is established using gas phase Fourier transform infrared spectroscopy (FTIR). For Ge_3H_8, the spectrum has peaks at (cm^{-1}) 2131 (m), 2077 (st), 2021 (sh), 928 (w), 879 (m), 794 (st), 700 (w), 632 (st), 594 (vw), 571 (vw), 517 (w), and 424 (w). The Ge_4H_{10} spectrum contains the peaks (cm^{-1}) 2129 (m), 2075 (vst), 2013 (sh), 874 (m), 852 (m), 793 (st), 785 (st), 692 (w), 640 (st), 592 (st), 445 (w). These spectra are illustrated in Figure 1 (a) and (b), respectively.

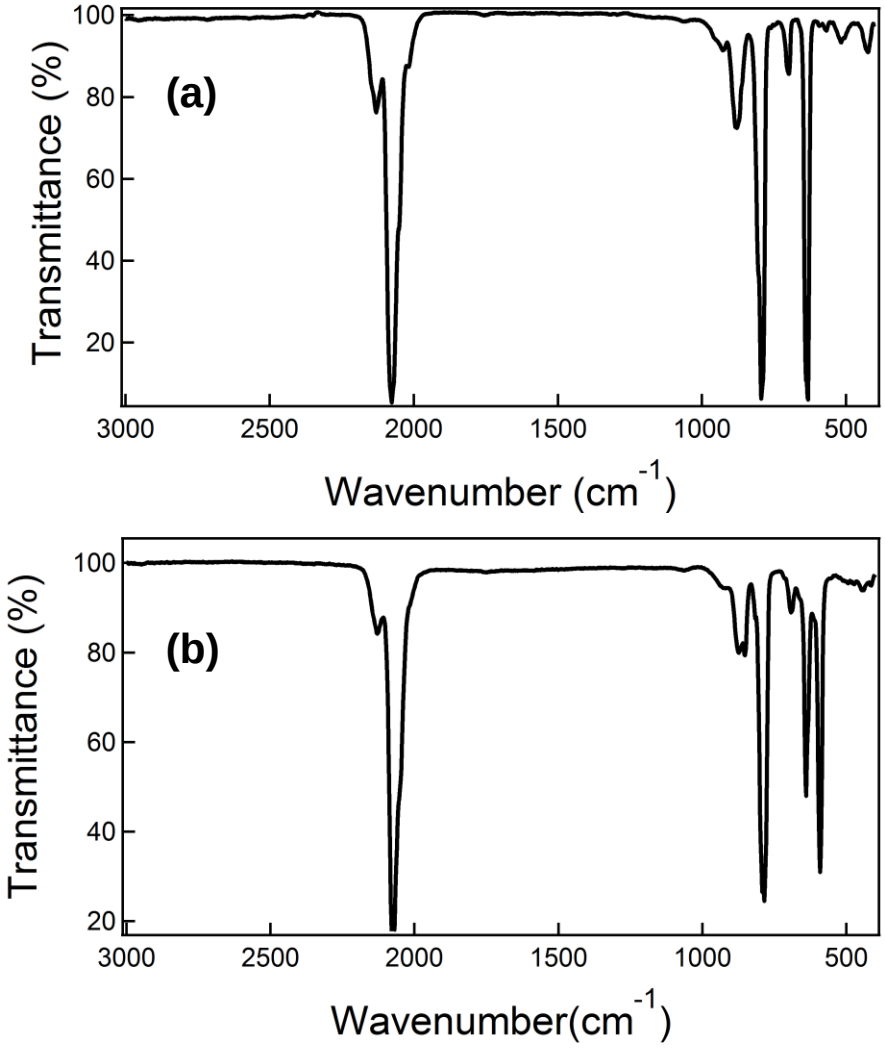

Figure 1 – FTIR spectra of (a) Ge_3H_8 and (b) Ge_4H_{10}

It is found that ≈70% of the Ge_2H_6 is recovered unreacted from this procedure. Typically 0.7-0.8 g of Ge_3H_8 can be recovered, and 0.2-0.3 g of Ge_4H_{10} is also obtained. If only reaction (2.1) is assumed as taking place, the amount of Ge_3H_8 obtained represents a yield of 45%. However, when both reactions (2.1) and (2.2) are considered, where some of the Ge_3H_8 produced from reaction (2.1) reacts with more Ge_2H_6 to form Ge_4H_{10}, the calculated percentage yield increases to 60%. Therefore this procedure is a convenient and efficient

method of obtaining higher order germanes. The ratio of Ge_3H_8 and Ge_4H_{10} products can also be adjusted if necessary. Reducing the flow rate of the carrier H_2 will increase the amount of Ge_4H_{10} produced. The same effect can be obtained by increasing the density of the Pyrex wool packing in the reaction zone.

The products were stored at room temperature under H_2 atmosphere. No decomposition was observed over a period of several months. The Ge_3H_8 product was used in the growth of doped Ge films described in Chapter 4, as well as in synthesis of GeSn described in Chapters 5, 6 and 7. The Ge_4H_{10} was used in the fabrication of virtual Ge substrates used in the same chapters.

3. Synthesis of Deuterostannane

Deuterostannane was synthesized using a modified version of the method reported by Norman *et al.*,[92] which has been employed in several earlier studies on GeSn.[50,93,94] The synthesis is achieved by reduction of tin(IV) chloride ($SnCl_4$) with lithium aluminium deuteride ($LiAlD_4$). The $SnCl_4$ was purchased from Sigma-Aldrich. The $LiAlD_4$ was typically purchased from Cambridge Isotopes, but when it was not available, was easily synthesized by reducing aluminium chloride ($AlCl_3$) with lithium deuteride (LiD) using the method described by Finholt and coworkers.[95] To conduct the $LiAlD_4$ synthesis, 4.5 g (500 mmol) of finely ground LiD is placed in a 250 mL round bottom flask along with 100 mL of diethyl ether. This is cooled to -78°C, and 12 g (90 mmol) of anhydrous $AlCl_3$ is dissolved in ≈60 mL of diethyl ether is slowly added to it via a liquid addition funnel while stirring under inert atmosphere. The initial stages of addition must be conducted especially slowly in order to prevent buildup of unreacted $AlCl_3$ in the mixture, which can prompt a

vigorous reaction at the start. Once all the $AlCl_3$ is added, the reaction is stirred overnight while allowing it to warm to room temperature. The liquid, containing dissolved $LiAlD_4$, is then cannular filtered to a separate vial from which the ether is removed under vacuum. Typical yield of the solid product obtained in this manner is ≈50%, which may be improved by successive washing of the residue remaining after the reaction to collect all of the soluble product.

The SnD_4 reaction was carried out in a 3-neck round bottom flask in which 2.5-3.0 g of $LiAlD_4$ (60-70 mmol) was placed along with 100 mL of dried diglyme, which acts as the solvent. The $SnCl_4$ (4-5 g, 15-19 mmol) was dissolved in a separate aliquot of diglyme (40 mL), and this solution is slowly added to the $LiAlD_4$ using a jacketed liquid addition funnel. The jacket was kept at -65°C and the solution in the round bottom flask was kept at -78°C throughout the addition. The gas generated from the reaction was continuously pumped out through two traps held at -196°C, while maintaining a slight pressure of ~20 Torr in the system. The reaction leading to the generation of SnD_4 is given below.

$$SnCl_4 + LiAlD_4 \Rightarrow SnD_4 + LiCl + AlCl_3 \qquad (2.3)$$

The collected SnD_4 may contain trace organic impurities, which can be easily removed by trap to trap distillation through a pair of -110°C traps, and a -196°C trap is used to collect the SnD_4. This procedure gave SnD_4 in yields up to 75%. The purity is verified using FTIR, and a sample spectrum is given in Figure 2. [FTIR (cm^{-1}): 2704 (vw), 1905 (vw), 1402 (m), 1367 (vst), 1334 (m), 540 (w), 501 (st), 486 (st)].

For long term storage of the product, liquid nitrogen temperatures must be used in order to prevent decomposition. The SnD_4 was used in the synthesis of GeSn alloys described in Chapters 5, 6, and 7.

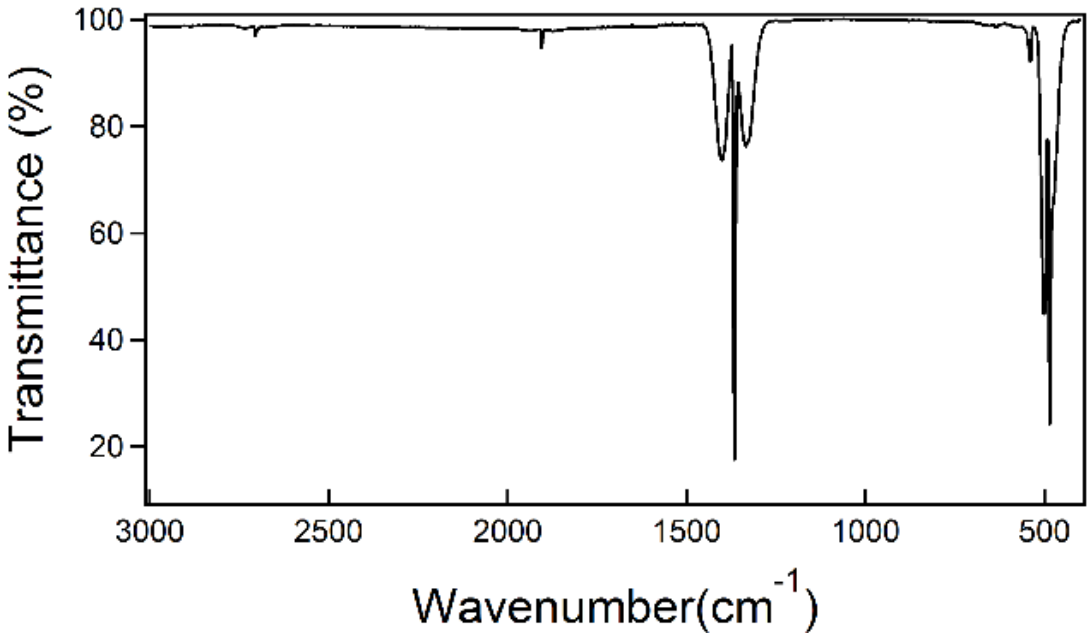

Figure 2 – FTIR spectrum of SnD_4.

4. Synthesis of Trisilylphosphine ($P(SiH_3)_3$), Trisilylarsine ($As(SiH_3)_3$) and Trisilylstibine ($Sb(SiH_3)_3$)

A convenient method for synthesis of trisilyl- group V compounds was reported by Grzybowki.[96] This involves the reaction of the lithium salt Li_3M (M=P, As, Sb) with bromosilane ($BrSiH_3$) or chlorosilane ($ClSiH_3$) in diethylether (Et_2O). It was found that while the use of solvent is more efficient, acceptable yields could be obtained by performing the reaction in neat $ClSiH_3$. The $ClSiH_3$ was purchased from Voltaix. The Li salts were synthesized in-house via the reaction of stoichiometric amounts of the respective elements at 450°C. The general reaction is given below:

$$Li_3M + 3\ ClSiH_3 \Rightarrow M(SiH_3)_3 + 3\ LiCl \quad (M=P, As, Sb) \qquad (2.4)$$

The reaction vessel is a stainless steel cylinder with a volume of ≈20 cm^3. The Li salt was added to the cylinder under inert atmosphere. Typical amounts of salt used were 0.5 g for Li_3P (10 mmol), and 1.0 g for Li_3As and Li_3Sb (10 mmol and 7 mmol respectively). The amount of $ClSiH_3$ used was 2.0 g (≈600 LTorr, 32 mmol) for the P and As compounds, and 1.5 g (≈450 LTorr, 24 mmol) for the Sb. This corresponds to a 10-15% excess of $ClSiH_3$, which was condensed on to the Li salt, and the reaction mixture was allowed to warm up to room temperature after sealing the vessel. At room temperature, the $ClSiH_3$ is expected to be in liquid form with a vapor pressure of 6.5 atm.

The reaction was allowed to proceed for 16 hrs for the P compound, and 5 days for the As and Sb compounds. The trisilylphosphine ($P(SiH_3)_3$) was purified by trap-to-trap distillation through -78°C and -196°C traps, and the -78°C trap contained the pure product, and the -196°C trap unreacted $ClSiH_3$. The yield of the reaction was 46%. The trisilylarsine ($As(SiH_3)_3$) compound was initially trapped in a -45°C trap, and further purified by a second distillation through -35°C traps, which removed more volatile impurities. The yield obtained was 14%. For trisilylstibine ($Sb(SiH_3)_3$), a -35°C trap was used to trap out the pure product. The yield was 2%. The purities of the products were determined through gas phase FTIR. The observed peaks for the three compounds are given in below in Table 1. All above compounds were stored at room temperature under inert atmosphere, and were used in the doping of Ge films and GeSn alloys as described in Chapters 4, 6 and 7.

Table 1 – FTIR absorption frequencies of $P(SiH_3)_3$, $As(SiH_3)_3$ and $Sb(SiH_3)_3$

FTIR(cm^{-1})		
$P(SiH_3)_3$	$As(SiH_3)_3$	$Sb(SiH_3)_3$
2171(st)	2165(st)	2162(st)
1866(vw)	1125(w)	1869(w)
1124(m)	933(st)	1119(w)
947(st)	873(st)	956(m)
937(st)	769(vw)	901(m)
746(w)	595(w)	851(st)
625(w)	542(w)	762(w)
572(w)		570(w)
467(w)		

5. Synthesis of Trigermylphosphine

Trigermylphosphine ($P(GeH_3)_3$) was synthesized through the reaction of chlorogermane ($ClGeH_3$) with lithium phosphide (Li_3P), as described by Grzybowski.[96]

$$Li_3P + 3\ ClGeH_3 \Rightarrow P(GeH_3)_3 + 3\ LiCl \qquad (2.5)$$

The Li_3P (1 g, 19 mmol) was placed in a 100 mL Schlenk flask under inert atmosphere. Thereafter, 1300 LTorr of $ClGeH_3$ (70 mmol) was condensed into the reaction vessel, together with approximately 50 mL of Et_2O, which acts as the solvent. The reaction was stirred overnight at -78°C. The product was separated from unreacted $ClGeH_3$ and the solvent by trap to trap distillation through -65°C and -196°C traps. The $P(GeH_3)_3$ is collected in the highest temperature trap, together with more volatile impurities believed to be partially substituted phosphines. These volatile species can be removed by a further distillation step using -25°C, -60°C, and -196°C traps. The purity of the final product is confirmed by FTIR [FTIR (cm^{-1}): 2134 (w), 2085 (st), 2001 (w), 957 (w), 882 (m), 838 (m), 802 (vst), 564 (w), 515 (w)].

The final yield obtained is 27%, similar to the 20% reported by Grzybowski.[96] $P(GeH_3)_3$ can be stored in a dry-box freezer kept at -25°C for several months with minimal decomposition. It was used for doping GeSn alloys as described in Chapter 6, and in the fabrication of *n*-type doped virtual Ge substrates, as described in Chapter 7.

6. Synthesis of Deuterostibine

Deuterostibine (SbD_3) was synthesized by reducing antimony(III) chloride ($SbCl_3$) with $LiAlD_4$, a method which was first described by Todd *et al.*[97] (who also used sodium borodeuteride as the reducing agent) based on the following reaction:

$$4\ SbCl_3 + 3\ LiAlD_4 \Rightarrow 4\ SbD_3 + 3\ LiCl + 3\ AlCl_3 \quad (2.6)$$

The reaction was conducted in a two-neck round bottom flask in which 0.3 g of $LiAlD_4$ (7 mmol) dissolved in 40 mL of diglyme was placed. This solution was cooled to -70°C, and a solution containing 0.5 g $SbCl_3$ (2 mmol) in diglyme held at -50°C was slowly added to it via an addition funnel. The system was dynamically pumped such that the pressure was kept at 20 Torr, and the removed gases were pulled through traps held at -78°C and -196°C. The first trap condenses most volatile organic impurities, while the product condenses in the -196°C traps. Once the addition was complete, the reaction mixture was allowed to warm up to room temperature to allow the reaction to reach completion. Continuous removal of the generated gases was maintained during the warm up process.

The product collected in the -196°C traps contains minor quantities of organic impurities, which can be removed by sequential trap to trap distillations through -110°C and -196°C traps, where the former collects the impurities. The final yield of pure product is 60%, and the FTIR spectrum [FTIR (cm^{-1}): 2686 (vw), 1892 (vw), 1628 (vw), 1400 (m), 1360 (st),

1321 (m), 1223 (vw), 592 (m), 559 (m)] was compared with accepted literature values to validate the purity.[97] The product can be stored at room temperature for several weeks when the pressure of the gas is kept below 10 Torr. SbD_3 was used for the doping of Ge films and GeSn alloys, as described in Chapters 4 and 6 respectively.

7. Synthesis of Disilylsulfide

Literature methods for the synthesis of disilylsulfide ($S(SiH_3)_2$) involves either toxic Hg compounds, or organic solvents.[98] Due to the difficulties posed when using these methods, an alternative synthetic route was developed to obtain viable quantities of semiconductor grade $S(SiH_3)_2$. This involves the reaction of bis(triphenyltin)sulfide ($S(SnPh_3)_2$) with bromosilane ($BrSiH_3$), as described by the equation below. The $S(SnPh_3)_2$ is commercially available from Gelest and was used as received, while the $BrSiH_3$ was synthesized in house by reacting phenylsilane ($PhSiH_3$) with hydrogen bromide (HBr).

$$S(SnPh_3)_2 + 2\ BrSiH_3 \Rightarrow S(SiH_3)_2 + 2\ BrSnPh_3 \qquad (2.7)$$

The above reaction was conducted by placing 3.6 g of $S(SnPh_3)_2$ (5 mmol) in a Schlenk flask under inert atmosphere and then condensing 90% excess of $BrSiH_3$ (350 LTorr, 19 mmol) onto this solid. The mixture was then allowed to warm up to -10°C, at which temperature the reaction was allowed to proceed for 1 hr. Trap to trap distillation was then used to purify the product. A -78°C trap was found to condense the $S(SiH_3)_2$, while unreacted $BrSiH_3$ was recovered using -196°C traps. The yield of the reaction is 60%.

FTIR and NMR were used to identify the product and to ensure its purity [FTIR (cm^{-1}): 2186 (st), 956 (st), 916 (vst), 907 (st), 640 (w), 529 (m), 510 (m)]. The NMR spectrum of the product collected using $CDCl_3$ solvent shows a strong singlet at 4.389 ppm and satellite

peaks at 4.108/4.672 ppm associated with the equivalent $-SiH_3$ protons and the splitting of this signal by the ^{29}Si isotope, as shown in Figure 3. This compound was used for doping Ge with S as described in Chapter 4.

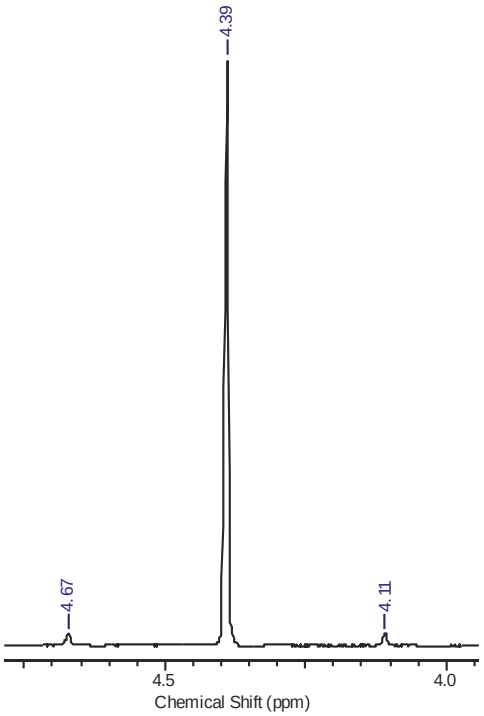

Figure 3 - ^{1}H NMR spectrum of $S(SiH_3)_2$ in $CDCl_3$ solvent

8. Synthesis of Digermylsulfide

For the synthesis of digermylsulfide ($S(GeH_3)_2$), a metathesis reaction was first reported by Goldfarb and Sujishi which used $S(SiH_3)_2$ and chlorogermane ($ClGeH_3$) as the starting materials.[99] The synthetic procedure for $S(SiH_3)_2$ was described above, while the $ClGH_3$ can be easily synthesized by chlorinating GeH_4 with $SnCl_4$.[100] The reaction was conducted in a thick walled Pyrex container equipped with a vacuum valve. Both reactants were condensed into the vessel and it was then allowed to warm up to room temperature. The reaction is instantaneous and is given below.

$$S(SiH_3)_2 + 2\ ClGeH_3 \Rightarrow S(GeH_3)_2 + 2\ ClSiH_3 \qquad (2.8)$$

After 5 min at room temperature, the product was purified using trap-to-trap distillation, and a trap held at -60°C was found to condense the product, which was further purified by passing through a pair of -30°C traps to remove volatile impurities. Starting from 35 LTorr (1.9 mmol) of $S(SiH_3)_2$ and 75 LTorr (4.0 mmol) of $ClGeH_3$, it was possible to obtain 15 LTorr (0.8 mmol) of the product, which is a yield of 45%. The purity of the product was verified by comparing the FTIR spectra (cm^{-1}) at 2104 (st), 2084 (st), 847 (m), 855 (m), 825 (vst), 578 (w), 555 (w), 412 (m) to literature values.[99] The NMR spectrum shows a singlet at 4.716 ppm associated with the $–GeH_3$ protons, as shown below in Figure 4.

The $S(GeH_3)_2$ is unstable at room temperature, but could be stored at -25°C in a dry-box freezer for extended periods. It was used for doping of Ge as described in Chapter 4.

9. Synthesis of Diborane

Diborane (B_2H_6) was synthesized using methods described by Norman *et al*.[101] In order to conduct the reaction, 35 mL of syrupy phosphoric acid (H_3PO_4) was added to a 500 mL round bottom flask and degassed by applying vacuum for several hours. The other reactant, potassium borohydride (KBH_4) was ground to a fine powder inside a dry-box, and placed in a side arm solid addition tube. The amount used was 1.7 g (32 mmol). The tube was connected to the flask using Schlenk techniques and the setup was evacuated. The solid was then slowly added to the acid over a period of ~1 hr with continuous stirring. The reaction generates B_2H_6 according to the following reaction.

$$2\ H_3PO_4 + 2\ KBH_4 \Rightarrow B_2H_6 + 2\ KH_2PO_4 + 2\ H_2 \qquad (2.9)$$

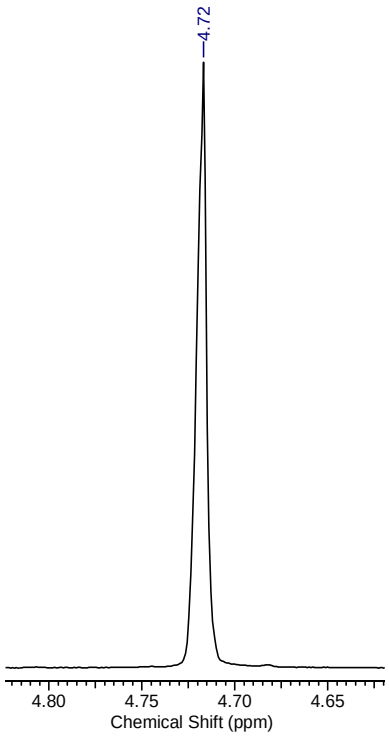

Figure 4 - ^{1}H NMR spectrum of $S(GeH_3)_2$ in $CDCl_3$ solvent

The generated gases are pumped through -78°C and -196°C traps. The former collects water vapor, and the product is trapped in the latter. The H_2 byproduct is pumped away. B_2H_6, which is a colorless gas at room temperature was obtained in a 35% yield. The FTIR spectrum exhibits peaks (cm^{-1}) 3660 (w), 2627 (m), 2594 (m), 2540 (m), 2519 (st), 2499 (m), 2345 (w), 1867 (w), 1622 (st), 1600 (vst), 1583 (st), 1194 (m), 1174 (m), 1153 (m), 974 (w), which agree well with literature values for B_2H_6.[99]

CHAPTER THREE

High-Order Ge-Hydride Chemistry for Low Temperature Ge Based Materials Fabrication: A Study of Pentagermane

Synopsis

This chapter presents a study of the synthesis of the high order Ge hydride pentagermane (Ge_5H_{12}) via thermolysis reactions previously used for the synthesis of Ge_3H_8 and Ge_4H_{10}. The thermodynamic properties of the various isomers and reaction pathways leading to the desired product are explored by computational methods, and the results are compared to experimental observations. Finally, Ge_5H_{12} is used in proof-of-principle experiments which demonstrate its viability as a precursor for epitaxy of high quality Ge on Si at low temperatures of ≈350°C.

Portions of this chapter were previously published by Grzybowski, G.; Chizmeshya, A. V. G.; Senaratne, C.; Menendez, J.; Kouvetakis, J. Fundamental experimental and theoretical aspects of high-order Ge-hydride chemistry for versatile low-temperature Ge-based materials fabrication. *J. Mater. Chem. C* **2013**, *1* (34), 5223. Reproduced by permission of The Royal Society of Chemistry.

1. Introduction

As mentioned in Chapter 1, Ge based materials are being extensively researched for use in fabricating components for optoelectronic and microelectronic devices integrated on to Si. Recent progress in growth of Ge directly of Si(100) has led to the development of novel devices such as Ge based lasers[10,11] and IR photodetectors.[8] Several techniques have been utilized for the production of atomically flat, defect free Ge on Si epilayers for such

applications, such as the use of $Si_{1-x}Ge_x$ graded buffer layers[102] or growth of an initiation layer at low temperatures (~320°C) followed by higher temperature (600°C) growth of the bulk material.[103–105] The former technique requires a graded buffer of several microns and is therefore difficult to implement in low cost applications. The major drawback of the latter technique is the incompatibility with CMOS processing conditions, due to the requirement of high growth temperature.

In this context, the high order Ge hydrides Ge_3H_8 and Ge_4H_{10} were first developed at ASU as an ideal way to simultaneously achieve the dual requirements of high crystalline quality and low growth temperatures.[91] The synthetic procedures for producing these precursors were described in Chapter 2. In addition to growth of Ge on Si, these compounds were later used for synthesis of GeSn binary and germanium-silicon-tin (GeSiSn) ternary alloys,[106,107] an aspect that will be further explored in later chapters. Among these compounds, Ge_4H_{10} was recently employed by Xu *et al.* to develop optimized synthetic procedures for producing Ge on Si films with device quality properties for subsequent applications as compliant platforms on Si.[77] The Ge films produced in the above work have thicknesses in the order of several microns and surface roughness < 1 nm indicating layer by layer growth. A maximum growth rate of 30 nm/min was observed at 400°C. Their deposition protocols have atomic incorporation efficiencies up to 50%, and are therefore suitable for low cost, high-throughput industrial processes. Ge on Si *pin* photodetectors were also fabricated using this technique, validating its practical utility. This procedure for producing high quality Ge films on Si will be extensively used in work described in subsequent chapters.

The successful introduction of Ge_4H_{10} as a viable deposition technology suggests that pentagermane (Ge_5H_{12}) and its various branched isomers are in principle the next logical choice in the oligomeric series of potential germyl hydride precursors for next generation, low temperature semiconductor processing. From a chemical point of view Ge_5H_{12} may in fact possess comparable reactivity to that of Ge_4H_{10}, but its significantly larger mass (375 amu) implies that the compound condenses as a high boiling point liquid with diminished vapor pressure at ambient conditions. The expected lack of volatility in this case represents a significant barrier towards adoption in vapor deposition techniques, suggesting that any further materials gains will be difficult to realize using standard vacuum based approaches. Alternatively, this compound may represent a useful delivery source in liquid form for atomic layer deposition (ALD) of devices requiring selective growth of nanoscale transistor architectures, since it may be potentially evaporated in situ as needed. On the other hand, the liquid compound may be suitable for solution-based depositions of semiconductor layers with bulk-like properties, since it exhibits a reasonable stability at room temperature and a facile thermal reactivity. The latter growth technique has attracted increasing attention recently in the ubiquitous silicon technology arena where thermal processing of liquid phase hydrides has been successfully implemented to manufacture electronic devices, opening the door for large-scale high-volume production via spin coating approaches. For example Si films have been grown via photochemical transformations or heat treatments of solutions containing either cyclopentasilane (Si_5H_{10})[108] or cyclohexasilane (Si_6H_{12}).[109] In this regard silicon films have also been produced via thermal decomposition of $Si_5(C_6H_5)_{10}$.[110] As in the case of Ge_5H_{12}, these compounds are of very limited utility as conventional CVD **s**ources due to negligible vapor

pressures. However, the enhanced reactivity of Si_5H_{10} allows complete and controllable elimination of the hydrogen atoms from the molecular cores to produce semiconductor structures and working thin-film transistors exhibiting state-of-the-art characteristics. In this context, analogous Ge-based technologies may be accessible using solvent-processable Ge_5H_{10} sources whose intrinsic properties seem to be ideal for this solution-type thin film crystal growth.

In view of the potential applications of Ge_5H_{12}, we explored synthetic pathways from both experimental and theoretical perspectives to produce this compound in high yield. As discussed in Chapter 2, high-order species can be obtained using a strategy based on reactions (3.1) and (3.2). The same strategy can be extended to obtain Ge_5H_{12} as described by reaction (3.3).

$$Ge_2H_6 + Ge_2H_6 \Rightarrow GeH_4 + Ge_3H_8 \quad Rx(3.1)$$

$$Ge_2H_6 + Ge_3H_8 \Rightarrow GeH_4 + Ge_4H_{10} \quad Rx(3.2)$$

$$Ge_2H_6 + Ge_4H_{10} \Rightarrow GeH_4 + Ge_5H_{12} \quad Rx(3.3)$$

To our knowledge, the synthetic scheme proposed above has never been reported. To study this possibility we conducted stoichiometric thermolysis reactions of gaseous Ge_2H_6 and Ge_3H_8 at 250°C , and we obtained Ge_4H_{10} (about 25-30 %) and small amounts of Ge_5H_{10}, suggesting the validity of eq. 3.2 and 3.3. To explain this outcome we propose a reaction mechanism by which the Ge_2H_6 starting material initially dissociates to form reactive GeH_2 intermediates. These in turn insert into existing Ge-Ge bonds of the co-reactant molecule to form the higher-order analog. To elucidate the thermodynamics underpinning the

observed tendency for the formation of Ge_3H_8 in (3.1), and its subsequent use to produce Ge_4H_{10} in (3.2), we calculated the free energies for (3.1)-(3.3) for a range of temperatures relevant to our experimental studies. The data indicate that the driving force for all above reactions is favorable, in agreement with the trends observed experimentally. In addition, as a part of our comprehensive study of germanium heavy hydrides we also carried out DFT-based simulations to obtain some fundamental properties of Ge_5H_{12}, as previously done for the Ge_4H_{10} analog.[107]

2. Thermochemistry Simulations

A distinctive aspect of Ge_5H_{12} is that it can adopt *neo*-, *iso*- and *n*-like isomeric forms corresponding to centered, branched or chained structures, with additional conformal variants within the branched and chained families. Here in our calculations we consider seven distinct isomers: *neo*-Ge_5H_{12}, two branched conformers (i_1-Ge_5H_{12} and i_2-Ge_5H_{12}) and four chained isomers derived from the linear chain *n*-Ge_5H_{12} but exhibiting various *anti-gauche* combinations. Accordingly, one objective of our computational work is to generate simulated IR spectra for all possible pentagermane isomers, for use in comparative "fingerprinting" with the observed spectra of gas phase precursor molecules, which are presumed to exist as an isomer mixture. Perhaps more importantly the purpose of our simulation studies is to: (i) identify the most thermodynamically stable pentagermane isomer species, and (ii) study reaction pathways to the desired Ge_4H_{10} and Ge_5H_{12} species as the main product in order to maximize their yield, as indicated above. In this connection, our related studies on tetragermane predicted that the free-energy of the *i*-Ge_4H_{10} species is ~4.4 kJ/mol lower than that of either the *n*-Ge_4H_{10} and *g*-Ge_4H_{10} isomers at standard conditions.[107] As demonstrated below the corresponding free-energy ordering in

pentagermane exhibits a very similar trend, with the *i*-Ge_5H_{12} being lower in free-energy than the *neo*-Ge_5H_{12} or *n*-Ge_5H_{12} isomers. These results are expected to provide valuable guidance in the design of experiments to produce Ge_4H_{10} and Ge_5H_{12}, which may be considered to be the ultimate high-efficiency Ge sources for the next generation device applications.

The computational approach adopted here follows that used in our prior successful studies on a wide range of lighter Ge-based hydrides, and is based on the use of B3LYP hybrid density functional theory (DFT) in conjunction with a standard 6-311G++(3df,3pd) basis set, as implemented in the *Gaussian03* code.[111] All calculations were performed using automatically generated auxiliary basis sets for charge density fitting and default convergence criteria for the self consistent field convergence and structure optimizations. Special care was taken to avoid grid pruning effects such as the generation of "noisy" structures leading to spurious soft-modes (typically associated with $–GeH_3$ rotor motion). Accordingly we consistently used the so-called "UltraFine" integration grid option in all calculations and verified that the harmonic normal mode frequencies are positive definite in all cases, indicating that the corresponding ground state structures are dynamically stable. The molecular structures and corresponding thermodynamic data for all isomers are summarized in Tables 2 and 3.

The standard thermochemistry output from *Gaussian03* at T=298K and P=1 atm is summarized in Table 3 and includes the static electronic energy of the molecules, E_0, as well as their thermally corrected counterparts for the free-energy (E_0+G_{th}). Based on a harmonic treatment for thermodynamic corrections the branched i_1-Ge_5H_{12} is predicted to

Table 2 - Summary of structural and energetic results for isomers of pentagermane. The α and β designations refer to external and internal Ge-Ge bond lengths, respectively. Ge-Ge-Ge bond angles containing a 3 or 4 centered Ge are denoted using γ, while those involving a sequence of chained atoms are labeled with ε. The subscripts "T" and "S" refer (respectively) to terminal and sagittal Ge-H bond length or H-Ge-H bond angle species, while an asterisk denotes a –Ge-H moiety bond length.

	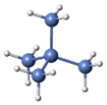	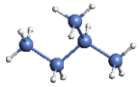	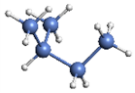	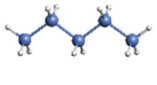	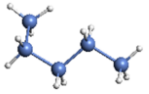	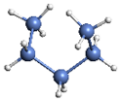	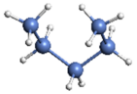
Designation	**neo-Ge_5H_{12}**	**i_1-Ge_5H_{12}**	**i_2-Ge_5H_{12}**	**n_1-Ge_5H_{12}**	**n_2-Ge_5H_{12}**	**n_3-Ge_5H_{12}**	**n_4-Ge_5H_{12}**
Point Group	T_d	C_1	C_s	C_{2v}	C_1	C_2	C_s
Bond Lengths (Å)							
α (Ge-Ge)	2.445 (×4)	2.451(x2), 2.446	2.450(×2), 2.445	2.446(×2)	2.445(×2)	2.444(×2)	2.444(×2), 2.451
β (Ge-Ge)	--	2.455	2.457	2.450(×2)	2.450(×2)	2.451(×2)	2.451(×2)
$(Ge-H)_T$	1.538 (×12)	1.538(×9)	1.538(×9)	1.538(×6)	1.538(×6)	1.537(×6)	1.537(×2), 1.538
$(Ge-H)_S$	--	1.542(×2), 1.546*	1.542(×2), 1.547*	1.542(×6)	1.542(×6)	1.542(×6)	1.542
Bond angles (degrees)							
γ ∠Ge-Ge-Ge	109.5	111.2, 111.6, 111.0	111.6, 111.7(×2)	--	--	--	--
ε ∠Ge-Ge-Ge	--	113.5	113.8	113.4(×2), 112.8	113.1(×2), 113.3	113.1(×2), 113.5	114.1(×2), 113.6
$(H-Ge-H)_T$	108.5 (×12)	108.4-108.5	108.3-108.5	108.4-108.5	108.4-108.5	108.4-108.5	108.4, 108.5(×2)
$(H-Ge-H)_S$	--	107.1	107.2	107.1(×2), 106.9	107.3(×2), 107.1	107.2(×2), 107.1	107.3
Dipole Moment (D)	0.0000	0.0623	0.0451	0.0225	0.0237	0.0031	0.0361

Table 3 - Thermochemistry data for the isomers depicted in Table 2, which includes the electronic ground state energy E_0, and the free-energy contribution G_{th}. Mode indices for rotors are listed together with their harmonic frequencies and their corresponding partition function contributions to the free energy. The net correction to the free-energy for the hindered rotor approximation are listed as ΔG_{th}^{HR}.

Designation	**neo-Ge_5H_{12}**	**i_1-Ge_5H_{12}**	**i_2-Ge_5H_{12}**	**n_1-Ge_5H_{12}**	**n_2-Ge_5H_{12}**	**n_3-Ge_5H_{12}**	**n_4-Ge_5H_{12}**
Thermochemistry (T=298K, P=1atm)							
E_0 (H)	-10392.32501	-10392.32357	-10392.32306	-10392.32333	-10392.32279	-10392.32228	-10392.32193
ΔE_0 (kJ/mol)	0	+3.8	+5.1	+4.4	+5.8	+7.2	+8.1
Harmonic (T=298K, 1 atm)							
G_{th} (H)	0.04867	0.04606	0.04772	0.04722	0.04783	0.04730	0.04812
E_0+G_{th} (H)	-10392.27634	-10392.27751	-10392.27534	-10392.27611	-10392.27496	-10392.27498	-10392.27381
$\Delta(E_0+G_{th})$ (kJ/mol)	+3.1	0	+5.7	+3.7	+6.7	+6.6	+9.7
Hind. Rotors Corrected (T=298K, 1 atm)							
ΔG_{th}^{HR}(H)	+0.000139	+0.000014	-0.000790	-0.000318	-0.000595	-0.000037	-0.000708
E_0+G_{th} (H)	-10392.27620	-10392.27750	-10392.27613	-10392.27643	-10392.27556	-10392.27502	-10392.27452
$\Delta(E_0+G_{th})$ (kJ/mol)	+3.4	0	+3.6	+2.8	+5.1	+6.5	+7.8

have the lowest free-energy, followed by *neo*-Ge_5H_{12} and the linear-chained n_1-Ge_5H_{12}. The free-energy of the latter species energies are +3.1 kJ/mol and +3.7 kJ/mol higher than the i_1-Ge_5H_{12} reference.

We note that while the normal mode frequencies used to compute the free-energy corrections for all isomers are positive definite, the manifold of "vibrations" corresponding to motion of the terminal $-GeH_3$ groups possess very low frequencies in the 50-100 cm^{-1} range. An examination of the potential energy surface corresponding to internal $-GeH_3$ rotation yields energy barriers in the range of 2-3 kJ/mol, indicating that these motions are more correctly described as hindered rotors. Accordingly, their individual contributions to the vibrational partition function were removed and replaced by appropriate hindered rotor counterparts, interpolated from the tables of Pitzer and Gwinn.[112] The net correction to the harmonic free-energy treatment, listed as ΔG_{th}^{HR} in the table, are typically small in magnitude (< 0.7 mH) and lead to a slight increase in the E_0+G_{th} free-energy values for the *neo*- and i_1- species, and lowering for the remaining isomers.

The main effect of the hindered rotor corrections to the thermochemistry is to the reverse the free-energy ordering between the *neo*- and n_1- isomers resulting in relative $\Delta(E_0+G_{th})$'s of +3.4 kJ/mol and +2.8 kJ/mol above that of i_1-Ge_5H_{12}. However, we note that the *neo*-Ge_5H_{12} value is very close to that of the second branched isomer i_2-Ge_5H_{12}, while the relative free-energies $\Delta(E_0+G_{th})$ of the remaining isomers chained conformers spans a range from 5-8 kJ/mol above the i_1-Ge_5H_{12} reference. Collectively, and perhaps most importantly, this suggest that the gas phase of Ge_5H_{12} is likely composed of a roughly equimolar mixture of i_1-, n_1- and *neo*- isomers.

3. Simulation of Vibrational Properties

Our main objective here is to systematically compare the vibrational spectra of pentagermane isomers in order to identify any features that could be used to distinguish or identify Ge_5H_{12} from its lighter Ge-hydride relatives, and tetragermane in particular which is expected to possess very similar properties. Typically these two compounds are separated by distillation and the gas phase IR spectra could in principle be used to establish their purity provided that distinguishing features exist. Figure 5 contains the main results of our calculations, separated into two categories corresponding to high-frequency Ge-H stretching vibrations (2000-2200 cm^{-1}), and lower frequency Ge-H wagging and bending motions as well as Ge-backbone vibrations (<1000 cm^{-1}). The frequencies in these plots were not scaled. However, well-established scale factors 0.995 and 0.975 for the low and high frequency ranges, respectively, are supported by much of our prior work on Si and Ge based hydrides at this level of theory and were used in our comparisons with observed spectra, below.

Here we describe the general trends by frequency range and intensity. For example, the very weak features occurring below about 400 cm^{-1} can be classified as follows: (i) The lowest frequency modes (< 100 cm^{-1}) are due to rotational motion of the terminal GeH_3 groups, (ii) torsional Ge-backbone vibrations occur between ~100-200 cm^{-1}, (iii) rocking $–GeH_2$- and -GeH_3 vibrations perpendicular to the -Ge-Ge- bonds are found in the 200-300 cm^{-1} range. More intense spectral features are found in the 400-700 cm^{-1} range and are assigned to in-phase $–GeH_2$- wagging motions parallel to the –Ge-Ge- backbone bonds (500-600 cm^{-1}), and their out-of-phase counterparts (600-700 cm^{-1}). A series of typically well-separated bands associated with in-phase proton wagging in the $–GeH_3$ groups occur

in the 700-850 cm^{-1} range. Finally, vibrations with frequencies 850-900 cm^{-1} are assigned to "scissor" motion of the protons in the $–GeH_2-$ and $–GeH_3$ groups, perpendicular to the -Ge-Ge- bonds. The most intense band among all of the isomers is found in *neo*-Ge_5H_{12} near ~780 cm^{-1}, and is due to concerted proton wagging directed along the axial Ge-Ge bond directions. The higher frequency portions of the calculated isomer spectra are also shown in the left panel of Figure 5, and indicate the usual complex band of frequencies corresponding to symmetric and anti-symmetric Ge-H stretches in various in-phase and anti-phase combinations. In general we find that the principal assignments are virtually identical to those reported in prior work on tetragermane. Another comparatively strong feature, found in the spectrum of the n_1-Ge_5H_{12} linear-chain conformer, devolves from highly coherent in-phase $–GeH_2-$ wagging motions parallel to the backbone. Due to its exclusive low-frequency position near ~560 cm^{-1} in relation to the spectra of all of the

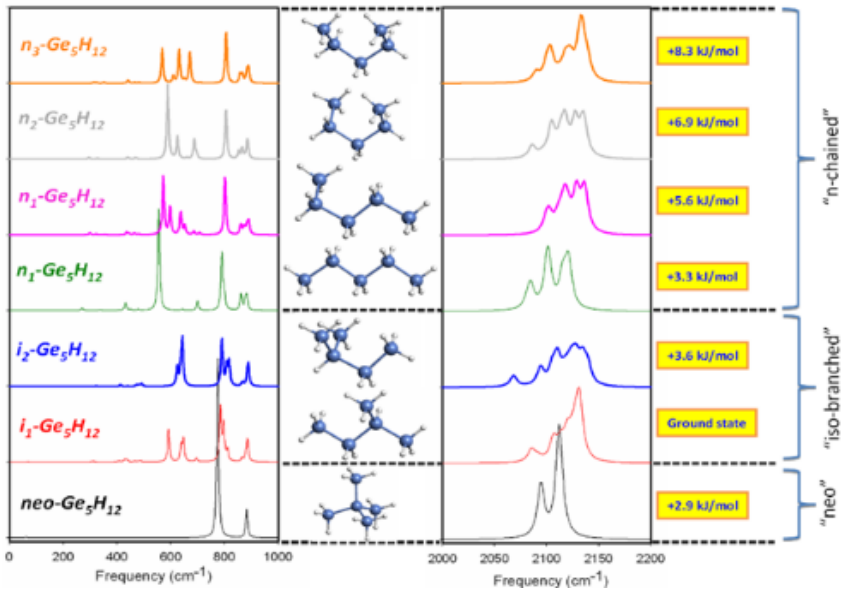

Figure 5 - Summary of simulated infrared spectra for the Ge_5H_{12} isomers in the low-frequency (left) and high-frequency (right) regimes. Relative free energies of the isomers are provided on the right and the dashed horizontal lines separate the three isomer families, identified as neo-, branched and chained.

remaining isomers the latter represents a key distinguishing "fingerprint" for the Ge_5H_{12} compound. This is discussed in more detail below, in the context of experimental characterization.

4. Reaction Thermodynamics of Higher Order Ge-Hydrides

Here we envision that all high order germanes can be formed from the pyrolysis of an initial mixture of lower order germanes such as digermane and trigermane via insertion reactions involving a reactive germylene intermediate GeH_2. The germylene is presumed to successively react with higher order polygermanes according to a cascade sequence, culminating in the formation of pentagermane according to the following reactions:

$$Ge_2H_6 \Rightarrow GeH_2 + GeH_4 \qquad \Delta G^0_{R,1} = +119.6 \text{ kJ/mol} \qquad \text{Rx(3.4)}$$

$$GeH_2 + Ge_2H_6 \Rightarrow Ge_3H_8 \qquad \Delta G^0_{R,2} = -128.9 \text{ kJ/mol} \qquad \text{Rx(3.5)}$$

$$GeH_2 + Ge_3H_8 \Rightarrow i\text{-}Ge_4H_{10} \qquad \Delta G^0_{R,3} = -127.2 \text{ kJ/mol} \qquad \text{Rx(3.6)}$$

$$GeH_2 + i\text{-}Ge_4H_{10} \Rightarrow i\text{-}Ge_5H_{12} \qquad \Delta G^0_{R,4} = -127.3 \text{ kJ/mol} \qquad \text{Rx(3.7)}$$

The reaction free energies listed here were all obtained using thermochemistry calculations as described earlier, namely at the B3LYP/6-311++(3pd,3df) level. Our simple model does not include isomeric branching in the tetra- and pentagermane reactions. Instead, for the purpose of our preliminary studies here we use the most thermodynamically favorable higher-order isomer species at 298K (i-Ge_4H_{10} and i_1-Ge_5H_{12}). The thermochemistry and structural trends for GeH_4, Ge_2H_6, Ge_3H_8, and i-Ge_4H_{10} closely follow those reported in our prior work,[107] while the values for i-Ge_5H_{12} were taken from Table 3 above. The 298K

equilibrium constants corresponding to the ΔG values listed in Rx(3.4)-Rx(3.7) are found to be $K^0_{P,4} = 1.1052 \times 10^{-21}$, $K^0_{P,5} = 3.8886 \times 10^{22}$, $K^0_{P,6} = 1.9884 \times 10^{22}$ and $K^0_{P,7} = 2.0288 \times 10^{22}$. Introducing extent of reaction variables {*x*,*y*,*u*,*v*} for the above processes, and assuming that the reactions are initiated using n^0_D moles of digermane, the mass balance the simultaneous equilibrium condition in the ideal gas approximation are represented by the set of coupled equations:

$$K^0_{P,4} = \frac{x}{(n^0_D - x - y)} M \; ; K^0_{P,5} = \frac{(y-u)}{(n^0_D - x - y)} \frac{1}{M} ; K^0_{P,6} = \frac{(u-v)}{(y-u)} \frac{1}{M} ; K^0_{P,7} = \frac{v}{(u-v)} \frac{1}{M} \quad (3.8)$$

where we have defined the function $M(x,y,u,v;P) = \frac{(x - y - u - v)}{(n^0_D + x - y - u - v)} \frac{P}{P^O}$. Solution of these simultaneous equilibrium equations at T= 300 K and P = 1 atm, yields a mixture of ~68% GeH_4, ~4% Ge_2H_6, ~8% Ge_3H_8, ~10% Ge_4H_{10} and ~12% Ge_5H_{12} and a vanishing concentration of the GeH_2 germylene intermediate. A simpler alternative approach is to subsume the germylene insertion reactions by subtracting Rx(3.4) from Rx(3.5), Rx(3.6) and Rx(3.7), respectively, to obtain a completely equivalent set of effective reactions equations given earlier in the chapter as Rx(3.1)-Rx(3.3):

$Ge_2H_6 + Ge_2H_6 \Rightarrow GeH_4 + Ge_3H_8$ $\quad \Delta G^0_{R,1} = -9.35$ kJ/mol

$Ge_2H_6 + Ge_3H_8 \Rightarrow GeH_4 + i\text{-}Ge_4H_{10}$ $\quad \Delta G^0_{R,2} = -7.67$ kJ/mol

$Ge_2H_6 + i\text{-}Ge_4H_{10} \Rightarrow GeH_4 + i\text{-}Ge_5H_{12}$ $\quad \Delta G^0_{R,3} = -7.76$ kJ/mol

with corresponding equilibrium constants $K_{P,1}^0 = 43.4455$, $K_{P,2}^0 = 22.1047$ and $K_{P,3}^0 = 22.8425$.

In the ideal gas approximation the pressure dependence of the reactions vanishes due to the equimolar balance between reactants and products yielding simultaneous equilibrium equations

$$K_{P,1}^0 = \frac{(n_T^0 + x - y)(n_G^0 + x + y + z)}{(n_D^0 - 2x - y - z)^2} \qquad \text{Eq(3.9)}$$

$$K_{P,2}^0 = \frac{(y - z)(n_G^0 + x + y + z)}{(n_T^0 + x - y)(n_D^0 - 2x - y - z)} \qquad \text{Eq(3.10)}$$

$$K_{P,3}^0 = \frac{z(n_G^0 + x + y + z)}{(y - z)(n_D^0 - 2x - y - z)} \qquad \text{Eq(3.11)}$$

where $\{x,y,z\}$ now represent the extent of reaction in Rx(3.1), Rx(3.2) and Rx(3.3), respectively, and n_G^0, n_D^0 and n_T^0 denote the amount of GeH_4, Ge_2H_6 and Ge_3H_8 in the initial reaction mixture. Numerical solution of these equations at T=298K and P=1 atm, with digermane as the sole reactant yields an equilibrium mixture of ~68% GeH_4, ~4% Ge_2H_6, ~8% Ge_3H_8, ~10% Ge_4H_{10} and ~12% Ge_5H_{12}, in accord with our earlier results obtained for the germylene reactions. Collectively the above models predict that germane is expected to be the dominant equilibrium species, with ~25-30% of the product represented by higher order germanes for a broad range of initial reactant mixtures. In future work this model could be further refined by incorporating fugacity corrections to the

ideal gas treatment, and more sophisticated statistical mechanics models for the thermodynamic functions.

Next the free energies were calculated for reactions Rx(3.1)-Rx(3.3) as a function of temperature up to ~ 430^{o}C (700K) and P = 1 atm, and the results are plotted in Figure 6. The graphs indicate that all reactions are expected to be spontaneous over this temperature range with trigermane production via Rx(3.1) representing the main "driving force". While the corresponding tetragermane and pentagermane reaction free energies are predicted to be comparable at ambient conditions our simulations predict that pentagermane reaction is slightly favored at high temperatures compared to its tetragermane counterpart. The data used to produce the latter figure was then used to explore the temperature dependence of the product yields by repeatedly solving the equilibrium equations over the 300-700K temperature range for various initial reactant mixtures. Figure 7 compares the temperature dependence of the equilibrium yields for reactions initiated with pure digermane and an initial equimolar mixture of digermane and trigermane. From the plots it is evident that the

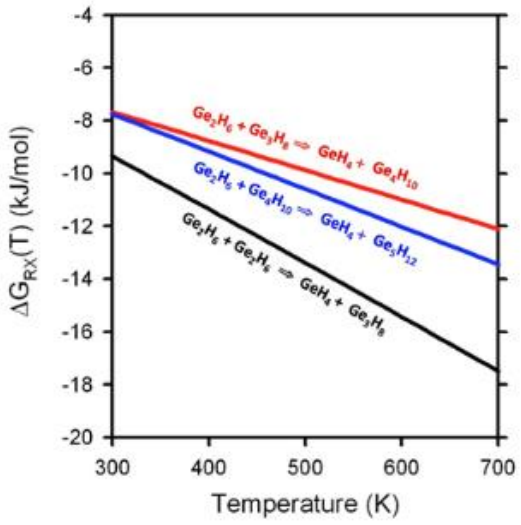

Figure 6 - Temperature dependence of the reaction free energies $\Delta G^{0}_{R,1}$ (black), $\Delta G^{0}_{R,2}$ (red) and $\Delta G^{0}_{R,3}$ (blue), in kJ/mol

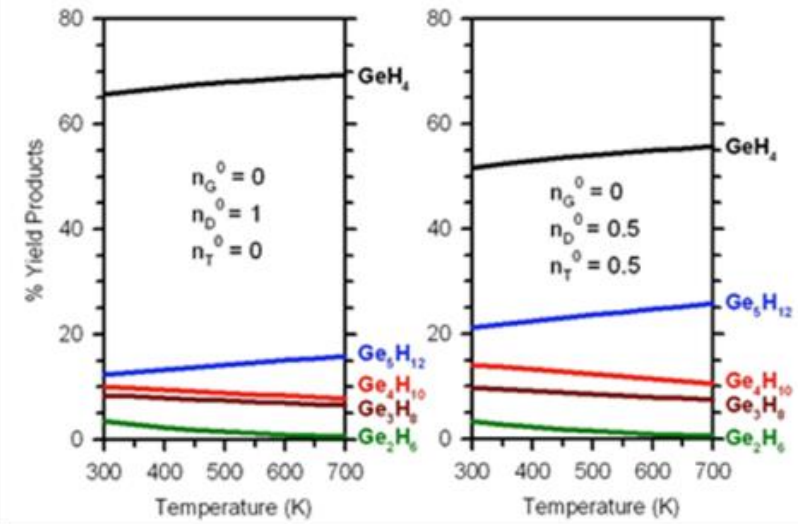

Figure 7 - Temperature dependence of the equilibrium concentrations for the reaction system described by Rx(3.1)-Rx(3.3) initiated using pure Ge_2H_6 (left panel) and an equimolar mixture of Ge_2H_6 and Ge_3H_8 (right panel) .

qualitative trends are similar for both initial conditions, and that GeH_4 is the dominant species across the entire temperature range.

The above conclusions are consistent with experimental thermolysis of pure digermane in a closed vessel yielding GeH_4 as the main product and relatively large concentrations of non-volatile liquid, which is tentatively identified as pentagermane. The vapor pressure of the corresponding gas phase above this liquid was estimated to be in the range of ~ 0.1-0.2 Torr, which is significantly smaller and distinct from that of tetragermane (~1.5 Torr).

The volatility of this liquid sample was nevertheless sufficient to acquire a reliable and reproducible gas-phase infrared spectrum, which bore a close resemblance to that of its tetragermane counterpart, with the exception of a sharp peak in the vicinity of ~ 570 cm^{-1} consistent with the theoretical predictions described above for pentagermane. This spectrum, along with its liquid phase counterpart are compared with the corresponding gas and liquid phase spectra of tetragermane in Figure 8. The gas phase reference IR spectrum

of tetragermane shown here is taken from our prior work, where isomer equilibrium thermochemistry and NMR were used to establish that the "iso" form of Ge_4H_{10} is dominant in the gas phase while the linear chain *n*-Ge_4H_{10} form is the primary liquid phase species, respectively. Thus, theoretical vibrational spectra obtained from molecular simulations provide a useful guide for interpreting the complex isomeric spectra obtained experimentally here. This is demonstrated in Figure 8 where preliminary theoretical spectra, obtained by combining the individual spectra of the lowest energy isomers in each case, are compared with their gas and liquid state counterparts. The admixtures employed are listed in the adjoining table (Table 4), where the asterisk indicates values determined from thermochemistry calculations. The remaining entries in the table are preliminary

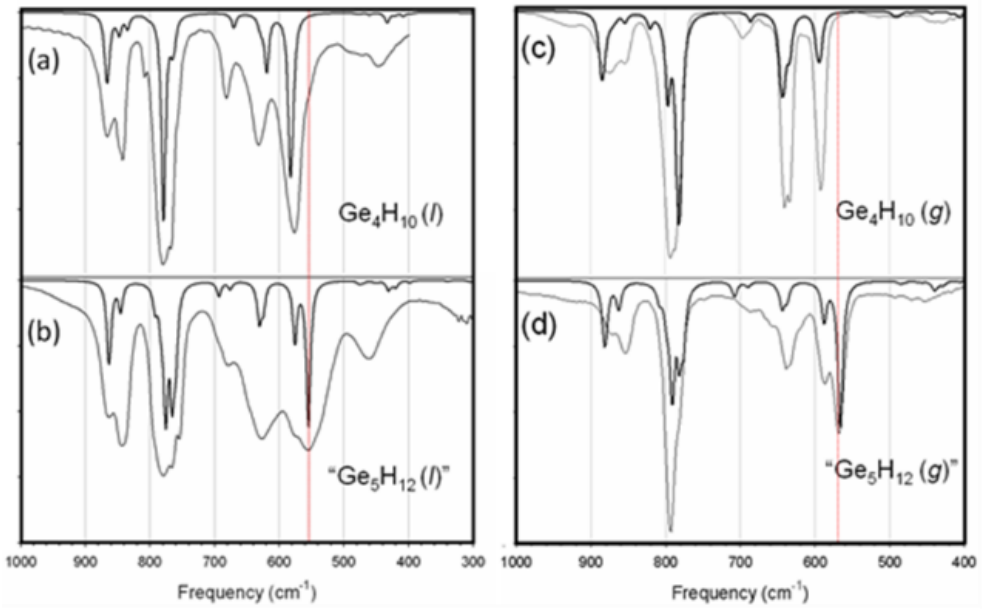

Figure 8 - Experimental and theoretical infrared spectra of liquid (left panels (a) and (b)) and gas (right panels (c) and (d)) phases of Ge_4H_{10} and Ge_5H_{12}. Observed and theoretical spectra are drawn as faint and bold curves, respectively. The theoretical spectra for Ge_4H_{10} and Ge_5H_{12} were obtained by combining isomeric spectra, as described in the text, using linear coefficients listed in Table 4. Frequency scale factor of ~0.975 and 0.995 were used in the theoretical spectra of the liquid and gas phase data, respectively. The red lines indicate the hallmark pentagermane signature associated with the n_1-Ge_5H_{12} isomer, as predicted by our simulations.

Table 4 - Isomer admixtures used to generate the theoretical spectra shown in Figure 8. The asterisk denotes values determined from thermochemistry calculations reported in Ref 107. The remaining entries are obtained using a simple linear combination fit.

		Ge_4H_{10}		
		iso	*linear*	*gauche*
gaseous	*	80 %	12 %	8 %
liquid		15 %	70 %	15 %

	Ge_5H_{12}		
	neo	*linear* (n_1)	*iso* (i_1)
gaseous	10 %	50 %	40 %
liquid	15 %	70 %	15 %

estimates based on fitting. Such simulations provide a useful guide for interpreting the complex isomeric spectra obtained experimentally.

As can be seen from our comparisons, all of the main features of the gas and liquid phase infrared spectra are reasonably accounted for using our thermochemistry simulations, and are also qualitatively consistent with observations from earlier studies.[113] In the latter, pentagermanes were generated in very small amounts relative to lower order analogs using silent discharge of monogermane. Chromatographic separation of the Ge_5H_{12} then yielded *iso*- and *n*- Ge_5H_{12} conformers as dominant components in the mixture, while the *neo*-analog fraction was found to be vanishingly small. These trends are in general agreement with both our fit, and our proposed assignment of the observed peak intensities associated with three isomers. In the case of our liquid phase comparisons the simulated spectra were obtained using 50% i_1-Ge_5H_{12}, 40% n_1-Ge_5H_{12} and 10% *neo*-Ge_5H_{12}. In this regard, the high concentration of the *iso*- species in our liquid samples is consistent with our high-

resolution NMR analysis which clearly resolves both conformers. We note that the corresponding NMR data reported in Ref. 113 lack the resolution needed to identify the structure of individual isomers (*e.g.*, *n*-Ge_5H_{10} is shown as a single peak).

The most striking feature in both the liquid and gas phase comparisons is the unequivocal presence of a unique peak near 555 cm^{-1} in the liquid spectrum, and 567 cm^{-1} in the gas phase (indicated by the dotted red lines in the figure), which originates exclusively from the n_1-Ge_5H_{12} isomer, having no counterpart in any of the other Ge_5H_{12} or Ge_4H_{10} isomers. We emphasize that our fitting procedures are based on combining the spectra of only the *neo*-, *n*- and *i*- species and that further improvements would result from the combination of all isomeric spectra.

5. Ge_nH_{2n+2} Yield Optimization

Finally, we used our equilibrium model to explore the dependence of the products on temperature, and initial reactant concentrations. For example, increasing temperature results in a moderate rise in pentagermane yield as the remaining Ge-hydride species are consumed, as expected. In particular, digermane reacts to produce trigermane via Rx(3.1), which then in turn reacts further to produce Ge_4H_{10} and finally, Ge_5H_{12}. Thus, under the equilibrium conditions considered here the thermodynamic "driving force" is the creation of the latter two species.

The equilibrium model above may also provide a route to tuning the reactions conditions as a function of initial reactant concentrations to favor the production of the desired product. This is illustrated in Table 5, where a number of equilibrium results are summarized at 600K (~327 ^oC), as a function of n_G^0, n_D^0 and n_T^0. The table lists the extents

Table 5 - Dependence of equilibrium Ge_nH_{2n+2} hydride yields at 600 K (~ 327 ºC) based on Rx(3.1)-Rx(3.3), as a function of the initial mixture of GeH_4, Ge_2H_6 and Ge_3H_8 (n_G^0, n_D^0 and n_T^0 respectively). Also listed are the extent of reaction x_{eq}, y_{eq}, z_{eq} for Rx(3.1), Rx(3.2) and Rx(3.3), respectively, and the ratio R of pentagermane to tetragermane in the final product mixture.

n_G^0	n_D^0	n_T^0	x_{eq}	y_{eq}	z_{eq}	% GeH_4	% Ge_2H_6	% Ge_3H_8	% Ge_4H_{10}	% Ge_5H_{12}	R
0.00	0.00	1.00	-0.4257	0.4911	0.3521	41.7	0.8	8.3	13.9	35.2	2.532
0.00	0.50	0.50	-0.0588	0.3613	0.2471	55.0	0.9	8.0	11.4	24.7	2.164
0.00	1.00	0.50	0.0936	0.4776	0.3208	59.5	1.0	7.7	10.5	21.4	2.046
0.50	0.00	1.00	-0.4064	0.4776	0.3208	59.5	1.0	7.7	10.5	21.4	2.046
0.00	1.00	0.00	0.1516	0.1168	0.0752	68.7	1.0	7.0	8.3	15.0	1.807
0.50	0.25	0.25	0.2711	0.2710	0.1762	75.8	1.0	6.1	6.5	10.5	1.614
1.00	0.00	0.50	-0.1880	0.2251	0.1366	78.3	0.9	5.8	5.9	9.1	1.544
0.50	1.00	0.00	0.3120	0.2251	0.1366	78.3	0.9	5.8	5.9	9.1	1.544
0.50	0.50	0.00	0.1591	0.1092	0.0635	83.2	0.9	5.0	4.6	6.4	1.389
1.00	0.50	0.00	0.1634	0.1040	0.0568	88.3	0.8	4.0	3.1	3.8	1.202

of reaction for the three primary reactions, the final equilibrium fractions of all Ge_nH_{2n+2} species, and the ratio of pentagermane to tetragermane in the final composition. In general we note that GeH_4 is the dominant species followed by the higher order tetra- and penta-germanes. These outcomes are consistent with the preliminary proof-of-principle experiments carried out to date at slightly different conditions (~250 ^oC). An intriguing aspect of the equilibrium thermodynamics is the mathematical equivalence (invariance) obtained from a simple simultaneous shift of the initial conditions and the extent of reaction. For example (see Table 5), the solutions obtained with n_G^0=½ and n_T^0=1 are identical to those obtained for n_D^0=1 and n_T^0=½ where the extent of reaction for Rx(3.1) is shifted by +0.5, yielding ~60% GeH_4, ~1% Ge_2H_6, ~8% Ge_3H_8, ~11% Ge_4H_{10} and ~21% Ge_5H_{12}. The tuning of the equilibrium concentrations can also be achieved by incorporating GeH_4 into the initial reactant mixture, which reduces the overall yield of both tetra- and penta-germane while reducing their ratio (R).

As mentioned Chapter 2, in the case of thermolysis reactions based on a continuous flow of Ge_2H_6 at 250^oC we typically observe the evolution of primarily gaseous GeH_4, as expected, but also obtain Ge_3H_8 as the other main product isolated in a flow trap. Clearly, this is not an equilibrium process because Ge_3H_8 is constantly being removed from the reaction zone thus diminishing the prospect for its complete reaction with Ge_2H_6 to form Ge_4H_{10} consistent with equilibrium expectations. Nevertheless the latter product is recovered in small amounts which are presumably formed by incomplete reactions of Ge_2H_6 with Ge_3H_8 whose residence time inside the thermolysis tube is sufficient to maintain a quasi-equilibrium state. In the same manner some of the Ge_4H_{10} produced in the flow system also likely reacts with Ge_2H_6 to from Ge_5H_{12} (see Rx(3.3)) in trace

amounts. Based on these observations we anticipate that the theoretical model above might be useful in guiding the optimizing of flow reactions that systematically enhance the yield of Ge_3H_8, Ge_4H_{10} or Ge_5H_{12}, as desired. For example, flow reactions of Ge_3H_8 and Ge_2H_6 could be optimized to yield predominately Ge_4H_{10} or Ge_5H_{12} by tuning temperature, pressure (retention time) and the co-reactant mixture.

6. Ge-on-Si Growth Studies via Pentagermane

Samples of Ge_5H_{12} whose spectra were presented in Figure 8 were next used to undertake simple proof-of-principle depositions of pure Ge on Si(100) wafers. Our only objective here is to provide a demonstration that the pure compound represents a viable deposition precursor in the extreme low temperature regime (T~ 350^{o}C). Future studies will be devoted to optimization of process conditions and yield, and the fabrication of rudimentary device structures. Briefly, depositions of Ge films via pentagermane were conducted on 4 inch Si(100) *p*-type wafers using a gas-source molecular epitaxy reactor described in Ref. 77. Prior to growth the substrates were first wet-cleaned, dipped in HF and then heated under ultrahigh vacuum on the sample stage at 550 ^{o}C for 5 minutes to obtain a clean surface as evidenced by reflection high energy electron diffraction (RHEED). The Ge_5H_{12} liquid source was kept in a glass ampule which was then attached to the injection manifold and pumped to 10^{-8} Torr. The room temperature vapor pressure of the compound was introduced into the chamber using a needle valve at 10^{-10} Torr base pressure. The deposition pressure was then adjusted at 1×10^{-5} Torr and was maintained constant during the course of the experiment via dynamic turbo pumping of the chamber ambient. The wafer was heated by a graphite element enclosed within a cylindrical quartz jar that is differentially pumped down to 10^{-10} Torr. The actual substrate temperature was estimated

to be in the vicinity of 360°C using a heater thermocouple located inside the enclosure, 3 mm removed from the backside of the wafer. We note that a standard pyrometer could not be used to read the wafer surface temperature due to the low emissivity of Si in this IR range. The time frame of a typical deposition was 15-20 minutes, producing films at growth rates of up of ~27 nm/min, which is unprecedented under these pressure/temperature conditions of 1×10^{-5} Torr/360°C. As a comparison, we obtained negligible growth rates <0.5 nm/min using our previous state-of-the-art Ge_2H_6/H_2 process,[114] and 17 nm/minute using a newly developed approach involving Ge_4H_{10}/H_2 depositions. The resultant pentagermane grown films exhibited a flat surfaces devoid of defects and imperfections (atomic force microscopy root mean square roughness ~ 0.5 nm) which is consistent with a layer-by-layer growth mechanism. Ellipsometry was used to determine the thickness profile which was found to be 85 % across the 4 inch diameter of the substrate under the initial conditions of our preliminary experiments.

Cross sectional transmission electron microscopy (XTEM) analysis revealed uniform films grown on silicon with flat surfaces and low levels of threading defects as shown in Figure 9 (a)-(c). The latter displays both phase-contrast and Z-contrast micrographs obtained from a 500 nm thick sample. High resolution images show misfit dislocations at the interface plane accommodating the lattice strain, as expected due to the dissimilar lattice dimensions of the two materials (Figure 9(c)). Corresponding Z-contrast data indicate a sharp and abrupt interface with no discernible interdiffusion between the two materials. X-ray diffraction (XRD) on-and off- axis measurements of the as-grown samples revealed a relaxed strain state with a bulk lattice constant of 5.658 Å and a 0.17 degrees full width at half maximum (FWHM) for the 004 rocking curve. The latter value indicates a high quality

crystal film in spite of the remarkably low deposition temperatures employed. Subsequent rapid thermal annealing (RTA) at 700°C resulted in a significant narrowing of the FWHM to a value of 0.06 degrees and produced a residual tensile strain of ~ 0.14% (Figure 9 (d)). The latter is induced by the annealing of the intrinsic layer as a consequence of the difference in thermal expansion with the Si substrate.

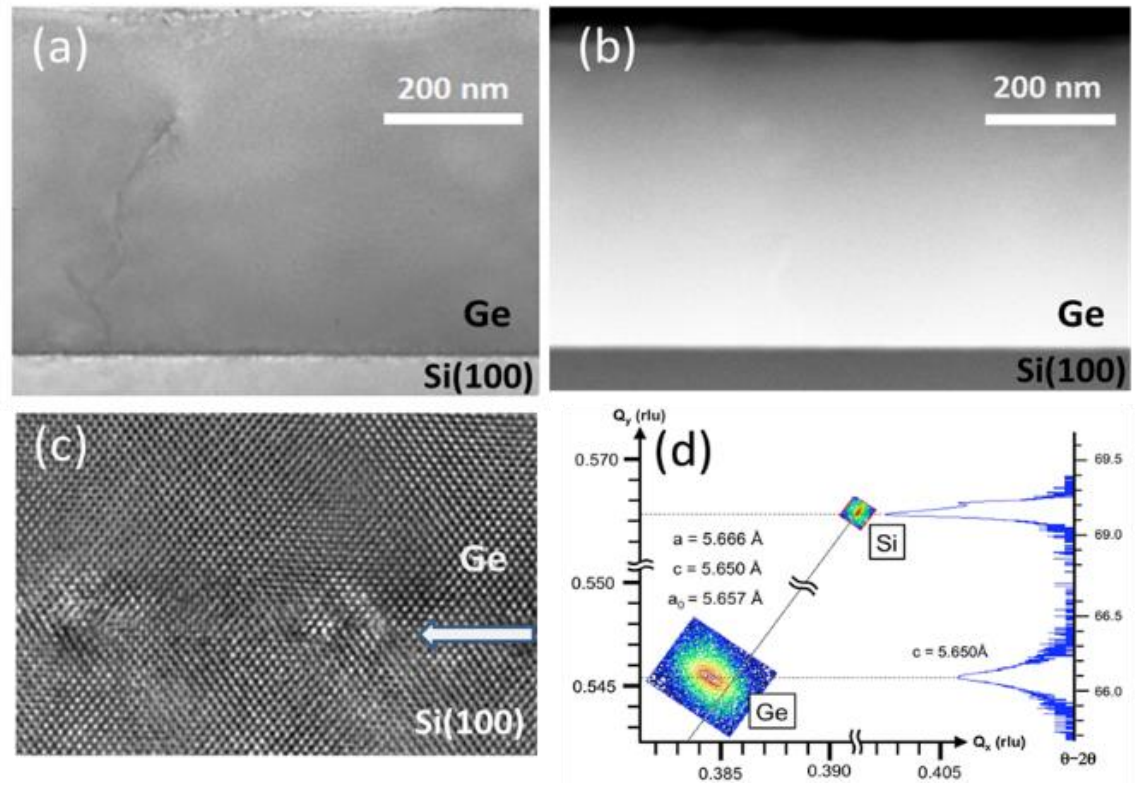

Figure 9 - (a) XTEM bright field image of Ge on Si film showing the typical microstructure observed within the field of view. (b) Corresponding Z-contrast micrograph of the same sample. (c) High resolution image of the interface marked by arrow. (d) XRD on and off axis plots of RTA processed sample indicating a significant level of tensile strain as evidenced by the measured lattice constants (inset) and the position of the 224 map relative to the relaxation line.

7. Conclusion

The search for chemical sources suitable for the fabrication of next generation Ge-based semiconductor technologies prompted us to undertake a comprehensive exploratory study

of Ge_5H_{12} spanning molecular level simulation, molecular synthesis and proof-of-concept germanium film growth. The structural, vibrational and thermochemical properties of Ge_5H_{12} isomers were simulated using first principles quantum chemistry methods to elucidate the essential characteristics of this compound. Structural analogies between Ge_4H_{10} and Ge_5H_{12} were used to interpret the vibrational spectrum of pentagermane and identify its unique spectroscopic fingerprint as a band near 560-570 cm^{-1}. Free-energies estimated using rotor-corrected thermochemistry were then used to obtain equilibrium constants, and solve the coupled reaction equilibrium equations among Ge-hydrides up to Ge_5H_{12}. Germane is predicted to be the dominant species, followed by Ge_4H_{10} and Ge_5H_{12} in various ratios depending on temperature and initial reactant concentrations.

Our experimental reaction studies corroborate this behavior and yield the Ge_5H_{12} compound in sufficient quantity and purity to enable deposition studies. Our work demonstrates that the growth of Ge on Si via high reactivity large molecular weight Ge_5H_{12} compounds represents a unique, reliable and reproducible low temperature route to straightforward Ge integration on Si(100) at commercial scale growth rates. Beyond simple demonstration this development represents a significant potential advance in crystal growth of thick and fully crystalline films in which the majority of the film volume exhibits bulk-like crystal behavior as required for applications in Si photonics including photovoltaics.

In addition to Ge_5H_{12}, the high order Ge hydrides Ge_3H_8 and Ge_4H_{10} produced in the series of thermolysis reactions outlined above are of significant interest in the fabrication of metastable Ge based materials. The latter compound, for which optimized procedures are

available for deposition of thick, atomically flat, highly crystalline Ge on Si epilayers will be used extensively in subsequent chapters to produced virtual Ge substrates for use in doping studies of Ge and fabrication of $Ge_{1-y}Sn_y$ alloys. The principle Ge source used in such studies is Ge_3H_8, which has suitable reactivity to allow deposition of Ge in the temperature range 340°C-260°C. Furthermore, this compound has compatible reactivity with $P(GeH_3)_3$, $P(SiH_3)_3$, $As(GeH_3)_3$, $As(SiH_3)_3$, SbD_3, $S(GeH_3)_2$ and $S(SiH_3)_2$ precursors, which allows the study of *n*-type doping of Ge with the above donor elements, as described in the next chapter. These doping studies have important implications for the production of Ge based field effect transistor (FET) and laser devices. In addition, Ge_3H_8 can be used in conjunction with SnD_4 for the deposition of direct gap $Ge_{1-y}Sn_y$ alloys. Since these alloys can also be *n*-type doped using $P(GeH_3)_3$, $P(SiH_3)_3$, $As(SiH_3)_3$, $Sb(SiH_3)_3$ and SbD_3 precursors, and *p*-type doped using B_2H_6, *pin* and *pn* LEDs with GeSn active components can be manufactured. This work, described in Chapters 5, 6 and 7, represent the first experimental demonstration of direct gap group IV diodes, and therefore has implications on fabrication of monolithically integrated lasers on Si.

CHAPTER FOUR

Epitaxial Ge on Si Films Degenerately *n*-type Doped with As, Sb and S through Low Temperature Deposition Techniques Utilizing High Reactivity Precursors

Synopsis

This chapter presents investigations on the doping of Ge on Si films with As, Sb and S donors with the aim of obtaining heavily doped material for field effect transistor and laser applications. The doping strategy was to use $As(GeH_3)_3$, $As(SiH_3)_3$, SbD_3, $S(GeH_3)_2$ and $S(SiH_3)_2$ molecular precursors as the sources of donor atoms for *in-situ* doping. The low temperature CVD of the above molecules in combination with Ge_3H_8 and Ge_4H_{10} results in high levels of donor incorporation while maintaining structural integrity, leading to films with superior electrical properties.

Portions of this chapter were previously published in Xu, C.; Gallagher, J. D.; Wallace, P. M.; Senaratne, C. L.; Sims, P.; Menéndez, J.; Kouvetakis, J. In situ low temperature As-doping of Ge films using $As(SiH_3)_3$ and $As(GeH_3)_3$: fundamental properties and device prototypes. *Semicond. Sci. Technol.* **2015**, *30* (10), 105028 © IOP Publishing. Reproduced with permission. All rights reserved.

Portions of this chapter are reprinted with permission from Kouvetakis, J.; Favaro, R.; Grzybowski, G. J.; Senaratne, C.; Menéndez, J.; Chizmeshya, A. V. G. Molecular strategies for configurational sulfur doping of group IV semiconductors grown on Si (100) using $S(MH_3)_2$ (M= Si, Ge) delivery sources: An experimental and theoretical inquiry. *Chem. Mater.* **2014**, *26* (15), 4447. Copyright 2014, American Chemical Society.

1. Introduction

The CMOS compatible growth methods for Ge on Si described in the previous chapter is but one requirement for using Ge in place of Si in microelectronic and optoelectronic applications. Another essential aspect is the synthesis of highly *n*-type doped materials for implementation of Ge based FETs and lasers. The most popular method for *n*-type doping is ion implantation, in which the difficulty in precisely controlling junction depth and donor distribution is a major drawback. This has led to investigation of *in-situ* doping methods as an alternative. Recent work has demonstrated the use of high order Ge hydrides together with trisilylphosphine and trigermylphosphine donor sources in order to achieve this purpose. The syntheses of these precursors were described in previous chapters. It was possible to achieve carrier concentration up to 6×10^{19} cm^{-3} using this method, and near full activation of the donors results in superior electrical properties compared to state of the art in situ doping methods using germane and phosphine.[115]

However, further advances are necessary to achieve carrier levels $>10^{20}$ cm^{-3} required for nMOSFET applications. In this work, the analogous As compounds trisilylarsine and trigermylarsine were pursued for As doping. The above donor was selected since it may provide a way to incorporate higher donor concentrations due to the similarity of the atomic sizes of As and Ge. In a series of experiments described below in Section 2, carrier concentrations in the 1×10^{19}-8×10^{19} cm^{-3} range were achieved with nearly full activation of the donors. The latter carrier level is higher than what was observed for P. Furthermore the resistivities of the films were comparable to bulk Ge:As. However, resistivities were greater than what was observed for P. This trend had also been observed earlier by Spitzer,

Trumbore and Logan, who also found that doping using Sb results in lower resistivities for a given donor concentration in comparison to As and P.[116]

Based on the above property, Sb is the ideal dopant for applications where lowest resistivities are required. While the solubility of Sb in Ge is less than that of As, it was hypothesized that low temperature deposition techniques may be capable of incorporating levels of donors similar to the P and As cases above, leading to lower resistivities. The best precursor for this purpose was found to be deuterated stibine. Although this hydride is simple, it has not previously been used for in-situ doping. In an extensive series of investigations described in Section 3 below, it was found that carrier levels up to 1.6×10^{20} cm^{-3}, which exceeds levels with P or As, were obtained in Ge:Sb. In addition, record low resistivities down to 1.8×10^{-4} Ωcm were measured, which compare well with values predicted for the above high donor levels based on trends observed in bulk Ge:Sb.

A possible route for further increasing carrier levels is through use of double donors such as sulfur. Sulfur doped Si has been used in photovoltaics and detectors. Ge:S can be expected to have similar applications at longer IR wavelengths, in addition to being of possible use in laser and FET technologies. The doping was achieved by using disilylsulfide and digermylsulfide sources. It was found that the depositions with digermylsulfide incorporate S in the range 1×10^{17}-4×10^{17} cm^{-3}. Due to the double donor nature of S, carrier concentrations as high as 7×10^{17} cm^{-3} were observed. Such full ionization of double donors is an advantage of the molecular doping approach compared with alternate methods reported in literature. However, increasing the carrier levels above this threshold was not possible.

Based on this data, it can be concluded that Sb is the donor of choice when doping $>10^{20}$ cm^{-3} with low resistivities, and the stibine based growth approach is the best method for achieving such high doping. Taken as a whole, the above results lead to the conclusion that the molecular sources described here are excellent agents for controlled doping of Ge on Si films with degenerate carrier concentrations, superior electrical properties, and uniform dopant profiles. In addition, the inherently low growth temperatures of this method are ideal for doping of metastable GeSn alloys, leading to its use in forthcoming chapters for emission enhancement and device fabrication purposes.

A detailed account of the above doping experiments and their outcomes are described in detail below. The description of the As doping experiments is based on Reference 117, and the details of S doping are reproduced from Reference 118. The results from the above publications are reproduced herein with the permission of the co-authors.

2. *In-Situ* Low Temperature As Doping of Ge Films Using Trisilylarsine and Trigermylarsine

2.1. Introduction

The possibility of using Ge as an alternative to Si in next-generation CMOS technologies, combined with recent advances in Ge-based optoelectronics, have stimulated the development of new and improved methods to dope Ge films with group-V donor atoms. Ultra-high doping densities are required in the shallow junctions of Ge-based NMOSFETs[119] as well as in Ge-based laser devices.[10,11] For straightforward compatibility with CMOS processing, ion implantation is the most attractive doping technique, and for this application phosphorus is the element of choice because it has a higher solubility and lower diffusivity than As and Sb.[120] In addition, the structural damage caused by P

implantation is less pronounced than in the case of As or Sb, making regrowth of the crystalline lattice much more straightforward.[121,122] However, P concentrations around 5×10^{19} cm^{-3} required for Ge based FETs are hard to achieve by implantation methods.[122] Other drawbacks of this method include the necessity of high temperatures to activate the dopants, and non-uniform composition profiles with ill-defined interfaces between the doped and undoped regions of the structures.[11,121–129] Therefore, *in situ* doping approaches have been receiving increasing attention over the past few years.[10,124,130–132] The rationale is that low temperature growth could enable the incorporation of dopants even beyond the solubility limit, while the elimination of recrystallization/activation anneals should contribute to the fabrication of shallow junctions. Unfortunately, in situ doping based on GeH_4 and PH_3 —the standard CVD sources for Ge and P— is not straightforward. The simultaneous optimization of the level of P incorporation and the electrical and optical properties of the grown films are hard to achieve,[124,132] suggesting that the temperature regimes for the two precursors are not perfectly compatible. Out-of-equilibrium approaches such as delta-doping and atomic-layer doping have been demonstrated,[11,125,133,134] but these increase the processing complexity.

The search of alternative *in situ* routes that are fully compatible with CMOS processing have very recently led to the development of radically new methods to dope Ge with P using the specially designed single-source precursors $P(MH_3)_3$ (M=Si,Ge), whose synthesis was described in Chapter 2.[115,135] These compounds contain purely inorganic SiH_3 and GeH_3 groups, making them both more reactive and less toxic than PH_3. Their high reactivity facilitates low-temperature decomposition via complete elimination of H_2, yielding crystalline systems with excellent structural, electrical, and optical properties. In

particular, systematic depositions via reactions of the compounds with Ge_3H_8 using UHV-CVD have led to carrier concentrations up to ~ 6×10^{19} cm^{-3} and higher mobilities than those found in films grown following the conventional GeH_4/PH_3 route.[115,135]

These promising results lead us to carry out a study of Ge doping using the analogous single source compounds $As(SiH_3)_3$ and $As(GeH_3)_3$. While the atomic solubility of active As in Ge is lower than that of P,[120] this result may not be relevant for $D(MH_3)_3$ (M=Si,Ge, D=P,As,Sb) compounds due to the possible incorporation of molecular fragments—as opposed to isolated donors—and to the presence of Si. Indeed, it was found that Ge films doped via $As(SiH_3)$ and $As(GeH_3)_3$ feature carrier concentrations as high as 8.4×10^{19} cm^{-3} - higher than those achieved using analogous P based compounds. As described in the following sections, a systematic study of these As doped films reveal excellent crystallinity and electrical properties identical to those of bulk As doped Ge.

In contrast with the substantial body of research into *in situ* doping of Ge with P, the analogous *in situ* doping of Ge with As has not been investigated to any significant extent. The near equal atomic sizes of As and Ge suggest that facile incorporation of the dopant atoms into the host structure should be possible with minimal bond distortion using judiciously designed reaction routes. Nevertheless, relatively fewer reports can be found in the literature describing the use of AsH_3 or alternative metalorganic compounds[136] to systematically dope Ge with ultra-high levels of As approaching 10^{20} cm^{-3}. Most *n*-type Ge studies using AsH_3 seem to target low doping densities up to ~ 2×10^{19} cm^{-3}.[126,137] Proof-of-concept experiments involving depositions of AsH_3 with GeH_4 show that As hinders Ge growth, producing morphological defects through surface segregation of the excess

dopants.[138] Similar obstruction of growth—attributed to surface poisoning—was reported for $Si_{1-x}Ge_x$ films doped using large AsH_3 doses.[130] Another issue is the formation of symmetrical As-As dimers that cannot be directly incorporated into the layers as isolated dopant atoms.[130] Finally, the scant research activity in this area may also be attributed to safety issues associated with the use of highly toxic AsH_3, and in the case of metalorganics, to the presence of carbon bearing ligands in the molecular structures, which make them incompatible with group-IV deposition processes.

In contrast with AsH_3, the results reported in this section based on $As(SiH_3)_3$ and $As(GeH_3)_3$ doping demonstrate controlled dopant incorporation in the range of 1×10^{19}-8.4×10^{19} /cm^3 facilitated by the ultra-low temperature deposition (330^{o}C) of the precursors. It was found that electrical and materials properties of films doped with either $As(SiH_3)_3$ or $As(GeH_3)_3$ are essentially indistinguishable. From a processing standpoint, a potential advantage of $As(SiH_3)_3$ over $As(GeH_3)_3$ is its higher vapor pressure by one order of magnitude, making the compound more practical and therefore attractive for commercial scale-up. In the case of $As(SiH_3)_3$ a collateral incorporation of Si in the 10^{19} cm^{-3} range was also observed, indicating that the reactions allow only impurity-level amounts of Si atoms to be incorporated into lattice sites. The Si:As contents deviate from the expected 3:1 ratio corresponding to the intact incorporation of the entire Si_3As molecular core. This suggest that the compound reacts via elimination of stable SiH_4 byproducts that are subsequently removed from the growth front and do not actively participate in film formation under the low temperature conditions employed. The extraction of SiH_4 limits the Si substitution to minimal levels that typically do not affect the fundamental properties of the Ge films in any meaningful manner.

These results will be described in detail in the subsections below in the following order: First, the deposition procedures developed to produce the Ge:As films will be described. Next, the structural properties of the films will be presented. This will be followed by a study of donor activation in the Ge:As films, and finally, the electrical properties of these films will be reported.

2.2. Deposition Procedure for Ge:As Films

The As doped *n*-type layers were grown on Ge-buffered Si platforms via reactions of the dopant compounds and Ge_3H_8. The use of the latter was motivated by the excellent crystal quality Ge films grown recently via low temperature dissociation of this compound.[91] The samples in this study were grown in two stages using two separate reactors. The undoped Ge buffers were grown in a gas source molecular epitaxy (GSME) chamber using the Ge_4H_{10} precursor. The growth was conducted on *p*-type Si(100) wafers with 4" diameter at substrate temperatures near 350^{o}C and pressures of 1.1×10^{-4} Torr, producing layer thicknesses ranging from 0.8 to 1 μm. The Ge buffers were subjected to an annealing step at 650 ^{o}C for 3 minutes *in situ* to reduce the dislocation densities. The wafers were then removed from the chamber and cleaved into four quadrants. These were cleaned by dipping them in a 5% aqueous HF to remove the surface oxide, rinsed with deionized water and blow-dried in a stream of N_2. They were then loaded into a separate UHV-CVD chamber to deposit the *n*-epilayer. In all cases the growth was carried out at 330 ^{o}C and 0.2 Torr by flowing into the chamber appropriate amounts of the Ge_3H_8 and $As(SiH_3)_3$ or $As(GeH_3)_3$ precursors intermixed with ultra-high purity H_2. A typical precursor stock mixture was prepared by combining 15 LTorr of Ge_3H_8, 750 LTorr of H_2 and varying amounts of $As(SiH_3)_3$ or $As(GeH_3)_3$ in the range of 0.03~0.45 LTorr depending on the target doping

concentration. The gaseous atomic ratios of As in the reaction mixtures were in the range 0.08-1.0% for $As(SiH_3)_3$ and 0.33-1.0% for $As(GeH_3)_3$. The gaseous mixtures were introduced into the chamber under a background flow of H_2. A typical deposition run lasted for about 45-60 min yielding *n*-type layers with thicknesses of 140-250 nm containing active carriers in the range of ~1 $\times 10^{19}$ to 8.3×10^{19} cm^{-3}.

2.3. Determination of Structural Properties and Donor Incorporation Levels

Secondary ion mass spectrometry (SIMS) of representative $As(SiH_3)_3$-doped samples, summarized in Table 6, reveals the presence of both As and Si in the doped layers. A typical plot is shown in Figure 10, illustrating a uniform signal profile through the doped

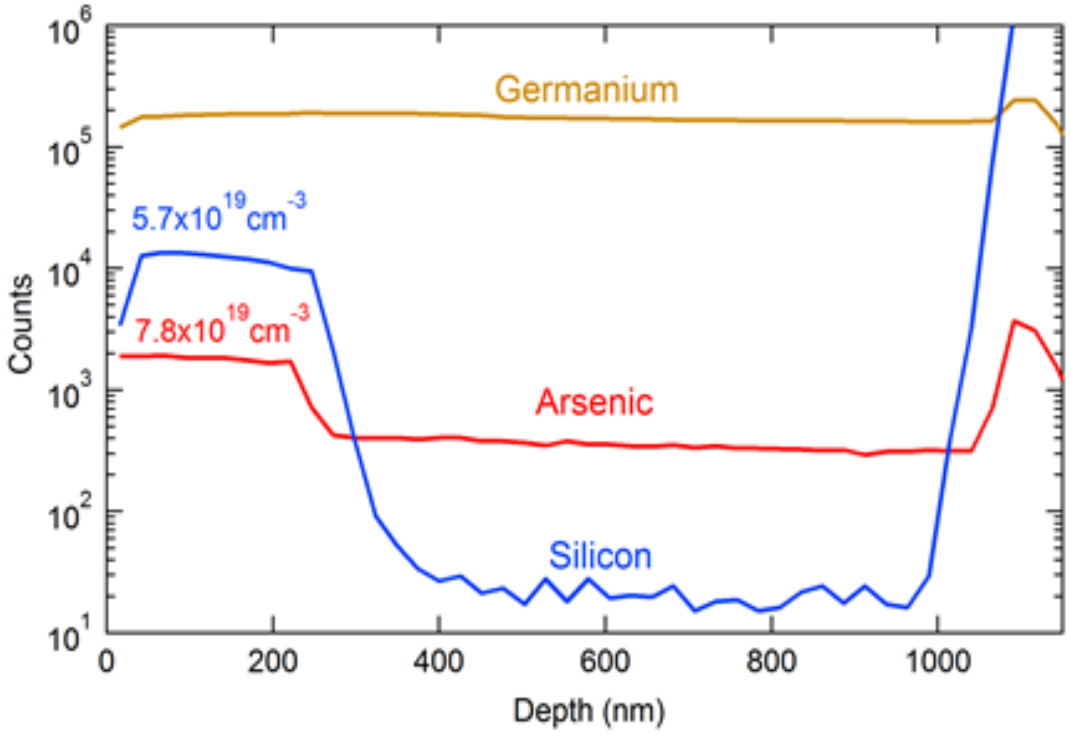

Figure 10 - SIMS depth profile of n-Ge sample grown using $As(SiH_3)_3$. The plots show uniform As and Si distributions throughout the *n*-type region of the structure. The corresponding concentrations were determined to be $7.8 \times 10^{19} cm^{-3}$ and 5.7×10^{19} cm^{-3}.

Table 6 – Growth parameters and compositions of As doped Ge films using $As(SiH_3)_3$

Atomic % As in mixture	Absolute Si by SIMS (cm^{-3})	Absolute As by SIMS (cm^{-3})	Carrier concentration from Hall	Carrier concentration from ellipsometry	Carrier activation ratio	Hall to ellipsometry ratio	SIMS Si/As ratio
0.08%	8.00×10^{18}	1.45×10^{19}	1.44×10^{19}	1.69×10^{19}	~100%	85.2%	0.55
0.17%	1.78×10^{19}	4.80×10^{19}	3.37×10^{19}	3.99×10^{19}	83%	84.5%	0.40
0.33%	6.59×10^{19}	9.09×10^{19}	6.11×10^{19}	7.31×10^{19}	80%	83.6%	0.72
0.66%	5.68×10^{19}	7.80×10^{19}	5.58×10^{19}	6.09×10^{19}	78%	91.6%	0.73
0.83%	7.25×10^{19}	1.04×10^{20}	$6.27x10^{19}$	8.30×10^{19}	80%	78.1%	0.70
1.0%	8.90×10^{19}	1.30×10^{20}	5.82×10^{19}	7.47×10^{19}	57%	77.9%	0.68

layer and a sharp transition of the signals down to background levels at the interface with the undoped Ge buffer layer. The SIMS data were analyzed using reference Ge standards implanted with As and Si at 5×10^{19} atoms/cm^3 and 1×10^{19} atoms/cm^3, respectively. The analysis yielded atomic concentrations spanning from 8×10^{18} - 8.9×10^{19} cm^{-3} for Si and 1.45×10^{19} - 1.3×10^{20} cm^{-3} for As, indicating that the incorporation increases roughly in proportion with the amount of $As(SiH_3)_3$ in the reaction mixtures. The average Si content is nearly half (1:2 ratio) of the corresponding As content within the error of the measurement. This 1:2 ratio deviates from the expected 3:1 ideal limit assuming intact incorporation of the entire $AsSi_3$ molecular core of the $As(SiH_3)_3$ precursor. The lower-than-expected amount of Si is likely due to gas-phase dissociation reactions eliminating SiH_4 or Si_2H_6 stable species that do not participate in the growth process under the conditions employed in the experiments. The remaining As-Si-H fragments at the growth front eventually incorporate As-Si bonding units into the films via desorption of H_2. It is possible that the presence of As-Si moieties at the growth front enhances the doping process by suppressing the dimerization of As atoms and thereby promoting the incorporation of isolated dopants in the films.

As seen in Table 6 the As concentration measured by SIMS is approximately proportional to the As concentration in the reaction mixture. In fact, since the total amount of As in the mixture is known, the incorporation efficiency of the gaseous As into the film can be estimated, and we find that it spans the 30-60% range, indicating a highly efficient reaction. For example a 1% As (atomic percent) mixture delivers 1.3×10^{20} As atoms/cm^3 into the solid, which is 30% of the ideal 4.4×10^{20} density expected from 1:1 gas to solid incorporation into the Ge lattice. The incorporation rate of a 0.33% As mixture is higher

by a factor of two at 61%. These trends further validate the practical importance of the $As(SiH_3)_3$ doping strategy. The compound represents a cost-effective and environmentally safer alternative to AsH_3, limiting the amount of waste typically generated in conventional CVD reactions where only a small fraction of the gaseous reactant is converted into solid product.

Figure 11 (a) shows an XTEM image taken from a sample comprising a 150 nm-thick *n*-type layer with ~$1\times10^{20}/cm^3$ donors. In spite of the ultra-high As incorporation, the *n*-layer is essentially defect-free. The surface is flat, the interface (marked by an arrow) is highly uniform, and the bulk crystal is devoid of dislocations, as expected due to the low concentration of inactive donors in the structure. The dark line in the direction of the arrow

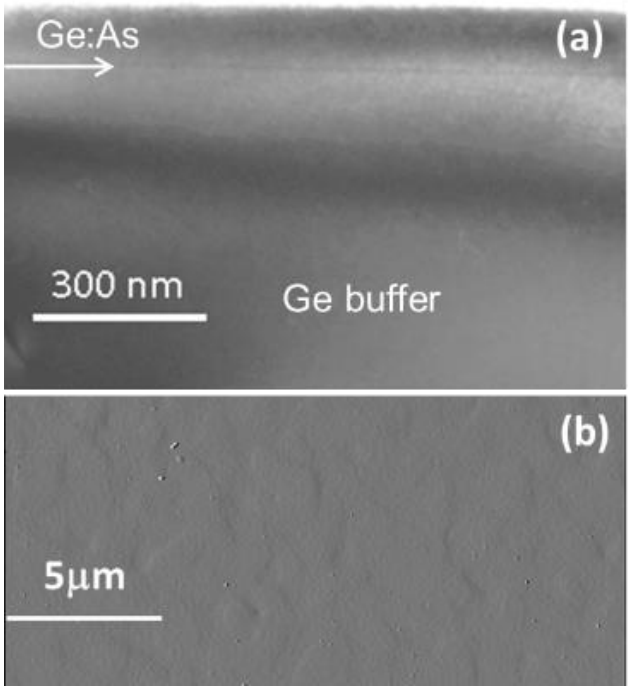

Figure 11 - (a) XTEM micrograph of sample doped with $As(SiH_3)_3$ at 330 °C showing the upper *n*-type portion of the film. The material appears to be defect free within the field of view. (b) AFM image of same sample. The RMS roughness from 20x20 μm^2 areas is 0.68 nm indicating that the surface is flat and mostly free of defects and imperfections.

marks a sharp transition between the buffer and top layer. Figure 11 (b) shows an atomic force microscopy (AFM) image of the same film confirming the flat surface morphology of the material. The structure/morphology data in the figure demonstrates that the growth proceeds seamlessly producing a smooth integration of the *n*-layer onto the underlying buffer.

If As-Si-H molecular fragments play a significant role in the incorporation of As to the growing film, as suggested above, the incorporation efficiency might change if instead of the $As(SiH_3)_3$ precursor we use the $As(GeH_3)_3$ derivative as the source of As. Due to its high reactivity, this compound has already been used to dope $Ge_{1-y}Sn_y$ alloys grown at temperatures as low as 350 °C.[139] The higher reactivity of $As(GeH_3)_3$ is attributed to the presence of weak Ge-H bonds which readily eliminate H_2 byproducts much more effectively than Si-H bonds, enabling the growth of crystalline products under highly metastable non-equilibrium conditions.

We find that the growth rates obtained from deposition of $As(GeH_3)_3$ are nearly double those of the $As(SiH_3)_3$ counterpart. The resultant films exhibit large thicknesses, flat surfaces, low defectivity and relaxed strain states, as demonstrated by XTEM, AFM and XRD characterizations. SIMS measurements, summarized in Table 7, revealed flat As profiles throughout the *n*-region and a precipitous drop of the mass count at the interface with the Ge buffer, indicating that no diffusion occurs across the junction under the ultra-low temperature conditions employed. This is illustrated in Figure 12, which shows the SIMS data for a sample with a donor density of 1.3×10^{20} cm^{-3}. We notice that the As donor concentrations from the SIMS data are in most cases higher when $As(GeH_3)_3$ is used

Table 7 – Growth parameters and compositions of As-doped Ge films using $As(GeH_3)_3$

Atomic As% in mixture	Absolute As by SIMS (cm^{-3})	Carrier concentration by Hall	Carrier concentration by ellipsometry	Carrier activation ratio	Hall to ellipsometry ratio
0.33%	2.52×10^{19}	2.27×10^{19}	2.48×10^{19}	98.4%	91.5%
0.66%	9.06×10^{19}	7.90×10^{19}	7.83×10^{19}	86.4%	100.9%
0.83%	1.30×10^{20}	7.59×10^{19}	8.44×10^{19}	65.2%	90.0%
1.0%	2.14×10^{20}	6.32×10^{19}	6.69×10^{19}	31.3%	94.5%

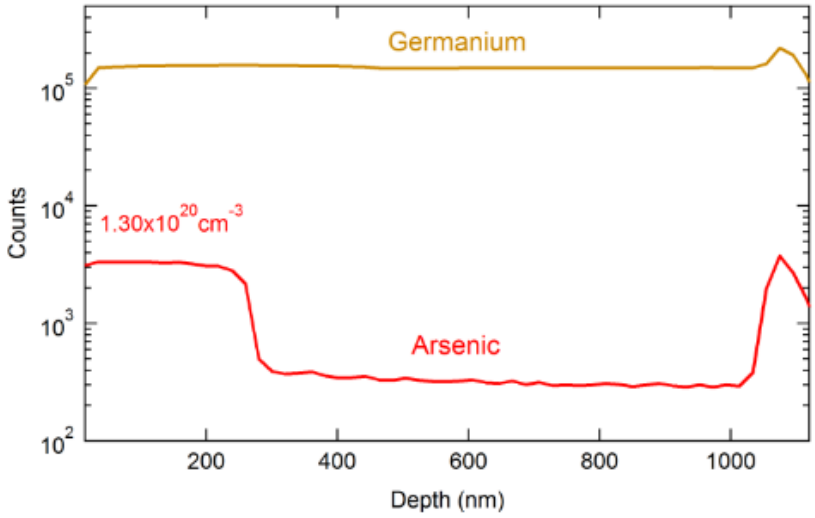

Figure 12 - SIMS depth profile of Ge structure grown by $As(GeH_3)_3$. The plot shows uniform As distribution in the n-type material and a sharp decrease of the spectrum intensity at the interface with Ge buffer. The As concentration is 1.3×10^{20} cm^{-3} which is slightly larger than the active 8.44×10^{19} cm^{-3} amount measured by ellipsometry.

instead of $As(SiH_3)_3$, but the maximum carrier concentrations are about the same. These similarities between $As(GeH_3)_3$ and $As(SiH_3)_3$ suggest that, to the extent that As-Si-H fragments play a role in the As incorporation when using the $As(SiH_3)_3$ precursor, the analogous As-Ge-H fragment should play a similar role when using $As(GeH_3)_3$.

High resolution X-ray diffraction (HRXRD) measurements of the Ge:As films show the expected (004) reflection of the diamond cubic structure as illustrated in Figure 13. The

peak corresponds to combined contributions from the un-doped Ge buffer and the *n*-type epilayer. Samples with low doping contents (<3×10^{19} cm^{-3}) show a single and symmetrical XRD peak indicating close correspondence between the *n*-layer and the buffer contributions within the resolution of the measurement. However, samples with doping concentrations above 3×10^{19} cm^{-3} show a distinct shoulder to the left side of the main Ge peak attributed to the *n*-type material. This is illustrated in Figure 13, which compares the XRD spectra of samples with As densities 2.5×10^{19} cm^{-3} and 7.8×10^{19} cm^{-3}. The latter exhibits a larger *c*-spacing due to the lattice expansion induced by the incorporation of As. The observed lattice expansion under As incorporation is qualitatively consistent with previous experimental and theoretical work.[80,140] A quantitative treatment of this

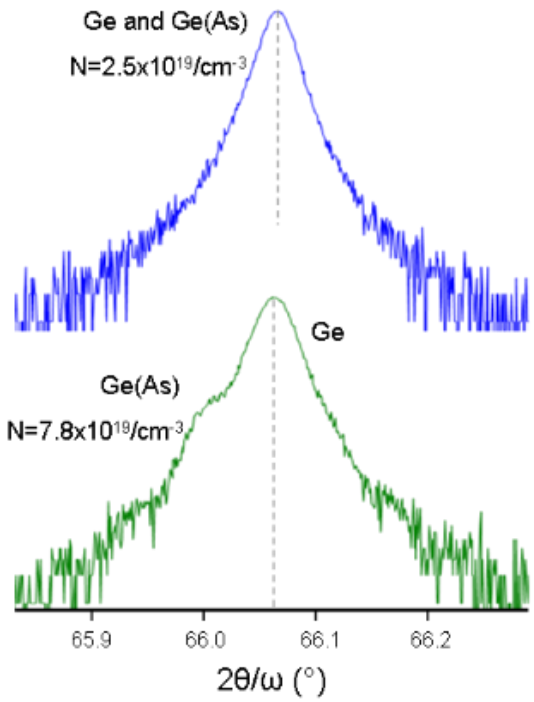

Figure 13 - XRD (004) peaks for As doped Ge samples with doping levels of 2.5×10^{19} cm^{-3} (top) and 7.8×10^{19} cm^{-3} (bottom). The latter sample shows a clearly resolved shoulder indicating a larger lattice parameter for the *n*- layer. The lower intensity shoulders above background on both sides of the peak are interference fringes.

observation, taking into account similar observations in Ge:Sb films discussed in the section below, is presented in Reference 141.

2.4. Donor Activation Studies

For the atomic As concentrations in Table 6 and Table 7, standard donor statistics predicts that at room temperature the corresponding carrier concentrations should barely exceed 1×10^{19} cm^{-3}. This is due to incomplete donor ionization as the Fermi level approaches and exceeds the position of the donor level. We have measured the carrier concentrations in our films using the Hall effect and infrared spectroscopic ellipsometry (IRSE). The Hall measurements were performed on an Ecopia NMS 3000 measurement system at a magnetic field of 0.53 T (as calibrated by the manufacturer) using In-Sn contacts. For IRSE, a J. A. Woollam IR-VASE system was used. The measurements ran over an energy range extending from 0.03 to 0.8 eV with a step size of 1 meV and an angle of incidence of 70°. The measured infrared dielectric function was fit with a Drude model with the resistivity and relaxation as adjustable parameters. Carrier concentrations were also derived from ellipsometric data by assuming an effective mass of 0.12*m*, where *m* is the free electron mass.[135] The results are shown in the tables, and we see that carrier concentrations as high as 8×10^{19} cm^{-3} are obtained. In the presence of incomplete ionization, such carrier concentrations would require donor concentrations approaching 1×10^{21} cm^{-3}. However, as shown for the case of phosphorous doping, incomplete ionization is frustrated and the donors are fully ionized at room temperature, even at the highest donor concentrations.[135] Given the fact that both As and P are shallow donors with similar binding energies, we expect the same frustration of incomplete ionization in As-doped materials, and in fact our results seem to confirm this prediction. The ratio of the carrier concentration measured by

IRSE and the donor concentration measured by SIMS is shown in Table 6 and Table 7 as the carrier activation ratio. We see that for donor concentrations below 1×10^{20} cm^{-3} the activation ratio is above 80%. This is consistent with full activation if we take into account possible measurement uncertainties. Moreover, these activation ratios are obtained from as-grown samples, without any attempt to enhance donor activation via thermal anneals. On the other hand, as the donor concentrations reach the highest levels above 1×10^{20} cm^{-3} we observe a clear drop in the activation ratio for both precursors. As a result of this drop, the maximum carrier concentration achieved is remarkably similar, just above 8×10^{19} cm^{-3} in the two cases. This suggests that above this concentration any additional As atoms furnished by the precursor will form inactive complexes that do not contribute to the material's conductivity.

It is interesting to compare the carrier concentrations from Hall measurements with those deduced from IRSE data. The former were obtained by assuming a Hall factor γ_H =1, whereas the IRSE carrier concentrations corresponds to a conductivity effective mass $m^* = 0.12m$, where m is the free electron mass. This value, discussed in Ref. 135, is the independently determined effective mass.[142] If we were to adjust the effective mass to match the Hall data we would obtain $m^* \sim 0.10m$, less than the known value. This is opposite to the finding of Spitzer, Trumbore and Logan (STL) in their classic 1961 article, where they report that an effective mass of about $m^* = 0.16m$, is required to match optical and Hall data.[116] Since it is by no means obvious that the Hall factor in heavily doped *n*-type Ge should be equal to unity, a discrepancy between Hall and optical measurements is not surprising, but the different sign of the discrepancy between STL and our work is puzzling. We point out, however, that our IRSE data processing involves a full fit of the

real and imaginary parts of the dielectric function, whereas STL seem to have obtained their values using the method discussed by Cardona, *et al.*[143] which avoids the use of non-linear fitting methods by concentrating on the short-wavelength limit of the reflectivity.

2.5. Electrical Properties

Figure 14 shows the doped samples' resistivities obtained directly from the IRSE fits. The results from the two As sources show no significant difference, despite the fact that $As(SiH_3)_3$-doped films contain Si. The solid line in the figure is a fit of the As-doped, bulk Ge resistivities measured by STL using a Hilsum[144] expression of the form $\rho = \left(1+\sqrt{n/n_0}\right)/\left(\mu_0 ne\right)$. The fit parameters μ_0 = 3,780 cm^2/Vs and $n_0 = 1.47\times10^{17}$ cm^{-3} give nearly perfect agreement with the bulk data. It is then apparent that the resistivities measured in our films are in excellent agreement with bulk resistivities, confirming the high quality of our samples. On the other hand, we notice that that the measured resistivities are systematically higher and the relaxation times are systematically shorter than those obtained in films doped with P. Combined with data for Sb-doped Ge as compiled by Cuttriss,[145] the results suggest an ordering $\rho_{Sb} < \rho_P < \rho_{As}$ at the same carrier concentration. This peculiar behavior is not due to the specific precursor used or to the properties of Ge-on-Si films but it is a bulk effect, as suggested by the excellent agreement between the resistivities reported here and those measured by STL. In fact, such ordering was predicted theoretically 40 years ago by Ralph, Simpson, and Elliott as a result of central cell corrections to the Coulomb scattering potential of the donor. The same ordering is seen in the binding energies of the donors.[146] This observation is confirmed by the results obtained from Ge:Sb films presented in the following section.

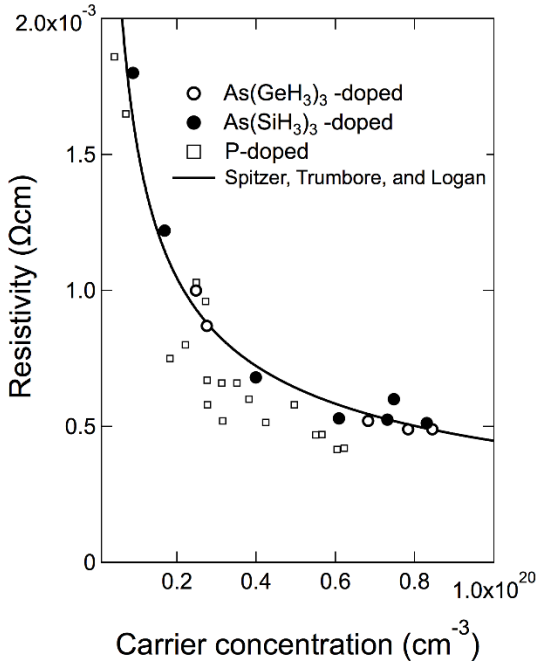

Figure 14 - Resistivity of Ge films doped with As using the $As(MH_3)_3$ (M = Si, Ge) precursors. The solid line is a fit to the resistivity of bulk Ge doped with As. Squares correspond to Ge films doped with $P(MH_3)_3$ (M = Si, Ge)

An important implication is that a lower resistivity of $\rho = 4\times10^{-4}$ Ωcm is observed in P-doped films with the highest carrier concentrations,[115,135] even though these concentrations are 30% lower than those obtained in the As-doping experiments. Thus for CMOS applications that seek the lowest possible sheet resistance, P-doping may be preferable. On the other hand, for laser applications that require the highest possible doping level to increase the population of the Γ-valley minimum in the conduction band, As-doping appears to be the best choice. For example, in a Ge film at room temperature, if the total carrier concentration increases from 6.0×10^{19} cm^{-3} to 8.4×10^{19} cm^{-3}, the Γ-valley population increases by a factor of 2.6.

The intriguing behavior of the resistivities, which are in accordance with the theoretical prediction of $r_{Sb} < r_{P} < r_{As}$,[146] suggest that Sb doped Ge films will perform better than

both P and As doped films, provided that the appropriate high concentration of active donors can be introduced into the Ge lattice. The pursuit of high reactivity hydride precursors that can achieve this purpose is described in the following section.

3. Antimony Doping of Ge Using SbD_3

3.1. Introduction

For bulk doping of Ge, Sb is known to be superior to both P and As donors in terms of obtaining highest mobilities (μ) and lowest resistivities (ρ) for a given dopant concentration, the latter of which is expected to follow the trend $\rho_{Sb} < \rho_P < \rho_{As}$, as described in the previous section.[116,146] However, epitaxial growth of Ge:Sb has proved difficult due to the segregation of the dopant atoms to the surface when high concentrations of the Sb donors are introduced.[147] To circumvent this problem, MBE techniques which use growth temperatures below 250°C were employed by Oehme *et al.* to produce Ge:Sb films with active Sb levels up to 2×10^{20} cm^{-3}.[147] However, such low temperatures are not optimal for growth of Ge, leading to a compromise between high donor levels and crystal quality. Alternatively, laser annealing of ion implanted samples by Thareja *et al.* led to active Sb concentrations greater than 10^{20} cm^{-3} required for Ge based nMOSFET applications.[148] A disadvantage of this method for Sb doping is the higher diffusivity of the donor in the Ge lattice compared to P or As, which can make it difficult to precisely control junction depths.[120] Furthermore, the greater size of Sb inflicts more damage on the host lattice during implantation, requiring more demanding recrystallization and donor activation procedures. Finally, due to the novelty of both techniques, their applicability in an industrial setting remains questionable.

Based on the successful application of P and As germyl and silyl compounds for *in situ* doping of Ge to produce highly doped films with bulk-like resistivities,[115,117] the notion of applying the analogous $Sb(GeH_3)_3$ and $Sb(SiH_3)_3$ compounds to produce epitaxial Ge:Sb seems promising. However, the extremely low vapor pressure (0.5 Torr at 23°C) of the former compound precludes its use in practical CVD applications. Experiments carried out using $Sb(SiH_3)_3$ did not produce Ge films with observable amounts of Sb incorporation. An alternate Sb precursor for low temperature CVD presents itself in the form of the reactive hydride SbH_3. This is in contrast to PH_3 and AsH_3, where the strong M-H bonds (M=P, As) require high temperatures for dopant incorporation to take place. Indeed, the Sb-H bond is so unstable that the hydride rapidly decomposes at room temperature.[97] Todd *et al.* have found that the stability of the hydride can be increased by substituting the H with D.[97] The increased reduced mass results in a 30% reduction of the zero point energy of the deuterated molecule. This is analogous to the higher stability of the SnD_4 precursor –whose use will be described in subsequent chapters- relative to SnH_4. The synthesis of SbD_3 with semiconductor grade purity standards was described in Chapter 2, and it was found that the compound was stable at room temperature when stored at pressures under 10 Torr, enabling its use as a CVD precursor. In addition, it has been found that use of atomic H in MBE growths suppresses the Sb surface segregation.[149] Therefore the presence of H_2 in a CVD environment may be expected to provide a similar benefit, facilitating the growth of uniform, highly doped films.

Despite its potential, and numerous mentions in patent literature, no peer reviewed study which has used SbD_3 for the purpose of doping semiconductors was found. Indeed the only CVD process where it has been used is the growth of III-V compound semiconductors such

as GaSb and InSb.[150,151] Therefore, this study represents the first use of SbD_3 in doping of group IV semiconductors. The systematic depositions described below using Ge_3H_8 and SbD_3 produced Ge:Sb films with carrier densities $n>1\times10^{20}$ cm^{-3}, and resistivities as low as 1.8×10^{-4} Ωcm, and thus validates the choice of this synthetic route.

3.2. Deposition Procedure

For the deposition of Sb doped Ge layers, two types of substrates were employed. The first was Ge buffered Si (100) used in the doping studies discussed in the previous section. In addition, Si(100) wafers with $Ge_{0.95}Si_{0.05}$ buffer layers were also used. Both types of buffer layers were deposited on 4" Si wafers using GSME techniques described earlier for fabricating buffers for As doping studies. The precursor used for the Ge buffers was Ge_4H_{10}, and in the case of GeSi buffers, the addition of tetrasilane (Si_4H_{10}) to the precursor mixture provided the Si. The GeSi buffers enabled the precise determination of the lattice parameter of Sb doped Ge for donor concentrations $N_d < 5\times10^{19}$ cm^{-3}, as described below. For higher donor incorporations, the lattice constant of the doped films were high enough to be distinguished even when the doped films were deposited on Ge/Si(100) substrates. The depositions were conducted at 380°C, and the target buffer layer thickness was ≈1500 nm. Post-deposition *in situ* annealing of the buffer introduces a slight tensile strain of ≈0.1% in the buffers. No evidence of misorientation or epilayer tilt was observed in the buffers, making them suitable platforms for growth of the doped layers.

The wafers were then cleaved into 45 mm × 45 mm quadrants and cleaned using aqueous HF in order to remove the native oxide prior to being introduced into the UHV-CVD reactor used for the doping experiments. This reactor format was chosen because it pre-

activates the reactants before they reach the growth front. The deposition of the doped layers was conducted at 330°C at a pressure of 0.2 Torr. Precursor mixtures for the depositions consisted of Ge_3H_8 and SbD_3 diluted with research grade H_2. For samples deposited on Ge buffers, the relative amounts of the two precursors was adjusted such that the percentage of Sb atoms in the gas phase relative to Ge varies between 0.117% - 0.699%. For the Ge:Sb layers on Ge, the above range was 0.070% - 0.676%. The mixture details are listed in Table 8. The duration for a typical deposition is 40-50 min, and produces a ≈200 nm thick film, which translates to growth rates of ≈4 nm/min.

Table 8 – Absolute Sb concentrations, carrier concentrations and resistivities of selected Ge:Sb films deposited on Ge and GeSi buffers as a function of the atomic % of Sb in the precursor mixtures used to produce the samples.

Sample name	Atomic Sb % in mixture	Buffer type	Absolute Sb concentration (N_d) ($\times 10^{19}$ cm^{-3})		Active carrier concentration (n) ($\times 10^{19}$ cm^{-3})		Resistivity (ρ) $\times 10^{-4}$ Ωcm	
			RBS	SIMS	IRSE†	Hall‡	IRSE	Hall
A	0.07%	GeSi	1.76	1.97	2.30	2.77	7.6	7.75
B	0.12%	GeSi	5.3	4.58	4.92	5.59	4.3	3.79
C	0.25%	GeSi	9.72	9.24	9.97	10.7	2.5	2.21
D	0.47%	GeSi	13.26	12.44	11.6	14.1	2.2	1.86
E	0.68%	GeSi	16.35	17.16	12.7	15.1	1.9	2.1
F	0.12%	Ge	3.09	3.84	3.88	4.48	5.7	5.07
G	0.23%	Ge	7.07	6.45	7.51	8.60	3.15	2.71
H	0.52%	Ge	13.7	12.93	12.6	14.3	1.95	1.77
L	0.70%	Ge	15.47	14.13	13.9	14.6	1.8	1.65

† m^*=0.16

‡ γ_H=1

3.3. Determination of Sb Concentrations and Structural Characterization

The properties of the Ge:Sb films resulting from the above deposition experiments are listed in Table 8. Unlike in the case of P and As, high levels of Sb can be readily detected using RBS, providing a standard-less alternative to SIMS for the determination of absolute

Sb contents in the thin films when the concentrations are above 2×10^{19} cm^{-3}. Furthermore, RBS channeling experiments provide an insight to whether the incorporated Sb occupies substitutional or interstitial positions in the lattice. It was observed that for films with near full activation listed in Table 8, similar degree of channeling was observed for both Ge and Sb signals. An example RBS spectrum for a sample which was measured to have 0.28% (1.24×10^{20} cm^{-3}) incorporated Sb in the film is shown in Figure 15. The inset of the figure shows the clear Sb signal that allows the determination of atomic concentration based on modelling. The ratio between channeled and random spectra (χ_{min}) for these samples does not exceed 15%. But in samples with very high levels of incorporated Sb ($N_d > 1.6\times10^{20}$ cm^{-3}, not shown in the table), de-channeling of the Sb signal is observed with respect to the

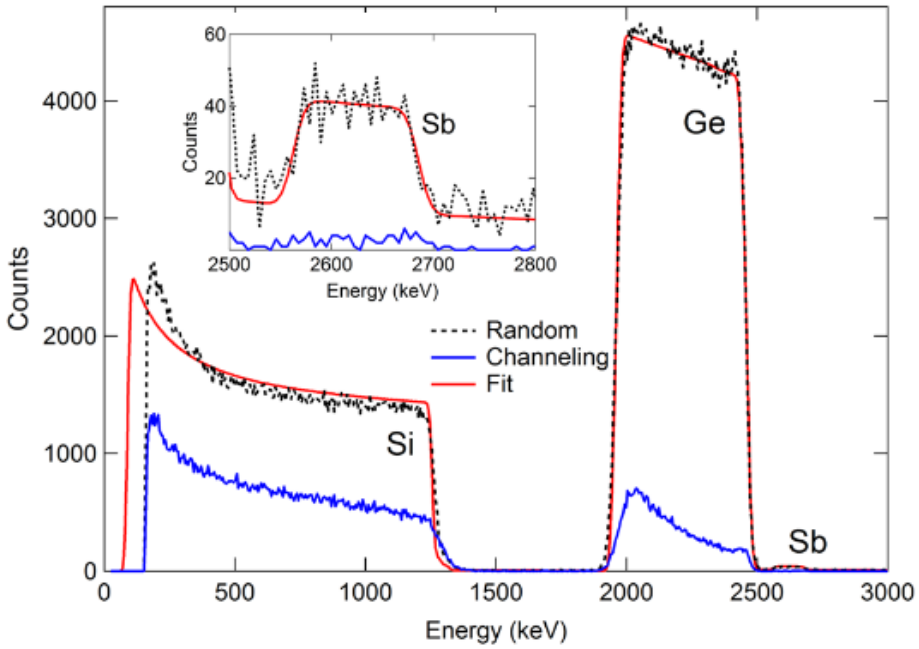

Figure 15 - RBS spectra and composition fit for a sample containing 9.2x10^{19} cm^{-3} carrier concentration. The random and channeled spectra are shown by the black dashed and blue colored lines respectively, whereas model fit is depicted by the red line. The Sb content is fitted to be 0.28%. Both Ge and Sb signals are showing excellent channeling, indicating full substitution. The inset is a close-up of the Sb peak.

Ge, and χ_{min} increases (>25%). The active carrier concentrations of these samples are substantially lower than the total Sb concentrations, indicating that incomplete activation arises from the donor atoms occupying interstitial sites.

SIMS measurements were also carried out on the above films using a CAMECA IMS 6f instrument using a Cs^+ primary beam. This allows a more accurate quantification to be carried out in samples with lower Sb concentrations. The Sb atom concentrations obtained by comparison with a Ge standard implanted with 5×10^{19} atoms/cm^3 of ^{121}Sb are presented in Table 8, and are in good agreement with the RBS results within error of measurement. In addition to corroborating the RBS data, the SIMS elemental profiles also reveal extremely uniform dopant distribution within the doped layer, and an abrupt decrease of the dopant atoms at the interface with the undoped portion of the film. This indicates the lack of any diffusion effects even at the highest Sb concentrations, and can be attributed to the ultra-low temperature deposition conditions. Figure 16 (a) depicts a typical SIMS elemental profile obtained for a sample with an absolute Sb concentration of 1.24×10^{20} cm^{-3} grown on $Ge_{0.95}Si_{0.05}$ substrate exhibiting abovementioned features. The arrangement of the various layers in this structure is depicted in Figure 16 (b). The concentration of Sb obtained using SIMS for this sample agrees well with the 1.33×10^{20} cm^{-3} value obtained via RBS.

In addition to diffusion of Sb to the substrate, another factor that is essential for obtaining uniform dopant profiles is the absence of Sb segregation to the surface. In order to verify this property for the SbD_3 doped Ge, a film was capped by an intrinsic Ge layer, as schematically depicted in Figure 16 (d). This capping layer was deposited immediately

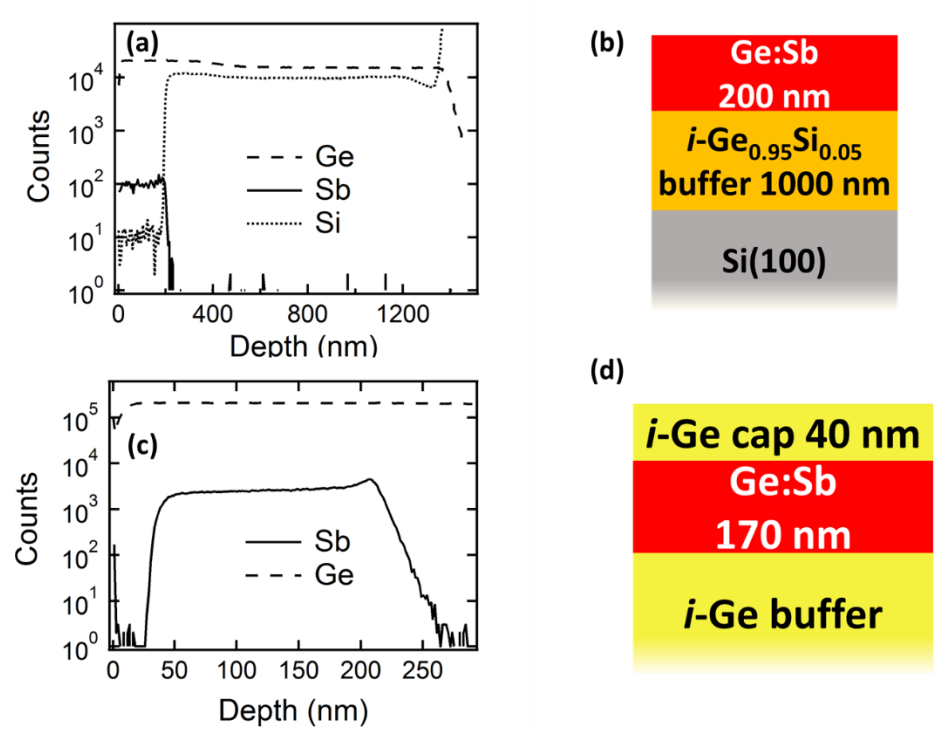

Figure 16 – (a) SIMS elemental profiles for a sample grown on $Ge_{0.95}Si_{0.05}$ buffered Si, the schematic for which is shown in (b). The absolute Sb level in the doped layer is 1.24×10^{20} cm^{-3}. (c) SIMS profile for a 170 nm thick layer with 1.75×10^{20} cm^{-3} donors which is capped with a 40 nm thick intrinsic Ge layer, as shown schematically in (d). The interface between the doped and undoped regions is sharp, indicating that no Sb has segregated to the surface despite Sb incorporation above the solubility limit in the doped layer.

after the Ge:Sb layer without removing the wafer from the growth chamber or subjecting the surface to any cleaning procedure. If any Sb segregation occurs, an increase in the Sb concentration should be evident at the interface between the doped layer and undoped capping layer. As seen from the SIMS profiles for the above sample presented in Figure 16 (c), the Sb counts drop sharply from the value in the doped film down to background levels at the interface. This indicates that the incorporated Sb is distributed uniformly in the doped film, with no enhancement of concentration at the surface.

The microstructure of the Ge:Sb films was analyzed using XTEM and AFM, as depicted in Figure 17 (a) and (b), respectively. The former technique reveals a flat, defect free *n*-

type epilayer, indicating that the growth is fully commensurate with the buffer layer, and the large Sb atoms does not disrupt crystal assembly. This is especially remarkable given that the epilayer depicted in Figure 17 (a) has a donor atom concentration of 1.05×10^{20} cm^{-3}, and a thickness of 200 nm. The flat surface is corroborated by AFM measurements which give a RMS surface roughness of <1 nm. A typical AFM from a sample with a carrier concentration of 8.8×10^{19} cm^{-3} is given in Figure 17 (b).

In order to gain additional insights into the Sb incorporation and donor activation, the lattice parameters of the doped films were measured using HRXRD. As in the case of As doped films described in Section 3, an expansion of the lattice is evident at high dopant levels. Figure 18 shows a series of (004) θ-2θ scans from a set of doped samples which illustrate the increase of the out of plane lattice parameter with increasing dopant concentration. All the layers are grown on $Ge_{0.95}Si_{0.05}$ buffers which facilitate the

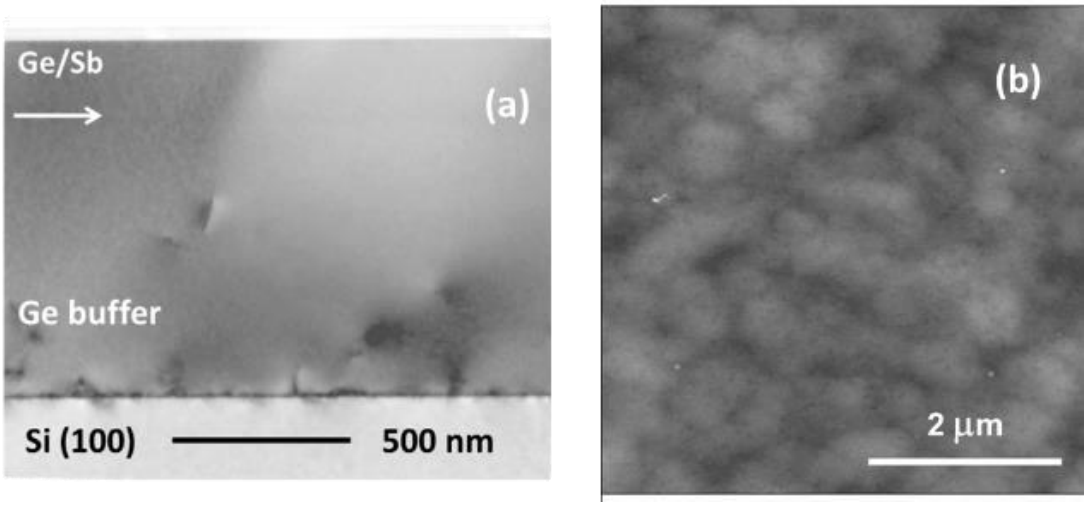

Figure 17 – (a) XTEM image of a Ge:Sb film (N_d=1.05×10^{20} cm^{-3}) on a Ge buffered Si substrate, with the interface between the doped and undoped regions marked by an arrow. The *n*-type layer is defect free within the field of view, with a flat surface (b) AFM image of Sb doped Ge film with an active carrier concentration of 8.8×10^{19} /cm^3. The RMS surface roughness calculated from this image is 0.97 nm.

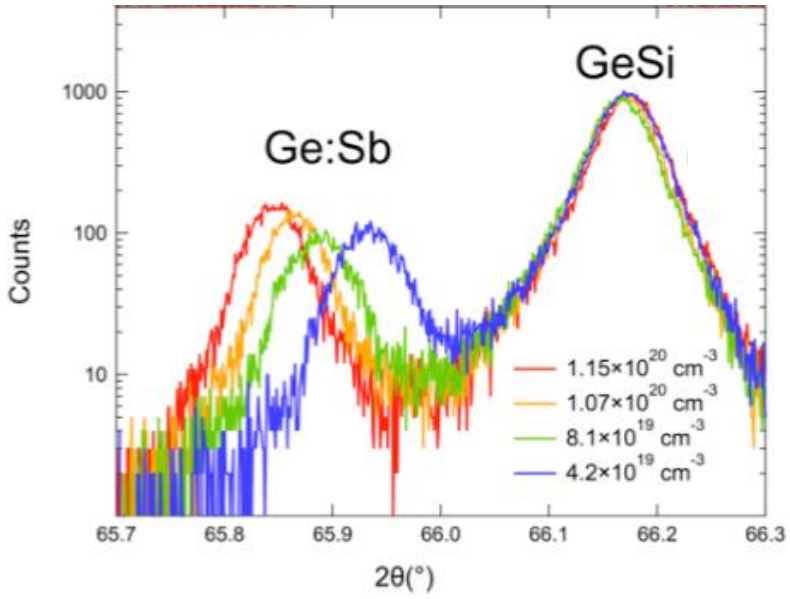

Figure 18 - θ-2θ scans for the 004 reflection in several Sb-doped Ge films grown on $Ge_{0.95}Si_{0.05}$. The peaks at high angles correspond to the buffer layers. Figure adapted with permission from Xu, C. *et al. Phys. Rev. B* 2016, *93* (4), 041201. Copyrighted by the American Physical Society

determination of the epilayer peak position due to minimal overlap with the buffer peak. Furthermore, since the epilayers are pseudomorphic to the buffer layers, they have the same in plane lattice parameter. Therefore the increase in the out of plane lattice constant observed in the figure corresponds to an increase in the relaxed lattice constant. This was further verified by obtaining (224) reciprocal space maps of the epilayer and buffer layer peaks. The in-plane and out-of-plane lattice constants can be measured using the maps, and by applying standard elasticity theory, it is possible to calculate the relaxed lattice parameter. The (224) RSM also enable the calculation of strains. The larger lattice parameters of the doped films will lead to compressive strain if deposited on bulk Ge, the tensile strain present in the Ge buffer layers opposes this effect, leading to largely strain relaxed films. The films deposited on GeSi buffer layers do exhibit compressive strain due to the greater lattice parameter difference in comparison to the substrate. However, in all

cases the (224) RSMs revealed that the strains are small, and are therefore not expected to affect the measurement of optical and electrical properties given here.

As a result of the work described thus far in this chapter, Ge films which are highly doped with two different group V donor atoms –namely As, and Sb– which exhibit nearly complete activation are now available. As discussed above, it is evident that the dopant incorporation has a significant effect on the lattice parameter of Ge. Combined with the data for similarly P doped Ge films provided in Reference 115, a detailed analysis of the differences in manifestation of this phenomenon among different group V dopant atoms allows the identification of the correct theoretical framework required for its description. Such an analysis is presented in Reference 141, and it was found that the lattice expansion could be described as a sum of contributions arising from electronic and size effects as described by the Cargill-Keyes theory. This can be expressed mathematically as:

$$\frac{\Delta a_0}{a_0} = bN_d = \left(b_{\text{size}} + b_{\text{e}}\right)N_d = \left(\frac{2}{a^{**}N_{\text{Ge}}}\frac{\Delta R}{R} - \frac{a_c}{3B}\right)N_d \qquad (4.2)$$

In the above equation, Δa_0 is the change in the lattice constant, a_0 is the lattice constant of the undoped material, and N_d is the dopant concentration. The coefficient of change in lattice parameter is denoted as β, which is separated in to the contribution from donor atom size (β_{size}) and electronic effects (β_{e}). The physical parameters that determine these contributions are the topological rigidity parameter (a^{**}=0.7 for diamond and zinc blende semiconductors),[152,153] relative difference between the donor-Ge and Ge-Ge bond lengths for an isolated donor ($\Delta R/R$, calculated to be 0.0674 for the Ge-Sb case by Chizmeshya *et al.* in Ref. 80), the bulk modulus (B=4.682×10^{23} eV/cm^3=75.01 GPa from Ref. 154), the

atomic density of bulk Ge (N_{Ge}=4.418×10^{22} cm^{-3}), and the absolute deformation potential for the conduction band states (a_c). The latter is calculated to be a_c = -1.5 eV by Van de Walle,[155] which compares well with the values given in References 156 and 157.

Figure 19 compares the lattice paramters calculated using Equation 4.2 with the experimantal lattice parametrs observed for samples with 1.0×10^{19} cm^{-3} < N_d < 1.6×10^{20} cm^{-3}. As noted earlier, these samples show excellent channeling of the RBS Sb signal which indicates substitutional incorporation of the donor atoms in the lattice. The fact that the experimental lattice parameters agree well with the theoretical predictions for Ge:Sb with full substitutional donor incorporation further validates the above conclusion, which can be used to explain the electrical properties of these films, presented below.

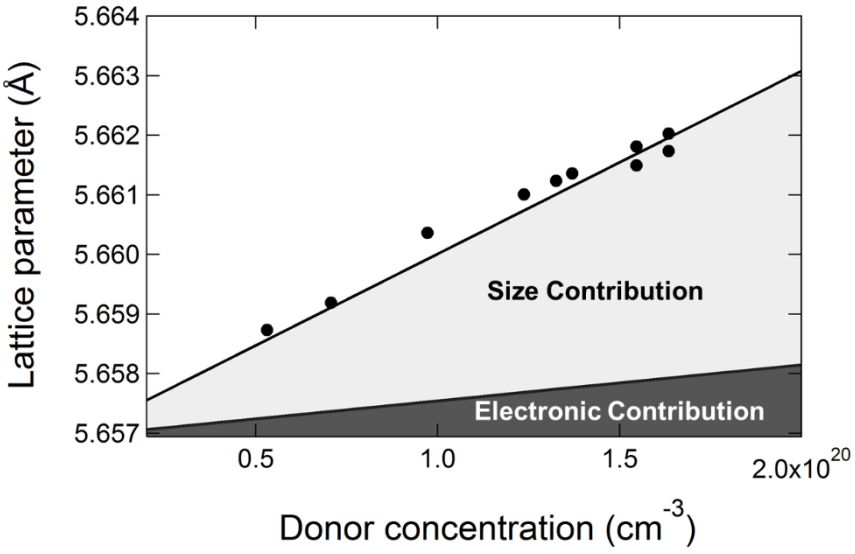

Figure 19 – Plot of the experimental relaxed lattice parameter determined from (224) RSMs vs. the total Sb content determined from RBS. The solid line is the calculated lattice parameter based on Cargill-Keyes theory as described in Equation 4.2. The light and dark shaded areas respectively represent the size and electronic contributions to the lattice expansion.

3.4. Electrical Properties of Ge:Sb Films – Carrier Concentration

The active carrier concentrations of the films listed in Table 8 were determined using both IRSE and Hall measurements. The former were conducted on a J. A. Woollam IR-VASE ellipsometer, while the latter measurements were made using an Ecopia 3000 Hall system. It can be seen that when the customary Hall factor of γ_H=1 is used, carrier concentrations are found to be greater than donor concentrations, which is unphysical. This discrepancy is resolved if a Hall factor γ_H=0.87 is used, which is obtained by assuming $N_d = n$ for concentrations up to 1.0×10^{20} cm^{-3}. This assumption can be validated by the Altermatt model for frustrated incomplete donor ionization as applied for the Ge case in Reference 135, and the Hall factor agrees well with the theoretical estimate of γ_H=0.83.[158,159] Best agreement of the Hall and ellipsometry results can be obtained when the effective mass value of m^*=0.16m is used. This is in contrast to the m^*=0.120m value used for the Ge:As films earlier. Such systematic differences may indicate a donor-dependent Hall factor or effective mass.

The carrier concentrations obtained from this analysis is plotted in Figure 20, and it can be seen that for high donor concentration in the 1.2×10^{20} $cm^{-3} > N_d > 1.6\times10^{20}$ cm^{-3} range, the carrier concentrations deviate from the complete ionization predicted by the Altermatt model. While it is possible to incorporated more Sb up to concentrations of 1.2% (5.3×10^{20} cm^{-3}), this does not result in a further increase in the active carrier concentrations. However, below the 1.6×10^{20} cm^{-3} limit, structural data presented earlier suggests that full substitutional donor incorporation occurs. This trend is in agreement with the electrical properties of the films, will be discussed in greater detail in the context of resistivity values presented below.

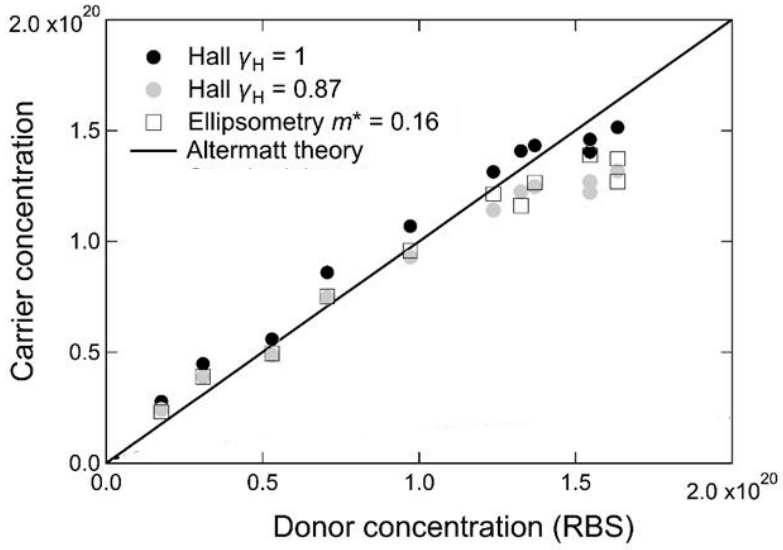

Figure 20 - Experimental carrier concentrations *n* as a function of the measured donor concentrations N_d in Ge:Sb films. The solid line is a prediction based on Altermatt's model of incomplete ionization.

3.5. Electrical Properties of Ge:Sb Films – Resistivity

The resistivity values given in Table 8 are plotted with respect to active carrier concentrations in Figure 21. The solid line in Figure 21 is a fit to the bulk Ge:Sb data compiled by Cuttriss, shown as black circles in the plot. The fit is of the form

$$\rho = \frac{1+(\frac{n}{n_0})^{\alpha}}{\mu_L n e} \qquad (4.1)$$

Where n_0 and α are adjustable parameters and μ_L=3800 cm^2/Vs is the lattice contribution to the electron mobility. This expression was proposed by Hilsum,[144] and was used earlier in a similar fit of the date obtained for Ge:As films in the previous section. In that instance, it was found that α=0.5. However, for Ge:Sb films, the fit parameters α=0.39 and n_0=9.21×10^{16} cm^{-3} provides the best fit shown in the figure. The resistivity values obtained from ellipsometry and Hall measurements for the films doped using SbD_3 are shown as

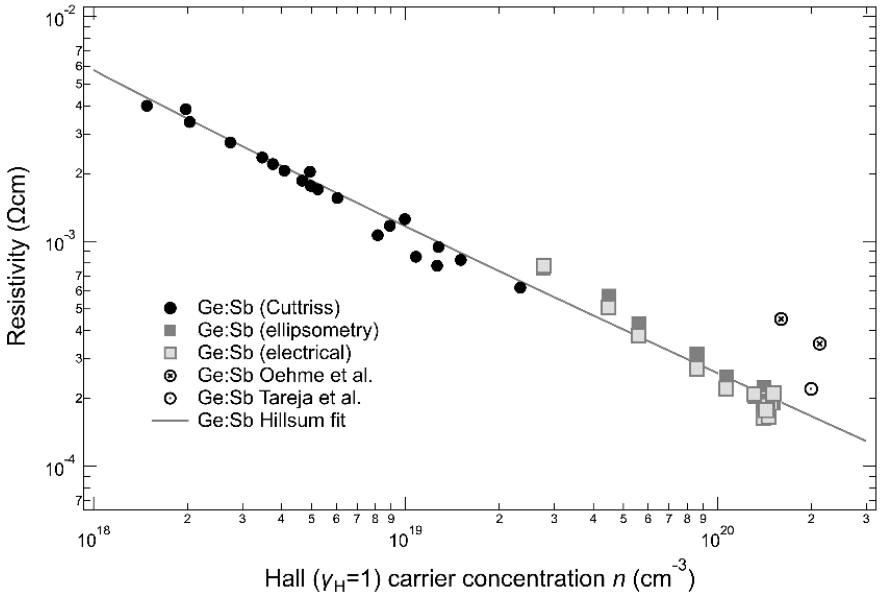

Figure 21 – The resistivity values (dark and light squares denote values obtained from ellipsometry and Hall measurements, respectively) from Ge:Sb films doped with SbD_3 compared with bulk data compiled by Cuttriss (solid circles).[145] The solid line is a Hilsum[144] fit to the Cuttriss data. Literature values from Oehme *et al.*[147] and Thareja *et al.*[148] are also included for comparison.

dark and light squares respectively in the same plot. For consistency with the literature data, a Hall factor of γ_H=1 is used in the comparison, and it can be seen that the resistivity values are in good agreement with the extrapolation from bulk values to the much higher carrier concentrations in the SbD_3 doped samples.

The resistivity values are compared to those reported by Oehme et al. and Thareja et al. for similar carrier concentrations. The trends show that only prior study that reports film resistivity comparable to bulk Ge is that by Thareja *et al.*,[148] in which Sb implanted samples were produced and laser annealed at the melting point. In this case carrier densities up to $2x10^{20}$ /cm^3 were measured but the corresponding resistivity is higher than expected from our observations as shown in the figure. Collectively the results above indicate that the Ge:Sb films doped with SbD_3 have superior structural properties that result in record low

resistivities. Indeed, the lowest resistivity value of 1.8×10^{-4} Ωcm is the best reported thus far in literature. It is interesting to note that the lowest resistivities are observed in the highest doped samples in the 1.4×10^{20} cm^{-3} < N_d < 1.6×10^{20} cm^{-3} range, for which it appears not all donors are fully active. However, RBS channeling experiments indicate that the Sb atoms in these samples occupy substitutional positions. As mentioned earlier, for N_d > 1.6×10^{20} cm^{-3}, the active carrier concentrations decrease and this is accompanied by an increase in the channeling yield (χ_{min}) in the RBS spectra. Donor-vacancy clusters, which have been shown to form preferentially in Ge:As and Ge:Sb, may be the cause of this donor deactivation.[160,161]

3.6. Doping Efficiency

The measurement of absolute Sb concentrations reveal that the incorporation of Sb via SbD_3 is highly efficient, with the Sb/Ge ratios of the precursor mixtures being equal to the Sb/Ge ratios of the deposited films at low doping levels. Even at high doping concentrations, the latter value is ≈50% of the former, as seen from the precursor and film Sb concentrations given in Table 8. This observation also supports the conclusion that all of the incorporated Sb is active, since no extra Sb is available to be in an inactive form. This is in contrast to the $As(SiH_3)_3$ and $As(GeH_3)_3$ precursors described earlier, where a greater portion of the dopant precursor does not contribute to dopant incorporation in the film. Indeed, SbD_3 has higher incorporation ratio compared to the molecules in the $D(MH_3)_3$ family (D=P, As; M=Si, Ge). This comparison is justified due to the essentially identical methods used for the deposition of the doped films using various precursors. In addition, a saturation point of donor activation is reached at ≈0.6% donor atoms in the precursor mixture for all precursors, beyond which further increase in carrier

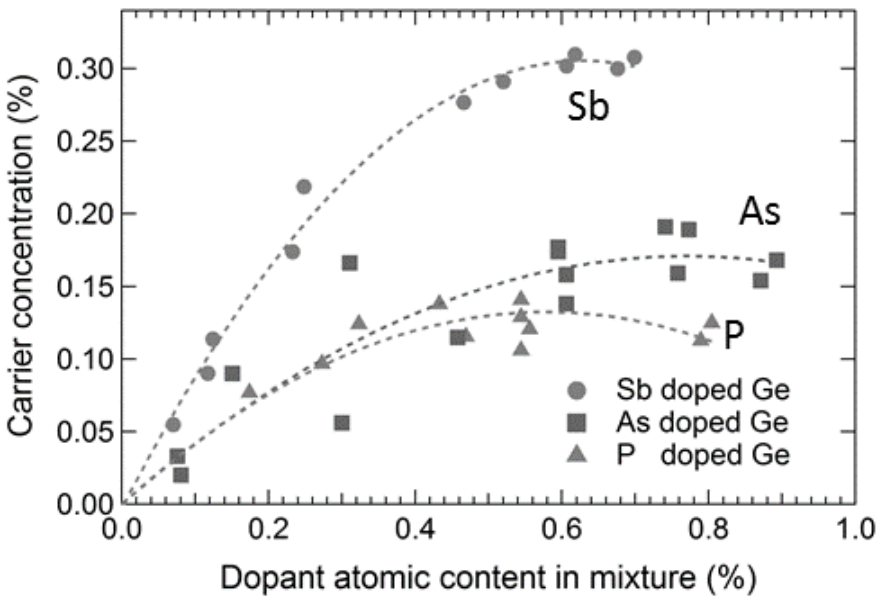

Figure 22 – Efficiency of doping for P, As, and Sb doped Ge films synthesized using single source CVD, which reveals SbD_3 has higher incorporation efficiencies than $D(MH_3)_3$ molecules.

concentrations is not reached. These trends are illustrated in Figure 22. The more efficient behavior SbD_3/Ge_3H_8 combination is reminiscent of the SnD_4/Ge_3H_8 precursor system used for deposition of GeSn alloys. As discussed in Chapter 5, the compatible reactivity of the two precursors allows depositions in which the film and precursor mixture element stoichiometries are nearly equal. Overall, the plots presented above can be used as a guide for incorporating target donor levels of P, As and Sb using novel low temperature precursors discussed above. It must be noted that even though donor incorporation efficiency of the $D(MH_3)_3$ molecules is less than SbD_3, they are nevertheless superior to the traditional PH_3 and AsH_3 sources. In addition, all of the abovementioned molecules present an opportunity to develop environmentally safer alternatives to traditional *in-situ* doping methods that utilize extremely toxic gaseous precursors.

From the donor activation and resistivity results presented above, it can be concluded that the novel chemical approaches to doping Ge with group V donors described above not only gave rise to technologically relevant highly doped semiconductor material, but also contributed to expanding the understanding of the fundamental properties of doped Ge. To extend this line of inquiry further, the properties of the double donor S in Ge was investigated next.

4. Sulfur doping of Ge using Disilylsulfide and Digermylsulfide

4.1. Introduction

Due to the success of using molecules with pre-formed bonds between group IV and group V atoms for the doping of Ge, this approach was next applied to the introduction of group VI doping atoms into the Ge matrix. This was made possible by the $S(SiH_3)_2$ and $S(GeH_3)_2$ precursor molecules introduced in Chapter 2. The motivation for pursuing this research avenue is the success obtained in doping Si to high levels with the group VI element S. This produces the material known as 'black silicon' which has been used to demonstrate prototype detector and solar cell devices.[162–166] The achievement of high carrier concentrations in this case is facilitated by the double donor nature of S. Similar applications at longer IR wavelengths can be envisioned for S doped Ge, where the first and second ionization energies are 0.28 eV and 0.59 eV respectively.[118,167]

The most common doping approaches for S doped Si to date include gas-phase diffusion of elemental sulfur, traditional implantation followed by laser annealing of the wafers and laser irradiations in an SF_6 ambient.[162,168–171] Most recently laser induced incorporation of S via overpressures of gaseous SF_6 has been reported to produce reasonably high amounts of S ($5x10^{19}$ cm^{-3}) although the degree of their activation is limited to 1%.[172] A common

issue in conventional synthesis techniques is the inability to precisely control the spatial and depth distribution of the S atoms and the inherent compositional non-uniformity with respect to the substitution of single S atoms or S_2 dimers in the target lattice.[167,170,171] In spite of this limitation intriguing optical physics have emerged from the pioneering work in this nascent semiconductor material arena including combinations of deep impurity as well as shallow donor levels. These fundamental discoveries have demonstrated potential for the design and development of possible device structures based on black silicon.

In the case of Ge, S doping has also been achieved by physical methods, including diffusion[173] and implantation.[174–176] An important area of application is the modulation of Schottky barrier heights at metal-Ge interfaces. In addition, since Ge is the material of choice for near-IR photodetector in the flourishing area of Si photonics, this S doping approach may also represent a direct and reproducible route to crystalline *n*-type Ge-on-Si layers for applications in a wide range of new device platforms, including Ge based lasers.[10] Several related reports also emerged of S doping in structurally compatible III-V systems, such as InP and GaAs, although these studies appear to be of a preliminary nature. Finally, and presumably because of its possible analogy to black silicon, S doped Ge has been mentioned in the patent arena, but without disclosure of specific methodologies for producing such materials.[177]

For actual device application the processing of doping semiconductors typically requires control of both uniformity of composition and amount of dopant that is incorporated into the growing film. In the case of sulfur in Si this is difficult to attain using most obvious sources such as H_2S and metal-organic analogs since these require growth and processing

at high temperature which precludes a substantial degree of dopant atom activation. Another issue is the propensity of introducing undesirable contaminants impacting the quality of the final material. To circumvent some of these issues here we propose an entirely new approach to achieve in situ doping during growth of group IV heterostructures using purposely designed molecular sources such as $S(SiH_3)_2$ and $S(GeH_3)_2$ that exhibit the required reactivity and structural compatibility with the parent diamond lattice. In the case of both of these molecules the S atom is pre-bonded to group IV atoms terminating with easily removable hydrogen ligands which can be readily eliminated as highly stable H_2 leaving behind SSi_2 and SGe_2 core structures with bonding properties akin to those present within the bulk group IV crystal. The bonding arrangements of the incorporated cores also strongly promote "automatic" activation of substitutional S atoms by virtue of the near tetrahedral electron domain geometry of their S central atoms. In addition these configurations are expected to suppress S-S near neighbor bond formation further increasing the electronic homogeneity of the active site distribution in the crystal. Although, to our knowledge, this strategy has not been implemented in S doped Si it has the potential to circumvent the deleterious effects that the diffusion and implantation may have on the crystalline properties of the final product. Since Ge is the material of choice for near IR photodetector in the flourishing area of Si photonics, this S doping approach may also represent a direct and reproducible route to crystalline *n*-type Ge-on-Si layers for applications in a wide range of new device platforms including Ge-based lasers.

To test the viability of our approach using $S(SiH_3)_2$ and $S(GeH_3)_2$ as sulfur delivery agents we adopted Ge films grown on Si as the candidate host material for our studies. The molecular cores of these compounds are structurally compatible with bond lengths in

germanium, making this lattice an ideal test bed, as corroborated by ab initio calculations.[118]

4.2. Growth of Ge:S layers on Si(100) using Digermylsulfide and Tetragermane

As a feasibility experiment we attempted minimally doping Ge films with S atoms in the 10^{18} target range which still represents a sufficient number of atoms to ensure full activation. The films were grown on 4 inch Si(100) high resistivity wafers via reactions of $S(GeH_3)_2$ and Ge_4H_{10} using a single wafer gas source MBE reactor described elsewhere.[77] The substrates were first dipped in HF to remove the native oxide layer and then heated on the sample stage at 550 ^oC for 5 minutes under ultra-high vacuum to desorb residual impurities and generate an epitaxy-ready surface as evidenced by in situ RHEED analysis. Crystal growth was commenced by inserting the gaseous mixture into the chamber through a nozzle terminating with a showerhead which was positioned at a distance of 3" from the substrate surface. The gas flow was controlled by a high precision needle valve and the growth pressure was maintained constant at 10^{-4} Torr via dynamic turbo-pumping. The wafer-heater temperature was kept constant at approximately 380 ^oC for all experiments while the reaction times varied from 25-40 minutes from sample to sample. The corresponding average growth rates were found to be in the range of 10 to 12.5 nm/min presumably due to slight deviations in $S(GeH_3)_2$ flux concentration. It is interesting to note that under similar conditions the Ge_4H_{10} compound has been previously shown to produce device quality Ge-on-Si films with large thicknesses of several microns and beyond using a comparable low temperature range of 380-400^oC yielding commercially viable growth rates approaching 30 nm/min. We see that the latter rates are

2-3 times higher than those obtained in this study indicating that the presence of $S(GeH_3)_2$ at the growth front significantly reduces the reaction kinetics for the Ge:S films.

Table 9 contains a summary of the Ge:S film parameters including thickness, active carrier concentrations and mobility values determined by Hall and the absolute amount of S incorporated in the film as measured by SIMS. The thicknesses was determined by spectroscopic ellipsometry and corroborated by RBS which was also used to show that the samples were fully commensurate to the substrate by measuring the ratio of the channeled and random signals in the spectra (connoted as χ_{min}). The RBS analysis yielded χ_{min} values as low as 5-10 % indicating a high level of film-crystal alignment with the wafer. High resolution XRD confirmed the single crystal character of the layers and indicated that they typically possessed residual compressive strains on the order of 0.15 % which were readily relieved by rapid thermal annealing at 600-700^{o}C. Further characterizations by XTEM revealed uniform mono-crystalline films possessing epitaxial hetero-interfaces and atomically flat surfaces indicating that the incorporation of sulfur does not significantly disrupt the high microstructural quality of the Ge layers as shown in Figure 23.

Table 9 - Summary of S-doped Ge film parameters produced using $S(GeH_3)_2$. The data includes thickness, SIMS and Hall concentrations as well as mobility values of the post-annealed samples.

No.	RBS thickness (nm)	As-grown Hall (cm^{-3})	Annealed Hall (cm^{-3})	SIMS conc. (cm^{-3})	Post-anneal mobility ($cm^2/(Vs)$)
001	300	3×10^{17}	4×10^{17}	1×10^{17}	530
003	400	8×10^{17}	7×10^{17}	4×10^{17}	750
007	400	3×10^{17}	3.3×10^{17}	2×10^{17}	830
008	500	3×10^{17}	3×10^{17}	1×10^{17}	960

All of the samples described in Table 9 were grown using one liter gaseous reaction mixtures comprising room temperature vapor pressure of Ge_4H_{10} (1.6 Torr) and varying amounts of the $S(GeH_3)_2$ co-reactant ranging from 0.50 Torr (sample 001) to 1.8 Torr (sample 003, 007 and 008) diluted with high purity H_2. Samples 003, 007, and 008 were all grown at 380°C within a time frame of 40 minutes. However, the flux concentration of 008 was slightly higher than that of 003 or 007 thus increasing the growth rate and yielding a thicker corresponding film, as expected. We find that among these samples 003 contains $8x10^{17}/cm^3$ active donor carriers while a similar but slightly lower value of ~ $3x10^{17}/cm^3$ is found for sample 007 and 008 as determined by the Hall method. It is interesting to note that the average amount of active S incorporated in these three samples after annealing is ~ 4 x 10^{17}as measured by Hall with inherent variations that may arise due to slight fluctuation of the growth conditions during deposition. For example we find that the threshold temperature for reaction of the dominant Ge_4H_{10} source is within the narrow

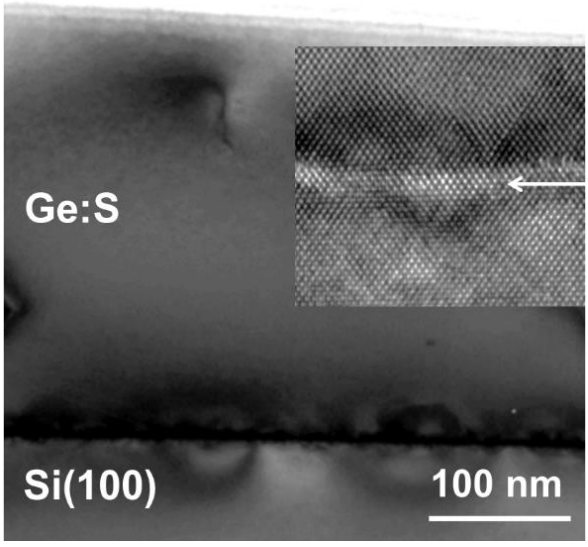

Figure 23 - XTEM micrograph of S doped Ge layer grown upon Si(100) at 380°C via reactions of $S(GeH_3)_2$ and Ge_4H_{10}. Inset shows a high-resolution image of the interface marked by the arrow.

range of 380 to 390 ^{o}C leading to a sharp rise in deposition rates within this temperature window. In this context the slightly reduced S incorporation in sample 008 relative to 003 and 007 may then be explained by a the inherent decomposition of the Ge_4H_{10} at the above temperature combined with the higher concentration of the reactants (lower dilution) employed for this sample. Sample 001 was grown using a significantly shorter deposition time or 25 minutes which accounts for the reduced thickness of the films. Interestingly in spite of the decrease in concentration of the $S(GeH_3)_2$ co-reactant in the growth flux of 001 the degree of S incorporation is comparable to the average of the other samples as determined by Hall.

The amounts determined by Hall represent the activated values of the dopant and has important implication for device applications. From a sample preparation perspective using a new protocol it is crucial to establish the actual amount of S contained in the film. For this purpose we conducted SIMS analysis using an implanted 300 nm thick sample containing $1x10^{19}$ S atoms/cm^3 as a standard. Compositional profiles were acquired using a Cameca-6F SIMS instrument and the data showed a uniform distribution of both S and Ge atoms throughout the bulk films listed in the table. In all cases the absolute S amounts measured by SIMS are found to be consistently smaller by a factor of 2-3 compared to the activated concentrations obtained from Hall. Given that our pure reference Ge films grown under the same conditions are *p*-type with $5x10^{16}$ cm^{-3} acceptor levels, the *n*-type character of our doped films provides strong evidence that S atoms must be both incorporated and activated. Although their concentration is small and may in some cases (samples 001 and 008) approach the detection limit of the instrument, the consistency in the procedures used makes the doubling of the ratio in the samples significant even though the absolute values

have large uncertainties. In fact Hall measurements on films 003 and 008 yield values of ~8 x10^{17}/cm^3 and ~3 x10^{17}/cm^3 whose ratio of ~2 is similar to that found in our SIMS concentrations. Since sulfur can be viewed as double donor the lower value of the atomic SIMS concentrations are expected to be lower by a factors of 2 as observed in the table, as can be expected for fully ionized double donors. These initial results are encouraging and indicate that S can be incorporated into Ge and hopefully these levels can be controlled by adjusting the process conditions. Finally we note that the above data were obtained from samples annealed via rapid thermal methods (RTA), which essentially showed no significant change in active levels and SIMS contents compared to those of the as-grown counterparts. However, as expected, the annealing essentially doubles the mobility from sample to sample, which is consistent with the improvements in crystallinity afforded by the RTA step and evidenced by XTEM and XRD characterizations. This is corroborated by the observation that the highest mobilities are observed in the thickest samples, which is consistent with increasing the volume fraction of defect-free material in the film (e.g., portion of the film not influenced by the highly dislocated interface region).

In spite of changes in concentration of $S(GeH_3)_2$, disparities in the ratio of co-reactants used, and growth rates obtained, the resultant films have very similar doping properties including comparable amounts of activated and incorporated S atoms. Thus the concentrations listed on Table 9 can be viewed as the upper bound for fully substitutional S for this family of samples. Therefore it appears that the reaction of $S(GeH_3)_2$ rejects the additional sulfur supplied by greater reactant flux, which desorbs as some form of volatile hydride, and ultimately results in a film devoid of undesirable interstitials or segregated impurities. Collectively, the strategy developed here for the systematic incorporation

sulfur into Ge represents a significant improvement compared to status of the "black silicon" analog in which the S in known to exist in great excess relative to the activated fraction.

4.3. Growth of Ge:S Using Disilylsulfide

Next we studied the feasibility of $S(SiH_3)_2$ as a dopant source using the above gas source MBE process to explore the incorporation of viable doping levels of S atoms similar to those achieved by the $S(GeH_3)_2$ analog. Initial experiments employed the same temperature of 380 ^oC and comparable reactant mixtures produced in a 1 L vessel containing the vapor pressure of Ge_4H_{10} and 0.1 Torr $S(SiH_3)_2$ co-reactant diluted with 30 Torr of H_2. This initial experiment designated as 013 in Table 10 resulted in an 800 nm thick film having an *n*-type carrier concentration of 2 x 10^{17} cm^{-3} determined by Hall and a total concentration of sulfur of 14x10^{17} cm^{-3} determined by SIMS. Materials characterizations of structure and bulk composition were conducted by XTEM, RBS and XRD. Figure 24 shows representative electron microscopy data for the sample after annealing at 700^oC. The microstructure is uniform within the field of view exhibiting occasional dislocations within the 800 nm layer thickness as well as interface defects. The

Table 10 - Summary film parameters for samples produced using $S(SiH_3)_2$ including Si content, film thickness, and sulfur concentrations as determined by SIMS/Hall.

No.	% Si RBS (SIMS)	RBS Thickness (nm)	As-grown Hall (cm^{-3})	Post-anneal Hall (cm^{-3})	As-grown SIMS (cm^{-3})
013-MBE	2.8 (1.7)	800	2×10^{17}	2×10^{17}	14×10^{17}
014-MBE	13	450	8×10^{15}		
016-MBE	10	250	2×10^{15}	1×10^{15}	
017-MBE	13	230	3×10^{15}		
009-CVD	~0.0 (0.04)	420	3×10^{17}	2×10^{17}	45×10^{17}

free surface shows roughness undulations presumably originating from the initially high sulfur levels incorporated in the as-grown material as shown in Table 10. This is in contrast to pure Ge films grown under similar conditions which are found to possess planar morphologies in all cases. The RBS spectra reveal small amounts of substitutional Si on the order of ~ 2-3 % which is consistent with the 2.8 % value obtained by XRD measurements of the lattice constant in conjunction with Vegrad's Law. The XRD/RBS plots also show that layers are largely devoid of epitaxial strains and are crystallographically aligned with the underlying substrate (see Figure 24).

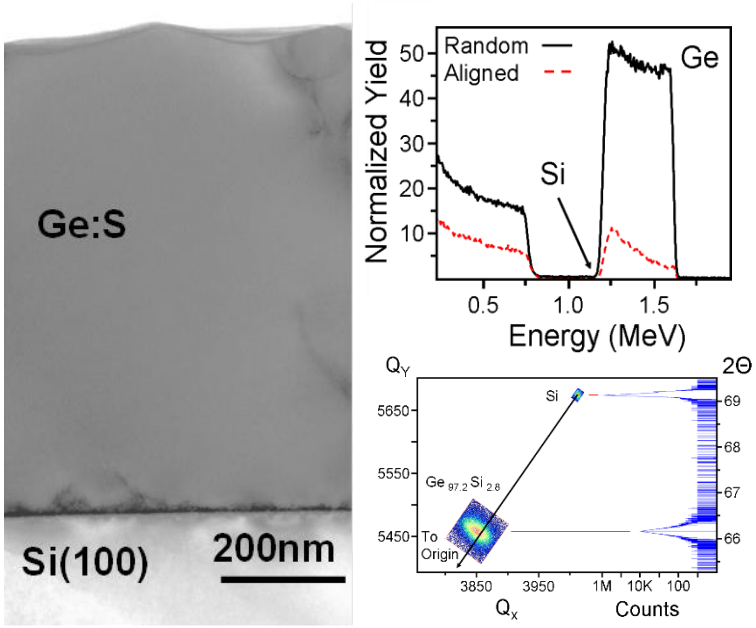

Figure 24 - (top left) XTEM micrograph of 800 nm thick Ge/Si(100) sample doped with S. The Ge layer contains sporadic dislocations scattered across the film and exhibits surface undulations. (top right) Corresponding random RBS spectra show the main Ge peak and a very low intensity shoulder corresponding to Si (marked by arrow). The channeled spectrum (red trace) indicates a high degree of epitaxial alignment. (Bottom right) HRXRD plots of the 004 peaks and 224 reciprocal space maps indicate that the layer is monocrystalline and virtually strain free. The measured lattice constant is used to estimate the Si content at 2.8 % following Vegard's Law.

The S and Si content for sample 013 were measured by SIMS to be $14x10^{17}$ cm^{-3} and $7.6x10^{20}$ cm^{-3} (1.7%), respectively. The latter value is in reasonable agreement with the XRD/RBS estimates given the large uncertainty with these techniques. The SIMS concentration in this sample were obtained using implanted reference standards and elemental profiles as shown in Figure 25 which also illustrates that the Si, and S atoms furnished by the $S(SiH_3)_2$ compound are evenly distributed across the 800 nm thick layer. In view of the order of magnitude discrepancy between the activated Hall value ($2x10^{17}$ cm^{-3}) and absolute ($14x10^{17}$ cm^{-3}) amounts of S in this sample determined by SIMS, we attempted to increase the charge carriers via RTA processing of the samples up to ~ 700°C for 5 seconds 3 times. In this case the number of carriers measured by Hall remained essentially unchanged at $2x10^{17}$ cm^{-3}. However, SIMS elemental profiles showed that the total sulfur concentration after annealing was highly uniform and with a nominal level of $6.1x10^{17}$ cm^{-3} which is a factor of 2 lower than the corresponding as-grown value ($14x10^{17}cm^{-3}$). Perhaps more importantly the above data shows that the Si content relative to that of S in the sample is ~ 10^2 times higher than the 2:1 ratio inherent to the molecular $S(SiH_3)_2$ delivery source. This indicates that under these conditions the precursor likely disproportionates to give volatile H_2S or $HS(SiH_3)$ species, which desorb and therefore do not participate in the growth, and highly reactive SiH_2 radicals that remain at the growth front and eventually incorporate Si into the film as shown by the equations:

$$S(SiH_3)_2 \rightarrow SH(SiH_3) + SiH_2 \rightarrow H_2S + 2\ SiH_2 \qquad (4.3)$$

$$SiH_2 \rightarrow Si + H_2 \qquad (4.4)$$

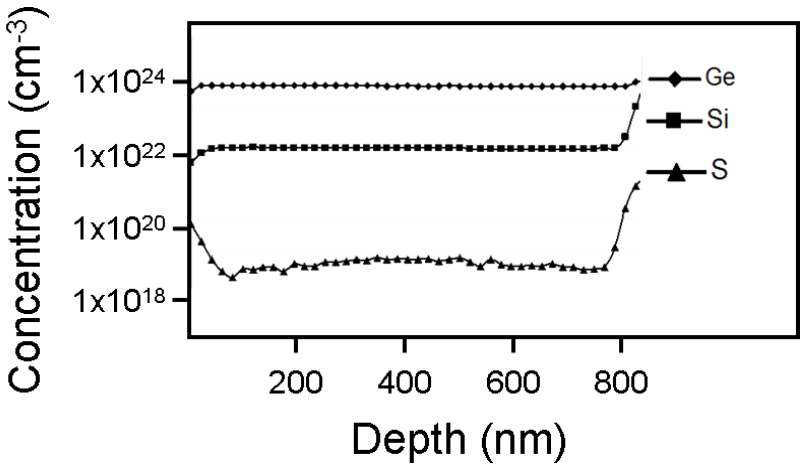

Figure 25 - SIMS elemental profile of the as-grown sample 013 showing uniform distributions of Si and S atoms throughout. The corresponding concentrations are measured to be $7.6x10^{20}$ and $1.4x10^{18}$ cm^{-3} using implanted standards.

To mitigate the aforementioned process depicted by equations (4.3) and (4.4) we next systematically lowered the deposition temperatures to 370, 360 and 350 ^{o}C to produce samples 014, 017 and 016, respectively. However, in all three experiments we found that the active carrier concentrations were in fact further reduced to levels below the SIMS detection threshold in the range of 10^{15} cm^{-3} measured by Hall. The latter value is opposite in sign and lower in magnitude than the intrinsic $5x10^{16}$ cm^{-3} *p*-type level of reference Ge grown using the same Ge_4H_{10} precursor indicating that the dopant has overcompensated to yield *n*-type material further supporting our assertion that sulfur is being incorporated even under the foregoing reactions conditions. In contrast to the lowering of the S substitution under the above conditions we find that the Si content in the materials increases dramatically to the 10-13 at % range as measured by RBS and XRD. These films therefore represent true $Si_{1-x}Ge_x$ alloys containing only trace amounts of sulfur as further evidenced by the anomalously large mobility (>1200 cm^2/Vs) measured in the as grown samples. The unexpected outcome of experiments 014, 016 and 017 suggest that the reactivity of $S(SiH_3)_2$ is significantly higher than that of the dominant Ge_4H_{10} source within this lower

temperature window (350-380ºC). This is manifested by a five-fold increase in growth rate observed for sample 013 (15 nm/min at 380ºC) compared to samples 016 (3 nm/min at 350ºC). A concomitant increase in the incorporation of Si in the films by a similar factor of ~5 is obtained for the lower rate film, as expected. This lends support to the decomposition mechanism proposed above (see equations) to explain the high Si content relative to that of S for the 380ºC deposition.

In view of this issue with the single-wafer MBE viability of the $S(SiH_3)_2$ doping process we also explored an alternative UHV-CVD strategy which may provide a more rigorous composition control of the Si and S co-dopant atoms using the same $S(SiH_3)_2$ reactant. The process involves preheating the chemical sources to promote the activation and gas phase interactions among the co-reactants thereby increasing the likelihood of intact incorporation of the corresponding molecular Si_2S cores into the target material. Here we adopted previously described UHV-CVD protocols which are known to produce device quality Ge layers by adding a small flux of SnD_4 into the reaction stream to yield Ge film doped with Sn in the range of 10^{19}-10^{20} cm^{-3}. The role of Sn is to promote layer-by-layer assembly of highly crystalline films with low dislocation densities and flat surfaces by suppressing the classic Stranski-Krastanov growth mode in which the crystal is formed by island coalescence. We note that the isovalent Sn dopant levels do not change key materials characteristics including lattice parameters, electronic structure and electrical properties.

A series Ge film was grown using one-liter mixtures of SnD_4 (0.12 Torr), $S(SiH_3)_2$ (0.73 Torr) and 54 Torr of Ge_2H_6 diluted by 600 Torr of H_2 (a representative material referred to here as sample 009 is listed as the last entry in Table 10). The reaction temperature was

390ºC and the working pressure was 0.300 Torr. Under these conditions high quality Ge on Si layers were produced with thickness of 400-450 nm as evidenced by RBS, XRD. SIMS profiles showed uniform distributions of S and Si with concentrations of $4.5x10^{18}$ cm^{-3} and $1.7x10^{19}$ (0.04 % Si), respectively, corresponding to a 1:3.5 atomic ratio. The latter is within error of the expected factor of 2 based the SSi_2 content of the molecular cores indicating that they may be largely incorporated intact into the lattice thus providing a good level of compositional control as anticipated. Hall measurements gave *n*-type carrier concentrations of $2.5x10^{17}$ cm^{-3} in the as grown films which remained essentially unchanged upon annealing at 600-700ºC for 10s 3 times. When the samples were annealed at 700ºC, Hall measurements showed a *p*-type carrier concentrations similar to that of intrinsic levels in Ge reference layer grown under same protocols indicating that the S atoms no longer occupied substitutional lattice sites. In light of this result it is instructive to compare this CVD sample (009) and the previously discussed MBE sample (013) which were both found to have similar active S contents ~ $2x10^{17}$ cm^{-3} by Hall and one order of magnitude higher via SIMS. The most striking difference between these two samples is that the Si content is several orders of magnitude greater in the MBE sample 013 than in the CVD sample 009. Since the latter CVD samples lose virtually all S donors and switch from *n*- to *p*-type when annealed at 700ºC while the S composition and dopant type of the corresponding MBE films remained unchanged up to at least 800ºC, our finding suggests that excess Si in sample 013 may be responsible for the apparent stability of the S sites in a Ge lattice.

The apparent stabilizing effect of Si with respect to S dopants and the consistency of incorporated S levels in the $S(GeH_3)_2$ grown samples are intriguing results which are best

explored from a theoretical perspective. Accordingly, density functional theory (DFT) calculations were carried out with the main goal of investigating the mutual defect interactions among S atoms, Ge vacancies and substitutional Si atoms on the Ge crystal. The results of these studies are presented in Reference 118, and reveal that doping using $S(GeH_3)_2$ results in the formation of both substitutional and non-substitutional S defect clusters, allowing the high level of activation observed in these samples. In contrast, doping using $S(SiH_3)_2$ leads to near substitutional defect clusters that act as deep donors and result in lower levels of activation.

The above results demonstrate the feasibility of using $S(GeH_3)_2$ and $S(SiH_3)_2$ sources for S doping of Ge, and explore fundamental aspects of donor incorporation and activation using these precursors. However, it must be noted that this preliminary study did not encompass the growth of doped Ge films on Ge buffered Si substrates under UHV-CVD conditions using Ge_3H_8 as the Ge source. The latter deposition method was used successfully in combination with $As(GeH_3)_3$, $As(SiH_3)_3$ and SbD_3 donor sources to produce doped Ge films, as described in previous sections. Future studies employing this technique to produce S doped Ge films may be able to achieve higher levels of active S incorporation than is reported here.

5. Conclusion

In this chapter, fabrication of *n*-type doped Ge thin films was described. The target was to achieve heavily doped films with active carrier concentrations $>5\times10^{19}$ cm^{-3} as required for Ge based FET and laser applications. For As donors, the synthetic approach utilized for incorporation of the target atoms was to use $As(GeH_3)_3$ molecules which have been

previously investigated for doping of GeSn alloys. The high reactivity of this compound allows depositions to be conducted at low temperatures which results in incorporation of donors at high concentrations of 8×10^{19} cm^{-3}. In addition, the analogous silyl compound $As(SiH_3)_3$ was also investigated as a dopant source. This compound were found to have comparable behavior to the germyl analog, and the films doped using it have similar electrical and structural properties. This data, in conjunction with the minimal degree of Si incorporation as indicated by SIMS, indicates that using the silyl analogs does not have a detrimental effect on the doped Ge films. Therefore $As(SiH_3)_3$ present a favorable alternative for $As(GeH_3)_3$ in an industrial setting, due to its superior thermal stability and greater volatility. Comparing the active carriers with the elemental donor concentrations in the films, it is found that great majority of the atoms are active, and therefore the resultant electrical properties are similar to what is observed in bulk doped Ge.

For doping of Ge with Sb, the reactive hydride SbD_3 was employed to conduct low temperature, non-equilibrium doping. This allowed the deposition of films with ultra-high levels of active donors up to 1.6×10^{20} cm^{-3}, and resistivities as low as 1.8×10^{-4} Ωcm. The latter resistivity values are the lowest reported thus far for *n*-type Ge, and agree well with extrapolation of resistivity values of bulk Ge:Sb to high carrier concentration observed here. The low resistivity values for Sb agree with the order of $\rho_{Sb} < \rho_P < \rho_{As}$ observed for bulk Ge by Spitzer, Trumbore, and Logan,[116] and also with theoretical predictions by Ralph *et al.*[146]

The Ge films produced in this work was also used to elucidate certain fundamental physical properties of heavily doped Ge. This includes confirmation of the Cargill-Keyes model for

the effect of donors on the lattice parameter of Si and Ge (see Reference 141). The donor activation studies of As and Sb also confirm the frustrated donor ionization first observed in P.[135]

Finally, the concept of using precursors with pre-formed donor-host atom bonds to enable low temperature doping was extended to include S doped Ge. In these experiments, the molecular sources $S(GeH_3)_2$ and $S(SiH_3)_2$ were employed for the fabrication of Ge:S films for the first time. Films with carrier concentrations in the 10^{15} – 10^{18} cm^{-3} range were experimentally demonstrated.

The techniques developed in this chapter present an important and novel pathway for fabricating heavily doped Ge films with controlled dopant profiles and junction depths as required for NMOSFET and optical applications. They underscore the importance of selecting compatible precursor combinations when preparing semiconductor films with extreme properties using CVD methods. Further optimization of the protocols developed in this work can potentially improve the levels of doping observed here, paving the way for new application areas.

CHAPTER FIVE

Growth of Germanium-tin Alloys on Ge Buffered Si Substrates

Synopsis

In this chapter, the deposition of $Ge_{1-y}Sn_y$ alloys in the y=0.01-0.11 composition range on Ge buffered Si substrates is described. For $y \leq 0.06$, Ge_2H_6 and SnD_4 were used as the precursors, and for $y > 0.06$, Ge_3H_8 was used in combination with SnD_4. Thick (~1 μm), largely relaxed films with low dislocation densities were produced. The microstructure and strain relaxation properties of GeSn alloys on this novel platform were studied.

Portions of this chapter were reprinted from Senaratne, C. L.; Gallagher, J. D.; Jiang, L.; Aoki, T.; Menéndez, J.; Kouvetakis, J. $Ge_{1-y}Sn_y$ (y=0.01-0.10) alloys on Ge-buffered Si: Synthesis, microstructure, and optical properties. *J. Appl. Phys.* **2014**, *116* (13), 133509 with the permission of AIP Publishing.

1. Introduction

The range of hydride precursors outlined in Chapter 2 contain compounds that can supply Ge and Sn atoms and serve as the basis from which the GeSn alloys can be synthesized, as well as other species enabling the extension of the electrical and optical properties of this semiconductor system. In this chapter, the focus will be on how the germanium precursors Ge_2H_6 and Ge_3H_8, which together with the Sn source SnD_4, were used for the fabrication of $Ge_{1-y}Sn_y$ alloys in a wide range of compositions y=0-0.11 on Ge buffered Si platforms.

As described in Chapter 1, the Ge_2H_6 and SnD_4 were first utilized for the growth of GeSn alloys by Bauer *et al.*,[50] whereas the Ge_3H_8/SnD_4 combination was first investigated by Grzybowski *et al.*[91,94] A major milestone achieved by using high-order Ge hydrides

together with SnD_4 was the demonstration of the first LED devices employing $Ge_{1-y}Sn_y$, which had active layer Sn contents up to y=0.02.[21] Also of note is the first observation of PL from GeSn thin films.[74]

All of the above results were obtained using GeSn alloys deposited directly on Si(100) substrates. The deposition of GeSn on Si must overcome the difficulties posed by the 4% (and higher) lattice mismatch between film and substrate. To avoid island formation, growth must be initiated at very low temperatures, which introduces a very high density of defects. In the case of Ge on Si, substantial improvements in film quality can be obtained by ramping up the growth temperatures and by applying high-temperature post-growth thermal annealings.[103,104,178–180] Unfortunately, these solutions are of limited value for the GeSn system. Increases in growth temperature lead to lower Sn incorporation, and the temperature range for post-growth annealing is reduced by the possibility of Sn segregation.[51,181] These limitations reduce the ultimate film thickness that can be achieved and preclude the optimal elimination of defects, with considerable impact on the optical properties. In particular, optical emission can be strongly suppressed in thin, highly defected films. In Ge-like materials such as GeSn, film thickness is a particularly important consideration because the diffusion length of electron-hole pairs can be as high as 0.4 mm,[182,183] so that the non-radiative recombination velocity at the film/Si interface will affect the overall emission intensity. These considerations suggest that there is significant room for improvement of these signals if the materials issues can be properly addressed.

Therefore in this chapter Ge buffered Si was explored as a platform on which strain relaxed, device quality, low defectivity GeSn alloys could be fabricated using the Ge_2H_6/SnD_4 and

Ge_3H_8/SnD_4 precursor combinations. This chapter will describe the protocols developed for this purpose, and will also present results from investigation of the microstructure and strain relaxation of the resultant materials. In the following chapter, their superior optical properties are also discussed, which provide the motivation for fabrication of LED devices on virtual Ge substrates, as described in Chapter 7.

2. Ge buffered Si Substrates – Significance and Fabrication Methods

Germanium provides a facile platform for the growth of GeSn alloys due to the relatively small lattice mismatch between the substrate and the alloy epilayer. Therefore it has been used as a substrate material from the early days of research on GeSn.[28,30] Furthermore, the band alignment between Ge and GeSn is known to be type I, which promotes carrier confinement in the alloy layer. However, using Ge wafers for this purpose has the obvious disadvantage that it excludes the possibility of integration of GeSn based materials on to Si platforms for microelectronic and photonic applications. In order to circumvent this issue while still retaining the advantage of a substrate material with low lattice mismatch for the growth of GeSn alloys, Ge buffered Si substrates -also known as virtual Ge substrates- were recently investigated by Vincent *et al*.[51] Further work on GeSn alloys deposited on Ge/Si has led to the successful fabrication of LED devices by several groups.[45,71,184] Despite these advances, several areas were identified as requiring further development in order to fabricate functional direct gap light emitting devices. Firstly, the alloys of the devices grown on Ge/Si platforms exhibit significant compressive strain. This is detrimental to achieving direct gap behavior in this alloy system, and is a major concern in all reported LED structures grown by MBE methods.[45,71] However, a relatively high degree of strain relaxation was observed in CVD grown samples.[76] Despite the importance

of this strain behavior for the development of direct gap alloys, a systematic study of strain relaxation of GeSn alloys on Ge/Si substrates was lacking. Therefore a phenomenological model was developed to describe strain relaxation behavior, and will be discussed later in this chapter. Furthermore, it will be shown that $Ge_{1-y}Sn_y$/Ge/Si materials are excellent candidates for investigation of the direct and indirect bandgaps using PL techniques, which offers a straightforward route for determining the indirect-direct crossover composition for this alloy system, as described in Chapter 6. Finally, high quality direct gap GeSn alloys grown on virtual Ge substrates had not been fully explored in device applications in the direct gap composition regime. The methodologies described in this chapter were found to be readily applicable for this purpose, as shown in Chapter 7.

The first requirement for growing low defectivity GeSn materials is a low defectivity substrate. The procedure used for making virtual Ge substrates suitable for this purpose was that developed by Xu *et al.*,[77] which makes use of the Ge_4H_{10} precursor. While methods for preparing similar buffer layers using the Ge_5H_{12} precursor was introduced in Chapter 3, the Ge_4H_{10} route represents a more mature technology in which all process parameters have been thoroughly explored in order to obtain the maximum crystal quality in the buffers. Furthermore, the greater volatility of Ge_4H_{10} facilitates its concomitant use with other precursors such as $P(GeH_3)_3$ used for doping purposes. Such doped epilayers were used extensively in device fabrication, as described in Chapter 7. For growth of alloys described here, a layer of Ge approximately 1 μm thick was deposited on RCA cleaned 4" Si(100) wafers at temperatures in the 350°C-390°C range using a GSME reactor. Thereafter, this Ge layer is subjected to a 3 min long annealing at 680°C-730°C. This annealing step is crucial in order to obtain buffer layers with low defectivities, since it leads

to the elimination of threading dislocations present in the film. Subsequently, these wafers were characterized using HRXRD, spectroscopic ellipsometry and Nomarski optical microscopy to ensure that they meet the standards of crystal quality, thickness uniformity and flat surface morphology required for use as substrates for the growth of GeSn alloys. The defect levels in these buffers are found to be in the 10^6-10^7 /cm^3 regime, where the higher values are found closer to the Ge/Si interface. As will be discussed below, these buffer layers have a unique ability of absorbing misfit strains, resulting in largely relaxed epilayers.

3. Growth of GeSn Alloys Using Ge_2H_6 and SnD_4 Precursors

The 4" Ge/Si(100) wafers described above were subsequently cleaved into 45 mm × 45 mm segments for use in the CVD reactors employed for the growth of $Ge_{1-y}Sn_y$ alloys. The native oxide on the surface was then removed by dipping in a 5% HF solution for 2 min, followed by a distilled water rinse for 5 min.

The growth of $Ge_{1-y}Sn_y$ alloys using Ge_2H_6/SnD_4 mixtures was conducted in a hot wall UHV-CVD deposition chamber. It is equipped with a load lock for introducing wafers into the chamber, which can be pumped down to a pressure of 1×10^{-7} Torr using a turbomolecular pump. This is connected to the main chamber section, which has a base pressure of 3×10^{-9} Torr, which is achieved using a combination of turbomolecular and cryogenic pumps. The growth section of the chamber consists of a quartz tube ≈70 cm in length and 7.6 cm in diameter, which is connected to the manifold containing the mass flow controllers (MFC) used to regulate the gas flow into the system, and a separate turbomolecular pump used as the process pump. The pumping rate in this case can be

controlled by a manual throttle valve. The heating of the growth chamber is done using a resistance furnace with three independently adjustable zones.

The growths were conducted with the substrate wafers placed in the central zone of the furnace, which was held at temperatures from 350°C to 295°C depending on the target Sn composition of the epilayer. The zone nearest to the gas inlet was kept at a temperature 20°C-25°C below this. In a typical experiment, the substrates were introduced into this growth chamber under flow of H_2. Then the temperature was allowed to equilibrate for a period of 2 min. Before starting the growth, a final cleaning step was carried out by flowing Ge_2H_6 through the chamber at a pressure of 50 mTorr for 5 min. This 'digermane clean' was first described by Moslehi,[185] and helps to ensure a clean substrate surface.

The precursor gases used for the depositions were combined to form a homogeneous mixture prior to the deposition process. This was done by combining ≈300 Torr of 10% Ge_2H_6 with 0.4-2 Torr of SnD_4 in a 3 L container. The Ge_2H_6 was used as purchased from Voltaix (now Air Liquide Advanced Materials), whereas the SnD_4 was synthesized using the method described in Chapter 2. The variation of the amounts of SnD_4 used for different growths were due to the different target compositions of the epilayers. By changing the atomic Sn/Ge ratios in the precursor mixtures between 0.006-0.03, it was possible to obtain films with compositions of y=0.01-0.07. The precise precursor mixtures used to obtain each target composition is described in detail in Appendix A.

Typically, a two-fold-excess of Ge_2H_6 relative to SnD_4 was found necessary to obtain the target alloy compositions. A possible mechanism that can account for the observation that

only half of the Ge_2H_6 atoms delivered by the reaction mixture are being incorporated in the crystal is the dissociation reaction

$$Ge_2H_6 \rightarrow GeH_2 + GeH_4 \qquad (5.1)$$

This dissociation produces highly reactive GeH_2 intermediates which then insert into the layer to deposit Ge via complete desorption of H_2 byproducts. The reaction also produces an equal amount of GeH_4 molecules that are essentially unreactive at our low growth temperatures, and are pumped away in the course of the experiment. The pressure used for the depositions was kept at 300 mTorr for all the experiments. Under these conditions, it was possible to obtain films with final thicknesses of 1000-450 nm at growth rates of 9-5 nm/min in the abovementioned alloy composition range.

The thicknesses of the samples were determined using RBS, which also enabled the determination of the Sn contents of the alloys films. The spectra were obtained at an energy of 2 MeV, and were modelled using the program RUMP[186] in order to obtain the relevant film parameters. Channeling experiments were also carried out, which show that the epitaxial layer consists of mono-crystalline, single phase materials exhibiting a high degree of epitaxial alignment with the substrate. The excellent channeling of both the Ge and Sn signals is indicative of fully substitutional Sn incorporation. Representative random and channeled RBS spectra for a $Ge_{0.97}Sn_{0.03}$ sample is shown in Figure 26 a).

Further evidence of the crystal quality and single phase nature of the materials was obtained using HRXRD θ-2θ scans of the (004) reflection, which show a single, sharp, symmetric peak for the epilayer material. In addition, 224 reciprocal space maps (RSM) were obtained

for the alloys, and were used to determine the strain states and the relaxed cubic lattice parameters of the materials. It is worth noting here that the relaxed lattice constant can also be used as a parameter for determining the amount of substitutional Sn present in the alloy, using the relationship given in Reference 14. The Sn contents obtained by this method for the samples discussed here are in excellent agreement with those obtained from the RBS measurements, indicating the substitutional nature of the Sn atoms within the Ge lattice. Representative (004) and (224) RSM scans for a $Ge_{0.97}Sn_{0.03}$ sample are shown in Figure 26 b).

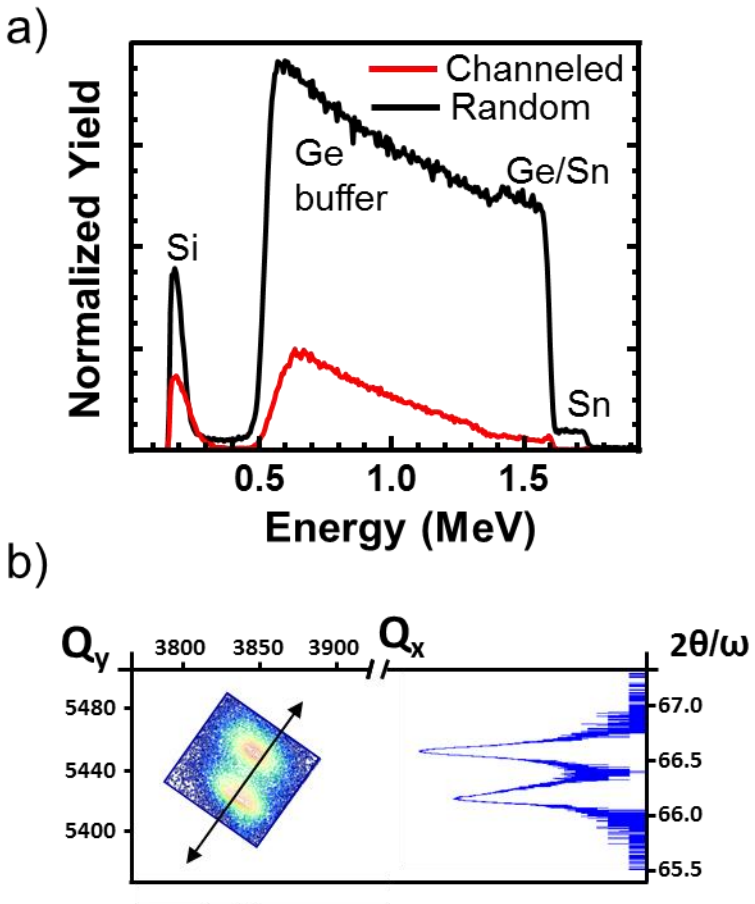

Figure 26 – a) 2 MeV RBS random (black) and channeling (red) spectra for a 540 nm thick $Ge_{0.97}Sn_{0.03}$ film grown on Ge/Si(100) substrate using Ge_2H_6 and SnD_4 precursors. b) A RSM from a (224) asymmetric HRXRD scan (left) and an on-axis (004) θ-2θ scan (right) from the $Ge_{0.97}Sn_{0.03}$ sample.

For alloys with compositions beyond y=0.06, the low temperatures (<320°C) that become necessary in order to prevent Sn segregation make the growth of thick films using Ge_2H_6 and SnD_4 challenging. As a solution to this problem, the Ge_3H_8 and SnD_4 precursor combination had been used by Grzybowski *et al.* for $Ge_{1-y}Sn_y$ alloys grown on Si.[94] Therefore the use of these precursors was investigated in this study for growth $Ge_{1-y}Sn_y$ alloys with y>0.06 on virtual Ge substrates.

4. Growth of GeSn Alloys Using Ge_3H_8 and SnD_4 Precursors

The growths using Ge_3H_8 were also conducted using a hot wall UHV-CVD chamber. The design of this chamber is similar to that used for the Ge_2H_6/SnD_4 experiments, with the exception that the growth chamber in this case is heated using a single zone furnace. The initial composition range explored was y=0.05-0.09, which requires temperatures of 320°C-295°C. The pressure in the chamber was kept at 200 mTorr during growth by controlling the pumping rate. In common with earlier procedures, the precursors were mixed in a single container in order to get a homogeneous gas phase mixture, which enabled precise controlling of the target epilayer compositions. The mixtures consisted of 35-40 LTorr of Ge_3H_8 in a 3 L glass bulb, together with 5-8 LTorr of SnD_4. The increasing amounts of SnD_4 in the mixture parallel increasing Sn contents of the target alloy. This mixture was then diluted with 1800-1900 LTorr of research grade H_2, which results in a constant concentration of ~2% Ge_3H_8. More information on growth parameters are given in Appendix A.

The films obtained from these experiments were initially characterized using RBS and HRXRD. A representative RBS data showing random and aligned RBS spectra for a

$Ge_{0.93}Sn_{0.07}$ sample is given in Figure 27 a). The alloy film in this case is modelled as being 610 nm thick exemplifying the suitability of the Ge_3H_8/SnD_4 system for obtaining thick bulk-like films of higher Sn alloys than can be achieved with Ge_2H_6/SnD_4. The growth rate for the sample was 4.9 nm/min, despite the low growth temperature of 310°C, and can be attributed to the higher reactivity of Ge_3H_8. The HRXRD results give relaxed lattice

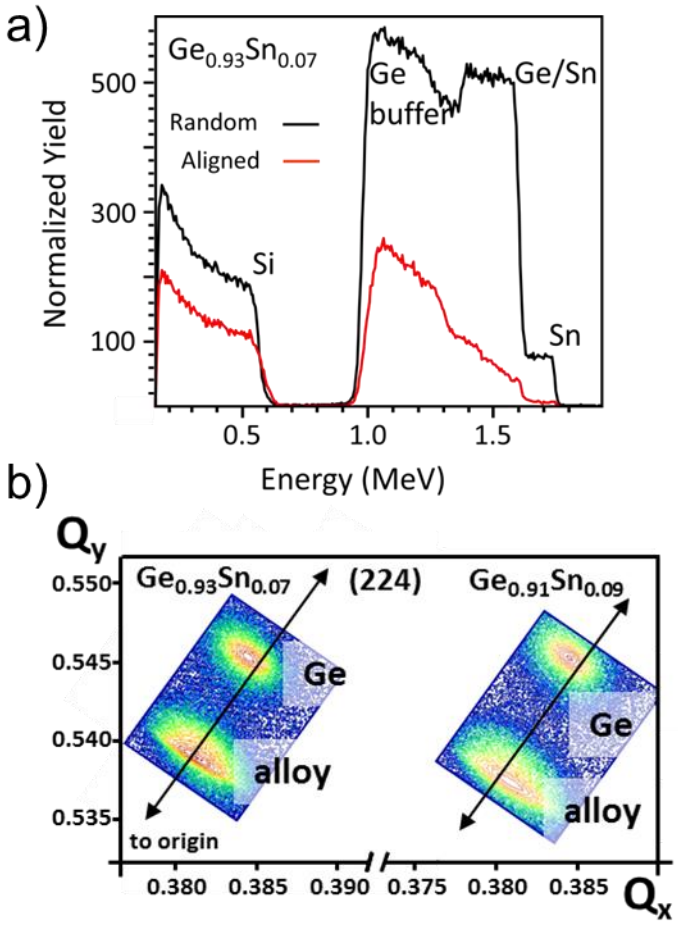

Figure 27 – a) RBS random and aligned spectra for a $Ge_{0.93}Sn_{0.07}$/Ge/Si(100) sample. The plots show distinct Ge and Sn peaks corresponding to the buffer and the epilayer indicating a high degree of epitaxial alignment with the Si wafer. $\chi_{min}^{Ge\ (GeSn)} = 6.2\%, \chi_{min}^{Sn} = 4.9\%$. Thickness = 615 nm. b) XRD reciprocal space maps near the off-axis 224 reflection for samples $G_{0.93}Sn_{0.07}$ and $Ge_{0.97}Sn_{0.03}$. In both cases the position of the Ge peak is located above the cubic relaxation line indicating that the buffer exhibits a slight tensile strain (~0.15 %) induced by the thermal expansion mismatch with the underlying Si platform.

parameters in excellent agreement with the values expected from RBS Sn compositions. The 224 RSM for the same $Ge_{0.93}Sn_{0.07}$ sample is compared in Figure 27 b) with the corresponding map for a $Ge_{0.91}Sn_{0.09}$ sample, and the increase of lattice parameter with increase of Sn content can clearly be observed. Furthermore, the XRD data indicate that the alloy films show a significant degree of strain relaxation. This can be attributed to their large thicknesses, which are significantly above the critical thickness of strain relaxation, as will be discussed in detail in later sections.

An additional factor that helps in attaining high growth rates at low temperatures using the current precursor system if the catalytic effect of SnD_4. The plot in Figure 28 shows the change in growth rate with the Ge/Sn atomic ratio in the precursor mixture at different deposition temperatures. The trend shows that the inclusion of more SnD_4 in the growth mixture tends to increase the growth rate. This is analogous to the increase in growth rate caused by GeH_4 during CVD of $Si_{1-x}Ge_x$ alloys using SiH_4 and GeH_4. This effect has been attributed to the increased hydrogen desorption from the growth surface in the presence of Ge, which forms a weaker bond with H than Si does. This in turn increases the probability of adsorption of precursor species.[187] Due to the weakness of the Sn-D bond in comparison to the Ge-H bond, it is probable that a similar phenomenon is responsible for the growth rate increase observed in the SnD_4/Ge_3H_8 precursor system.

For compositions of $y>0.08$, which entail growth temperatures below 300°C, it was found that the concentrations of the precursor mixtures could be reduced without adversely affecting the growth rate, leading to a reduction in process cost. The plot in Figure 29 summarizes growth rates obtained from a series of depositions done at 295°C with mixtures

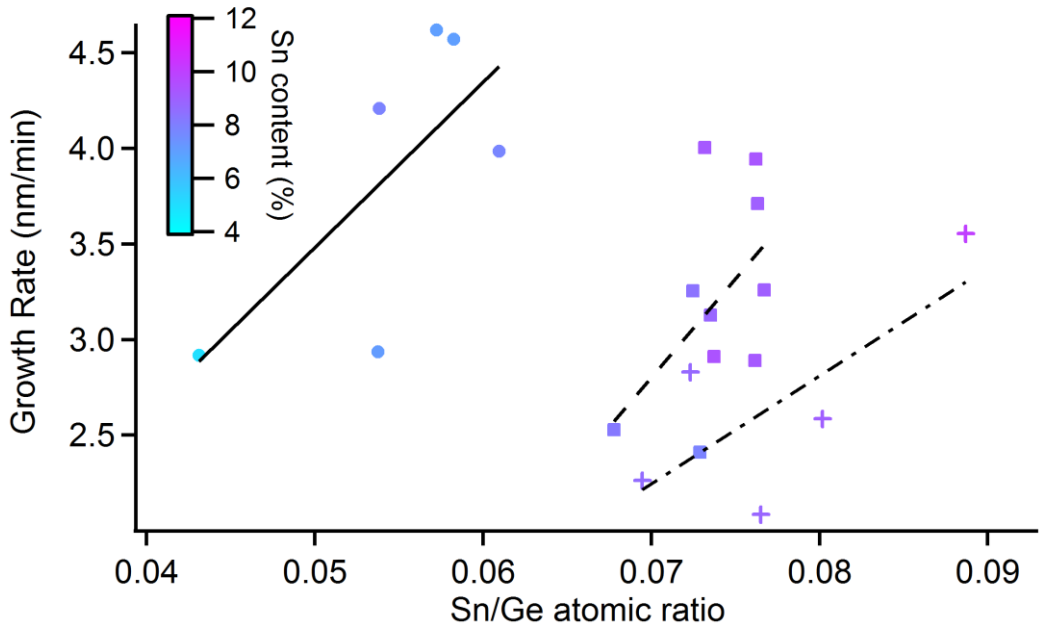

Figure 28 – Growth rates observed for varying Sn/Ge atomic ratios in the precursor mixtures at temperatures of 305°C (circles), 295°C (squares) and 290°C (crosses). The solid, dashed and dashed-dotted lines represent the linear fits to the data at each respective growth temperature. It can be seen that a general increase in growth rate is observed at all temperatures when the amount of Sn in the mixture is increased (by increasing the amount if SnD_4). The symbols are color-coded to represent the Sn composition of the resultant films.

with approximately constant Sn/Ge ratios in the mixtures. The variable factor is the dilution of the precursor mixtures, which is represented by the molar ratio of Ge_3H_8 to H_2. It is found that for mixtures where the Ge_3H_8 concentration is only 1%, the growth rates are comparable, if not greater than for the mixtures with a Ge_3H_8 concentration is 2%. This translates to an increase in efficiency by allowing the growth of thicker films with the same amount of precursors. Therefore, lower concentrations were used for growths which explored the alloy Sn composition range beyond 9%. The maximum composition achieved using these techniques was y=0.11.

In addition to providing a method to explore the highly metastable $Ge_{1-y}Sn_y$ composition range reported above, the Ge_3H_8/SnD_4 system has the added advantage of more efficient

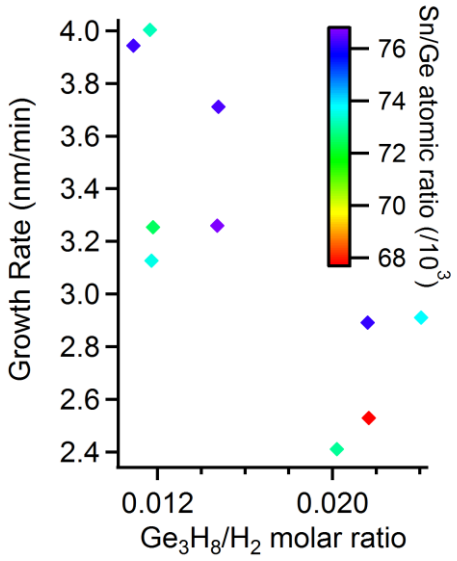

Figure 29 – Growth rates obtained at 295°C using mixtures with varying concentrations of Ge_3H_8. The points are color coded according to the Sn/Ge ratio mixtures to show that the observed trend in growth rates is independent of the growth rate increase observed at high Sn/Ge atomic ratios as was illustrated in Figure 28.

Ge incorporation compared to the Ge_2H_6/SnD_4 system. The efficiency can be defined as$K = \frac{r_{gas}}{r_{film}}$, whre r_{gas} and r_{film} represent the Sn/Ge atomic ratios of the precursor mixture and the epilayer respectively. The atomic ratios of the precursor mixtures and films from a series of growths spanning the composition range y=0.05-0.11 explored by using Ge_3H_8 as the Ge source is plotted in Figure 30. The average K value obtained in 1.27, which indicates that only a 27% excess of Ge atoms in the growth mixture is required for obtaining the target alloy composition. This is in contrast to the twofold excess Ge required for growths using the Ge_2H_6/SnD_4 combination.

5. Microstructure of GeSn Alloys Grown on Ge/Si Substrates

The RBS and HRXRD characterization techniques described in the previous section provide a good outline of the macroscopic properties of the $Ge_{1-y}Sn_y$ alloys produced in this study. However, a detailed knowledge of the microstructure of these thin films is

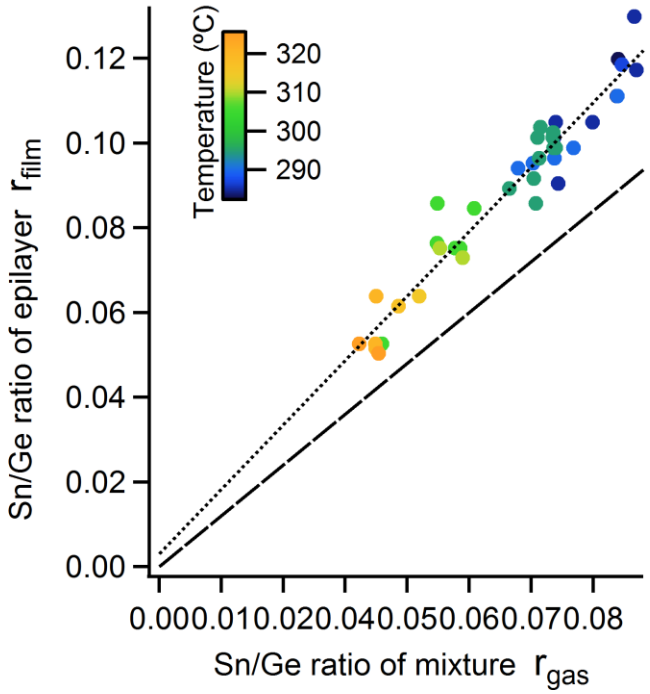

Figure 30 – r_{film} vs. r_{gas} for samples grown using Ge_3H_8 and SnD_4 spanning the *y*=0.05-0.11 composition range. The dashed line represents the $r_{film}=r_{gas}$ positions. The actual points lie above this line, hence a 27% excess of Ge atoms are present in the mixture with respect to the film, reflecting the slightly higher reactivity of SnD_4 relative to Ge_3H_8. The dotted line is the best linear fit to the data points, which passes (within error) through the origin. This observation supports the conclusion that a constant percentage of excess Ge is present in the gas phase for all compositions.

necessary in order to understand their potential in optical applications. Therefore electron microscopy techniques were utilized in order to study structural properties of alloys with several different Sn contents.

Figure 31 shows an XTEM micrograph of a $Ge_{0.91}Sn_{0.09}$ film obtained with a JEM-4000EX high-resolution electron microscope operated at 400 keV with a resolution of 1.7 Å. Inspection of the $Ge/Ge_{0.91}Sn_{0.09}$ interface reveals occasional 60° dislocations and widely spaced short stacking faults penetrating down into the buffer layer rather than propagating through the bulk crystal. Despite these defects, the greater portion of the interface displays full commensuration of the lattice planes, as seen in the high resolution image in the inset.

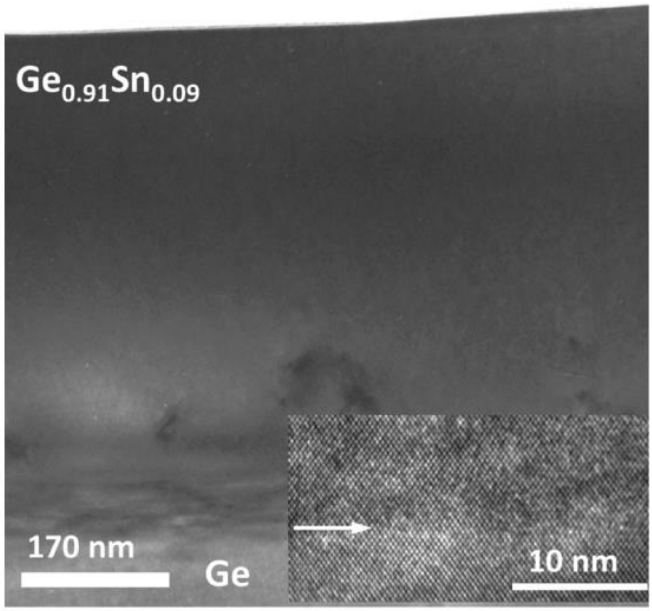

Figure 31 – XTEM micrograph of a 550 nm thick $Ge_{0.91}Sn_{0.09}$ film grown on Ge buffered Si. The image was obtained using a JEM-4000EX high-resolution electron microscope operated at 400 keV. The inset is a high-resolution image of the interface showing full commensuration of the lattice planes over an extended field of view.

The bulk crystal is seen to be mostly devoid of threading defects and other types of structural imperfections arising from the high concentration of mismatched Sn atoms embedded in the parent Ge lattice.

An essential requirement when using these samples to probe the optical properties of $Ge_{1-y}Sn_y$ is that they are homogeneous with respect to the Ge and Sn atomic distributions within the layer. In other words, no Sn rich regions or precipitates should be present within the alloy film, and no Sn diffusion should occur at the $Ge_{1-y}Sn_y$/Ge interface. The interface sharpness was characterized using Electron Energy Loss Spectroscopy (EELS) with a probe size of 1.3 Å in scanning transmission electron microscopy (STEM) high angle annular dark field (HAADF) mode. Typical elemental maps were generated over large areas across the films encompassing a significant segment of the interface region. In all

cases the Ge and Sn maps showed that both elements appeared together in every atomic-scale region probed, without any indication of segregation of the individual constituents. Figure 32 shows the characteristic EELS map of Sn acquired from a $Ge_{0.96}Sn_{0.04}$/Ge thin specimen. The average Sn concentration profile obtained from a crystal with dimensions of 1.6 nm ×1.6 nm × 60 nm, in [110] projection, is indicated in a red-black scale. The dark area thus corresponds to the Ge buffer layer, where no measurable amounts of Sn above background levels are detected. The Sn map shows a sharp and well-defined transition of the atomic profile along the interface, indicating that no discernible Sn diffusion into the buffer has taken place. The above elemental map was then used to compute a series of line scans across the interface and average them over an area of 70nm

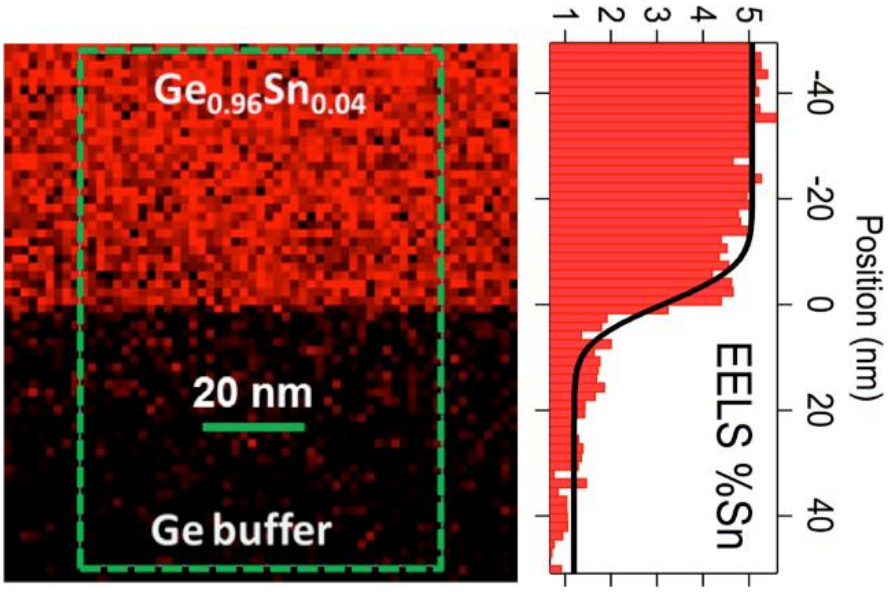

Figure 32 - STEM/EELS elemental map and concentration plots of a $Ge_{0.96}Sn_{0.04}$/Ge sample. The left panel shows Sn mapping profiles over a large film region across the interface. The red color denotes the presence of significant Sn concentrations whereas the black indicates only background levels of the atom. The right panel illustrates a quantitative composition profile indicating an approximate 4 % Sn content in the sample, as expected. The latter profile was measured from a 70 nm × 100 nm area marked by the green box. The plot/map in this case show highly uniform distributions of Sn atoms and a sharp, well-defined transition of Sn composition at the interface with the Ge buffer.

×100 nm marked by the green box. This process generated a profile of the Sn content as a function of vertical distance, plotted on the right panel of Figure 32 for the $Ge_{0.96}Sn_{0.04}$ film. The fluctuations seen in the Ge region of the plot are characteristic of the data processing methods used to average the individual EELS spectra, and represent the typical background noise level intrinsic to the technique. Assuming that the interface is Gaussian-broadened, with a standard deviation σ, the predicted composition profile has the lineshape of a complementary error function. A fit with such a profile is shown as a solid line. It gives a broadening value σ = 6.7 nm and a step size of 3.87± 0.10, in very good agreement with the Sn concentration determined from RBS. The unique aspect of this type of analysis is that it incorporates an average of 50 or more lines scans across the interface (an individual line scan covers a 1.5 nm swath of material) and provides a more representative estimate of the lateral concentration average parallel to the interface plane. The sharp and abrupt transition in the composition profile across the GeSn/Ge boundary indicates that the interface plane is atomically smooth over a large area across the film.

Elemental maps of the atomic columns were acquired along the [110] projection using element-selective EELS and STEM (see Figure 33) in order to investigate the Sn and Ge distribution and gain insights into the local bonding configurations at the atomic scale. These experiments were performed on a JEOL 200 F ARM equipped with a GATAN Enfinium spectrometer. The EELS spectra were collected from 2x2 nm^2 areas with spatial resolution of 0.12 nm and beam penetration distance of 60 nm. In all cases the EELS scans revealed well defined ionization edges of Ge (L) and Sn (M) at 483 eV and 1217 eV, respectively. The spectra were then used to create atomic resolution maps of the lattice shown in Figure 33 b) and c) which illustrates the Ge and Sn contributions with green and

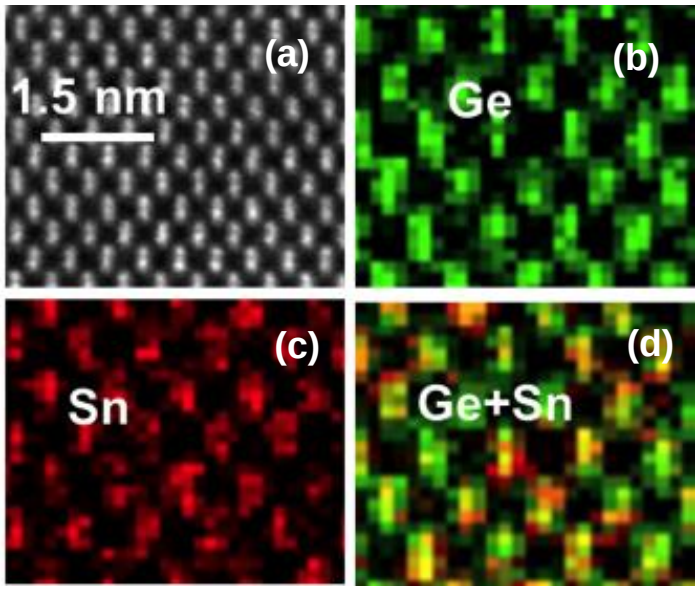

Figure 33 - EELS and STEM images of $Ge_{0.96}Sn_{0.04}$ film (a) high-resolution image showing the area of the crystal analyzed by EELS. (b-c) individual EELS maps of Ge (green) and Sn (red) constituent atoms (d) composite map of Sn plus Ge illustrating a uniform distribution of the green and red features indicating that Sn and Ge atoms occupy the same lattice.

red color, respectively. The maps show the characteristic dumbbell-shaped dimers in the [110] projection for both elements, corroborating the notion that the Sn constituents are evenly distributed throughout the parent Ge lattice and occupy random substitutional sites. Panel (c) is an overlay image of the Sn and Ge maps indicating a close alignment of the crystal columns, as evidenced by the uniform distribution of the red and green features within individual columns throughout the crystal pattern. In addition we see no diffraction intensity above the background between the projected columns, indicating that the material is a pure, single-phase alloy devoid of precipitates and interstitials.

To further investigate the local microstructure at the interface and identify the type and distribution of the dislocations generated under our reaction conditions we conducted atomic resolution experiments using a JEOL ARM 200 F microscope equipped with a

STEM aberration corrector. STEM bright field (BF) images of the samples were acquired using a large collection angle (22 mrad), which enables atomic resolution as well as high contrast of interfaces and defects. Representative data are presented in Figure 34 for a $Ge_{0.96}Sn_{0.04}$/Ge sample. Figure 34(a) reveals the presence of a smooth, uniform and crystalline film exhibiting sharp and well-defined hetero-interfaces. The dark contrast areas in panel Figure 34(b) show the location of a stacking fault originating at the interface and

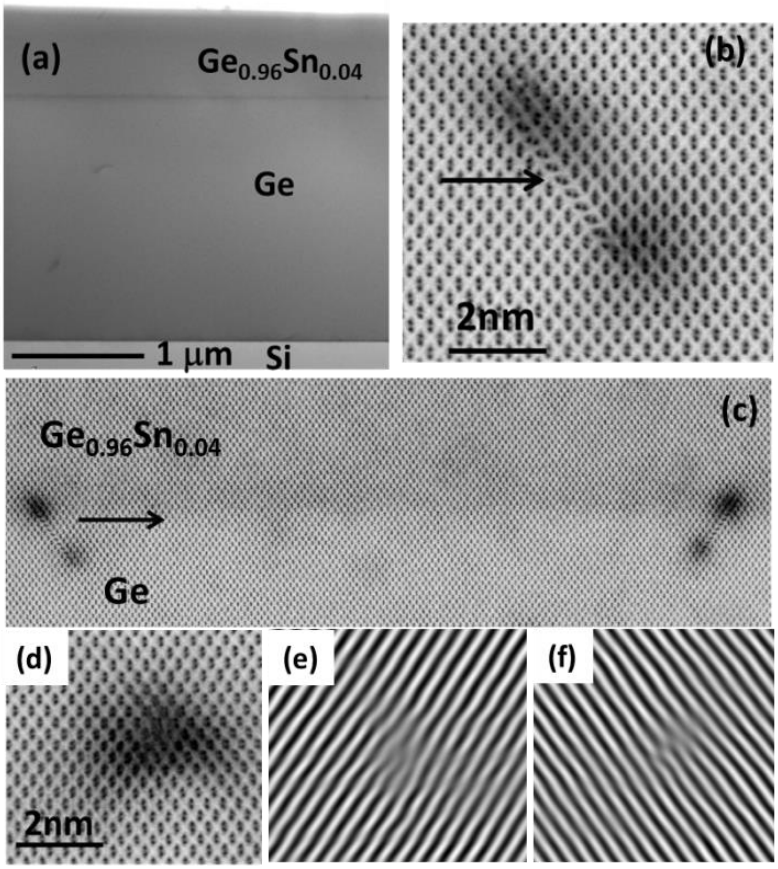

Figure 34 - XTEM high-resolution micrographs of a 700 nm thick $Ge_{0.94}Sn_{0.04}$layer grown upon Si using a 1500 nm thick Ge buffer layer. (a) Image of the entire film structure showing good quality crystal morphology throughout. (b) STEM BF image of the interface marked by arrow showing a magnified view of a single stacking fault site penetrating downward into the Ge buffer. These defects appear as dark contrast areas on the images at the film buffer-boundary on panel (c) and are well separated from one another by 42 nm. Typical Lomer dislocation accommodating the misfit strain is shown on panel (d). This features are identified by subjecting selected {111} planes to inverse FFT to generated the graphics on panels (e) and (f).

penetrating through a short distance into the buffer layer rather than threading upwards into the film. These features represent the most common (most frequently visible) defects found at the interface of our materials and appear to be to be well separated from one another by a significant spacing of 42 nm in the lateral direction, as shown in Figure 34(c) for a pair pointing at different directions along 111 planes in 110 projection. In addition to stacking faults we also identified Lomer dislocations randomly distributed along the interface plane, shown as dark contrast area in Figure 34(d). These features were characterized by subjecting selected pairs of lattice planes {(-1,-1,1) (1,1,-1) and (-1,1,-1) (1,-1,1)} to inverse Fourier transform (FFT) processing to produce corresponding filtered images shown in panels (e) and (f). Both of these show two lattice planes terminating at the same point at the interface, as expected for this type of dislocation.

The presence of Lomers and stacking faults in the current samples represents a departure from typical relaxation behavior for Sn based alloys integrated on Si platforms, and may be attributed to the less pronounced lattice mismatch of the epilayer and Ge template in the $Ge_{1-y}Sn_y$/Ge system. Our atomic scale structural observations are nevertheless consistent with similarly mismatched Si–rich $Si_{1-x}Ge_x$ films produced on Si wafers by low temperature CVD of Si and Ge hydrides.[188] These films also showed high relaxation ratios combined with the generation of stacking faults crossing down into the Si substrate, as well as misfit dislocations localized at the interface plane as in our materials. Other factors that may play a significant role in controlling the relaxation behavior in our films is the low growth temperature and the heavy, high reactivity Ge/Sn sources employed in the deposition experiments. The latter enhance hydrogen desorption from the growth front, thus promoting organized assembly of planar films, as evidenced by AFM

characterizations which showed low RMS roughness in the 1-3 nm range for large areas of 20μm × 20μm throughout the surface. AFM also revealed cross-hatch patterns presumably generated by dislocations penetrating to the surface or residual strain fields.

6. Quantification of Defect Density and Modeling Strain Relaxation Behavior of $Ge_{1-y}Sn_y$/Ge Alloys

The defect formation at the interface described in the previous section has an adverse effect on the crystalline quality of the GeSn thin films. On the other hand, relaxation of compressive strain in the epilayers which accompanies the defect formation has a beneficial effect on achieving direct gap behavior in GeSn alloys. The lowering of the epilayer-substrate lattice mismatch by use of Ge/Si as a substrate rather than Si has a significant advantage in this regard. It allows a greater degree of strain relaxation to occur while minimizing the number of interfacial defects required for the process. The XRD patterns of samples across the entire composition range produced in this study indicate that the crystallinity is superior to that of similar films grown directly on Si. The FWHM of the on axis (004) rocking curves is typically at least 3–4 times lower than observed for GeSn/Si. For example the FWHM of ~4.5–5% Sn alloys is approximately 0.15°, which should be compared with 0.7° for Si analogs. Furthermore, the peak profiles of the reciprocal space maps are markedly sharper and narrower due to reduction in mosaic spread with increasing thickness and crystallographic alignment. Moreover, the crystallinity of the samples grown on Ge buffers is comparable across the 3–9% Sn concentration range, while in the case of GeSn/Si the structural quality degrades significantly with increasing Sn incorporation.

In order to quantify the defect density, the samples were further characterized by transmission electron microscopy in plan-view geometry to study the local microstructure

and estimate the threading dislocation density in the bulk layer. The plan-view studies were conducted using a JEM-4000EX high-resolution electron microscope operated at 400keV with a resolution of 1.7 Å. Multiple micrographs taken from various samples showed intermittent dislocations evenly distributed throughout the 25×25 μm^2 field of view of the experiment. The average areal density of these features for the 700 nm thick $Ge_{0.96}Sn_{0.04}$ in Figure 35(a) was estimated to be in the range of 5×10^7 cm^{-2}, which is substantially above the defect concentrations found for the Ge buffer layer using similar measurement protocols. As shown earlier in Figure 34, XTEM images of the same samples showed a largely defect-free bulk layer with only occasional threading dislocations terminating within the lower segment of the film. A semi-quantitative estimate of the defect concentration appears to be on par with the average densities obtained from the plan view images, suggesting that our measurements may include some of these defects confined to the lower portion of the film along with those penetrating thought to the top surface.

Ayers and coworkers[189] developed a methodology to extract the dislocation density n from the width of the x-ray rocking curves as a function of the Bragg angle. According to these authors, the FWHM β of a Bragg reflection, after correction for extinction, finite size, and specimen curvature, satisfies the equation

$$b^2 = K_a(n) + K_e(n)\tan^2\theta_B \qquad (5.2)$$

where θ_B is the Bragg angle, and the functions $K_\alpha(n)$ and $K_\varepsilon(n)$ depend on geometrical factors and the size of the Burgers vector. Explicit functional forms are given in Reference 189. We have fit the width of our rocking curves in Figure 35(b) with Eq. (5.2), using n as the single adjustable parameter, and we obtain $n = (4.7\pm1.0)\times10^8$ cm^{-2}. Alternatively, since

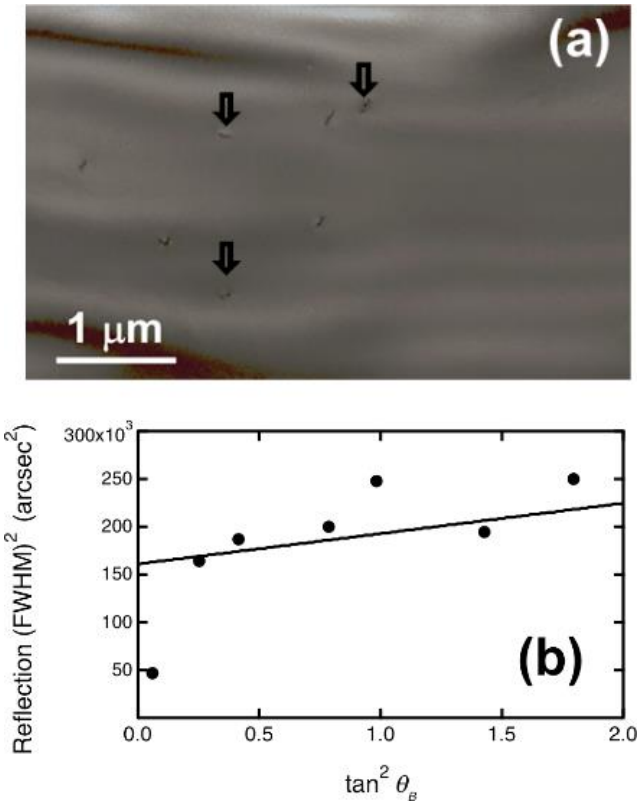

Figure 35 - (a) Plan view TEM image shows dislocations (examples marked by arrows) with an estimated density of 5×10^7 cm^{-2}. (b) Corrected FWHM of several Bragg reflections for a $Ge_{0.96}Sn_{0.4}$ sample. The solid line is a fit with Eq. (1), in which the dislocation density is the only adjustable parameter. The fit value is n = $(4.7\pm1.0)\times10^8$ cm^{-2}.

the determination of $K_\varepsilon(n)$ is affected by a large error due to the small range of Bragg angles in our experiments, we can equate $K_\alpha(n)$ to the square of the width of the (111) reflection, which has the smallest Bragg angle. Using this approach, we obtain $n = 1.5\times10^8$ cm^{-2}. Given the fact that only order-of-magnitude estimates can be expected from the x-ray method, as well as from the direct counting approach from the plan-view electron micrographs, the agreement between the two methods can be considered to be satisfactory.

Next, a systematic study of the strain relaxation behavior of the $Ge_{1-y}Sn_y$/Ge/Si samples was carried out with the hope of gaining insights that will allow the growth of fully strain relaxed films in the direct gap composition regime. HRXRD was used to determine the

strain state and relaxed cubic lattice parameters of the films, an example for which was given earlier in Figure 27. We define the fraction of strain relaxation as $R = 1-\varepsilon/\varepsilon_{max}$, where $\varepsilon_{max} = (a_{Ge} - a_0)/ a_0$. This fraction is shown in Figure 36, and we see that the strain in the

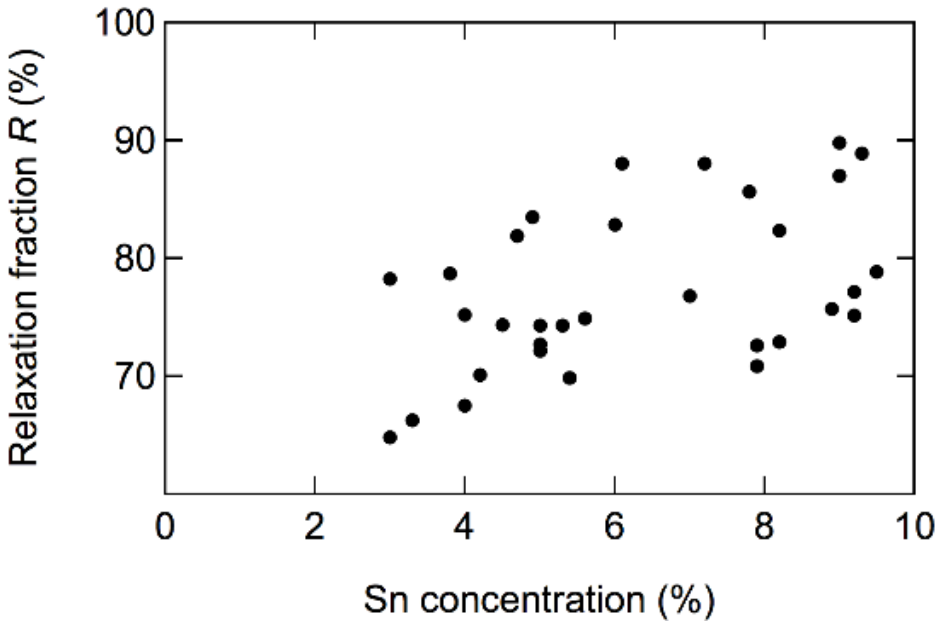

Figure 36 - Relaxation fraction *R* for as-grown $Ge_{1-y}Sn_y$ films on Ge-buffered Si.

as-grown samples is largely relaxed. The residual compressive strain can be further reduced or eliminated by subjecting the samples to rapid thermal annealing (RTA) treatments. For example, the 7% Sn sample in Figure 27 possessed an as-grown strain ε= -0.10 %, corresponding to a relaxation fraction $R = 0.88$. After three 2s-RTA cycles between 550°C-600 °C, the strain was reduced down to ε= -0.05 %, which implies R =0.94, without any indication of phase segregation or roughening of the surface. In other samples, the relaxation after RTA exceeds 100%, indicating the appearance of tensile strain due to thermal-expansion mismatch.

To understand the high-level of relaxation, we computed the critical thickness for growth of GeSn/Ge using standard Mathews-Blakeslee theory.[190] Starting from the effective stress expressions proposed by Houghton,[191,192] we obtain the solid black curve in Figure 37. The elastic parameters needed for the calculation were obtained by performing Voigt averages[193,194] of the elastic constants of Ge (Ref. 154) and α-Sn (Ref. 195). From these averages we obtain for Ge a shear modulus $\mu = 56.1$ GPa, and a Poisson ratio $\nu = 0.200$, whereas for α-Sn we compute $\mu = 29.7$ GPa, and $\nu = 0.217$.

It is apparent from Figure 37 that all of our samples exceed the critical thickness by at least one order of magnitude. However, since the growth temperatures are extremely low, the possibility of significant kinetic barriers to strain relaxation cannot be ruled out. In fact, Gencarelli *et al.* recently showed that fully strained $Ge_{1-y}Sn_y$/Ge samples can be fabricated with thicknesses that far exceed the Mathews-Blakeslee prediction.[76] These are shown as black squares in Figure 37. The empty squares correspond to slightly thicker films—grown by the same authors—that show evidence of strain relaxation. Samples grown by MBE on Ge substrates are also found to be fully strained at thicknesses well in excess of the Mathews-Blakeslee curve.[196]

A phenomenological strain relaxation model was proposed by Hull *et al.*[197] and systematically developed by Houghton to study $Ge_{1-x}Si_x$ alloys grown on Si.[191] The model assumes that the strain relaxation is proportional to the density of dislocation threading segments times the dislocation velocity, while threading dislocations are created at a rate that is proportional to an initial density n_0 of incipient dislocation nuclei. A detailed account of the model, including the effect of dislocation pinning, is given in Reference 192. We

have applied the same model to strain relaxation in $Ge_{1-y}Sn_y$/Ge. Houghton proposed Arrhenius expressions for the dislocation velocity and the rate of dislocation creation, with parameters adjusted to his own experiments in the $Ge_{1-x}Si_x$ system near the Si-rich end.[191]

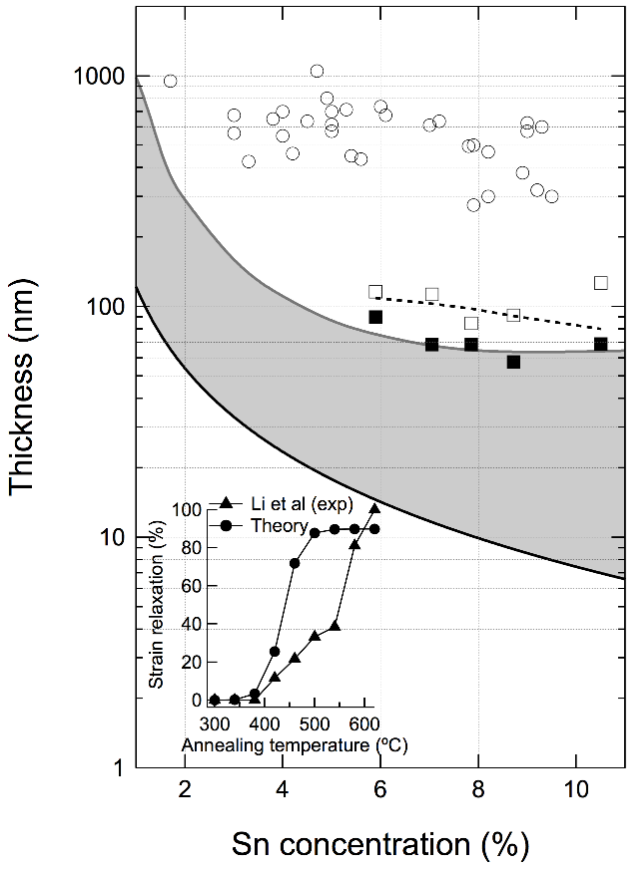

Figure 37 - $Ge_{1-y}Sn_y$ film thicknesses (empty white circles) compared with calculations of critical thickness for strain relaxation. The solid black line is a Mathews-Blakeslee calculation. Black squares correspond to fully strained samples reported by Gencarelli *et al.* (Ref. 76), and empty squares are the thicknesses of partially relaxed layers by the same authors. The dotted line corresponds to $|\varepsilon_{dis}| = 10^{-5}$ according to Houghton's kinetic relaxation model (Ref. 191). The parameters of the theory were adjusted to obtain a line between Gencarelli's fully strained and relaxed samples. When the same parameters are used to compute the thickness at which $|\varepsilon_{dis}|=10^{-5}$ for the empty circle samples, the solid gray line is obtained. The gray area thus indicates the region of strain "metastability". All samples studied here are beyond this region, which explains their high level of strain relaxation. The inset shows the annealing-induced strain relaxation measured by Li *et al.* (Ref. 181)and the prediction from our model using the same parameters as in the simulation of strain relaxation during growth.

For pure Ge, detailed measurements of dislocation velocities were carried out by Yonenaga *et al*. (Ref. 198), and the resulting expressions are somewhat different from those proposed by Houghton. Since our samples are closer to pure Ge, we use the Yonenaga *et al*. results in our simulations. The dislocation generation mechanism is the least known aspect of the relaxation process, but recent results on $Ge_{1-x}Si_x$ layers on Si (Ref. 199) confirm the importance of heterogeneous nucleation, as proposed by Houghton.[191] We assume that the expressions derived by Houghton for dislocation nucleation are valid for the $Ge_{1-y}Sn_y$ system, so that the only adjustable parameter in our model is the density n_0 of incipient dislocation nuclei. The strain relaxation produced by dislocations is defined as $\varepsilon_{dis} = \varepsilon_{max} - \varepsilon$. The fit is carried out by computing the film thickness at which this strain relaxation reaches a value $|\varepsilon_{dis}| = 10^{-5}$, which is close to the limit of detectability using x-ray methods. The dotted line in Figure 37, which gives this threshold thickness, was obtained using $n_0 = 7.3\times10^{11}$ cm^{-2} and the experimental growth rates from Gencarelli *et al*.(Ref. 200). Returning to our samples, we use the value of n_0 obtained from the fit to the samples in Ref. 76, combined with our growth rates and temperatures, to compute the thickness that satisfies the $|\varepsilon_{dis}| = 10^{-5}$ condition. This gives the solid grey line in Figure 37. To obtain a smooth curve, we adjusted a linear function of composition to the growth temperatures and growth rates, which gives a good empirical account of the data for all samples in Figure 37. We see that the calculated line is well below the actual sample thicknesses, so that we predict an observable strain relaxation level for all of our samples, as found experimentally. In principle, the calculations can be continued beyond the solid line in Figure 37 to predict the observed strain relaxation ε_{dis} at the actual sample thicknesses, but the values obtained are typically lower in magnitude than those observed. This is not surprising, since the

model neglects dislocation multiplication, and therefore it can only be expected to be accurate at the initial stages of strain relaxation.

The value $n_0 = 7.3\times10^{11}$ cm^{-2} for the initial density of dislocation nuclei is orders of magnitude larger than the value found by Houghton ($n_0 = 5\times10^3$ cm^{-2}) for growth of $Ge_{1-x}Si_x$ alloys on Si wafers at temperatures close to 500°C, but comparable to the values found for $Ge_{1-x}Si_x$ films grown at temperatures near 300°C, (Ref. 192) which are much closer to the growth temperatures of our $Ge_{1-y}Sn_y$ layers. One factor that may contribute to the large value of n_0 is the use of a Ge buffer grown on Si, since the unavoidable defects in the buffer layer may act as dislocation seeds in the $Ge_{1-y}Sn_y$ layers.

To test this hypothesis we grew $Ge_{1-y}Sn_y$ films directly on Ge substrates, and we find that films with thicknesses close to 500 nm and Sn concentrations around y=0.05-0.06, well above the metastable relaxation line in Figure 37, are still fully strained. This implies $n_0 < 3\times10^9$ cm^{-2}. A representative (224) RSM of such a fully strained sample is given in Figure 38. It has a composition of y=0.06, and was grown at a temperature of 315°C, and the thickness is 485 nm. The lack of strain relaxation in these films suggest that these films should be devoid of the defects observed in the $Ge_{1-y}Sn_y$/Ge/Si films. The resultant superior crystallinity was corroborated by examining the films using XTEM. Figure 39 a) shows a typical cross section of the film, which has large areas of defect free crystal. In contrast to the defected $Ge_{1-y}Sn_y$/Ge interfaces observed in the films grown on Ge buffered Si, the interfaces of the alloys grown directly on Ge are virtually defect-free. Figure 39 b) shows a portion of the interface which contains one of the occasional defects.

The lack of defects within the film is also evident when the surface of the sample is studied using AFM. Whereas the samples grown on Ge/Si show a regular array of crosshatch patterns on the surface, such features are absent in the films on Ge. This also results in a smoother surface on these films with the RMS surface roughness being 0.3 nm. A representative image is shown in Figure 40. While defect free crystals are desirable for optical applications, the high degree of compressive strain negates this advantage by rendering the band structure less direct gap, despite the high level of Sn incorporation. Therefore the possibility of relaxing the films was investigated. The method chosen was subjecting them to RTA. For the *y*=0.06 sample discussed earlier, it was possible to reduce the strain to from -0.80% to -0.18% by three RTA cycles of 2 s duration at 550°C. However, this was accompanied by a significant degradation of the crystal quality, with the FWHM of the (004) RC increasing to 0.248° from an earlier value of 0.096°. The formation of

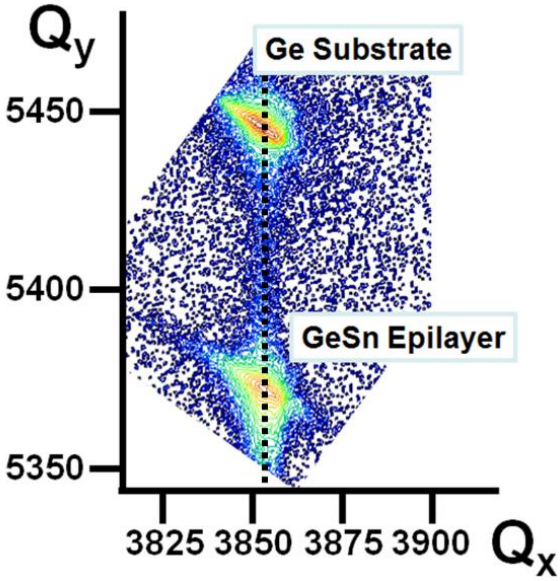

Figure 38 – (224) RSM of a 500 nm thick $Ge_{0.94}Sn_{0.06}$ alloy film deposited on Ge(100) substrate. The epilayer is fully strained to the substrate, in contrast to $Ge_{1-y}Sn_y$ films deposited on Ge buffered Si substrates under similar conditions. The dashed line emphasizes the equal in-plane lattice parameters in the substrate and epilayer.

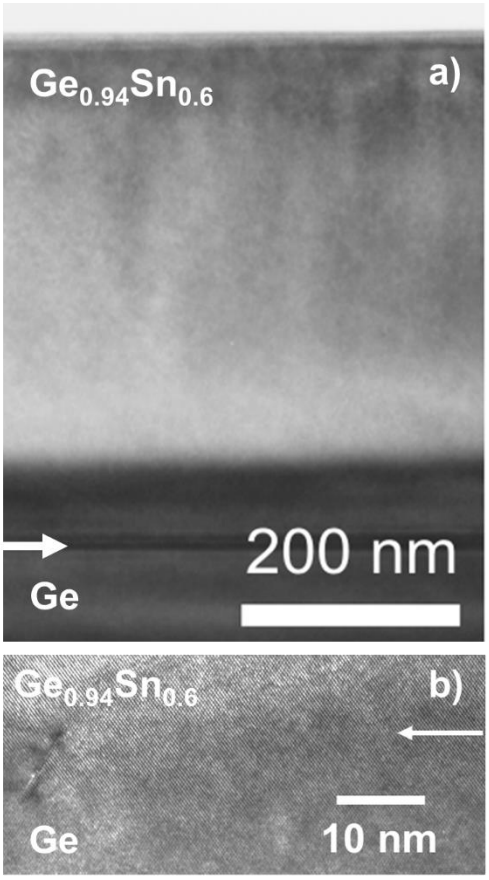

Figure 39 – a) XTEM micrograph of a $Ge_{0.94}Sn_{0.06}$ film fully strained to the Ge substrate. b) Magnified view of the GeSn/Ge interface region exhibiting markedly fewer defects compared to GeSn/Ge/Si samples.

threading dislocations in the film was also manifest in AFM images. As shown in Figure 40 b), crosshatch patterns generated by dislocations propagating to the surface are evident after the annealing step. From these results, it can be concluded that using Ge as a substrate is unsuitable for obtaining direct gap GeSn alloys, and that Ge-buffers on Si are a preferred platform if the goal is to obtain strain-relaxed GeSn films.

7. Conclusion

GeSn films were grown on Ge-buffered Si, and their structural properties were studied in detail. Our low temperature synthesis approach combined with the use of highly reactive

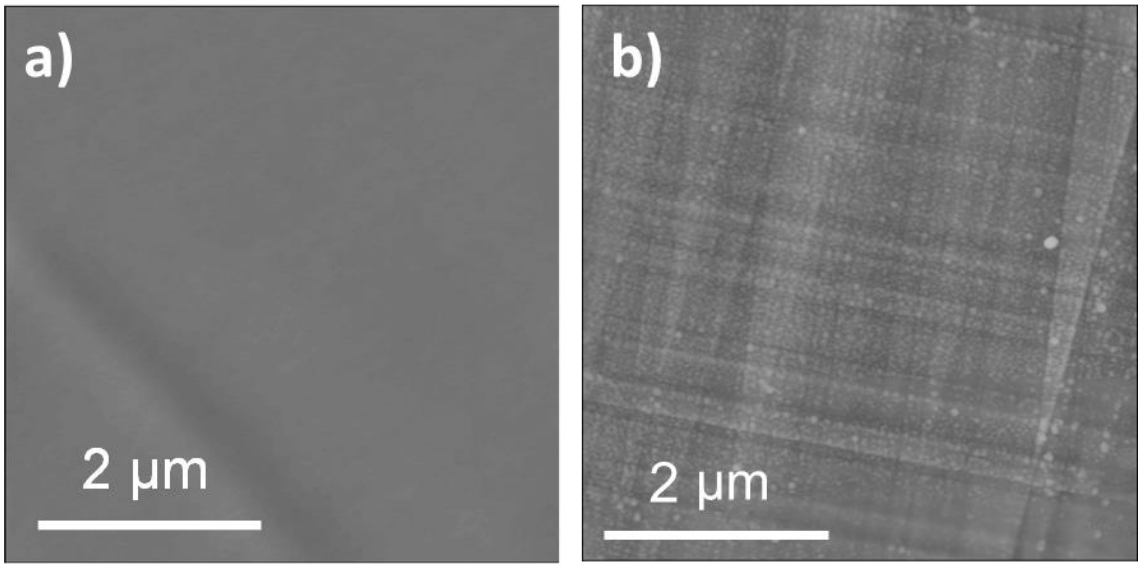

Figure 40 – a) AFM image of a 5μm×5μm area of an as-deposited, fully strained $Ge_{0.94}Sn_{0.06}$/Ge film exhibiting atomically flat surface with a RMS roughness of 0.3 nm. b) The surface of the same film after strain relaxation induced by thermal processing, exhibiting crosshatch patterns arising from propagation of dislocations to the surface. The RMS roughness increases to 1.1 nm in this case.

Ge_2H_6/Ge_3H_8 and SnD_4 sources provides access to material with compositions near the direct gap threshold. Substantially lower defect levels are seen in these films compared with films deposited directly on Si substrates, which make it possible to easily achieve thicknesses up to 1 μm prior to the onset of epitaxy breakdown. At these thicknesses, we find very high levels of strain relaxation, as expected from theoretical simulations of the strain relaxation process.

In the next chapter, it will be shown how the elimination of compressive strains and the lower defect levels leads to dramatic improvement in the intensity of optical emission. This suggests that relaxed GeSn films on Ge-buffered Si substrates are the most promising pathway to GeSn lasers on Si, which are the ultimate aim of this field of inquiry. The synthetic procedures developed for fabrication of such devices is described in Chapter 7. These methods are developed based on the procedures described in this chapter, but include

improvements that support the deposition of thick, low defectivity alloy films with compositions $y>0.11$. They include the growth of Ge refreshing layers that help mitigate defect formation, and temperature programmed growth approaches that allow increased growth rates at ultra-low temperatures <300°C. A detailed description of these procedures is provided in Chapter 7, and specific details on sample growth are also given in Appendix A.

CHAPTER SIX

Photoluminescence Studies of GeSn Alloys and Emission Enhancement via *n*-Type Doping

Synopsis

In this chapter, PL characterization of undoped and doped GeSn alloys is described. The intense, well resolved PL spectra from the former allowed the determination of the indirect-direct crossover composition for the GeSn alloy system. The doped samples were mainly synthesized using $P(GeH_3)_3$, $P(SiH_3)_3$, and $As(SiH_3)_3$ precursors at low temperatures compatible with GeSn alloy growth near the indirect-direct crossover composition of ≈9% Sn. The donors introduced by this method are fully activated, and carrier concentrations as high as 7×10^{19} cm^{-3} could be achieved, resulting in an order-of magnitude and greater enhancement in PL intensity in the doped samples compared to intrinsic counterparts.

Portions of this chapter were adapted with permission from Senaratne, C. L.; Gallagher, J. D.; Aoki, T.; Kouvetakis, J.; Menéndez, J. Advances in light emission from group-IV alloys via lattice engineering and n-type doping based on custom-designed chemistries. *Chem. Mater.* **2014**, *26* (20), 6033. Copyright 2014 American Chemical Society.

1. Introduction

Elemental Ge exhibits significant direct gap light emission in spite of the indirect character of its fundamental band gap. This is due to the sizable population of photoexcited electrons in the Γ valley of the conduction band at the Brillouin zone (BZ) center, resulting from the small energy difference between the minimum of this valley and the lowest-energy valley in the conduction band near the *L* point in the Brillouin zone. As mentioned above, alloys

of Ge and Sn were recently introduced as a means of extending the optical capabilities of Ge in the group IV photonics arena.[9,20,51,68,69,201,202] In $Ge_{1-y}Sn_y$ the separation between the Γ and *L* valleys of the Ge-like band structure is further reduced as Sn is incorporated into the Ge lattice.[36,39,41] This causes an increase in the carrier concentration in the Γ valley, thereby inducing more radiative transitions and thus significantly enhancing light emission relative to pure Ge.[20,38]

$Ge_{1-y}Sn_y$ alloys are purported to undergo an indirect to direct gap cross-over for y~ 0.06-0.10, indicating widespread applications in future generations of light emitting devices compatible with existing silicon technologies.[36,40,41] In spite of recent advances in mapping the electronic structure of these materials, the unambiguous determination of the cross over composition point is very challenging.[27,33–35,39,42–44,203,204] This is because it is difficult to separate the individual contributions from two very close optical transitions if—as is the case in GeSn —one of them (the direct gap) has an oscillator strength about two orders of magnitude larger, and in addition the two transitions are broadened due to the alloy potential. The only technique in which the direct and indirect gaps produce comparable signals is room temperature photoluminescence spectroscopy, and even in this case, measurements of the indirect gap are only possible for $y \leq 0.06$. A complete and accurate mapping of the two transitions over a broader range of compositions may require a combination of PL with direct absorption measurements in very thick films and/or measurements of the electrical characteristics of intrinsic and doped samples as a function of temperature. A key requirement to accomplish this goal is the availability alloy films of comparable quality and thickness over the entire $y < 0.1$ range of compositions. The

synthesis of such a series of films was described in the previous chapter. In this chapter, room-temperature PL is of these alloys is measured.

The initial observation of tunable PL was obtained from sample prototypes grown directly on Si substrates by CVD reactions Ge_2H_6 with SnD_4.[51] In this case indirect and direct gap PL was only observed from layers with up to 3 % Sn, while the corresponding signals from more concentrated analogs degraded significantly with increasing Sn content. This was likely due to the increased defectivity associated with the progressively lower growth temperatures needed to achieve higher Sn concentrations. The introduction of higher reactivity Ge_3H_8 in place of Ge_2H_6 enabled the growth of thicker layers on silicon with Sn contents up to 10 % Sn, spanning the direct gap composition crossover.[106] These samples were found to possess a significant volume fraction of optical quality material away for the defective interface region, leading to sizable PL emission over the entire range of the samples. The latter optical data were sufficient to allow an initial determination of the compositional dependence of the direct gaps vs. Sn content. However the quality of the PL signal was insufficient to unambiguously resolve both the direct and indirect signals needed to determine the crossover composition and establish the nature of the fundamental band gap. Furthermore, from a device perspective the low intensity and suboptimal quality of the PL signal for high Sn content alloys (4-10 % Sn) indicated that the materials, as grown on Si wafers, are not suitable for the fabrication of laser diodes.

In contrast, the GeSn alloys deposited on Ge buffered Si substrates described in the previous chapter exhibit exceptionally strong PL signals in which it is possible to clearly distinguish the contributions from the direct and indirect edges, as described below. This

stems from the fact that the virtual substrates allow the formation of thick and largely relaxed epilayers with interface microstructures engineered to significantly reduce non-radiative recombination velocities relative to samples grown directly on Si. Spectra from a series of samples reveal diminishing separation between the indirect and direct band gaps, together with dramatically increasing PL intensity with higher incorporation of Sn in the alloys. These results, described in detail in Section 2, lead to the conclusion that the indirect-direct crossover for the GeSn alloy system occurs in the range of 8-10 % Sn.

The PL intensity of $Ge_{1-y}Sn_y$ alloys with compositions near the direct gap threshold (y=0.05-0.09) is further enhanced by populating the Γ-valley in the band structure with electrons through heavy doping with P atoms at levels up to $3x10^{19}$ atoms cm^{-3} using the single sources $P(GeH_3)_3$ and $P(SiH_3)_3$ whose synthesis was described in Chapter 2. In Section 5, it is shown that show that the PL intensities of the doped films are approximately 10 times those of the intrinsic counterparts with similar thicknesses possessing the same Sn concentration. Experiments using the $As(SiH_3)_3$ compound yielded higher carrier densities of $7x10^{19}/cm^3$ allowing additional performance gains in the PL response. The results suggest desirable direct gap conditions for possible laser applications can be achieved in *n*-type materials at relatively modest Sn contents below the direct gap threshold.

2. Determination of Indirect-Direct Crossover in Intrinsic GeSn Alloys

PL measurements were carried out with the samples held at room temperature and illuminated with 400 mW of radiation generated from a continuous wave (CW) 980 nm laser focused to a 100 μm spot. The emitted light was collected by an f =140 mm Horiba

MicroHR spectrometer equipped with a 600 grooves/mm blazed at 2 μm. The spectrometer is fitted with a liquid nitrogen (LN_2) cooled extended InGaAs detector with a detection range of 1300-2300 nm. A 1400 nm long pass filter is employed to remove possible emission of visible radiation from the Si substrate. In spite of this filter, a clear 2nd order laser signal at 1960 nm is seen in all raw spectra and is subtracted from the data by fitting the laser peak with a Gaussian. The raw spectrum is further corrected to account for filter transmission and spectrometer response using calibration curves obtained from measurements of a tungsten lamp.

Figure 41 shows corrected PL spectra from selected $Ge_{1-y}Sn_y$/Ge/Si samples compared with $Ge_{1-y}Sn_y$ /Si analogs with similar Sn concentrations and thickness, collected under identical conditions. The most striking feature in the spectra is the much stronger PL intensity from the samples grown on Ge-buffer layers. The intensity enhancements average one order of magnitude, and are assigned to reduced non-radiative recombination rates in the $Ge_{1-y}Sn_y$/Ge/Si films. There are two main sources of non-radiative recombination in $Ge_{1-y}Sn_y$ films: bulk-like defects, such as threading dislocations, and defects localized at the interface with Si, which are responsible for a very high recombination velocity at this interface.[205] Both sources of non-radiative recombination are suppressed in our $Ge_{1-y}Sn_y$/Ge/Si films: the bulk-like defect concentration is lower, as evidenced by the reduced widths of the XRD rocking curves, and the carriers are likely confined to the $Ge_{1-y}Sn_y$ layer, away from the Ge/Si interface, because the valence and conduction band offsets between $Ge_{1-y}Sn_y$ and Ge are of type I.[206] The separation between the two contributions will require

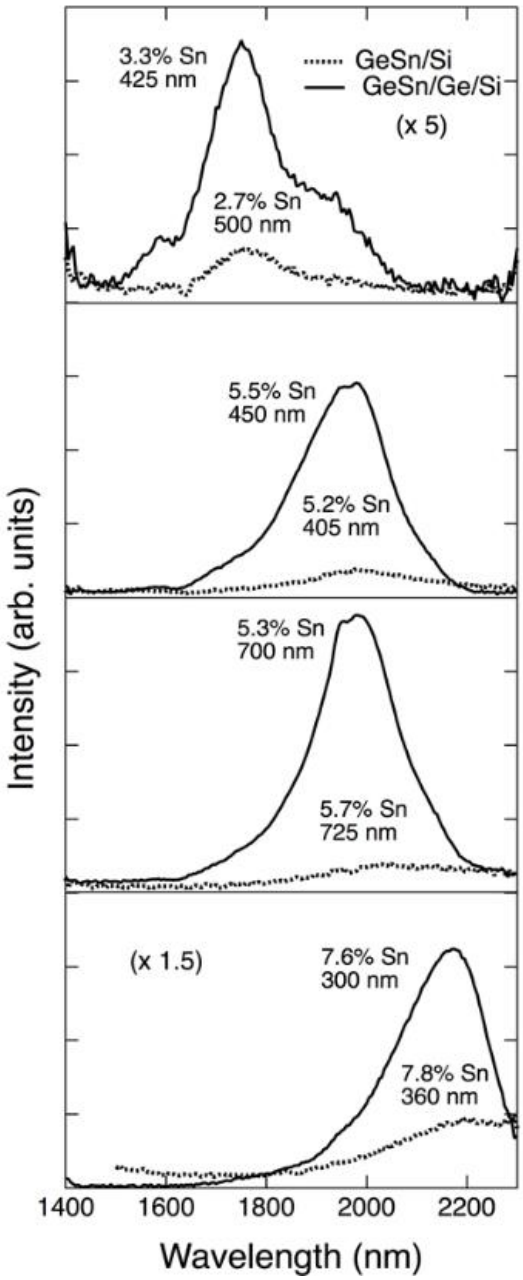

Figure 41 - Photoluminescence spectra from a $Ge_{1-y}Sn_y$/Ge/Si and a $Ge_{1-y}Sn_y$/Si counterpart with similar Sn-concentration and thickness.

systematic measurements and modeling of the PL intensity as a function of layer thickness for a fixed Sn concentration.

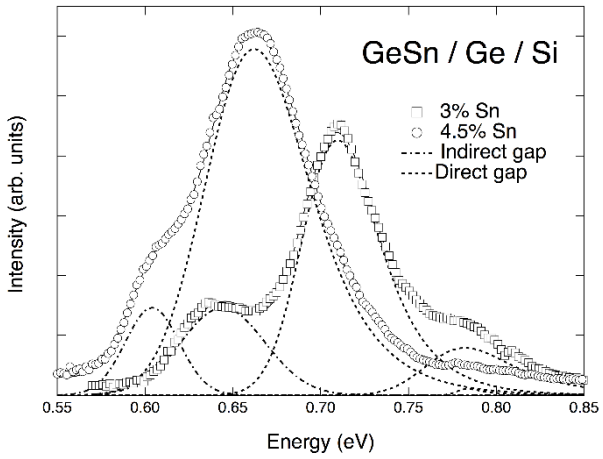

Figure 42 - Circles and squares show photoluminescence from two selected $Ge_{1-y}Sn_y$/Ge/Si samples. The solid line adjusted to the spectra is a fit with a combination of a Gaussian for the indirect gap emission and an EMG for the direct gap emissions from the $Ge_{1-y}Sn_y$ top layer and the Ge buffer. The dotted and dash-dotted lines show the three components of the fit for the two samples.

The increased intensity of the PL signal makes it far easier to study the detailed structure of the PL spectra, including the contributions from the direct and indirect edges. Unlike most semiconductors, in which PL arises from the lowest band gap, whether direct or indirect, in Ge one sees evidence for both direct and indirect gap emission.[207–209] This unique property reflects Germanium's peculiar band structure, in which the direct band gap is only 140 meV above the indirect edge. Even for very small thermal occupation of the conduction band minimum associated with the direct gap, the much higher oscillator strength of the direct optical transition leads to a signal that is comparable to the indirect gap emission, and in fact stronger if reabsorption effects are corrected for or eliminated, as in thin films. Figure 42 shows two examples of samples in which the direct and indirect edge are clearly visible. As discussed in prior work,[209,210] the indirect emission is fit with a simple Gaussian and the direct gap emission is fit with an Exponentially Modified Gaussian (EMG) function that accounts from the observed and expected asymmetry of the emission profile. The fit with these functions is indicated as dotted (direct gap) and dash-dotted

(indirect gap) lines in the figure. From such fits one can extract the energies of the direct and indirect band gaps in $Ge_{1-y}Sn_y$ alloys and study their compositional dependence, as discussed below. Notice, however, that the separation between the direct and indirect emission decreases, and the direct gap emission intensity increases, as the Sn concentration is raised from 3% to 4.5%, approaching concentration for which the material transitions from indirect to direct-gap semiconductor.

Figure 43 shows PL spectra from representative alloys with a common thickness of ~600 nm and varying Sn contents from 0.3 % to 9 % Sn. The PL plots for y = 0.003-0.05 show

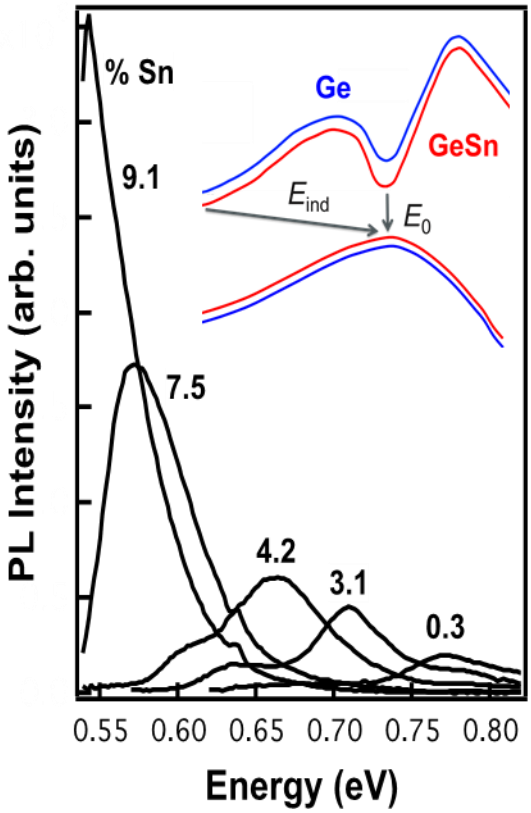

Figure 43 - Room temperature PL plots vs. Sn fraction for $Ge_{1-y}Sn_y$ (y = 0.003- 0.09). Main peak is due to direct recombination (E_0) and the weak shoulder is attributed to indirect emission (E_{ind}). Peak energies redshift and intensities increase as a function of Sn content. Inset is a schematic of $Ge_{1-y}Sn_y$ band structure showing the two transitions measured in the PL spectra and the band gap narrowing in relation to elemental Ge.

a strong main peak corresponding to direct gap emission and a weak lower energy shoulder which is assigned to indirect transitions from the *L* minimum of the conduction band. The two peaks appear to merge into a single broad peak in the spectra of the more concentrated samples ($y > 0.06$) due to the decreasing separation of the direct and indirect edges with increasing Sn content. The trends here illustrate a shift of the PL maximum to lower energies as a function of Sn content and a sharp increase in the signal intensity as the indirect-direct crossover point is approached. The direct and indirect gap energies are extracted by fitting the PL peaks using methods described above. The same techniques have been utilized in prior work for extracting the band gaps of (Si)GeSn analogs, as discussed in in References 210, 211, and 212. The fitting procedure corrects for strain effects (which are rather small due to the large strain relaxation) and yields the band gap values corresponding to unstrained films.

The band gap energies determined using these procedures for intrinsic samples with compositions y=0-0.11 were then fit according to quadratic expressions of the following forms:

$$E_0(y) = E_0^{Ge}(1-y) + E_0^{Sn}y - b_0y(1-y) \qquad (6.1)$$

$$E_{ind}(y) = E_{ind}^{Ge}(1-y) + E_{ind}^{Sn}y - b_{ind}y(1-y) \qquad (6.2)$$

In the above expressions the E_0 and E_{ind} for $y = 0$ and $y = 1$ are taken as equal to those of elemental Ge and α-Sn, corrected for temperature dependence. The fitting function then contains the bowing coefficients b_0 and b_{ind} as its only adjustable parameters. Using E_0^{Ge} = 0.796 eV, E_0^{Sn} = -0.413 eV, E_{ind}^{Ge} = 0.655 eV, and E_{ind}^{Sn} = -0.035 eV (Ref. 211), we obtain

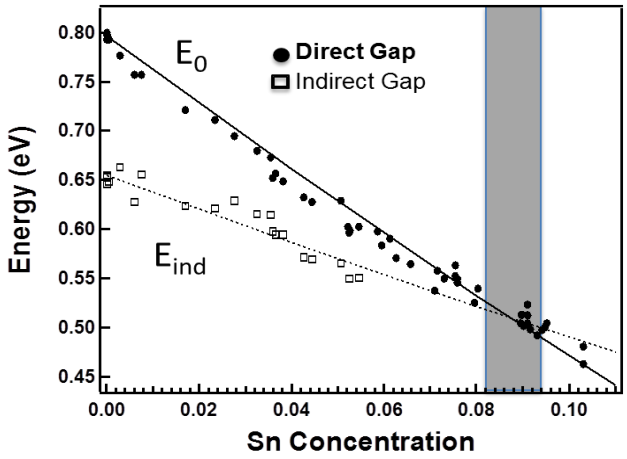

Figure 44 - Energies of direct gaps (circles) and indirect gaps (squares) vs. Sn concentration for $Ge_{1-y}Sn_y$ alloys with 0<y<0.11. The solid lines are the quadratic fits of the data. The intersection near 9 % Sn denotes the onset of the crossover from indirect to direct gap semiconductor. The gray area marks the uncertainty in cross over composition

bowing parameters b_0 = 2.26±0.03 eV and b_{ind} = 1.06±0.09 eV. These bowing parameters represent a cross over point composition y_c from indirect to direct gap semiconductor for bulk like $Ge_{1-y}Sn_y$ in the vicinity of 8-9%, as illustrated in Figure 44. This range is significantly lower than predicted using virtual crystal approximation theory (y_c = 0.2) but much closer to recent calculations using supercells to simulate the alloy (4.5-6%). A more detailed treatment of the determination of y_c is given in Reference 213, which takes into account the compositional dependence of the bowing parameters. This yields a crossover composition of y_c=0.087.

3. Growth of *n*-doped $Ge_{1-y}Sn_y$ Alloys (*y*=0.04-0.09) Using $P(GeH_3)_3$ as the Doping Agent

As noted in the introduction, the PL intensity of GeSn alloys near the indirect-direct crossover composition can be further enhanced by *n*-type doping. The initial investigations on doping was done by using $P(GeH_3)_3$ as the doping agent. The conditions used for the growth experiments replicate the parameters used for intrinsic $Ge_{1-y}Sn_y$ alloys. The growths

were conducted on Ge buffered Si substrates, which were cleaned before epitaxy using the HF and Ge_2H_6 cleans described in Chapter 5. The growths were conducted in a hot wall UHV-CVD reactor heated by a single zone furnace, with Ge_3H_8 and SnD_4 as the other precursors. The amounts of Ge_3H_8 used were 40-25 LTorr, with the lower amounts being used for the higher Sn samples, for which the mixtures were diluted to 1% Ge_3H_8 using H_2, in contrast to the lower Sn samples, for which the concentration of Ge_3H_8 was 2%. The amount of SnD_4 was chosen such that the atomic percentage of Sn in the mixtures was 3-8%, which results in the 4-9% epilayer compositions. The target doping level was ~2-3×10^{19} cm^{-3}, which was achieved by adding 0.15-0.30 LTorr of $P(GeH_3)_3$ into the precursor mixture. The higher amounts of $P(GeH_3)_3$ were required for the samples with higher Sn contents, presumably because of the lower growth temperatures and lower precursor concentrations in the mixtures. The temperatures utilized for the growths were in the range 325-295°C. Specific growth parameters for representative samples are given in Appendix A.

4. Materials Properties of P Doped GeSn Samples

Rutherford backscattering was used to determine the thickness and Sn content of the doped samples. Channeling experiments were also carried out, the results of which demonstrate a high degree of epitaxial alignment of the epilayers, as well as the complete substitutionality of the Sn atoms within the Ge lattice. The RBS results are further corroborated by high-resolution X-ray diffraction experiments. The (004) ω rocking curves show FWHM values in the order of 0.18° for alloys in the 5-7% Sn and slightly higher for the 8-9% materials depending on the final thickness. Such data indicate that the crystal quality of the doped alloys is comparable to the intrinsic samples described in Chapter 5.

Measurement of the (224) reciprocal space maps indicated a high degree of lattice relaxation in the as grown films in spite of the mismatch induced by increasing the Sn content, as shown in Figure 45 a). Residual compressive strains of 0.13% corresponding to 80% relaxation were found which can be further reduced by rapid thermal annealing. The cubic lattice constants were obtained and the Sn contents were determined from them using the compositional dependence relationship from Ref. 14.

The compositions derived from HRXRD data are in excellent agreement with the values obtained from RBS analysis. The active carrier concentrations in the alloys were determined using spectroscopic IR ellipsometry yielding values of 8×10^{18}-3×10^{19} cm^{-3} in all of the samples produced in this study. Nomarski optical microscopy and AFM were used to determine the surface topology. In common with intrinsic $Ge_{1-y}Sn_y$/Ge/Si epilayers, the doped samples exhibit cross-hatch patterns on the surface arising from the defects generated at the interface (see Figure 45 b)). The RMS roughness as determined by AFM was ~3-4 nm.

Further structural characterizations were performed by cross sectional transmission electron microscopy using a JEM -4000 EX microscope operated at 400 kV. The low magnification images revealed single phase mono-crystalline epilayers with uniform morphologies and planar surfaces. Figure 46 shows representative micrographs of a $Ge_{0.936}Sn_{0.064}$ film (t= 580 nm) grown upon a Ge buffer layer (t=780 nm) at 315 ^{o}C. The STEM bright field image shows signs of defects and strain fields confined to the interface region. The bulk film exhibits a uniform phase contrast with no threading defects visible within the field of view of several microns in the lateral direction. This observation

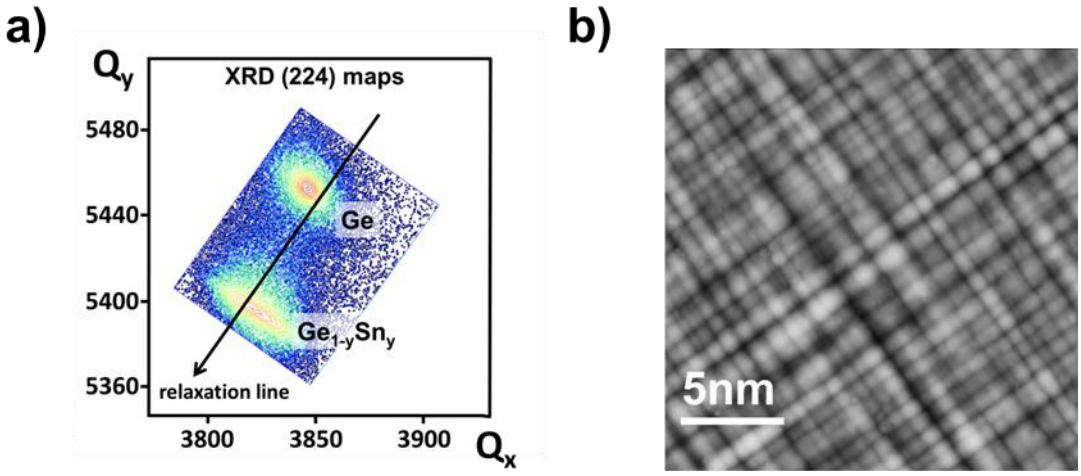

Figure 45 – a) 224 reciprocal space maps of a $Ge_{0.94}Sn_{0.06}$/Ge sample. The in plane and vertical lattice parameters are determined to be 5.6984 Å and 5.7113 Å, respectively indicating compressive strain of 0.1292%. The buffer layer exhibits a slight tensile strain of 0.1291 % due to the thermal expansion mismatch with the Si wafer. b) AFM image of the same film exhibits cross hatch patterns arising from dislocation patterns near the interface penetrating through to the free surface.

indicates that the dislocation densities propagating through the film are relatively low and that the misfit strain is mostly compensated at the interface. Hence we conducted a detailed high resolution analysis to identify the type and distribution of dislocations generated under the low temperature process conditions used in this study. The experiments were performed on JEOL ARM 200F microscope equipped with probe aberration corrector. STEM bright field images were acquired using large collections angles up to 22 mrad and representative data are shown in the Figure 46 and Figure 47. The top panel in the latter illustrates an extended view of the interface region indicating the location of stacking faults shown as dark contrast lines along the growth direction. The features are separated from one another by distances ranging from 42 to 15 nm as illustrated in the high resolution image in the inset of Figure 46. These defects are randomly distributed at the GeSn/Ge interface and they penetrate down a short distance into the buffer layers. An enlarged view of an

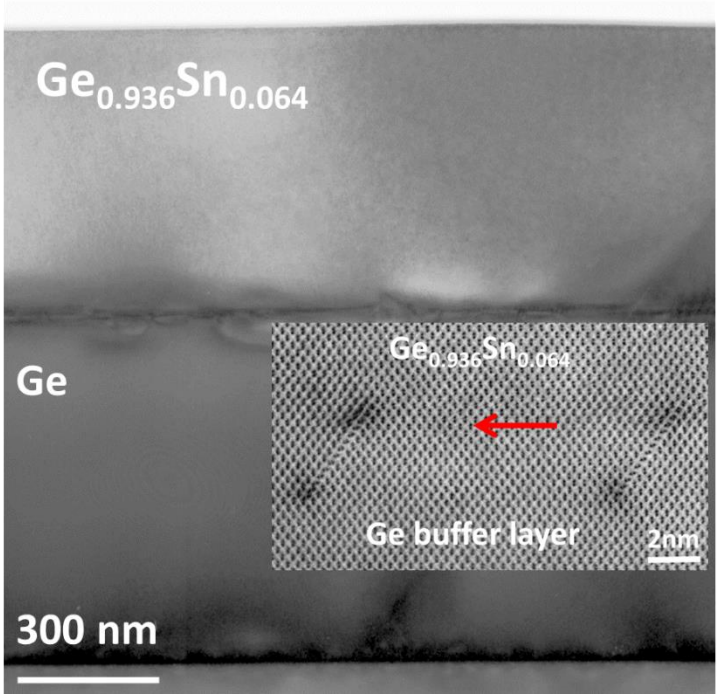

Figure 46 - XTEM micrograph of *n*-type $Ge_{0.936}Sn_{0.064}$ film grown upon a Ge buffered Si substrate at 315 ºC. Inset is a high resolution STEM bright field image of the film/buffer interface region showing the position of the interface marked by arrow and the location of a pair of stacking faults separated by 15 nm. The doping concentration in this sample is $3x10^{19}/cm^3$ as determined by spectroscopic ellipsometry.

individual stacking fault (panel (b)) shows that the disruption of the stacking sequence of the 111 planes is caused by rotation of the dimer columns in [110] projection. This imperfection is likely spawned by localized strain fields found in the vicinity of these defects as a means of minimizing the residual stress induced by the lattice mismatch. In addition to stacking faults, the STEM images also reveal 60º dislocations randomly arranged throughout the hetero-junction. The dark contrast in panel (c) indicates the location of such a defect which was identified by first calculating Fourier Transform of the STEM image, and second, applying masks to only two specific {111} reflections, for example, -1 11 and 1-1-1, filtering out everything else, and finally calculating reverse Fourier transform of a masked FFT. The process was repeated to another set of {111}

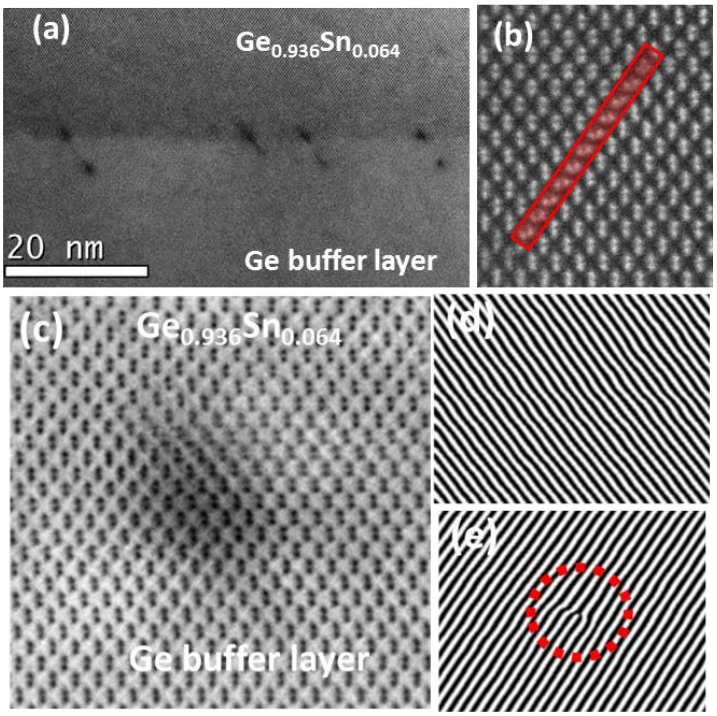

Figure 47 - STEM images of the *n*-type $Ge_{0.936}Sn_{0.064}$ film grown on Ge showing defects present in this sample. (a) Enlarged bright field view of the interface showing stacking fault patterns commonly found in this class of materials. (b) An individual defect is highlighted by red box illustrating rotated dimer column along {111} direction. (c) Dark contrast in the center of the image indicates the location of the 60º partial dislocation. (d, e) Inverse FFT images of selected {111} lattice planes in the vicinity of the 60º dislocation is used to identify in this case the defect type denoted by the red circle.

reflections (1-11 and -11-1) and then their reverse FFT was calculated. The two reverse FFT images are displayed in panels (d) and (e) and show that only one of them (e) contains an extra (111) plane terminated at a point marked by the red circle indicating the presence of a 60 degree perfect dislocation.

Finally the $Ge_{0.936}Sn_{0.064}$ sample was characterized by "element-selective" mapping using STEM and EELS to investigate the distribution of the constituent atoms in the lattice at the sub-nanometer scale. The atomic arrangements in these materials are of particular relevance to the PL studies that will be described in subsequent sections, since deviations

from alloy randomness may have significant implications on the electronic structure of the crystals. The EELS spectra were collected with spot size 0.13nm in aberration corrected STEM HAADF mode using a GATAN Enfinium spectrometer. Figure 48 (a) is a high resolution STEM-HAADF image showing projections of atomic columns displayed as bright spots. These correspond to dimers or dumbbells comprising Ge and Sn aligned along the growth direction. The region of the sample analyzed by EELS is identified by the square box with dimensions of 3x3 nm^2 in the lateral direction. The thickness of the specimen is 40 nm as determined by the low loss spectra. The EELS spectra in all cases shows peaks corresponding to Ge (L) and Sn (M) ionization edges at 1217 eV and 483 eV, respectively. These were then used to generate atomic maps for the Ge (green) and Sn (red) columns as shown in Figure 48 (b) and (c) respectively. The Ge map shows distinct Ge-

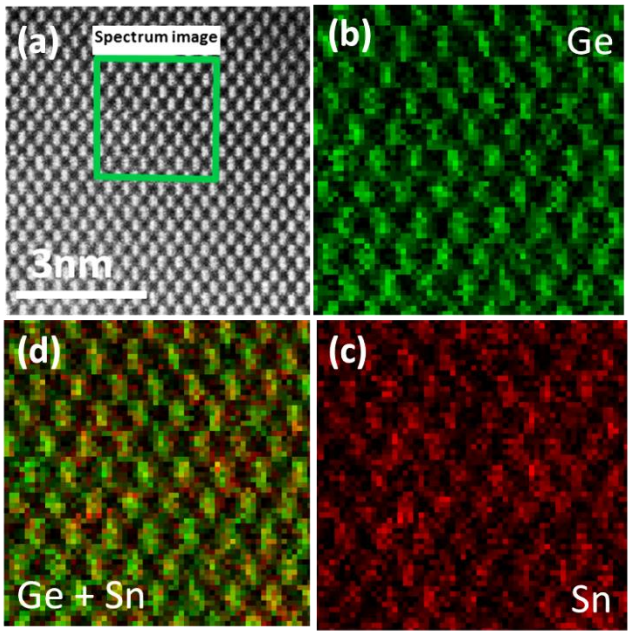

Figure 48 - STEM and element selective EELS mapping show random Sn substitution in diamond lattice. (a) STEM image of *n*-type $Ge_{0.936}Sn_{0.064}$ film identifying the region analyzed by EELS; (b) Ge map created from the L edge showing dimer columns in 110 projection; (c) Sn map generated from the M edge; (d) hybrid Ge and Sn map.

Ge dimer rows of the host lattice. The Sn maps exhibit similar features corresponding to projected bonding sites. The color overlay in Figure 48 (d) of the Ge and Sn maps illustrates a uniform distribution of the green and red spots down each column indicating that both atoms occupy the same lattice and that they are randomly located along [110] projected columns. Collectively the XTEM and EELS analysis results support the notion that the Ge buffers provide a structurally compatible low energy platform that serve as compliant templates to reduce the initial lattice mismatch with Si wafers making it possible to integrate highly concentrated alloys with large thickness, low concentrations of threading defects and random alloy structures devoid of interstitials and precipitates as required for meaningful investigation of the optical properties.

5. Photoluminescence Measurements and Band Gap Determination of *n*-type doped films

As indicated above, heavy *n*-type doping of GeSn alloys by introducing group V donor atoms leads to significant enhancement of PL emission. Figure 49 compares the spectrum of an *n*-type 6 % Sn alloy containing $3x10^{19}/cm^3$ carriers grown and characterized as described in the previous sections. This sample exhibits an order of magnitude higher PL intensity (dotted curve) relative to that of the corresponding intrinsic specimen (gray curve), which has a similar Sn content and thickness. This increase in thickness arises from the higher population of electrons in the Γ valley of the doped sample, which increases the radiative recombination probability. In addition there is a slight redshift of the doped sample peak maximum due to the renormalization of the band gap induced by the significant doping level.

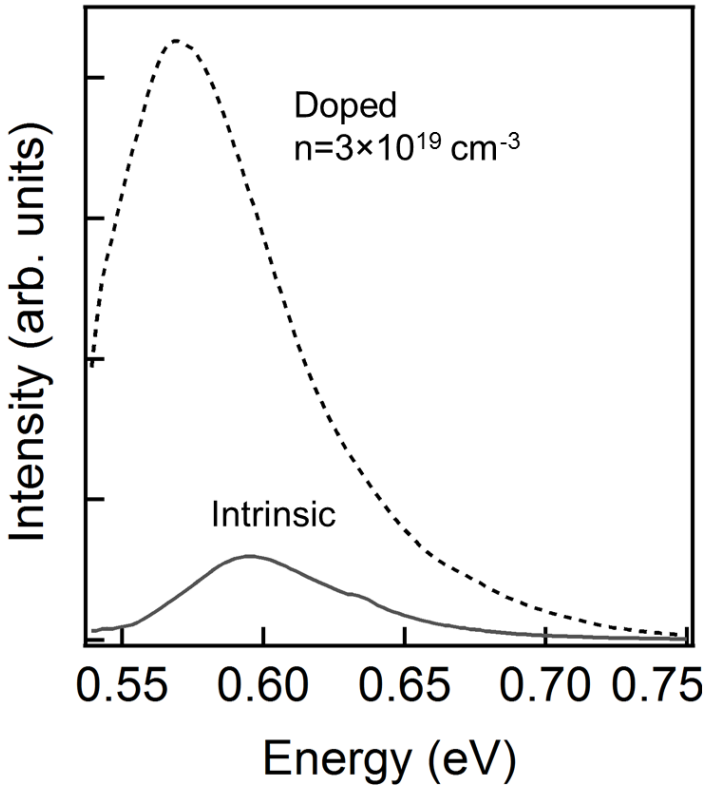

Figure 49 - PL plots of intrinsic and phosphorus doped 6 % Sn alloy showing the optimized the emission intensity in the doped $Ge_{0.94}Sn_{0.06}$ alloy. The intensity of the in the *n*-type material is ~10 times higher than that for the as grown intrinsic counterpart representing a significant improvement in sample performance.

Figure 50 shows PL peaks of several *n*-type alloys containing 4.5%, 7% and 9 % Sn and doped with P atoms at ~ $3x10^{19}$ cm^{-3} active carrier concentrations. The maxima of all curves have been normalized to facilitate comparison between films with different thicknesses. The peaks are distinct, well-resolved and by far more intense relative to intrinsic analogs (not shown) that were measured using the same protocols. These observations further validate the point that *n*-type GeSn alloys possess enhanced emission capabilities and these materials are uniquely suited to be employed as requisite active components for the manufacturing of light emitters based on GeSn. The band gap energies from *n*-type $Ge_{1-y}Sn_y$ samples are extracted from PL spectra measured using both the InGaAs and PbS

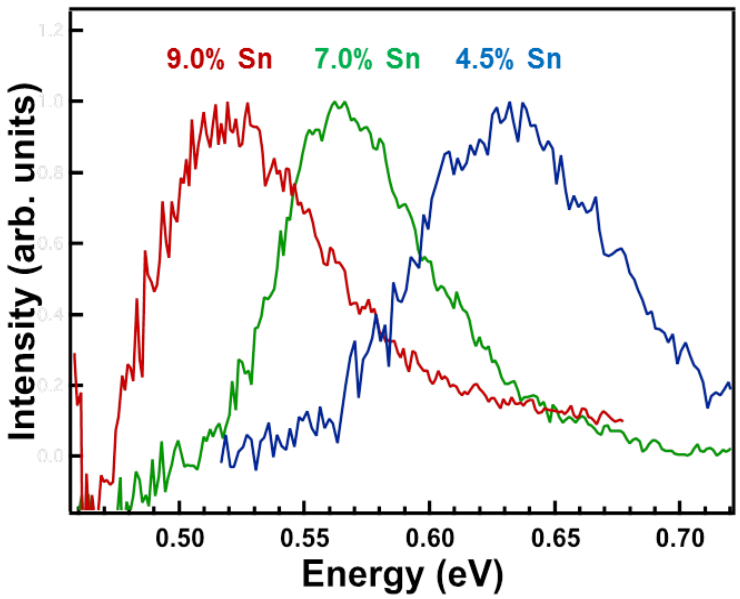

Figure 50 - Normalized PL spectra of n-type $Ge_{1-y}Sn_y$ (n~1-3x10^{19} cm^{-3}) samples with y= 0.04, 0.07 and 0.09 recorded at room temperature using a PbS detector. The latter enables full spectral resolution of the PL peaks at this range of Sn compositions and P doping levels allowing an unambiguous determination of the band gap energies.

detectors (the latter detector was employed for measuring emission in the 2300-2700 nm spectral range) following the fitting procedure applied previously for the intrinsic analogs. The direct and indirect gaps (circles and squares, respectively) are plotted in Figure 51 and compared with the corresponding gaps of the intrinsic samples. The compositions of all films described in the plots straddle the range for practical band gap engineering beyond Ge into the mid IR from 0.8 eV down to 0.45 eV at 11 % Sn. The active carrier concentrations are found to be in range of 0.8-3 x $10^{19}/cm^3$ as indicated by the color coded bar in the inset of the Figure 51. It is apparent from the plots that both the direct and indirect band gap energies are lower than those of intrinsic alloys with the same Sn content. This renormalization effect is due to the incorporation of phosphorous donor atoms in the lattice.[211] As expected there is significant noise in the indirect gap values, however in the

case of the direct gap the energy redshift trend is clearly apparent and seems to be independent of composition over the entire range up to 9.5 % Sn.

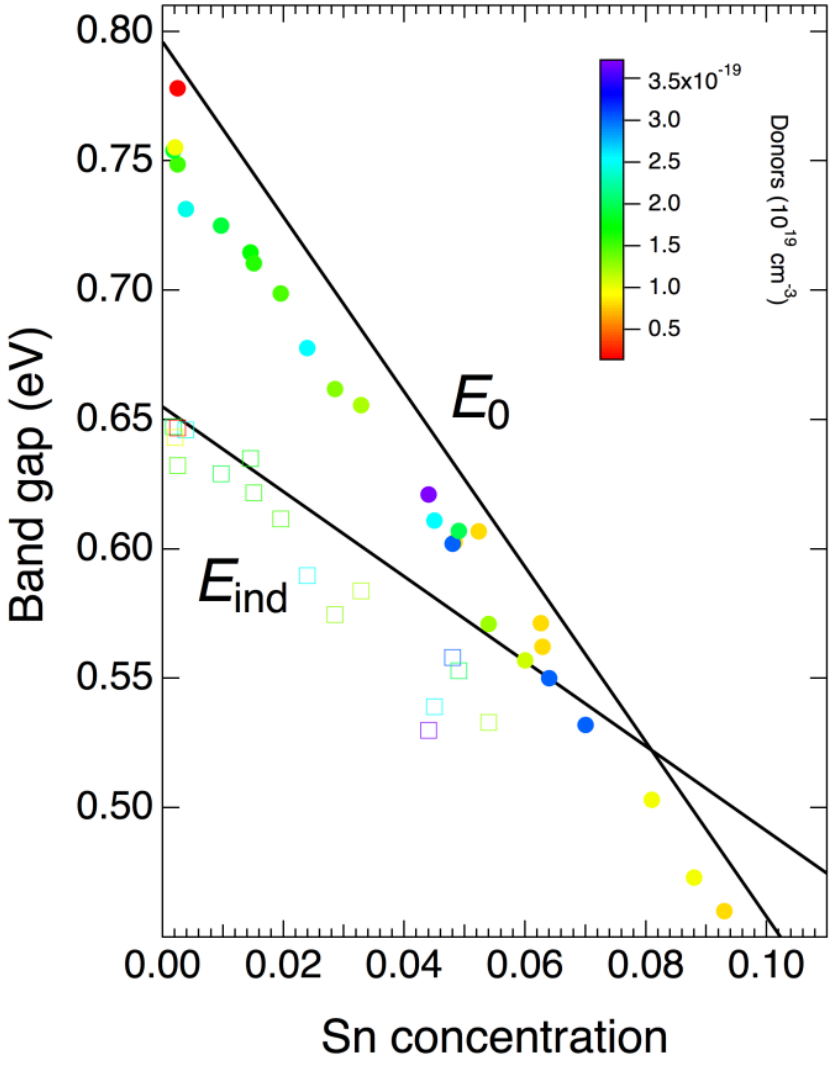

Figure 51 - Direct and indirect band gaps extracted from fits of the PL spectra of phosphorus doped alloys. The color code indicates the carrier density in these materials. The solid lines are fits of the direct and indirect gaps for intrinsic samples. The trends reveal a systematic redshift of the emission energies between doped and intrinsic materials with same compositions. This outcome is attributed to band gap renormalization effects due to the phosphorus doping. The band gap renormalization energies is similar (in Ge based materials) for both direct and indirect transitions in the doped samples therefore direct crossover point should not be strongly affected by doping.

6. Group V Silyl Compounds for Doping of GeSn Alloys

In this study we expanded the single source doping strategy beyond $P(GeH_3)_3$ to examine the use of the analogous -SiH_3 precursors $P(SiH_3)_3$ and $As(SiH_3)_3$ as low-temperature high-efficiency delivery agents of donor atoms into the group IV lattice.

6.1. Trisilylphosphine Source

The $P(SiH_3)_3$ compound is potentially a more practical CVD source than $P(GeH_3)_3$ for scalable semiconductor processing due to its superior volatility (22 Torr vs. 2 Torr at 22 ^oC) and enhanced thermal stability in comparison to $(PGeH_3)_3$. With regards to the latter we see no indication of decomposition or degradation of the molecule when it is stored under inert conditions for several months at room temperature.

The viability of using $P(SiH_3)_3$ as a doping agent was initially investigated producing samples in the same composition range as for the $P(GeH_3)_3$ case (i.e. $y \approx 0.04$-0.08). The growths were conducted using precursor mixtures with compositions similar to those described earlier. These samples show maximum doping concentration of $3x10^{19}/cm^3$, indicating that the $P(SiH_3)_3$ compound does not show a decrease in efficiency as a dopant delivery agent when compared to $P(GeH_3)_3$. Furthermore, the PL energies and emission intensities of the corresponding samples were measured to be similar within the uncertainty of the technique to those found in films produced via $P(GeH_3)_3$ indicating the presence of -SiH_3 or -GeH_3 functionalities in the dopant compound does not significantly influence the course of the growth process or the properties of the final product. For example samples with composition $Ge_{0.96}Sn_{0.04}$ produced using $P(GeH_3)_3$ and $P(SiH_3)_3$ exhibited nearly identical direct band gap energies at ~ 0.62 eV and similar PL intensities in the range of ~ 1400-1600 μV. The film morphology, crystal quality and final thicknesses were also

comparable in all films obtained using these approaches. The absolute P and Si concentration in films grown by $P(SiH_3)_3$ were measured by SIMS using reference standards and were found to be essentially equal at ~ 2-3 $x10^{19}$. This value is consistent with the above mentioned donor carrier densities measured by ellipsometry ($3x10^{19}/cm^3$) indicating that the P atoms in the material are fully activated. The dopant profile obtained by SIMS for P within the samples proves to be flat, in common with the samples obtained using the germyl analog. An example of elemental profiles obtained from SIMS is given in Figure 52. From these results, it can be concluded that the $P(SiH_3)_3$ is a viable substitute for doping of GeSn alloys at low temperatures.

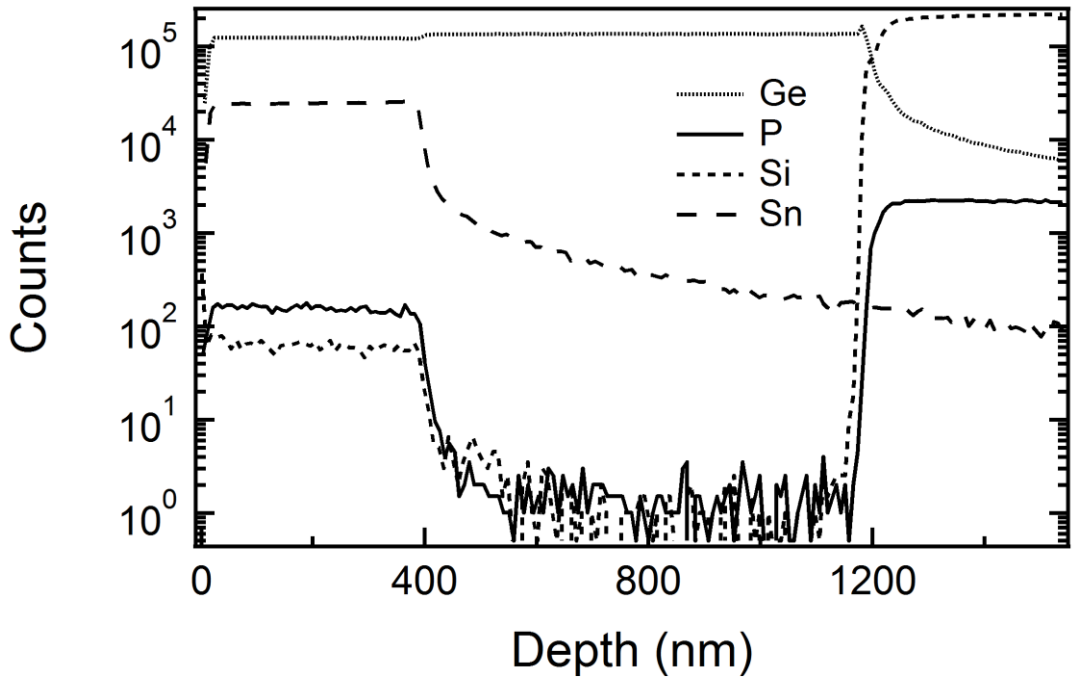

Figure 52 – Elemental profiles of Ge, P, Si and Sn obtained from a 400 nm thick $Ge_{0.95}Sn_{0.05}$ alloy film deposited on Ge/Si(100). The absolute amounts of P and Si obtained by comparison with an implant standard are 1.5×10^{19} cm^{-3} and 2.0×10^{19} cm^{-3} respectively. The former is within error equal to the carrier concentration of 2.0×10^{19} obtained from IRSE.

6.2. Trisilylarsine Source

For applications such as *n*-channel MOSFETs, higher active carrier concentrations than can be achieved with either P compound are required. As a potential solution for this requirement, we were able to obtain $Ge_{0.96}Sn_{0.04}$ samples doped by $As(SiH_3)_3$ that exhibit significantly higher active carrier densities of $7x10^{19}$ /cm^3 compared to the P analogs with similar thickness. These densities were determined by the Hall method and corroborated using spectroscopic ellipsometry modeling of the dielectric function. The SIMS measurements of these samples indicated that the absolute As content is fully activated within the error of the analysis as in the case of the $P(SiH_3)_3$ doped materials above.

In the case of the $As(SiH_3)_3$ doped films the PL spectra showed significantly higher peak intensities than those of the $P(SiH_3)_3$/$P(GeH_3)_3$ doped analogs as expected due to the two fold increase of the free carriers. This is illustrated in Figure 53 which compares the spectra of two representative samples with the same average $Ge_{0.96}Si_{0.04}$ composition containing $3x10^{19}$/cm^3 P and $7x10^{19}$/cm^3 As donor atoms. The peak intensity of the latter is nearly double to that of the former while the corresponding peak emission energies are very similar. Since band filling effects push this maximum to higher energies, the result implies a larger band gap renormalization for the n =$7x10^{19}$/cm^3 sample, as expected. The ability of the $As(SiH_3)_3$ to introduce larger amounts of dopant atoms in the GeSn lattice may be attributed to the higher reactivity of the delivery compound. Another factor may be the larger size of the As atom which is similar to that of the bulk Ge constituents, allowing a more facile incorporation into substitutional positions relative to the smaller P counterpart.[214] As mentioned in Chapter 4, similar behavior was observed when doping Ge with As compared to P, where higher active carrier concentrations could be obtained using

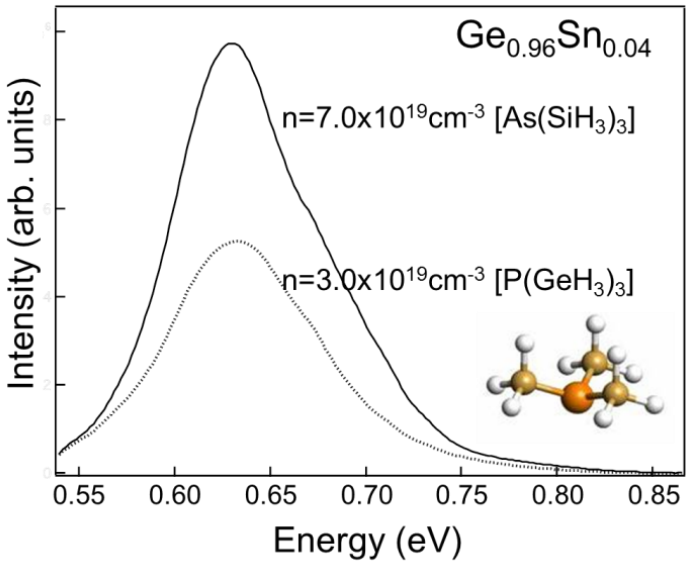

Figure 53 - Room temperature PL spectra of *n*-type $Ge_{0.96}Si_{0.04}$ grown by $P(GeH_3)_3$ and $As(SiH_3)_3$. The plots show a significant enhancement in the emission intensity with increasing carrier concentration.

the former donor. Lastly it is worth noting that the $As(SiH_3)_3$ molecule possesses comparable volatility to $P(GeH_3)_3$ but significantly enhanced thermal stability making it more viable for widespread CVD use. Again in this case liquid bulk samples do not decompose when kept under inert conditions at room temperature for prolonged time periods. These results indicate that both $P(SiH_3)_3$ and $As(SiH_3)_3$ may offer significant advantages over $P(GeH_3)_3$ for activation of Ge based semiconductors. In this regard, it is important to note that the co-doping with Si atoms furnished by the highly reactive $-SiH_3$ ligands remains low for both precursors. As in the case of P descried in the previous section, SIMS measurements were used to verify the Si contents in the As doped films, and the concentrations are found to be close to that of the donor atom.

To account for the fact that the P/Si and As/Si ratios are nearly unity (within error) in all doped alloys we propose that the $M(SiH_3)_3$ (M=As,P) precursors decompose under the

deposition conditions to eliminate volatile and relatively stable SiH_4 or Si_2H_6 molecules, which are then pumped away and therefore do not participate in the growth, and highly reactive As-Si-H intermediates that remain adsorb on the growth surface and eventually incorporate intact M-Si units into the films as shown by the equations below.

$$M(SiH_3)_3 \rightarrow Si_2H_6 + M\text{-}Si + 3/2H_2 \quad (6.3)$$

$$M(SiH_3)_3 \rightarrow 2SiH_4 + M\text{-}Si + 1/2\ H_2 \quad (6.4)$$

Due to the low level of co-doping, the basic properties of the parent lattice do not change in any significant fashion with the incorporation of Si. This is especially important in direct gap alloys, where incorporation of large amounts (several percent) of Si will increase the indirect-direct crossover composition.[210]

For doping of Ge described in Chapter 4, Sb proved a superior donor to both P and As in terms of achieving high carrier concentration and record low resistivities. Therefore preliminary investigations were conducted in order to determine the possibility of using Sb as a donor for doping GeSn in order to achieve similar advantages. It was found that $Sb(SiH_3)_3$ source could be used as a doping agent to incorporate active Sb donors up to levels of 5×10^{18} cm^{-3}. However, when attempting to achieve higher carrier concentrations, segregation of the Sb to the surface of the alloy film was observed in the RBS spectra of the resultant films. While it is possible that this phenomenon can be circumvented by using growth conditions more compatible with Sb incorporation such as lower temperatures, from earlier investigations on doping of Ge it is evident that the SbD_3 precursor provides a more facile route for incorporating Sb into the Ge lattice. It was found that donor levels of 2×10^{19} cm^{-3} can be readily incorporated without any process optimization using the latter

precursor. In addition, the deposition was conducted at 273°C, and the Sn content of the resultant epilayer was 12.5%. Therefore it can be concluded that SbD_3 presents a viable doping agent for high Sn content alloys deposited at ultra-low temperatures. Further investigations are necessary to optimize the deposition methods involved, but based current results the prospects for obtaining heavily Sb doped GeSn alloys with direct gap compositions suitable for laser applications is promising.

7. Summary and Conclusions

The large thickness, low dislocation density and largely relaxed microstructure of GeSn alloys deposited on virtual Ge substrates make them ideal candidates for band gap determination via PL studies. This is due to the strong emission signal from such alloys where contributions from both direct and indirect gap recombinations are present in the same spectrum, and can be easily resolved. In the work described in this chapter, factors leading to the enhanced emission intensity were identified, and the direct and indirect bandgaps were measured for alloys with a wide range of compositions. This data was used for determination of the indirect-direct crossover composition of the $Ge_{1-y}Sn_y$ alloy system.

Furthermore, the work described in this chapter presents *n*-type doping of $Ge_{1-y}Sn_y$ alloys, which can further enhance emission intensity. The doping was carried out using both established doping agents such as $P(GeH_3)_3$, as well as novel precursors such as $M(SiH_3)_3$ (M=P, As, Sb) and SbD_3, to obtain carrier concentrations of up to 7×10^{19} cm^{-3}. The heavy *n*-type doping results in an order of magnitude or greater enhancement in PL intensity in the doped samples compared to intrinsic analogs. This presents a pathway for obtaining direct gap behavior in $Ge_{1-y}Sn_y$ alloys at modest Sn contents below the indirect-direct

crossover composition. Indeed, stimulated emission has been observed in optically pumped waveguides fabricated using *n*-type doped material described in this chapter in experiments conducted at the University of Dayton.[81] While such preliminary results are encouraging, future work focused at identifying the optimum precursor for doping $Ge_{1-y}Sn_y$ alloys at target direct-gap compositions can be expected yield further improvement in optical performance.

The Si containing doping agents were found to incorporate only doping levels of Si into the GeSn alloy. This prevents the indirect-direct crossover occurring at higher Sn contents, as has been observed for GeSiSn alloys with high silicon concentrations.[210] Therefore they represent a commercially viable option for *n*-type doping GeSn at low temperatures, due to their higher thermal stability and greater volatility than previously used group V germyl compounds.[139]

Finally, the excellent crystal quality of the doped alloys produced above paves the way to their being used as platforms for further depositions. In Chapter 7, a series of *pin* diodes were fabricated in which all the device components are made up of GeSn alloys. The *n*-type doped bottom contact layers in these devices were fabricated using the methods outlined above. In addition, temperature programmed growth techniques developed in Chapter 7 for fabrication of thick (~500 nm) $Ge_{1-y}Sn_y$ alloys with compositions $y>0.10$ were used in conjunction with the $P(SiH_3)_3$ doping agent introduced here to synthesize *pn* junction diodes with direct gap compositions. These results, described in greater detail in Chapter 7, prove the practical utility of the synthetic methods developed above.

CHAPTER SEVEN

Growth of GeSn Based Diode Structures and Enhancing Device Performance by Regulation of Microstructure

Synopsis

In order to employ GeSn in optoelectronic applications, electrically injected light emission devices must be produced. Strong PL observed from GeSn alloys deposited on Ge buffered Si indicate that the optical properties of this platform should be suitable for developing GeSn based LEDs. The deposition methods based on SnD_4 and high order Ge hydrides was used to produce diodes of an *n*-Ge/*i*-$Ge_{1-y}Sn_y$/*p*-$Ge_{1-z}Sn_z$ design which exhibit strong, tunable EL over the wavelength range 1550 - 2700 nm and beyond. Correlation of the microstructure of these devices with their respective EL intensities led to an optimized *n*-$Ge_{1-x}Sn_x$/*i*-$Ge_{1-y}Sn_y$/*p*-$Ge_{1-z}Sn_z$ design which exhibits enhanced emission efficiency by eliminating interface defects. Finally, GeSn diodes with a *pn* junction design that acts as the fundamental component of an electrically injected GeSn laser were fabricated, in order to practically demonstrate the light emission capability of such devices.

Portions of this chapter were reprinted from Gallagher, J. D.; Senaratne, C. L.; Xu, C.; Sims, P.; Aoki, T.; Smith, D. J.; Menéndez, J.; Kouvetakis, J. Non-radiative Recombination in $Ge_{1-y}Sn_y$ Light Emitting Diodes: The Role of Strain Relaxation in Tuned Heterostructure Designs. *J. Appl. Phys.* **2015**, *117* (24), 245704 with the permission of AIP Publishing.

Portions of this chapter have been reproduced with permission from Senaratne, C. L.; Gallagher, J. D.; Xu, C.; Sims, P.; Menendez, J.; Kouvetakis, J. Doping of Direct Gap

$Ge_{1-y}Sn_y$ Alloys to Attain Electroluminescence and Enhanced Photoluminescence. *ECS Trans.* **2015**, *69* (14), 157. Copyright 2015, The Electrochemical Society.

1. Introduction

The design and fabrication of electrically injected devices on Si platforms has attracted considerable research attention in recent years due to potential applications in monolithic integration of group IV photonics with Si electronics at CMOS-compatible conditions. Recently, the lasing viability of a pseudo direct Ge-on-Si system was demonstrated.[10,11] In this case the Ge active layer was driven toward direct-gap conditions via application of tensile strain and heavy ($n > 10^{19}$ cm^3) *n*-type doping. The main limitation of this device type is the free-carrier absorption associated with the dopants. Furthermore, attaining high levels of tensile strain in Ge requires high growth/annealing temperatures, which may be incompatible with CMOS processing. An attractive alternative to overcome the limitations of pure Ge methods is the GeSn alloy system, in which the direct-indirect band gap difference in the material can be adjusted via compositional tuning, thus reducing and or eliminating the need for *n*-type doping and tensile strain.[26,215] As described in the previous chapter, an indirect-to-direct transition occurs at ~9% Sn in the GeSn alloy system.[213] This crossover threshold is lower than early predictions, raising hopes for laser devices with emission at wavelengths of 2400 nm and beyond.[213,216] These expectations are further supported by the recent demonstration of lasing in optically pumped GeSn devices.[23]

The first step to an electrically injected device using GeSn alloys is the creation of working photodiodes. Prototype *pin* structures in heterostructure geometry were initially introduced by Mathews *et al.* in 2009 using $Ge_{0.98}Sn_{0.02}$ active layers grown directly on *p*-type

Si(100).[20] These devices were shown to exhibit enhanced responsivities, tunable absorption edges and an extended IR coverage beyond that of Ge into the mid IR. A direct-gap EL signal was also reported, clearly demonstrating the laser potential of this class of materials.[68] A key to the successful fabrication of such GeSn/Si devices was the substantial progress achieved in suppressing the island-like growth of Ge-like materials on Si substrates. However, the resulting Ge(Sn)-Si interface is still severely defected and represents a primary concern for the operation of light-emitting devices due to its extremely high recombination velocity approaching 1 km/s, as shown by recent studies.[217]

A route to achieving improved emission is via the use of a Ge buffer layer. This introduces a separation between the active device component containing the carriers and the defected Ge/Si interface due to the type I band alignment between Ge and GeSn. The effectiveness of this method is clearly demonstrated in the studies described in the previous chapter, where GeSn alloys deposited on Ge/Si substrates display an order of magnitude enhancement in PL intensity compared to analogous material deposited directly on Si. The same concept underlies the development of new generations of GeSn diodes exhibiting EL.[69,71,73] These devices were fabricated in *pin* or *pn* geometries grown fully-strained on Ge or Ge-buffered Si substrates by MBE methods. The Sn concentrations of the active regions varied between studies from 2% to 8%, while the layer thickness in all cases were kept below 300 nm. Similar results were presented more recently based on commercially-grown CVD samples containing 6 and 8% Sn.[72] In this case the synthetic procedures were not disclosed and pertinent film parameters including strain and microstructure were not made available or applied to interpret the outcomes. Nevertheless, these prior studies are

highly encouraging and indicate that the fabrication of practical light emitting diodes with tunable response in the mid IR is within reach.

The compressive stress in fully-strained GeSn layers on relaxed Ge buffers raises the crossover concentration from indirect to direct gap material to $y_c \sim 0.2$, (Ref. 211) which is undesirable from a device perspective. On the other hand, the emission efficiency improvement –in the form of PL– in $Ge_{1-y}Sn_y$/Ge structures relative to $Ge_{1-y}Sn_y$/Si analogs is observed even when substantial strain relaxation has taken place at the $Ge_{1-y}Sn_y$/Ge interface, as described in the previous chapter. This initially suggests that the defects associated with such relaxation which are observed at the $Ge_{1-y}Sn_y$/Ge interface have a relatively benign impact on the emission properties, so that the use of Ge buffer layers might represent an acceptable compromise to achieve good quality emission from relaxed GeSn layers. In contrast to the single defected interface in the above stacks, strain relaxed GeSn devices reported in literature which employ Ge cladding layers as *p*- and *n*- type contacts contain two defected Ge/GeSn interfaces. The increased defectivity of such a structure may compromise the optical performance of when used for fabrication of LEDs. In view of this, the growth of a novel *n*-Ge/*i*-$Ge_{1-y}Sn_y$/*p*-$Ge_{1-z}Sn_z$ (as depicted in Figure 54) design was pursued here, in which the composition of the top *p*-type contact layer (*z*) is tuned such that it grows pseudomorphic to the intrinsic layer, thereby creating a device stack with only one defected interface. The growth of these diode structures, which span the concentration range y=0.02-0.137, is described in Sections 2.1 – 2.3 of this chapter. Given that the indirect-direct crossover composition was determined to be y_c=0.087 using PL measurements,[213] these represent the first report of GeSn diodes with direct gap compositions.

The microstructure of these *n*-Ge/*i*-$Ge_{1-y}Sn_y$/*p*-$Ge_{1-z}Sn_z$ devices (described in Section 2.5), can be correlated to the electroluminescence efficiency, as presented in Reference 82. It was observed that when strain relaxation defects are present at the GeSn/Ge interface, the EL efficiency of the diodes decreases relative to devices with the same architecture but with a non-defected GeSn/Ge interface. This analysis leads to the conclusion that even a single defected interface has a detrimental effect on emission by increasing the non-radiative recombination rates. A possible solution to this issue is the use of *n*-type doped GeSn layers as the bottom contact. The experimental methods required for the deposition of thick, strain relaxed, *n*-type GeSn alloys suitable for this purpose was described in the previous chapter. In an *n*-$Ge_{1-x}Sn_x$/*i*-$Ge_{1-y}Sn_y$/*p*-$Ge_{1-z}Sn_z$ diode structure (shown in Figure 55), tuning the bottom contact layer composition (x) to closely match the active layer composition (y) can minimize the lattice mismatch between the two layers and prevents strain relaxation. This additional design flexibility allows for the fabrication of fully pseudomorphic, low strain structures even at high Sn concentrations, and can be used to

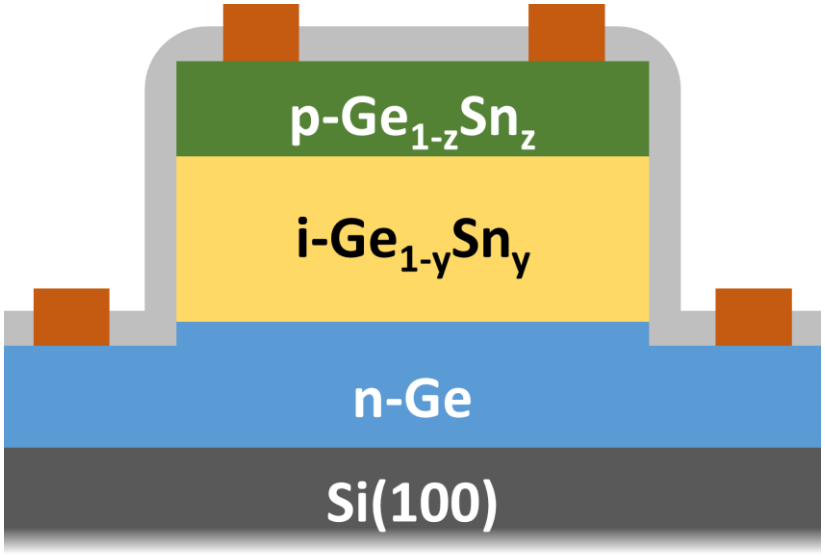

Figure 54 – Schematic of *n*-Ge/*i*-$Ge_{1-y}Sn_y$/*p*-$Ge_{1-z}Sn_z$ device depicting the active layer deposited on *n*-doped Ge and capped by a *p*-type doped GeSn layer

carry out a detailed and systematic study of the effect of the interface defects on the emission properties of the diodes. The growth procedures for producing devices for this purpose are described in Section 3, together with the properties of the resultant device stacks. It was found that the mitigation of strain relaxation between the *n*, *i* and *p* device components and the resultant elimination of misfit defects substantially enhances EL performance. Furthermore, the injection-current dependence of the electroluminescence signal in these devices was studied, which yields the recombination lifetimes for all structures and provides compelling evidence that eliminating strain relaxation at the device interfaces is critical to achieving high-efficiency GeSn light-emitting diodes.

The ultimate aim of research into GeSn light emitters is the fabrication of an electrically pumped laser diode monolithically integrated with Si. Based on the work described thus far in this thesis, it was possible to develop deposition methods for thick, strain relaxed GeSn films with Sn compositions above the indirect-direct crossover suitable for this

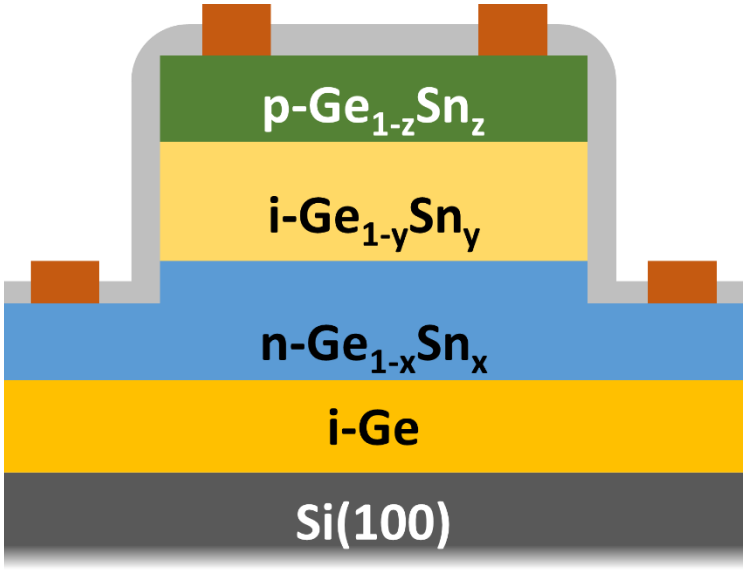

Figure 55 – Device schematic for the *n*-$Ge_{1-x}Sn_x$/*i*-$Ge_{1-y}Sn_y$/*p*-$Ge_{1-z}Sn_z$ architecture

purpose. In addition, the doping techniques were developed that can provide degenerate *n*- and *p*-type doping which is essential for achieving population inversion via electrical pumping.[24] A laser diode based on GeSn has several fundamental advantages. First, the true direct gap nature of a GeSn alloy can reduce or eliminate the requirement for heavy *n*-type doping, minimizing free carrier absorption seen in aforementioned Ge lasers. Second, tensile strain is not necessary in order to obtain direct gap conditions, thereby removing the CMOS incompatible annealing procedure from the fabrication process. As an additional advantage GeSn alloys offer the ability to tune the wavelength into the mid-IR, allowing access to wavelengths that cannot be reached with pure Ge. In Section 6 of this chapter, the growth techniques developed thus far are combined to produce prototype *pn* junction devices spanning the indirect-direct crossover composition regime. A schematic of such a device is shown in Figure 56. These LEDs exhibit EL, demonstrating the emission viability of this class of devices for the first time, and can be considered as a prelude to fabricating an electrically injected laser using GeSn. In Reference 84 an analysis of the EL from the various *pn* heterostructures described here is presented. The ability to precisely tune the doping and composition of the device components allows the study of EL for devices with a wide variety of parameters in the *p* and *n* device components. This work serves to expand the fundamental understanding of factors affecting the emission performance of quasi-direct light emitting devices.

The remainder of this chapter is organized as follows. In Section 2, the growth and properties of diodes with the *n*-Ge/*i*-$Ge_{1-y}Sn_y$/*p*-$Ge_{1-z}Sn_z$ design is described. Section 3 describes the *n*-$Ge_{1-x}Sn_x$/*i*-$Ge_{1-y}Sn_y$/*p*-$Ge_{1-z}Sn_z$ diode architecture, whereas Section 4 presents the study of *n*-$Ge_{1-y}Sn_y$/*p*-$Ge_{1-z}Sn_z$ diodes. Section 5 contains concluding remarks.

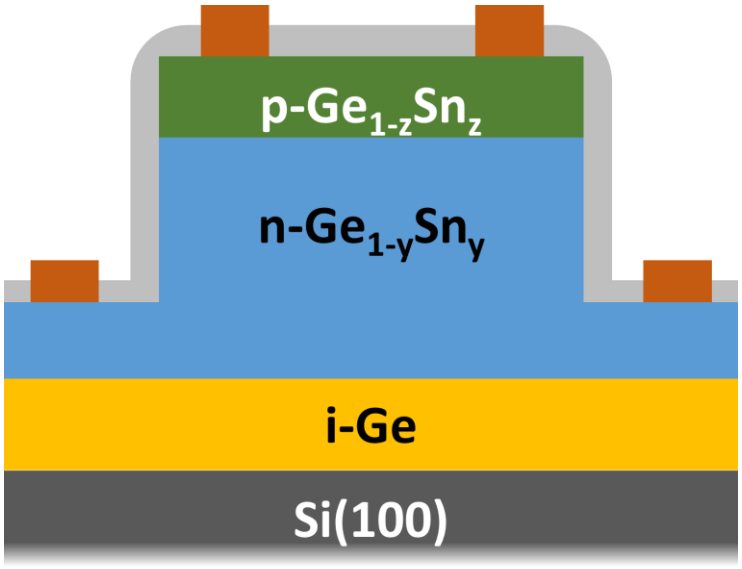

Figure 56 – Schematic of *p*-$Ge_{1-z}Sn_z$/*n*-$Ge_{1-y}Sn_y$ LED

2. Device Design: *n*-Ge/*i*-$Ge_{1-y}Sn_y$/*p*-$Ge_{1-z}Sn_z$ Diodes

In the initial experiments, diode structures with the *n*-Ge/*i*-$Ge_{1-y}Sn_y$/*p*-$Ge_{1-z}Sn_z$ architecture were produced with active layers ranging from y=0-0.137. The intrinsic GeSn alloys of the devices were deposited on Ge buffered Si substrates. The Ge buffer layer was *n*-type doped, and also used as the bottom contact of the diodes. The devices were completed by depositing a layer of *p*-doped $Ge_{1-z}Sn_z$ on top of the intrinsic layer. For active layer compositions of y<0.05, the top layer composition (z) was the approximately equal to the active layer. For later devices with y=0.07-0.137, the devices were optimized by maximizing carrier confinement in the active layer which increases the external quantum efficiency. This was achieved by choosing the top layer composition to be z<y, which has the additional advantage of minimizing the reabsorption of the light emitted from the active area of the device.

2.1. Buffer Layer Growth

The Ge buffer layers were produced by following the methods first described by Xu *et al*, which were also used for the growth of Ge buffered Si substrates employed in Chapters 5 and 6.[77] In brief, a mixture of Ge_4H_{10} and $P(GeH_3)_3$ with H_2 as carrier gas was used to deposit micron thick layers of Ge on Si(100) substrates using a GSME reactor. Commercially purchased 4-inch Si wafers were subjected to RCA cleaning prior to use as substrates. In addition, the surface was treated with a HF/Methanol solution immediately before loading the wafers into the growth chamber. As a final cleaning step, the wafer was flashed at 800°C at a pressure of 10^{-9} Torr.

During the deposition, a 1:50 ratio of P:Ge atoms in the gaseous precursor mixture yields films with active carrier concentrations of ~2×10^{19} cm^{-3}. After deposition, which was conducted at ~350°C under a pressure of 10^{-4} Torr, the Ge layers were annealed at 650°C for three cycles each of 1 min duration. This significantly improves the crystallinity and minimizes the threading dislocation density, thereby producing more suitable virtual substrates on which further growth can be conducted. Therefore the final doped Ge buffer layers, which have thicknesses of 800-1500 nm, have the same high degree of crystalline quality as the intrinsic Ge buffer layers used for the depositions described in Chapters 5 and 6. The annealing step also introduces tensile strain in the Ge as a result of the thermal expansion mismatch between Ge and Si. This is advantageous in that it allows alloys with larger lattice parameters than Ge to be grown on these buffer layers, while avoiding strain relaxation in the heterostructure design. The resultant microstructure and its effect on diode performance will be described in detail in later sections.

2.2. Growth of Active $Ge_{1-y}Sn_y$ Layers (y=0.02-0.137)

In the PL studies described in the previous chapters, it was found that alloy films with thicknesses of 300 nm or greater are best suited in order to successfully obtain strong emission with clearly resolved direct and indirect band edges. This is due to the large volume fraction of material away from the defected interface in thicker films. The same principle applies to electroluminescence measurements. The methods described in Chapter 5 to grow films with compositions up to y=0.11 proved a starting point for the growth of similar thick films for the purpose of fabricating devices. Since these procedures were described in detail earlier, only a brief description will be provided here. However, further refinements that were necessary in order to improve the materials quality to the high standards required to produce functional diodes will be emphasized.

For deposition of the intrinsic layers, the *n*-type doped virtual Ge substrates described above were cleaned into quadrants and cleaned with HF/H_2O. In addition, the surfaces were subjected to an additional *in-situ* cleaning step by flowing 5% Ge_2H_6/H_2 at a pressure of 30 mTorr prior to growth. For the device containing the y=0.02 active layer, growth was conducted using a Ge_2H_6 and SnD_4 precursor mixture. The deposition temperature was 335°C. When pursuing higher Sn alloys for device fabrication purposes, the use of Ge_3H_8 in place of Ge_2H_6 proved beneficial in obtaining thick films at low temperatures by enhancing the growth rates. The y=0.05-0.07 range of compositions were achieved using Ge_3H_8/SnD_4 mixtures under temperatures of 315-305°C. The target Sn compositions in the films was achieved by tuning the Ge_3H_8/SnD_4 ratio in the precursor mixture.

When depositing films with higher Sn concentrations, it was found that the structural quality of the stack could be further improved by growing a Ge 'spacer' layer on the wafer surface using Ge_3H_8. This refreshing layer deposition was conducted at 340°C for ~25 min. Thereafter continuous flow of Ge_3H_8 was maintained while the chamber cooled to the low temperatures required for GeSn deposition. This procedure yields Ge spacers ~150 nm thick.

The deposition of the active layer alloys with higher Sn contents was conducted at temperatures from 295°C for y=0.085, down to 283°C for y=0.11. The precursor mixtures were made with 22-27 LTorr of Ge_3H_8, and the amount of SnD_4 added was varied between 5-7 LTorr. Glass containers with a volume of 3 L was used for this purpose, and the precursors were finally diluted with of research grade H_2 to a pressure of ~750 Torr to complete the mixtures. Specific precursor amounts used for each composition are listed in Appendix A.

At temperatures near 280°C required for the growth of alloys with compositions y>0.10, the growth rates obtained could be further improved by following a two-stage temperature programmed approach. This method is in contrast to the single growth temperature used for the depositions reported thus far, and allows the growth of films with the necessary thickness to obtain strong emission. In this new procedure, the $Ge_{1-y}Sn_y$ layer deposition was initiated at a temperature known to be conducive for the growth of $Ge_{1-y}Sn_y$ layers of the target composition. For epilayers in the y=0.11-0.137 range, this corresponds to initiation temperatures from 280°C-270°C. Growth was allowed to proceed at this temperature for a period of ~50 min. This procedure is expected to create a strain relaxed

seed layer of $Ge_{1-y}Sn_y$ of the target composition, which provides a more facile template on which further growth can proceed. The low growth temperature ensures full substitutionality of the Sn atoms in this seed layer. Subsequently, the temperature was slowly increased by 5°C-10°C, which increases the growth rate. The growth was then allowed to complete at this higher temperature. A complete deposition requires ~150 min. By following this procedure, it was possible to obtain films of $Ge_{1-y}Sn_y$ in the target composition range (y=0.12 – 0.137), whilst preventing Sn surface segregation that accompanies $Ge_{1-y}Sn_y$ growth at high temperatures. The precise temperature ranges used are given in Appendix A, together with additional growth parameters.

In conclusion, the deposition protocols described above are capable of producing thick (>300 nm), strain relaxed, intrinsic $Ge_{1-y}Sn_y$ active layers that span the composition range y=0.02-0.137. This broad range allows the tuning of the emission of $Ge_{1-y}Sn_y$ alloys to be tuned beyond the 1550 nm of Ge to mid-IR wavelengths of 2700 nm and beyond. Also, it is possible to study the properties of the GeSn alloy system as an emitter material in practical LEDs from near Ge to compositions well above the indirect-direct crossover. These results are discussed in Section 2.7.

2.3. Growth of p-type Doped $Ge_{1-z}Sn_z$ Capping Layers

The deposition of the *p*-type top contact layer of the devices was carried out as a separate deposition after growing the intrinsic layer. Before completing the top layer, the *n-i* stacks resulting from the two previous steps were characterized using HRXRD and IRSE in order to confirm that the intrinsic layer had the required thickness and composition for an active layer of a *pin* diode. Prior to growth of the top contacts on the samples chosen based on

these criteria, the surfaces were cleaned using aqueous HF cleaning solution following a procedure identical to that used for the Ge buffer layers in the previous stage. Thereafter they were introduced into the growth chamber, and an additional surface clean was performed by flowing Ge_2H_6 over the surface. The chamber used for the *p*-layer depositions was a hot-wall CVD reactor which was heated using a three zone furnace, and therefore had a temperature profile suitable for pre-activating the doping precursor B_2H_6. The starting materials for depositing the $Ge_{1-z}Sn_z$ epilayer was provided by a Ge_2H_6 and SnD_4 precursor mixture. This mixture is fed into the growth chamber concomitantly with the B_2H_6/H_2 mixture used for doping using separate MFCs. The separation of the two mixtures prevents reaction between the different compounds prior to entry into the growth chamber. By adjusting the SnD_4/Ge_2H_6 ratios and the B_2H_6 concentrations, *p*-type layers with Sn contents z=0.02-0.10 which are doped in the 10^{19} cm^{-3} range were produced. The temperature range used was 345°C-295°C, and the resultant epilayers have thicknesses of 80-275 nm. These properties were elucidated by studying the completed *pin* device stacks via RBS, HRXRD and IRSE.

*2.4. Materials Properties of n-Ge/*i-*$Ge_{1-y}Sn_y$/p-$Ge_{1-z}Sn_z$ Device Stacks*

A representative RBS spectrum for a *n*-Ge/*i*-$Ge_{0.863}Sn_{0.137}$/*p*-$Ge_{0.92}Sn_{0.08}$ device stack is given in Figure 57. The RBS random spectrum, shown in the black trace, is modelled such that the contributions from the *p*, *i*, and *n* layers can be separated, giving the respective thicknesses and Sn contents. Furthermore, channeling experiments (red trace) indicate a high degree of crystalline alignment in the separate layers.

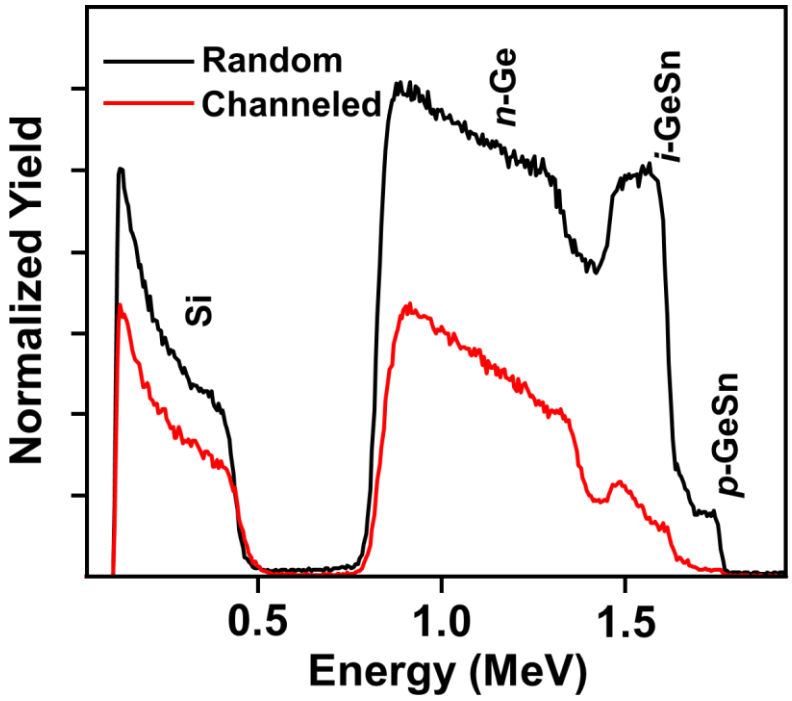

Figure 57 – RBS spectrum of a *n*-Ge/*i*-$Ge_{0.863}Sn_{0.137}$/*p*-$Ge_{0.92}Sn_{0.08}$ device. Contributions from the three device components in the random spectrum (black trace) can be separated based on the differences in Sn content. The Sn profiles also indicate uniform Sn distribution within the layers. The excellent channeling (red trace) indicates a high degree of crystalline perfection despite the high Sn content.

The device stacks were also subjected to HRXRD analysis. From (224) RSMs, the Sn contents of each layer can be corroborated by calculating the relaxed lattice parameter and determining the corresponding Sn content based on the relationship given in Reference 14. Figure 58 shows a sample HRXRD RSM for a *n*-Ge/*i*-$Ge_{0.87}Sn_{0.13}$/*p*-$Ge_{0.90}Sn_{0.10}$ device stack. The intrinsic layer exhibits a compressive strain of -0.522%, and is therefore 67% relaxed with respect to the *n*-Ge buffer. This strain relaxation is enabled by the formation of defects at the $Ge_{1-y}Sn_y$/Ge interface. A detailed account of the defect microstructure is presented in Section 2.5. The compressive strain on the top *p*-contact layer, however, is only -0.167%, which is a result of the growth of the latter on the intrinsic layer with a large in-plane lattice constant. The pseudomorphic nature of the *p*-type layer growth can be seen

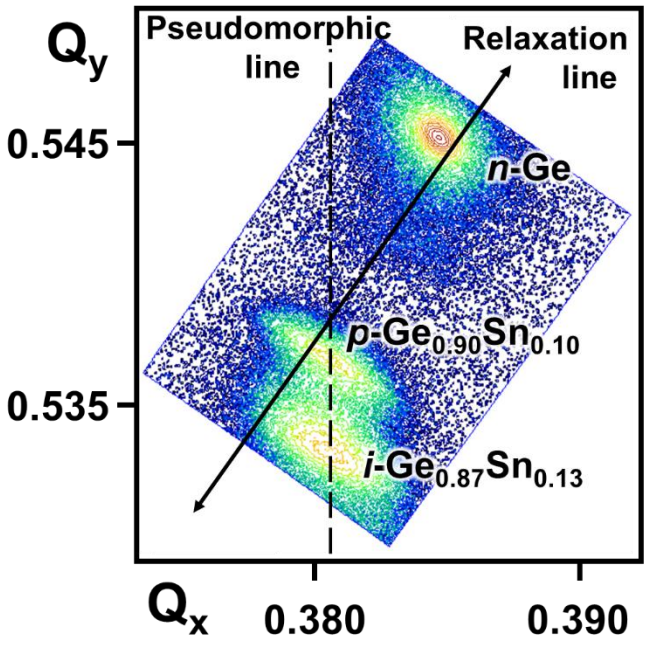

Figure 58 – The (224) RSM of a *n*-Ge/*i*-$Ge_{0.87}Sn_{0.13}$/*p*-$Ge_{0.90}Sn_{0.10}$ device structure exhibiting the strain relaxation of the active layer relative to the Ge buffer and the pseudomorphic growth of the top contact layer on the intrinsic layer.

from the vertical alignment of the two peaks and the close correspondence of the in-plane lattice parameters of the two layers (5.724 Å for the *p*-type layer and 5.725 Å for the intrinsic). The relative lack of stain relaxation between the intrinsic and *p*-type layers is the result of choosing the compositions such that *z* is close enough to *y* to allow lattice matched growth. This results in a microstructure where the top *i*-*p* interface is defect free. The strain features described above are common for all *n*-Ge/*i*-$Ge_{1-y}Sn_y$/*p*-$Ge_{1-z}Sn_z$ diodes fabricated in this study.

Finally, it must be noted that the *n*-Ge/*i*-$Ge_{0.87}Sn_{0.13}$/*p*-$Ge_{0.90}Sn_{0.10}$ and *n*-Ge/*i*-$Ge_{0.863}Sn_{0.137}$/*p*-$Ge_{0.92}Sn_{0.08}$ device stacks described in Figure 57 and Figure 58 above were deposited using the variable temperature growth method. The uniform Sn profiles in seen in the RBS spectra and the sharp, symmetric peaks obtained from HRXRD measurements

provide evidence that this novel approach does not result in any compositional inhomogeneity.

2.5. Microstructure of n-Ge/i-$Ge_{1-y}Sn_y$/p-$Ge_{1-z}Sn_z$ Device Stacks

As mentioned above, device structures produced using the deposition procedures described above have active layers which span in composition from near Ge up to GeSn alloys with direct gap Sn contents. Therefore they allow the study of the effect of increasing direct gap behavior on EL, as will be discussed in Section 4. However, another factor which must be considered together with the direct nature of the material when seeking to explain trends in EL is the defect microstructure of the material, which has a direct impact on non-radiative recombination processes. In this respect, the devices produced here have specimens ranging from samples where *n*, *i*, and *p* layers are fully pseudomorphic to each other, to samples where there is a large lattice mismatch between substrate and epilayer resulting in strain relaxation with concomitant defect formation.

Figure 59 presents the XTEM micrograph and (224) RSM of a device of the former category. Both intrinsic and *p*-type layers of the device have a composition of 2.0% Sn.

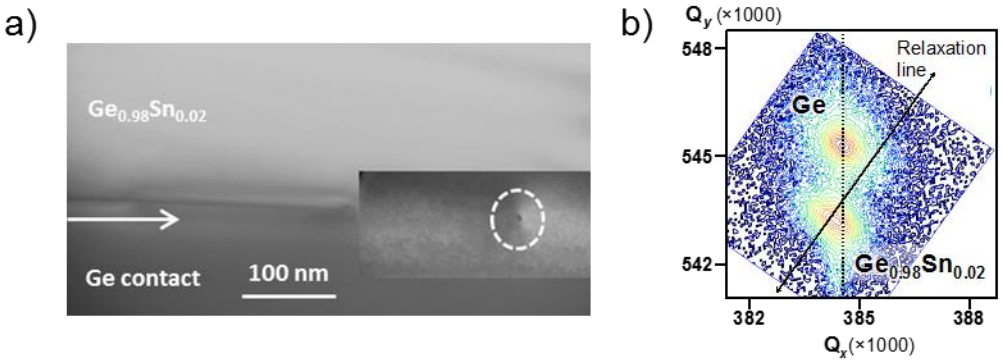

Figure 59 - (a) XTEM image of Ge/ $Ge_{0.98}Sn_{0.02}$ film. Inset contains a rare edge dislocation marked by a white circle. Reprinted with modification from Reference 83. (b) 224 XRD RSM for a $Ge_{0.98}Sn_{0.02}$ device showing that in this case all layers are fully coherent. Reprinted with modification from Reference 82.

Due to the fact that the *n*-Ge virtual substrates are under tensile strain, the in plane lattice parameter is larger than that of Ge. Therefore it is possible to grow a y=0.02 GeSn alloy which is essentially strain relaxed and lattice matched on this substrate. By using intrinsic and *p*-type doped alloys to complete a device structure of this composition, it is possible to avoid forming interfacial defects between the different device components. The XTEM micrograph in Figure 59 (a) was obtained from a JEOL 4000 EX microscope and illustrates the virtually defect free interface Ge buffer layer and the GeSn alloy obtained for the above device stack. The inset depicts a rare edge dislocation visible at the Ge/GeSn interface. The lack of strain relaxation is corroborated by the (224) RSM given in Figure 59 (b), in which the vertical alignment of the peaks indicate that the in-plane lattice parameters of the Ge and GeSn layers are nearly perfectly matched. Furthermore, the proximity of the GeSn peak to the relaxation line indicates that the epilayer is stain relaxed.

However, when the active layer contains larger amounts of Sn, the lattice mismatch becomes greater, and strain relaxation of the epilayer ensues, as seen in the (224) RSM of the *n*-Ge/*i*-$Ge_{0.87}Sn_{0.13}$/*p*-$Ge_{0.90}Sn_{0.10}$ stack given in Figure 58. The strain relaxation is accompanied by the formation of defects at the *n*-Ge/*i*-$Ge_{1-y}Sn_y$ interface. A detailed TEM analysis of different samples was carried out in order to fully characterize the types of defects that result from strain relaxation of the active layer. Common types of defect visible at the interface are short stacking faults originating at the $Ge_{1-y}Sn_y$/Ge interface and propagating into the buffer layer, and 60-degree dislocations. Figure 60 shows high resolution STEM bright field (BF) images of defected *n*-Ge/*i*-$Ge_{1-y}Sn_y$ interfaces that exhibit both type of defects. The dark contrast areas seen in Figure 60 (a) are short stacking faults that extend along the [111] direction and extend a short distance into the Ge buffer.

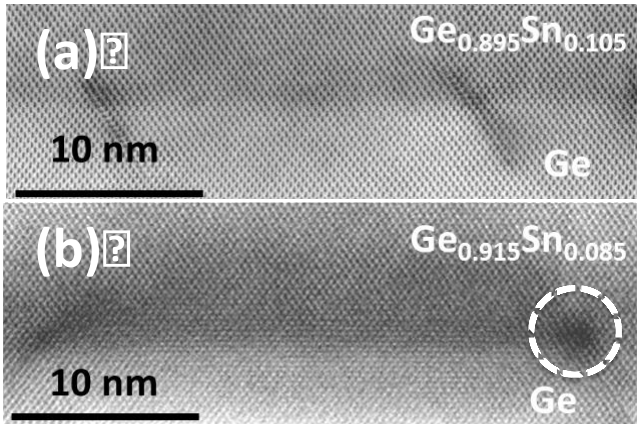

Figure 60 – High resolution STEM BF images of defected Ge/i-$Ge_{0.895}Sn_{0.105}$ and Ge/i-$Ge_{0.915}Sn_{0.085}$ interfaces are shown in panels (a) and (b), respectively. The images were acquired in an aberration-corrected JEOL ARM 200F microscope. The common defects in both cases are short stacking faults and 60º dislocations (dashed white circle) compensating the misfit strain between the bottom contact and the intrinsic layer of the devices. Reproduced with modification from Reference 82.

A similar feature seen on the left hand side of Figure 60 (b), but the defect on the right hand side marked by a dashed circle is a 60° dislocation. These images were obtained from *n*-Ge/*i*-$Ge_{0.895}Sn_{0.105}$ and *n*-Ge/*i*-$Ge_{0.915}Sn_{0.085}$ interfaces respectively. Another feature observed at the *n*-*i* interface is the intersection of the stacking faults within the Ge buffer. Such a feature is shown in Figure 61. Panel (a) of the figure shows the presence of an intersecting pair of stacking faults together with other edge type dislocations. Panel (b) is a close-up high resolution BF STEM micrograph of the above defect structure. The same type of behavior was observed in GeSn alloys grown on Ge buffered Si reported in Chapter 5, and also in the growth of SiGe on Si or Ge substrates.[188,218] The penetration of the defect into the buffer rather than the active layer is beneficial for optical performance of the device.

In contrast, the *p*-type top contact layer grows pseudomorphic to the active $Ge_{1-y}Sn_y$ layer, as mentioned earlier. Therefore no defect formation is observed at the *i*-*p* interface. This

feature is seen in the XSTEM micrograph given in Figure 62, which was obtained from a *p*-$Ge_{0.92}Sn_{0.08}$/*i*-$Ge_{0.863}Sn_{0.137}$/*n*-Ge device. The micrograph was collected using a JEOL ARM 200F microscope. Figure 62 a) shows the entire *n*-*i*-*p* device stack. The top surface is flat, and the medium angle annular dark field (MAADF) image allows the three device components to be identified based on contrast difference dependent on Sn content and strain differences in the constituent layers. The interfaces between the different layers are marked by arrows. Figure 62 b) and c) are high resolution bright field (BF) images of the top *i*-*p* interface and the bottom *n*-*i* interfaces, respectively. Typical 60° dislocations arising due to strain relaxation can be seen at the bottom interface, while the defect free nature of the top interface is also evident.

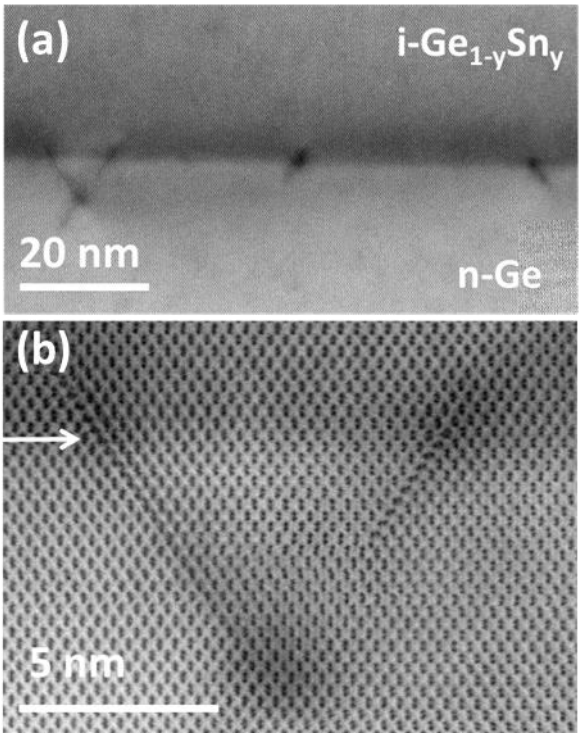

Figure 61 - XTEM images of the interface microstructure of a $Ge_{0.93}Sn_{0.07}$ device. (a) Micrograph of bottom *n*-*i* interface showing edge dislocations and short stacking faults appearing as dark contrast areas along the heterojunction. (c) Enlarged view of two stacking faults crossing down into the Ge buffer along distinct [111] directions. Reproduced with modification from Reference 83.

As mentioned earlier strain relaxation and concomitant defect generation are unavoidable in $Ge_{1-y}Sn_y$ alloys near the direct gap composition regime that have thicknesses far above the metastable strain relaxation limits determined in Chapter 5. Indeed minimization of compressive strain is essential to obtain direct gap behavior.[211] However, the presence of defects has a significant effect on EL performance, as described below in Section 2.7.

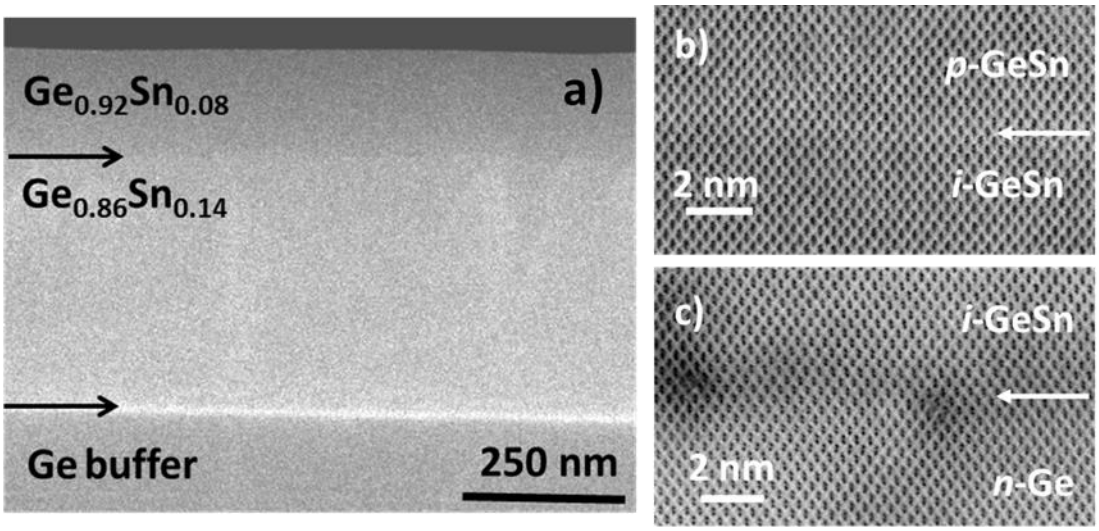

Figure 62 – a) XSTEM MAADF image of a *p*-*i*-*n* heterostructure device comprised of an *n*-Ge bottom contact, *i*-$Ge_{0.863}Sn_{0.137}$ active layer and *p*-$Ge_{0.92}Sn_{0.08}$ top contact. b) High resolution BF image of the *p*-GeSn/*i*-GeSn interface. The absence of defects is due to pseudomorphic growth. c) High resolution BF image of defects at the *n*-Ge/*i*-GeSn interface (marked by arrows). Reproduced with permission from Senaratne, C. L. *et al. ECS Trans.* 2015, *69* (14), 157.

2.6. Device Fabrication and Diode Behavior

The *pin* device stacks produced using the methods outlined above were fabricated into diodes using standard microelectronic processing procedures described in Reference 21. The room temperature IV curves for the devices in the 0-13.7% composition regime are plotted in Figure 63. The diodes show excellent rectifying behavior. The reverse bias dark currents for the devices with Sn contents in the 5.5% - 8.5% regime, shown in Figure 63 (a), are comparable to devices with similar Sn contents reported in literature. However,

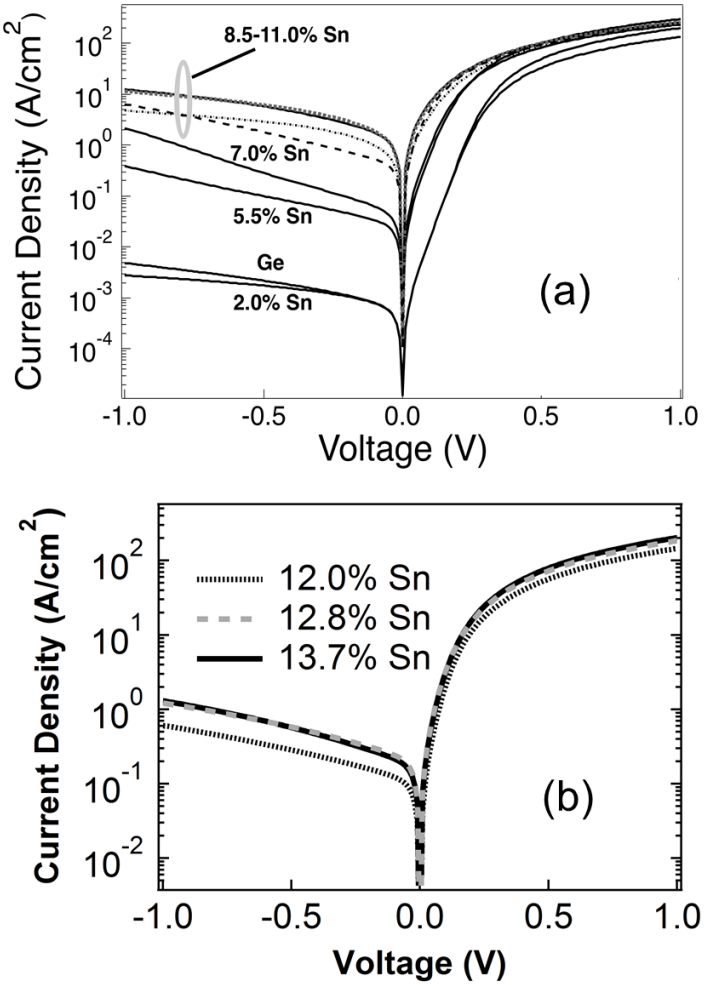

Figure 63 – IV plots of *n*-Ge/*i*-$Ge_{1-y}Sn_y$/*p*-$Ge_{1-z}Sn_z$ devices (a) in the 0 – 11% Sn regime, reproduced with modification from Reference 82. (b) in the 12 – 13.7% Sn regime, where improved device processing procedures result in an approximately order of magnitude lowering of the dark currents.

currents at forward bias for the same devices are an order of magnitude higher. This indicates that our device fabrication procedures lead to devices with better ideality factors, which for the 0-10.5% Sn devices shown in Figure 63 (a) range from 1.10 – 1.55. In addition, it is also possible that our devices have lower parasitic series resistance. It was found that by improving the device processing procedures, the dark currents which were obtained could be lowered substantially, as shown in Figure 63 (b) for devices in the composition range 12.0% - 13.7%. In these devices, the dark currents obtained are ~ 1

A/cm^2, which is an order of magnitude lower than the highest dark currents observed for devices in the 0% – 11% range depicted in Figure 63 (a). This indicates that the materials quality of the device stacks is not a limiting factor to obtaining further performance improvements by employing optimized device processing procedures.

The dark currents depicted in Figure 63 (a) exhibit a compositional dependence, with higher values being observed for samples with higher Sn contents. This behavior can be understood by studying the temperature dependence of the dark current, as described in Reference 82. The activation energies obtained from these measurements exceed $E_g/2$ for the lower Sn samples (y<0.085), where E_g is the fundamental band gap. This indicates a significant diffusion contribution to the dark current, as expected for devices with low defect densities. However, for higher Sn samples (y=0.085 – 0.11), the activation energies approach $E_g/2$, indicating a Shockley-Reed-Hall generation mechanism. Therefore it is

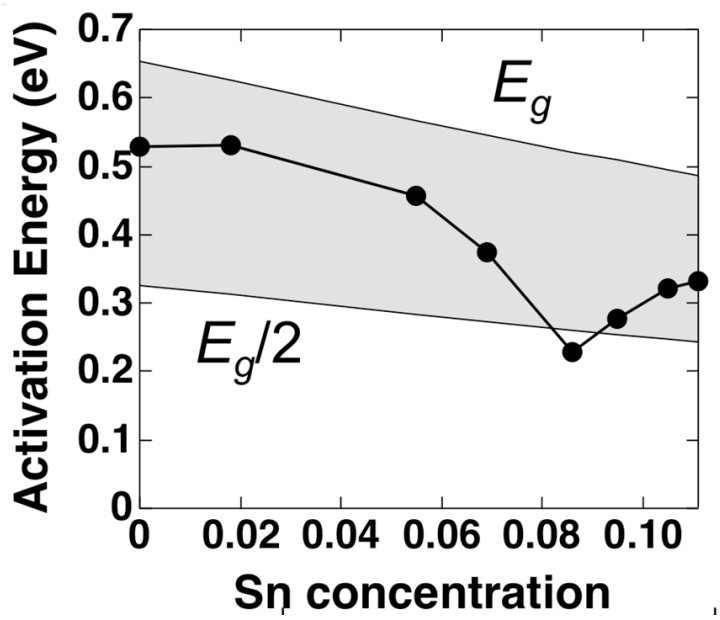

Figure 64 – Activation energies of dark currents at 0.2 V for devices with y=0-0.11, plotted vs. Sn content and compared with the fundamental band gap and half its value. Reproduced with modification from Reference 82.

evident that the higher defect densities of the higher Sn samples play a role in the dark current increase. The activation energies for the above devices are plotted as a function of Sn content in Figure 64.

2.7. Electroluminescence Performance of n-Ge/i-$Ge_{1-y}Sn_y$/p-$Ge_{1-z}Sn_z$ Devices

The EL of the above devices were measured at room temperature. A Keithley 2602A source was used, and the emitted light was passed through a grating spectrometer before being detected. For the wavelength range 1300-2300 nm, a liquid nitrogen cooled InGaAs detector was used for this purpose. For larger wavelengths in the 1500-2700 nm range, a thermoelectrically cooled PbS detector was necessary.

Figure 65 shows the EL spectra obtained from devices with 2.0% Sn and 7.0% Sn active layers. The solid traces indicate the dependence of EL intensity on the injection current. The dashed lines are the PL spectra, which in the case of Figure 65 (a) is obtained from a single layer reference sample grown under identical conditions containing the same Sn percentage. For of Figure 65 (b), the spectrum is from the *pin* device stack for which the EL is depicted. Both PL spectra are normalized to the highest EL intensity. For the 2.0% device, clear signals corresponding to the both direct and indirect band recombinations are observed, whereas in the 7.0% device, the only a single peak corresponding to the direct gap emission is seen. This is commensurate with the reduction of the separation of the direct and indirect gaps at higher Sn concentrations elucidated from PL studies described in the previous chapter, and indicates transition towards a direct band gap material. The higher energy shoulder observed in the PL spectrum of the 7.0% sample is attributed to the lower Sn *p*-type layer and Ge buffer that completes the device stack. The excellent

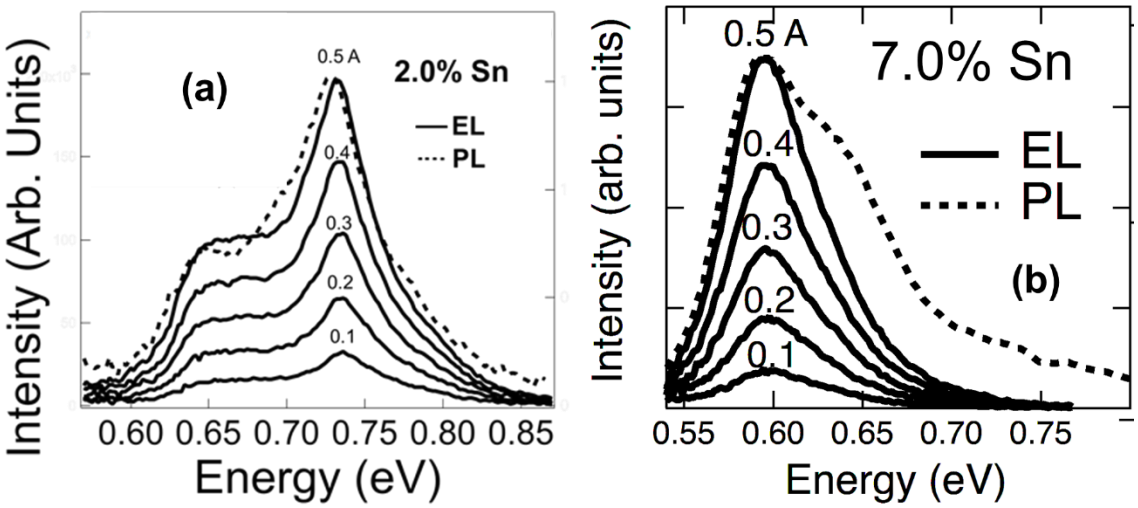

Figure 65 – Current dependence of the EL spectra in the 0.1 – 0.5 A range for devices with 2.0% Sn (a) and 7.0% Sn (b) active layer Sn compositions are depicted by the solid black lines. For the 2.0% Sn device, the EL spectrum is compared with a PL from a reference sample (dashed line) with the same Sn composition grown under the same conditions. Good agreements between the direct and indirect gap emission from the two experiments can be observed. For the 7.0% Sn device, the EL spectrum is compared with the PL spectrum obtained from the entire device stack. Contributions from the lower Sn *p*-GeSn layer and the Ge buffer can be seen in the latter, but good agreement is observed in the direct gap emission from the active layer in both experiments. The PL spectra are normalized to the EL spectra at 0.5 A in both cases. The spectra are reproduced with modification from References 83 and 82 respectively.

agreement between the PL and EL spectra indicate that the same modelling procedures used for the former can be applied to the latter. These techniques are described in detail in References 213 and 211, and were applied in determining the band gap values from PL spectra as described in Chapter 6. In the above work, it was found that the line shape of the direct gap emission can be described well by an EMG, while the indirect gap emission can be modelled as a Gaussian function. These fits are used for comparing the EL spectra from various devices below.

Figure 66 shows EMG fits to the direct gap from EL spectra obtained from a series of devices with compositions y=0.0-0.12, normalized to layer thickness of the active layers.

For devices in the range y=0-0.09, the EL spectra were obtained using the LN cooled InGaAs detector, and for the y=0.105 and y=0.12 the PbS detector was employed. The EMG fits to the experimental data allows the comparison of intensities between the spectra collected by different methods. The peak maxima span the range 1570-2640 nm which demonstrates the tuning of Ge emission into the mid-IR via Sn incorporation. This series of devices also provides the first experimental evidence that high Sn contents above the indirect-direct crossover composition in active layers does not have a detrimental effect on LED performance.

At room temperature, the emission intensity is expected to monotonically increase across the composition range. Such an increase occurs as the separation between the direct and indirect gaps is reduced with increasing Sn incorporation, resulting in greater proportion

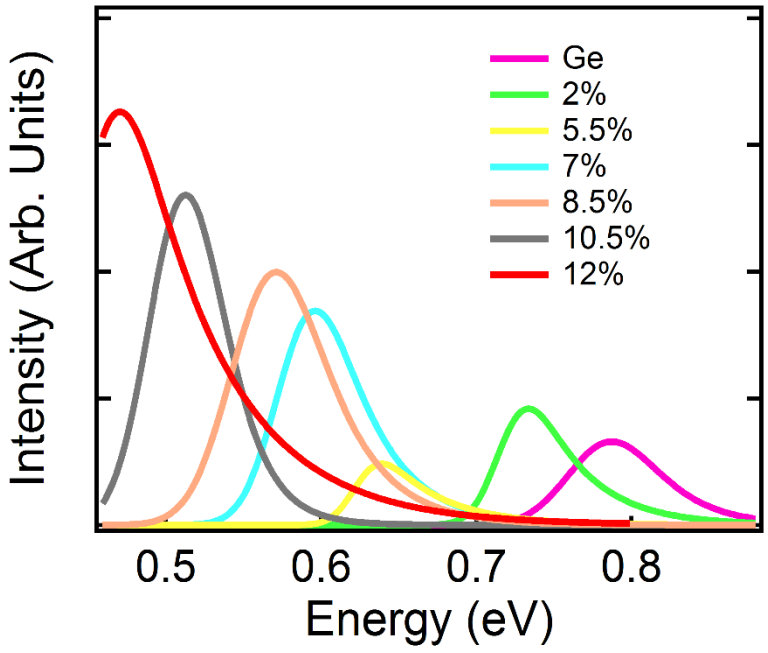

Figure 66 – EMG fits to EL spectra obtained from a series of devices with active layers in the composition range y=0-0.12.

of carrier recombinations occurring radiatively from the Γ valley. Such an intensity increase is observed when comparing the y=0.02 device with the Ge (y=0) device, as well as the series of devices from y=0.055-0.12. However, the decrease in intensity between the y=0.02 and y=0.055 devices runs contrary to this trend.

In order to explain this observation, the details of the microstructure of these devices outlined in Section 2.5 must be considered. By limiting the defect formation to a single interface (between the *n*-type and intrinsic layers), the current device design simplifies the study of the effect of defected interfaces on optical device performance.

For both the Ge and y=0.02 devices, all three *p*, *i* and *n* layers are pseudomorphic. In contrast, for the devices with $y \geq 0.05$, the intrinsic active layer is strain relaxed with respect to the *n*-Ge bottom contact layer due to their large thicknesses. The resultant change in microstructure where interfacial defect formation has taken place can be used to explain the decrease in intensity between the y=0.02 and y=0.055 devices. The defect formation increases the non-radiative recombination in these devices compared to the pseudomorphic devices which lack such defects. Therefore, the EL intensity obtained from the y=0.055 device is less than that observed for the y=0.02 device, despite the active layer of the latter being more direct in nature. The recombination lifetimes extracted from the EL spectra given in Figure 66 are described in Reference 82, and the trend observed is a drastic reduction of these lifetimes by approximately a factor of 2 when the *n*-*i* interface becomes defected between the y=0.02 and y=0.055 samples. At higher Sn contents, the lifetimes remain essentially constant, since for all devices contain defected interfaces. This allows the decreasing separation between the direct and indirect gaps to be the dominant factor

determining the EL intensity. Therefore the intensities again increase in the range y=0.055-0.12.

Based on the above results, it was identified that interfacial defect formation reduces the emission efficiency of a device. Therefore an improved device design was developed in which emission from relaxed alloys near the indirect-direct crossover composition could be obtained while minimizing defect dependent non-radiative recombination. This was achieved through Sn alloying of the buffer layer to produce devices with an *n*-GeSn bottom contact, which reduces the lattice mismatch and prevents strain relaxation as described below.

3. Eliminating Interface Defects: *n*-$Ge_{1-x}Sn_x$/*i*-$Ge_{1-y}Sn_y$/*p*-$Ge_{1-z}Sn_z$ Diodes

The key to minimizing the formation of interfacial defects is reducing the lattice mismatch between the *p, i* and *n* components of a diode. This is evident when considering the *i*-*p* interfaces of the above devices, where due to the small difference in the lattice parameters the *p*-layer growth is pseudomorphic to the *i*-layer. Using an *n*-type Ge buffer layer is no longer a suitable option if lower lattice mismatch is to be achieved, since in the composition range of interest strain relaxation between Ge and GeSn is unavoidable, as discussed in Chapter 5.

A suitable alternative material that can act as an *n*-type contact layer and also possesses large lattice constant is GeSn itself. As described in Chapter 6, it is possible to *n*-type dope GeSn alloys to high levels using group V silyl and germyl precursors. These procedures were now utilized in order to produce the bottom contacts of *n*-$Ge_{1-x}Sn_x$/*i*-$Ge_{1-y}Sn_y$/*p*-$Ge_{1-z}Sn_z$ device stacks.

The first device produced according to this design contained Sn contents of x=0.06 in the *n*-layer, y=0.07 in the intrinsic layer and z=0.06 in the *p*-layer. The *n*-layer was deposited on an intrinsic Ge virtual substrate similar to those described in Chapter 5, grown using the methods described by Xu *et al*. The growth was conducted in a single zone UHV-CVD reactor using procedures described in Chapters 5 and 6. The thickness of the layer was 410 nm, and it was doped to a level of 2.8×10^{19} cm^{-3} using $P(SiH_3)_3$. The above doping agent was mixed together with Ge_3H_8 and SnD_4 to make the precursor mixture for the *n*-layer. After completing the growth of the *n*-layer, the chamber was flushed with H_2 in order to remove any residual P containing molecules which may interfere with the growth of the intrinsic active layer. Thereafter, the Ge_3H_8/SnD_4 mixture used for the intrinsic layer deposition was introduced into the chamber, and the second device component was also completed without removing the wafer from the chamber. The thickness was 550 nm. These two layers were characterized to get the thickness and composition data from IRSE and HRXRD. In the next step, the wafer was cleaned using aqueous HF before growing the *p*-type layer, which was deposited in a 3-zone UHV-CVD reactor using Ge_2H_6 and SnD_4, a procedure in common with the earlier *pin* devices. The doping, to a level of $\sim3\times10^{19}$ cm^{-3}, was achieved using B_2H_6. All depositions were done in the 305-315°C temperature range, and further details are given in Appendix A.

The completed device structure, a schematic of which is shown in Figure 67 (a), was subjected to characterization using RBS, HRXRD, SIMS and IRSE techniques. This allowed the determination of compositions, thicknesses, strains and the doping levels of the separate layers. The peak FWHM observed in XRD RC scans and channeling RBS data indicate excellent crystal quality of the *i*-$Ge_{1-y}Sn_y$ layer. The Ge, Sn and P elemental

profiles for the device stack obtained from SIMS is shown in Figure 67 (b). The SIMS results obtained for this structure are not only useful in establishing that full dopant activation has occurred, but also exemplify the use of low growth temperatures in order to obtain sharp doping transitions. Despite the intrinsic layer being grown directly after the *n*-doped layer in the same chamber without an intermediate passivation step, there is no observable P atoms in the former. This indicates that all the P precursors were removed

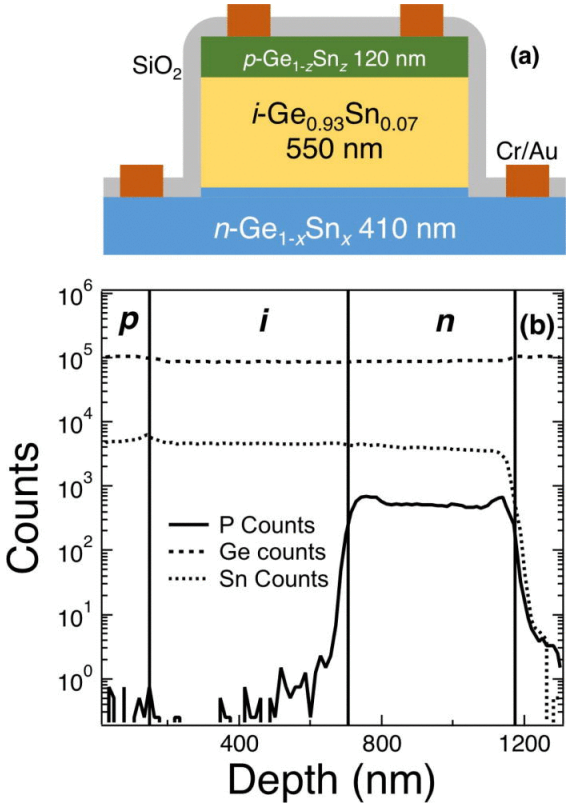

Figure 67 - (a) Schematic of device prototypes comprising *pin* layers with no strain relaxation at the device interfaces. (b) SIMS elemental profile of a $Ge_{0.93}Sn_{0.07}$ sample showing a uniform distribution of Ge and Sn atoms across the entire sequence of device layers as expected. The P atom content is constant through the n region and drops sharply down to levels representative of background noise through the intrinsic layer precluding the possibility of inter-diffusion or cross contamination from the reactor ambient. Reprinted from Gallagher, J. D. *et al. J. Appl. Phys.* 2015, *117* (24), 245704, with the permission of AIP publishing.

from the chamber ambient by flushing with H_2 after growth of the *n*-type layer, eliminating any memory effects. Furthermore, the doping profile at the interface has a sharp decrease, which indicates that the amount of dopant diffusion which takes place is negligible. It is possible to conclude from these results that low temperature *in-situ* doping techniques which makes use of high reactivity dopant delivery agents described in this work are capable of controlling doping to the high standards of dopant activation and precise dopant distribution required for state of the art applications.

Despite the more complicated growth process, the advantages offered by using designs with defect free interfaces is evident when the EL obtained from the *n*-$Ge_{0.94}Sn_{0.06}$/*i*-$Ge_{0.93}Sn_{0.07}$/*p*-$Ge_{0.94}Sn_{0.06}$ device is compared with the earlier, *n*-Ge/*i*-$Ge_{1-y}Sn_y$/*p*-$Ge_{1-z}Sn_z$ series of devices. In Figure 68, the EMG fits to the direct gap emission peaks from the series of devices shown in Figure 66 are compared to the EL from the improved design. It can be clearly seen that its intensity is higher by a factor of four or more than any of the previous devices. This is despite the fact that the emitting layers of many of the earlier devices contain material which have higher Sn content, and therefore greater directness, than the y=0.07 material used in the active layer of the new design. This supports the conclusion that strain relaxation defects, and the resultant non-radiative recombination, have a dramatic effect on the emission efficiency of GeSn devices. The role of recombination lifetimes in each of the different structures that quantify this observation is discussed in detail in Reference 83. These results provide valuable guidance for optimizing future device designs.

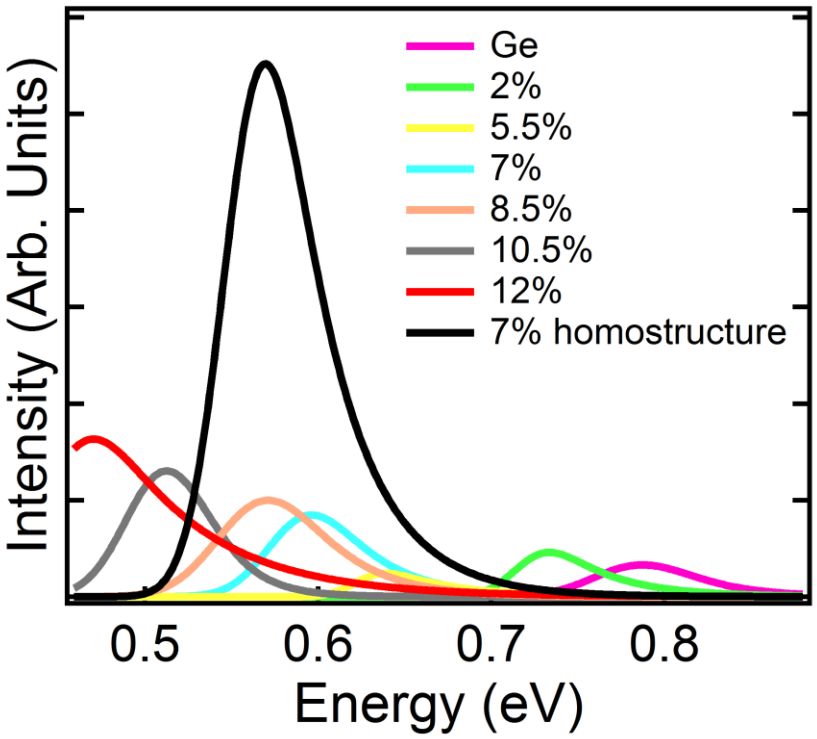

Figure 68 – Comparison of EL intensity of *n*-$Ge_{0.94}Sn_{0.06}$/*i*-$Ge_{0.93}Sn_{0.07}$/*p*-$Ge_{0.94}Sn_{0.06}$ diode design (black line) with intensities obtained from earlier *n*-Ge/*i*-$Ge_{1-y}Sn_y$/*p*-$Ge_{1-z}Sn_z$ diodes (colored lines) where *y*=0-0.12, as shown in Figure 66.

As well as providing a route to enhanced electroluminescence, lattice engineering of the bottom *n*-type contact allows the synthesis of higher Sn *pin* diodes than can be achieved directly on Ge. This is because a larger lattice parameter template provided by the *n*-GeSn layer allows the pseudomorphic growth of the active layer, preventing the formation of strain relaxation defects that are detrimental to the growth of high Sn diodes directly on Ge. As an example, a 275 nm thick *n*-doped GeSn layer with ~11% Sn was deposited on an *n*-doped Ge wafer. This deposition was designed by combining the doping techniques developed in Chapter 6 with the variable temperature growth techniques used to obtain

thick layers of direct gap materials described earlier in this chapter. This allows the growth of highly *n*-type doped, thick, strain relaxed GeSn alloys.

After characterizing the above film to ensure its suitability as a growth platform, the device structure was completed by depositing both *i* and *p* layers on it in a single growth. This procedure was used to produce diode structures with active layer compositions in the y=0.15-0.16 range. The precursor mixture used to deposit the active layer consisted of 21.3 LTorr of Ge_3H_8 and 10.5 LTorr of SnD_4, which corresponds to a Sn/Ge ratio of 14%. The *p*-type top contact was produced by flowing a 17% mixture of B_2H_6/H_2 during final phase of the growth. Different Sn compositions (i.e. 15% and 16%) were obtained by placing the substrates at different positions in the growth chamber. This also resulted in a thickness difference in the active layers, with the 15% layer being 130 nm thick and the 16% 120 nm thick. Further experimental details on the growth of these samples can be found in Appendix A.

Due to the reduction of the lattice mismatch and the low growth temperatures (down to 260°C) used for these growths, the active layer growth is pseudomorphic to the *n*-$Ge_{0.89}Sn_{0.11}$ layer. This was verified by analyzing the device structure with XTEM, shown in Figure 69 (a). The figure depicts the *n*-Ge/*n*-$Ge_{0.89}Sn_{0.11}$/*i*-$Ge_{0.85}Sn_{0.15}$/*p*-$Ge_{0.85}Sn_{0.15}$ device stack and the *n*-Ge/*n*-$Ge_{0.89}Sn_{0.11}$ and *n*-$Ge_{0.89}Sn_{0.11}$/*i*-$Ge_{0.85}Sn_{0.15}$ interfaces are marked by arrows. The former interface is defected, due to the relaxation of the *n*-GeSn layer relative to the Ge buffer. However, the *n*-$Ge_{0.89}Sn_{0.11}$/*i*-$Ge_{0.85}Sn_{0.15}$ interface is defect free, indicative of pseudomorphic growth of the intrinsic layer on the *n*-GeSn template. The *i*-$Ge_{0.85}Sn_{0.15}$/*p*-$Ge_{0.85}Sn_{0.15}$ interface cannot be distinguished in the micrograph,

possibly due to the identical Sn compositions of the two layers and continuous nature of the growth.

The current voltage plots for the 15% and 16% devices are shown in Figure 69 (b), and the rectifying behavior observed in the diodes indicate that using *n*-GeSn buffer layers is a viable pathway to obtaining functional GeSn devices with high Sn contents well above the indirect-direct crossover composition. These devices can be considered as preliminary experiments that establish a path towards more complicated devices made of GeSn or GeSiSn with direct gap compositions which can function as laser diodes.

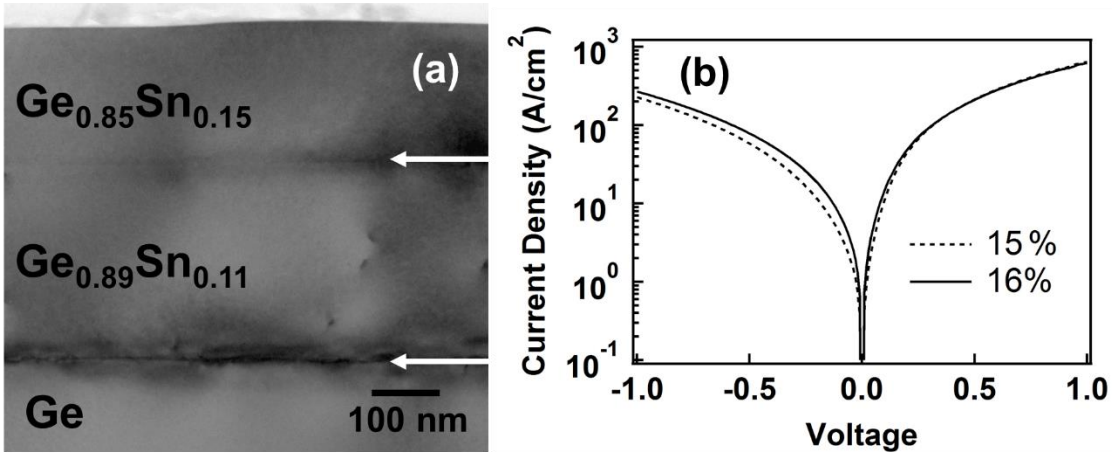

Figure 69 – (a) XTEM micrograph of *n*-Ge/*n*-$Ge_{0.89}Sn_{0.11}$/*i*-$Ge_{0.85}Sn_{0.15}$/*p*-$Ge_{0.85}Sn_{0.15}$ device stack with the *n*-Ge/*n*-$Ge_{0.89}Sn_{0.11}$ and *n*-$Ge_{0.89}Sn_{0.11}$/*i*-$Ge_{0.85}Sn_{0.15}$ interfaces are marked by arrows. (b) IV plots of the 15% and 16% Sn devices.

4. Growth of *pn* Diode Structures

Another class of emission devices investigated as a part this work were *pn* junctions. A range of these devices were synthesized with compositions spanning the indirect-direct crossover composition. As mentioned earlier, diodes with a *pn* architecture have been successfully employed for obtaining electrically pumped lasing from quasi-direct Ge.[11] GeSn diodes present an attractive alternative which is CMOS compatible and can eliminate

the disadvantages of free carrier absorption and lack of wavelength tunability seen in Ge devices.

A key factor in the successful growth of these structures were the techniques developed earlier which allows the growth of thick, *n*-doped GeSn alloy films at low temperature on Ge buffered Si substrates, which have high Sn contents that make them direct gap semiconductors. These layers formed the bottom contact layer of the *pn* junctions. The mixtures used for the *n*-$Ge_{1-y}Sn_y$ layer growths consisted of ~27 LTorr of Ge_3H_8 and 4.3-8.8 LTorr of SnD_4. The resultant film compositions were y=0.065-0.123. The lower compositions were grown at a constant temperature of 305°C, while for the high Sn content films the initial temperature was 280°C, which was increased to 287°C during growth. The *n*-type doping was achieved by adding 0.14-0.40 LTorr of $P(SiH_3)_3$ to the aforementioned Ge_3H_8/SnD_4 growth mixture. The ensuing active carrier concentrations were 5×10^{18} cm^{-3} – 2.5×10^{19} cm^{-3}. The above reactants were combined in 3 L glass containers, and were diluted with ~750 LTorr of H_2. Specific deposition parameters for representative samples are listed in Appendix A.

The properties of the *n*-type layers mentioned above were measured using HRXRD, RBS and IRSE prior to the growth of the *p*-type layers which completes the device. Thereafter the surfaces were cleaned using procedures outlined above. The top contact layers were grown in a separate reactor using Ge_2H_6 and SnD_4 precursors, using the same procedures used to for the final layers of the *n*-Ge/*i*-$Ge_{1-y}Sn_y$/*p*-$Ge_{1-z}Sn_z$ devices. The composition range chosen was 3.5% to 12%, and these layers were doped to levels of 1.2×10^{20} cm^{-3} –

1×10^{19} cm^{-3}. The temperature range used for the depositions was 305°C - 285°C, and resulted in *p*-type doped layers with thicknesses up to 300 nm.

An important feature of these devices in terms of obtaining efficient EL is that regardless of whether the Sn contents of the two layers are equal or not, the growth of the top layer is pseudomorphic to the bottom layer. This results in a defect-free *p*-*n* junction, which is especially important in this device design, since the emission occurs from the depletion region at the interface of the two layers. The presence of defects would result in increased non-radiative recombination processes, degrading light emission. An example of the microstructure is shown in the XSTEM image in Figure 70 a). The device in this case has a *n*-$Ge_{0.907}Sn_{0.093}$/*p*-$Ge_{0.914}Sn_{0.086}$ structure where the *n*-type layer is 71% relaxed with respect to the Ge buffer. The top contact layer is pseudomorphic to the latter, as seen in the (224) RSM given in Figure 70 b).

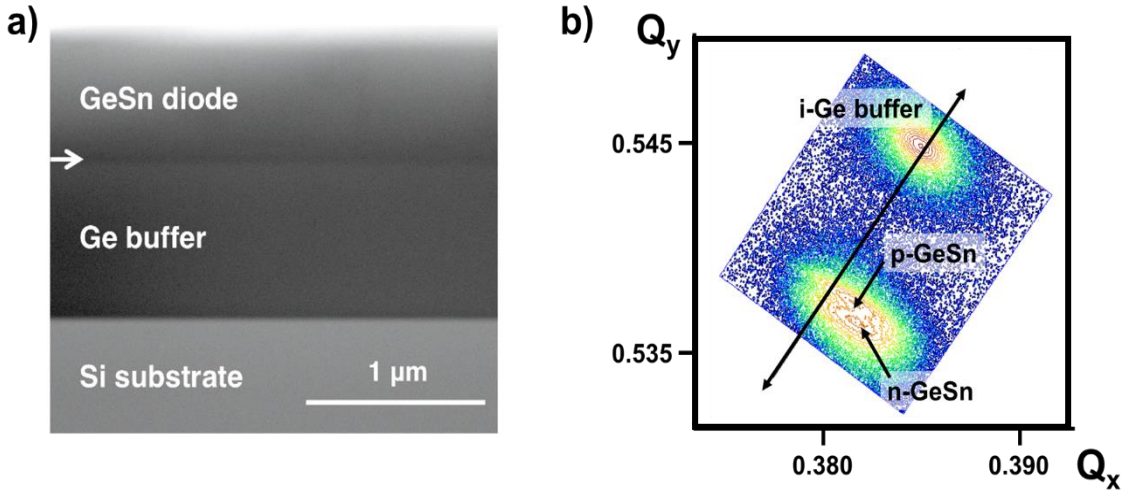

Figure 70 – a) XSTEM BF image of *n*-$Ge_{0.907}Sn_{0.093}$/*p*-$Ge_{0.914}Sn_{0.086}$ diode structure deposited on Ge/Si(100) substrate. The buffer-diode interface is marked by the arrow. The top segment of the *p*-layer in the device is partially etched by ion milling the thin TEM specimen. Reprinted with modification from Reference 84. b) (224) RSM of the device structure in a).

Another notable feature of the interface region is the sharp transitions of the dopant profiles at the interfaces. The elemental distribution in the different layers was obtained from SIMS, and a representative plot for a *p*-$Ge_{0.88}Sn_{0.12}$/*n*-$Ge_{0.88}Sn_{0.12}$ device is shown in Figure 71. The measurements were conducted using a CAMECA IMS 6f instrument, and the B profile was obtained using an O_2^+ primary beam. For the heavier elements a more suitable Cs^+ primary beam was used, with high mass resolution setting to prevent interference to the ^{31}P signal arising from the $^{30}Si^1H$ molecular ion. The profiles obtained from the two measurements are combined in the figure to facilitate comparison. The absolute B and P levels agree well with the carrier concentrations determined by ellipsometry, which are $\approx 2\times10^{19}$ cm^{-3} for both layers. Most significantly, the transition from *p*- to *n*-type region is sharp, resulting in a well-defined depletion region. Low temperature growth (≈285°C for

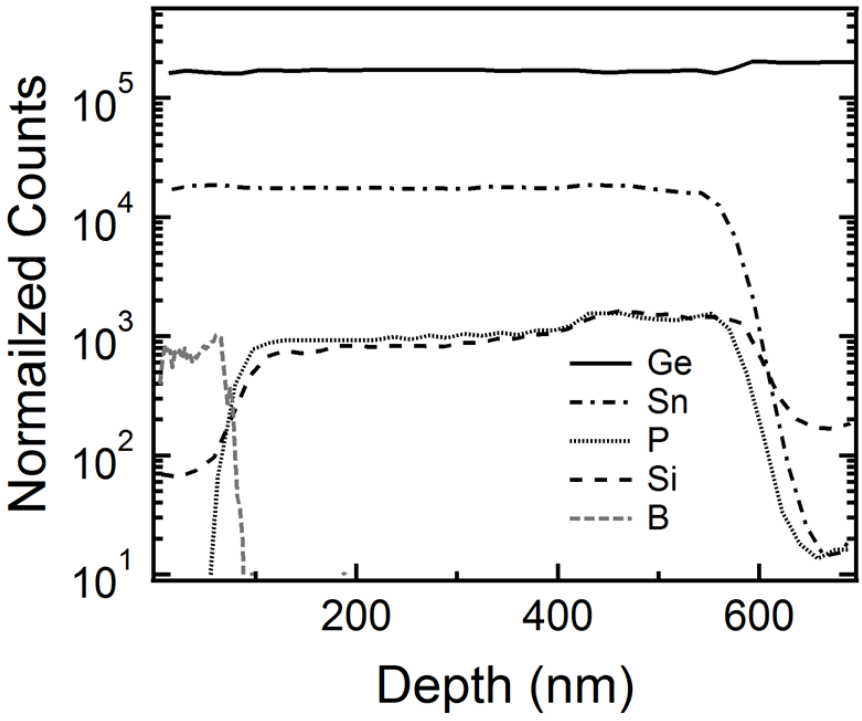

Figure 71 – Elemental profiles of Ge, Sn, B, P and Si obtained from SIMS for a *n*-$Ge_{0.88}Sn_{0.12}$/*p*-$Ge_{0.88}Sn_{0.12}$ diode structure.

Table 11 – Thickness, composition and doping of the *n* and *p* layers of representative *n*-$Ge_{1-y}Sn_y$/*p*-$Ge_{1-z}Sn_z$ diode stacks.

Sample	Composition		Thickness (nm)		Doping (/cm^3)	
	y	*z*	*y*	*z*	*y*	*z*
A	0.064	0.033	400	100	1.3×10^{19}	1.2×10^{20}
B	0.123	0.077	535	100	5.6×10^{18}	3.0×10^{19}
C	0.105	0.085	360	125	1.8×10^{19}	1.0×10^{19}
D	0.093	0.086	525	300	4.8×10^{18}	2.4×10^{19}

both layers) eliminate dopant diffusion which can mar the sharpness of the interfaces. The novel dopant delivery agents discussed in Chapter 2 are the enabling factor for doping at such conditions. Also of note is the flat and uniform Sn profile which corroborates RBS and HRXRD results indicating homogeneous composition throughput the layers.

Properties of representative device stacks produced in this study are listed in Table 11, which describes the Sn content, thickness and doping for *p* and *n* layers of each stack. As can be seen from the data, the compositions and doping of the two layers was chosen in such a way that several variants of *pn* junctions were produced.

In the first series of devices, the dopant level of the *n*-doped layer was kept low, while the top layer was heavily doped. Furthermore, the Sn content of the top layer was chosen to be less than that of the *n*-layer. In this design, the emission occurs predominantly from the bottom layer, since the depletion region, and hence carrier recombination occurs predominantly from the *n*-type layer. An example is shown in Figure 72 (a), which is depicts the current dependent EL spectra obtained from sample A, and is reproduced with modification from Reference 84. Due to the significant difference of Sn content between the two device components (6.5% and 3.5% for *n* and *p* layers respectively), emission occurring from both would result in two separate, clearly resolvable peaks. The presence

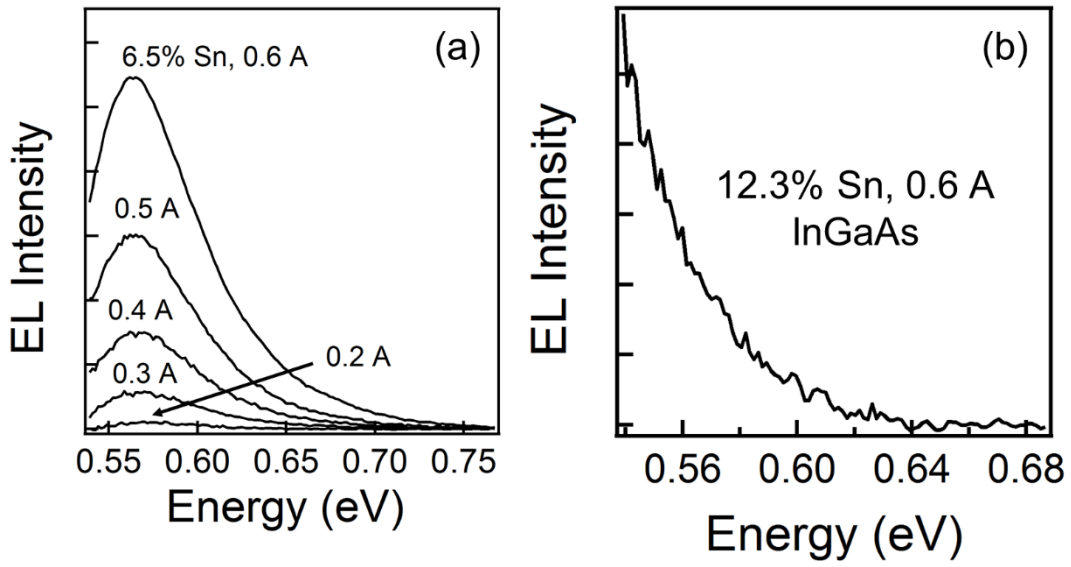

Figure 72 – (a) Room temperature EL spectra from sample A exhibiting superlinear current dependence. (b) Room temperature EL spectrum of sample B. Emission from both devices occur from the *n*-type layer, and were collected using a LN cooled InGaAs detector. Figure reproduced with modification from Reference 84.

of only a single emission peak with an energy in agreement with the 6.5% Sn *n*-type epilayer clearly demonstrates that the carrier recombination occurs in this region. In addition, the current dependence of the EL intensity of the device is observed to be super-linear, a feature in common with the *pin* devices described above. In sample B, the above device design was extended to GeSn material with direct gap compositions. As shown in Figure 72 (b), this device also exhibits clear EL arising from only the bottom *n*-type doped layer, which has a composition of 12.3% Sn. Based on the composition and strain, the emitting alloy is expected to be direct gap based on work described in Chapter 6. Peak emission for this device is expected to be at ~2860 nm, which is beyond the cutoff point of our detectors, and explains the observation of only the tail of the emission peak. However, demonstration light emission from a direct gap *pn* junction device is an important step on the road to an electrically injected GeSn laser.

Next, by keeping the high/low Sn contents in the bottom/top layers, but by adjusting the doping levels to be approximately equal in both layers, it was possible to obtain two color emission, arising from the different band gaps of the two layers. An example is sample C, in which the *n* and *p* layer compositions are 10.5% and 8.5% Sn respectively, but doping of both layers is comparable at 1-2×10^{19} cm^{-3}. In Figure 73 (reproduced from Reference 84), the EL spectrum obtained from this sample is shown. The contributions from both *p* and *n* layers are clearly visible, as can be expected from the more symmetric depletion

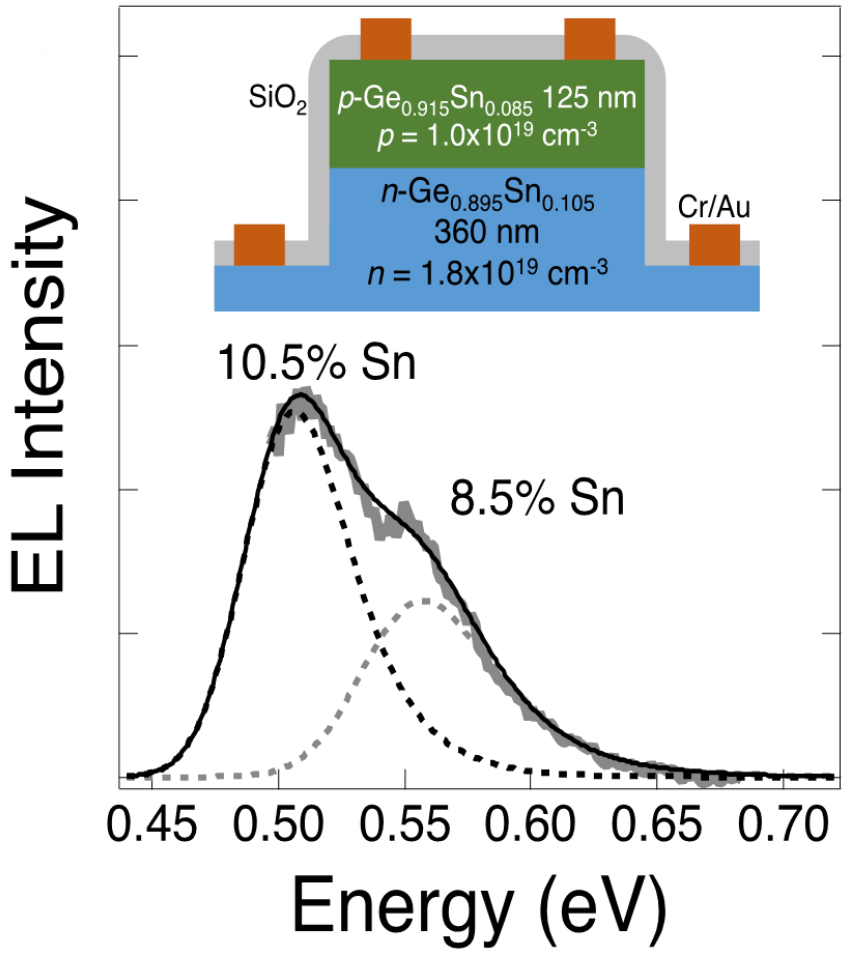

Figure 73 – Schematic and EL spectrum (grey line) of a *pn* diode with different Sn contents in the two layers but with similar doping levels. The device possesses a symmetric depletion region where carrier recombination occurs in both layers, resulting in two color emission, fit by EMGs depicted by the dashed lines. Reprinted with permission from Gallagher, J. D. et al. *Appl. Phys. Lett.* 2015, *107* (12), 123507.

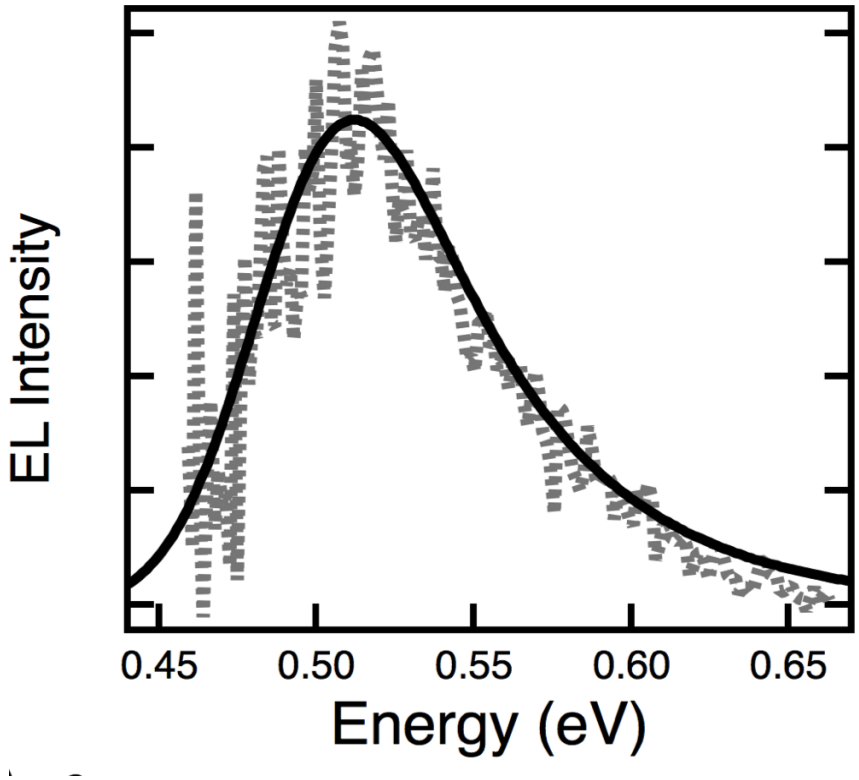

Figure 74 – Room temperature EL spectrum of sample D (grey dashed line). The higher noise level of the spectrum arises from the use of a PbS detector in order to resolve the full peak. The solid line is an EMG fit to the peak. Reproduced with modification from Reference 84.

region. The spectrum can be separated into its constituent components by performing EMG fits to the two peaks, as depicted by the dashed lines in the figure. This modelling shows that the two peaks are centered at 0.504 eV and 0.557 eV.

In the devices described thus far, the requirement of both device components having separate and clearly resolved spectral signatures necessitated the use of significantly different Sn contents in the *n* and *p* layers. However, this design is not necessary for practical *pn* LEDs. Furthermore, having different Sn contents in the two layers may result in strain relaxation between the layers during device processing. Therefore we finally investigated the EL performance of *pn* devices with similar Sn compositions in both layers.

An example is sample D, where the *n* and *p* layers have similar Sn contents of 9.3% and 8.6% respectively. The EL spectrum of the device is given in Figure 74, and is a single peak centered at 0.512 eV. The emission is attributed to the *n*-type layer. This is due to the fact lighter doping of the latter should result in emission predominantly confined in the *n* region of the diode, similar to samples A and B described above. The results from these EL studies are presented in greater detail in Reference 84.

The current-voltage data for samples A, B and D are given in Figure 75. The plots depict differential current vs. applied bias, and all devices show a conductance minimum at forward bias values of 0 - 0.2 V. Such minima are associated with Esaki-type diodes which show negative differential resistance. In the diodes shown in Figure 75, only sample D has a truly negative differential resistance. This may be a result of the lower strain between the

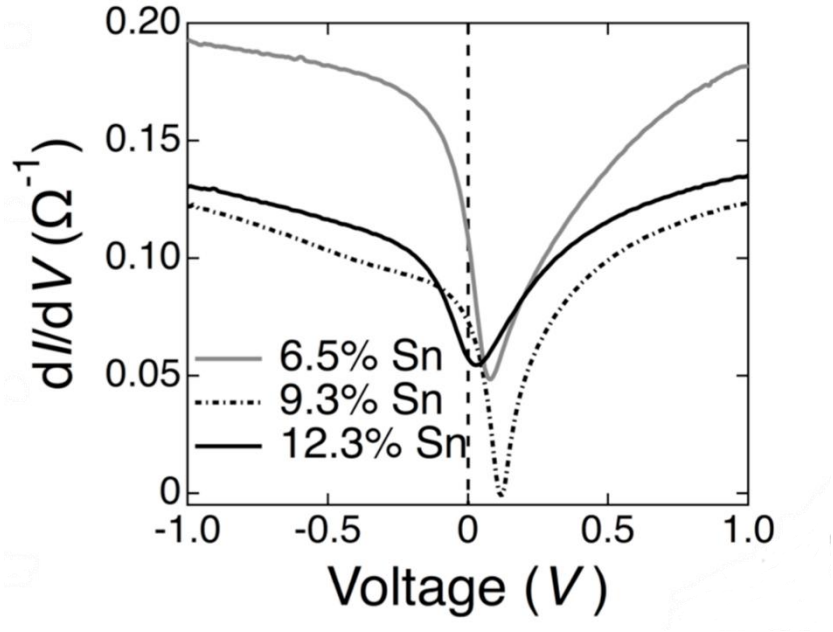

Figure 75 – Differential current vs. applied bias for samples A, B and D. Reproduced with modification from Reference 84.

two components of this device, which minimizes excess currents originating from interfacial defects.[219]

Overall the work described here demonstrate that GeSn *pn* junctions with direct gap compositions can exhibit electrically injected light emission, and that the emission properties of such devices can be finely tuned. Therefore these results can be considered a strarting point for designing GeSn *pn* laser diodes.

5. Conclusion

In this chapter, the growth and materials characterization of GeSn diode designs were described. The GeSn active materials of the diodes were deposited using either Ge_2H_6 or Ge_3H_8 as the source of Ge and SnD_4 as the source of Sn. The substrate chosen for the first group of diodes was *n*-type doped Ge/Si(100). These provide a facile substrate for deposition of intrinsic $Ge_{1-y}Sn_y$ alloys with compositions up to y=0.14, and also act as bottom contact layers. Therefore, by depositing *p*-type doped $Ge_{1-z}Sn_z$ capping layers, it is possible to obtain diodes with an *n*-Ge/*i*-$Ge_{1-y}Sn_y$/*p*-$Ge_{1-z}Sn_z$ design. The diodes fabricated in this work were the first report of electrically induced light emission from GeSn alloys with compositions above the indirect-direct crossover point. Furthermore, the influence of defects induced by strain relaxation at the Ge/GeSn interface on EL intensity was investigated. This was made possible by the broad range of compositions present in the fabricated diodes, which leads to varying degrees of strain relaxation. Based on the results of this study, a new diode design of the *n*-$Ge_{1-x}Sn_x$/*i*-$Ge_{1-y}Sn_y$/*p*-$Ge_{1-z}Sn_z$ type which eliminates interface defects was proposed and fabricated, and was shown to have enhanced light emission capabilities. Such designs which minimize defect densities are an essential

step in fabricating electrically injected GeSn lasers. Furthermore, the new design was also found to be beneficial for further increasing the Sn content of the active layers of the diodes (up to y=0.16) by minimizing the lattice mismatch between the layer and its immediate substrate. Finally, diodes with a *pn* architecture were also fabricated. It was found that the region of the diode contributing to light emission could be precisely controlled by adjusting the Sn composition and doping level of the two layers. Such designs are important for obtaining light emission from *n*-type doped GeSn, which has greater directness in emission compared to intrinsic material. Therefore such devices represent viable candidates for obtaining electrically pumped lasing from GeSn alloys at room temperature. It must be noted that these devices are preliminary prototypes, and in future work, more complicated architectures incorporating additional GeSn or GeSiSn components can further enhance performance by ensuring carrier confinement in the active material while maintaining defect-free interfaces.

REFERENCES

(1) Moore, G. E. *Electronics* **1965**, *38* (8), 114.

(2) Moore, G. E. *1975 Int. Electron Devices Meet.* **1975**, *21*, 11.

(3) Ghani, T.; Armstrong, M.; Auth, C.; Bost, M.; Charvat, P.; Glass, G.; Hoffmann, T.; Johnson, K.; Kenyon, C.; Klaus, J.; McIntyre, B.; Mistry, K.; Murthy, A.; Sandford, J.; Silberstein, M.; Sivakumar, S.; Smith, P.; Zawadzki, K.; Thompson, S.; Bohr, M. In *IEEE International Electron Devices Meeting 2003*; IEEE, 2003; Vol. M, pp 11.6.1–11.6.3.

(4) Mistry, K.; Allen, C.; Auth, C.; Beattie, B.; Bergstrom, D.; Bost, M.; Brazier, M.; Buehler, M.; Cappellani, A.; Chau, R.; Choi, C.-H.; Ding, G.; Fischer, K.; Ghani, T.; Grover, R.; Han, W.; Hanken, D.; Hattendorf, M.; He, J.; Hicks, J.; Huessner, R.; Ingerly, D.; Jain, P.; James, R.; Jong, L.; Joshi, S.; Kenyon, C.; Kuhn, K.; Lee, K.; Liu, H.; Maiz, J.; McIntyre, B.; Moon, P.; Neirynck, J.; Pae, S.; Parker, C.; Parsons, D.; Prasad, C.; Pipes, L.; Prince, M.; Ranade, P.; Reynolds, T.; Sandford, J.; Shifren, L.; Sebastian, J.; Seiple, J.; Simon, D.; Sivakumar, S.; Smith, P.; Thomas, C.; Troeger, T.; Vandervoorn, P.; Williams, S.; Zawadzki, K. In *2007 IEEE International Electron Devices Meeting*; IEEE, 2007; pp 247–250.

(5) Pillarisetty, R. *Nature* **2011**, *479* (7373), 324.

(6) Weiner, C. *IEEE Spectr.* **1973**, *10* (1), 24.

(7) Wolff, M. F. *IEEE Spectr.* **1976**, *13* (8), 45.

(8) Michel, J.; Liu, J.; Kimerling, L. C. *Nat. Photonics* **2010**, *4* (8), 527.

(9) Soref, R. *Nat. Photonics* **2010**, *4* (8), 495.

(10) Liu, J.; Sun, X.; Camacho-Aguilera, R.; Kimerling, L. C.; Michel, J. *Opt. Lett.* **2010**, *35* (5), 679.

(11) Camacho-aguilera, R. E.; Cai, Y.; Patel, N.; Bessette, J. T.; Romagnoli, M.; Kimerling, L. C.; Michel, J. **2012**, *20* (10), 11316.

(12) Olesinski, R. W.; Abbaschian, G. J. *Bull. Alloy Phase Diagrams* **1984**, *5* (3), 265.

(13) Thewlis, J.; Davey, A. R. *Nature* **1954**, *174* (4439), 1011.

(14) Beeler, R.; Roucka, R.; Chizmeshya, A. V. G.; Kouvetakis, J.; Menéndez, J. *Phys. Rev. B* **2011**, *84* (3), 035204.

(15) Takagi, S. In *Advanced Gate Stacks for High-Mobility Semiconductors SE - 1*; Dimoulas, A., Gusev, E., McIntyre, P., Heyns, M., Eds.; Advanced Microelectronics; Springer Berlin Heidelberg, 2007; Vol. 27, pp 1–19.

(16) Sau, J. D.; Cohen, M. L. *Phys. Rev. B* **2007**, *75* (4), 045208.

(17) Liu, L.; Liang, R.; Wang, J.; Xu, J. *J. Appl. Phys.* **2015**, *117* (18), 184501.

(18) Vincent, B.; Shimura, Y.; Takeuchi, S.; Nishimura, T.; Eneman, G.; Firrincieli, A.; Demeulemeester, J.; Vantomme, A.; Clarysse, T.; Nakatsuka, O.; Zaima, S.; Dekoster, J.; Caymax, M.; Loo, R. *Microelectron. Eng.* **2011**, *88* (4), 342.

(19) Kotlyar, R.; Avci, U. E.; Cea, S.; Rios, R.; Linton, T. D.; Kuhn, K. J.; Young, I. A. *Appl. Phys. Lett.* **2013**, *102* (11), 113106.

(20) Mathews, J.; Roucka, R.; Xie, J.; Yu, S.-Q.; Menéndez, J.; Kouvetakis, J. *Appl. Phys. Lett.* **2009**, *95* (13), 133506.

(21) Roucka, R.; Mathews, J.; Beeler, R. T.; Tolle, J.; Kouvetakis, J.; Menéndez, J. *Appl. Phys. Lett.* **2011**, *98* (6), 061109.

(22) Soref, R. In *Proceedings of SPIE*; Kubby, J., Reed, G. T., Eds.; 2013; Vol. 8629, pp 862902–1.

(23) Wirths, S.; Geiger, R.; von den Driesch, N.; Mussler, G.; Stoica, T.; Mantl, S.; Ikonic, Z.; Luysberg, M.; Chiussi, S.; Hartmann, J. M.; Sigg, H.; Faist, J.; Buca, D.; Grützmacher, D. *Nat. Photonics* **2015**, *9* (2), 88.

(24) Homewood, K. P.; Lourenço, M. A. *Nat. Photonics* **2015**, *9* (2), 78.

(25) Farrow, R. F. C.; Robertson, D. S.; Williams, G. M.; Cullis, A. G.; Jones, G. R.; Young, I. M.; Dennis, P. N. J. *J. Cryst. Growth* **1981**, *54* (3), 507.

(26) Goodman, C. H. L. *IEE Proc. I Solid State Electron Devices* **1982**, *129* (5), 189.

(27) Jenkins, D. W.; Dow, J. D. *Phys. Rev. B* **1987**, *36* (15), 7994.

(28) Shah, S. I.; Greene, J. E.; Abels, L. L.; Yao, Q.; Raccah, P. M. *J. Cryst. Growth* **1987**, *83* (1), 3.

(29) Asom, M. T.; Fitzgerald, E. A.; Kortan, A. R.; Spear, B.; Kimerling, L. C. *Appl. Phys. Lett.* **1989**, *55* (6), 578.

(30) Pukite, P. R.; Harwit, A.; Iyer, S. S. *Appl. Phys. Lett.* **1989**, *54* (21), 2142.

(31) Bowman Jr., R. C.; Adams, P. M.; Engelhart, M. A.; Hochst, H. *J. Vac. Sci. Technol. A Vacuum, Surfaces, Film.* **1990**, *8* (3), 1577.

(32) Piao, J.; Beresford, R.; Licata, T.; Wang, W. I.; Homma, H. *J. Vac. Sci. Technol. B Microelectron. Nanom. Struct.* **1990**, *8* (2), 221.

(33) He, G.; Atwater, H. *Phys. Rev. Lett.* **1997**, *79* (10), 1937.

(34) Ladrón de Guevara, H. P.; Rodríguez, A. G.; Navarro-Contreras, H.; Vidal, M. A. *Appl. Phys. Lett.* **2004**, *84* (22), 4532.

(35) Pérez Ladrón de Guevara, H.; Rodríguez, A. G.; Navarro-Contreras, H.; Vidal, M. a. *Appl. Phys. Lett.* **2007**, *91* (2007), 161909.

(36) D'Costa, V.; Cook, C.; Birdwell, A.; Littler, C.; Canonico, M.; Zollner, S.; Kouvetakis, J.; Menéndez, J. *Phys. Rev. B* **2006**, *73* (12), 125207.

(37) Lin, H.; Chen, R.; Lu, W.; Huo, Y.; Kamins, T. I.; Harris, J. S. *Appl. Phys. Lett.* **2012**, *100* (10).

(38) Chen, R.; Lin, H.; Huo, Y.; Hitzman, C.; Kamins, T. I.; Harris, J. S. *Appl. Phys. Lett.* **2011**, *99* (18), 181125.

(39) Tonkikh, A. A.; Eisenschmidt, C.; Talalaev, V. G.; Zakharov, N. D.; Schilling, J.; Schmidt, G.; Werner, P. *Appl. Phys. Lett.* **2013**, *103* (3), 032106.

(40) Wirths, S.; Ikonic, Z.; Tiedemann, A. T.; Holländer, B.; Stoica, T.; Mussler, G.; Breuer, U.; Hartmann, J. M.; Benedetti, A.; Chiussi, S.; Grützmacher, D.; Mantl, S.; Buca, D. *Appl. Phys. Lett.* **2013**, *103* (19), 192110.

(41) Yin, W.-J.; Gong, X.-G.; Wei, S.-H. *Phys. Rev. B* **2008**, *78* (16), 161203.

(42) Chibane, Y.; Ferhat, M. *J. Appl. Phys.* **2010**, *107* (5), 0.

(43) Lu Low, K.; Yang, Y.; Han, G.; Fan, W.; Yeo, Y.-C. *J. Appl. Phys.* **2012**, *112* (10), 103715.

(44) Gupta, S.; Magyari-Köpe, B.; Nishi, Y.; Saraswat, K. C. *J. Appl. Phys.* **2013**, *113* (7), 073707.

(45) Oehme, M.; Werner, J.; Gollhofer, M.; Schmid, M.; Kaschel, M.; Kasper, E.; Schulze, J. *IEEE Photonics Technol. Lett.* **2011**, *23* (23), 1751.

(46) Shimura, Y.; Tsutsui, N.; Nakatsuka, O.; Sakai, A.; Zaima, S. *Thin Solid Films* **2010**, *518* (6), S2.

(47) He, G.; Atwater, H. A. *Nucl. Instruments Methods Phys. Res. Sect. B Beam Interact. with Mater. Atoms* **1995**, *106* (1-4), 126.

(48) Tseng, H. H.; Li, H.; Mashanov, V.; Yang, Y. J.; Cheng, H. H.; Chang, G. E.; Soref, R. A.; Sun, G. *Appl. Phys. Lett.* **2013**, *103* (23), 231907.

(49) Taraci, J.; Tolle, J.; Kouvetakis, J.; McCartney, M. R.; Smith, D. J.; Menendez, J.; Santana, M. A. *Appl. Phys. Lett.* **2001**, *78* (23), 3607.

(50) Bauer, M.; Taraci, J.; Tolle, J.; Chizmeshya, A. V. G.; Zollner, S.; Smith, D. J.; Menendez, J.; Hu, C.; Kouvetakis, J. *Appl. Phys. Lett.* **2002**, *81* (16), 2992.

(51) Vincent, B.; Gencarelli, F.; Bender, H.; Merckling, C.; Douhard, B.; Petersen, D. H.; Hansen, O.; Henrichsen, H. H.; Meersschaut, J.; Vandervorst, W.; Heyns, M.; Loo, R.; Caymax, M. *Appl. Phys. Lett.* **2011**, *99* (15), 14.

(52) Wirths, S.; Buca, D.; Mussler, G.; Tiedemann, A. T.; Holländer, B.; Bernardy, P.; Stoica, T.; Grützmacher, D.; Mantl, S. *ECS J. Solid State Sci. Technol.* **2013**, *2* (5), N99.

(53) Margetis, J.; Ghetmiri, S. A.; Du, W.; Conley, B. R.; Mosleh, A.; Soref, R.; Sun, G.; Domulevicz, L.; Naseem, H. A.; Yu, S.-Q.; Tolle, J. *ECS Trans.* **2014**, *64* (6), 711.

(54) Suda, K.; Ishihara, S.; Sawamoto, N.; Machida, H.; Ishikawa, M.; Sudoh, H.; Ohshita, Y.; Ogura, A. *Jpn. J. Appl. Phys.* **2014**, *53* (11), 110301.

(55) Zaima, S.; Nakatsuka, O.; Taoka, N.; Kurosawa, M.; Takeuchi, W.; Sakashita, M. *Sci. Technol. Adv. Mater.* **2015**, *16* (4), 43502.

(56) Wirths, S.; Buca, D.; Mantl, S. *Prog. Cryst. Growth Charact. Mater.* **2016**, *62* (1), 1.

(57) Taylor, M. E.; He, G.; Atwater, H. A.; Polman, A. *J. Appl. Phys.* **1996**, *80* (8), 4384.

(58) Zheng, J.; Wang, S.; Liu, Z.; Cong, H.; Xue, C.; Li, C.; Zuo, Y.; Cheng, B.; Wang, Q. *Appl. Phys. Lett.* **2016**, *108* (3), 033503.

(59) Loo, R.; Vincent, B.; Gencarelli, F.; Merckling, C.; Kumar, A.; Eneman, G.; Witters, L.; Vandervorst, W.; Caymax, M.; Heyns, M.; Thean, A. *ECS J. Solid State Sci. Technol.* **2013**, *2* (1), N35.

(60) Ike, S.; Moriyama, Y.; Kurosawa, M.; Taoka, N.; Nakatsuka, O.; Imai, Y.; Kimura, S.; Tezuka, T.; Zaima, S. *Thin Solid Films* **2013**, *557*, 1.

(61) Gupta, S.; Chen, R.; Vincent, B.; Lin, D.; Magyari-köpe, B. *ECS Trans.* **2012**, *50* (9), 937.

(62) Schulze, J.; Blech, A.; Datta, A.; Fischer, I. A.; Hähnel, D.; Naasz, S.; Rolseth, E.; Tropper, E.-M. *Solid. State. Electron.* **2015**, *110*, 59.

(63) Wang, H.; Liu, Y.; Liu, M.; Zhang, Q.; Zhang, C.; Ma, X.; Zhang, J.; Hao, Y.; Han, G. *Superlattices Microstruct.* **2015**, *83*, 401.

(64) Wirths, S.; Tiedemann, A. T.; Ikonic, Z.; Harrison, P.; Holländer, B.; Stoica, T.; Mussler, G.; Myronov, M.; Hartmann, J. M.; Grützmacher, D.; Buca, D.; Mantl, S. *Appl. Phys. Lett.* **2013**, *102* (19), 10.

(65) Lei, D.; Wang, W.; Zhang, Z.; Pan, J.; Gong, X.; Liang, G.; Tok, E.; Yeo, Y.-C. *J. Appl. Phys.* **2016**, *119* (2), 024502.

(66) Gupta, S.; Vincent, B.; Yang, B.; Lin, D.; Gencarelli, F.; Lin, J.-Y. J.; Chen, R.; Richard, O.; Bender, H.; Magyari-Kope, B.; Caymax, M.; Dekoster, J.; Nishi, Y.; Saraswat, K. C. In *2012 International Electron Devices Meeting*; IEEE, 2012; pp 16.2.1–16.2.4.

(67) Nishimura, T.; Nakatsuka, O.; Shimura, Y.; Takeuchi, S.; Vincent, B.; Vantomme, A.; Dekoster, J.; Caymax, M.; Loo, R.; Zaima, S. *Solid. State. Electron.* **2011**, *60* (1), 46.

(68) Roucka, R.; Mathews, J.; Weng, C.; Beeler, R.; Tolle, J.; Menendez, J.; Kouvetakis, J. *IEEE J. Quantum Electron.* **2011**, *47* (2), 213.

(69) Oehme, M.; Kasper, E.; Schulze, J. *ECS J. Solid State Sci. Technol.* **2013**, *2* (4), R76.

(70) Oehme, M.; Kostecki, K.; Arguirov, T.; Mussler, G.; Ye, K.; Gollhofer, M.; Schmid, M.; Kaschel, M.; Korner, R. A.; Kittler, M.; Buca, D.; Kasper, E.; Schulze, J. *IEEE Photonics Technol. Lett.* **2014**, *26* (2), 187.

(71) Tseng, H. H.; Wu, K. Y.; Li, H.; Mashanov, V.; Cheng, H. H.; Sun, G.; Soref, R. A. *Appl. Phys. Lett.* **2013**, *102* (18), 182106.

(72) Du, W.; Zhou, Y.; Ghetmiri, S. A.; Mosleh, A.; Conley, B. R.; Nazzal, A.; Soref, R. A.; Sun, G.; Tolle, J.; Margetis, J.; Naseem, H. A.; Yu, S.-Q. *Appl. Phys. Lett.* **2014**, *104* (24), 241110.

(73) Gupta, J. P.; Bhargava, N.; Kim, S.; Adam, T.; Kolodzey, J. *Appl. Phys. Lett.* **2013**, *102* (25), 251117.

(74) Mathews, J.; Beeler, R. T.; Tolle, J.; Xu, C.; Roucka, R.; Kouvetakis, J.; Menéndez, J. *Appl. Phys. Lett.* **2010**, *97* (22), 221912.

(75) Grzybowski, G.; Chizmeshya, A. V. G.; Senaratne, C.; Menendez, J.; Kouvetakis, J. *J. Mater. Chem. C* **2013**, *1* (34), 5223.

(76) Gencarelli, F.; Vincent, B.; Demeulemeester, J.; Vantomme, A.; Moussa, A.; Franquet, A.; Kumar, A.; Bender, H.; Meersschaut, J.; Vandervorst, W.; Loo, R.; Caymax, M.; Temst, K.; Heyns, M. *ECS J. Solid State Sci. Technol.* **2013**, *2* (4), P134.

(77) Xu, C.; Beeler, R. T.; Jiang, L.; Grzybowski, G.; Chizmeshya, A. V. G.; Menéndez, J.; Kouvetakis, J. *Semicond. Sci. Technol.* **2013**, *28* (10), 105001.

(78) Cook, C. S. Growth and optical properties of novel doped and undoped group IV materials based on silicon, germanium, and tin, Arizona State University, 2006.

(79) Bauer, M. R. Synthesis of new tin-germanium-silicon semiconductors with tunable direct band gaps, Arizona State University, 2003.

(80) Chizmeshya, A. V. G.; Ritter, C.; Tolle, J.; Cook, C.; Menéndez, J.; Kouvetakis, J. *Chem. Mater.* **2006**, *18* (26), 6266.

(81) Li, Z. Room Temperature Lasing in GeSn Alloys, University of Dayton, 2015.

(82) Gallagher, J. D.; Senaratne, C. L.; Sims, P.; Aoki, T.; Menéndez, J.; Kouvetakis, J. *Appl. Phys. Lett.* **2015**, *106* (9), 091103.

(83) Gallagher, J. D.; Senaratne, C. L.; Xu, C.; Sims, P.; Aoki, T.; Smith, D. J.; Menéndez, J.; Kouvetakis, J. *J. Appl. Phys.* **2015**, *117* (24), 245704.

(84) Gallagher, J. D.; Senaratne, C. L.; Wallace, P. M.; Menéndez, J.; Kouvetakis, J. *Appl. Phys. Lett.* **2015**, *107* (12), 123507.

(85) Al-Kabi, S.; Ghetmiri, S. A.; Margetis, J.; Du, W.; Mosleh, A.; Alher, M.; Dou, W.; Grant, J. M.; Sun, G.; Soref, R. A.; Tolle, J.; Li, B.; Mortazavi, M.; Naseem, H. A.; Yu, S.-Q. *J. Electron. Mater.* **2015**, 1.

(86) Stange, D.; Wirths, S.; von den Driesch, N.; Mussler, G.; Stoica, T.; Ikonic, Z.; Hartmann, J. M.; Mantl, S.; Grützmacher, D.; Buca, D. *ACS Photonics* **2015**, *2* (11), 1539.

(87) Yu, S. Q.; Ghetmiri, S. A.; Du, W.; Margetis, J.; Zhou, Y.; Mosleh, A.; Al-Kabi, S.; Nazzal, A.; Sun, G.; Soref, R. A.; Tolle, J.; Li, B.; Naseem, H. A. In *Proc. SPIE 9367, Silicon Photonics X*; Reed, G. T., Watts, M. R., Eds.; 2015; Vol. 9367, p 93670R.

(88) Pham, T.; Du, W.; Tran, H.; Margetis, J.; Tolle, J.; Sun, G.; Soref, R. A.; Naseem, H. A.; Li, B.; Yu, S.-Q. *Opt. Express* **2016**, *24* (5), 4519.

(89) Stange, D.; von den Driesch, N.; Rainko, D.; Schulte-Braucks, C.; Wirths, S.; Mussler, G.; Tiedemann, A. T.; Stoica, T.; Hartmann, J. M.; Ikonic, Z.; Mantl, S.; Grützmacher, D.; Buca, D. *Opt. Express* **2016**, *24* (2), 1358.

(90) Schulte-Braucks, C.; Stange, D.; von den Driesch, N.; Blaeser, S.; Ikonic, Z.; Hartmann, J. M.; Mantl, S.; Buca, D. *Appl. Phys. Lett.* **2015**, *107* (4), 042101.

(91) Grzybowski, G.; Jiang, L.; Beeler, R. T.; Watkins, T.; Chizmeshya, A. V. G.; Xu, C.; Menéndez, J.; Kouvetakis, J. *Chem. Mater.* **2012**, *24* (9), 1619.

(92) Norman, A. D.; Webster, J. R.; Jolly, W. L.; Gorse, R. A.; Bornhorst, W. R.; Ring, M. A. *Inorg. Synth.* **1968**, *11*, 170.

(93) D'Costa, V. R.; Fang, Y.; Mathews, J.; Roucka, R.; Tolle, J.; Menéndez, J.; Kouvetakis, J. *Semicond. Sci. Technol.* **2009**, *24* (11), 115006.

(94) Grzybowski, G.; Beeler, R. T.; Jiang, L.; Smith, D. J.; Kouvetakis, J.; Menéndez, J. *Appl. Phys. Lett.* **2012**, *101* (7), 072105.

(95) Finholt, A. E.; Bond, A. C.; Schlesinger, H. I. *J. Am. Chem. Soc.* **1947**, *69* (5), 1199.

(96) Grzybowski, G. Epitaxy of group IV optical materials and synthesis of IV/III-V semiconductor analogs by designer hydride chemistries., Arizona State University, Tempe, AZ, 2013.

(97) Todd, M. A.; Bandari, G.; Baum, T. H. *Chem. Mater.* **1999**, *11* (3), 547.

(98) Drake, J. E.; Glavincevski, B. M.; Hemmings, R. T.; Henderson, H. E.; Ebsworth, E. A. V; Henderson, S. G. D. *Inorg. Synth.* **1979**, *19*, 274.

(99) Goldfarb, T. D.; Sujishi, S. *J. Am. Chem. Soc.* **1964**, *86* (9), 1679.

(100) Bentham, J. E.; Cradock, S.; Ebsworth, E. A. V. *Inorg. Nucl. Chem. Lett.* **1971**, *7* (11), 1077.

(101) Norman, A. D.; Jolly, W. L.; Saturnino, D.; Shore, S. G. *Inorg. Synth.* **1968**, *11*, 15.

(102) Luryi, S.; Kastalsky, A.; Bean, J. C. *IEEE Trans. Electron Devices* **1984**, *31* (9), 1135.

(103) Baribeau, J. M.; Jackman, T. E.; Houghton, D. C.; Maigné, P.; Denhoff, M. W. *J. Appl. Phys.* **1988**, *63* (100), 5738.

(104) Colace, L.; Masini, G.; Galluzzi, F.; Assanto, G.; Capellini, G.; Di Gaspare, L.; Palange, E.; Evangelisti, F. *Appl. Phys. Lett.* **1998**, *72* (24), 3175.

(105) Luan, H.-C.; Lim, D. R.; Lee, K. K.; Chen, K. M.; Sandland, J. G.; Wada, K.; Kimerling, L. C. *Appl. Phys. Lett.* **1999**, *75*, 2909.

(106) Grzybowski, G.; Beeler, R. T.; Jiang, L.; Smith, D. J.; Kouvetakis, J.; Menéndez, J. *Appl. Phys. Lett.* **2012**, *101* (100), 0.

(107) Xu, C.; Beeler, R. T.; Grzybowski, G. J.; Chizmeshya, A. V. G.; Smith, D. J.; Menéndez, J.; Kouvetakis, J. *J. Am. Chem. Soc.* **2012**, *134* (51), 20756.

(108) Shimoda, T.; Matsuki, Y.; Furusawa, M.; Aoki, T.; Yudasaka, I.; Tanaka, H.; Iwasawa, H.; Wang, D.; Miyasaka, M.; Takeuchi, Y. *Nature* **2006**, *440* (7085), 783.

(109) Han, S.; Dai, X.; Loy, P.; Lovaasen, J.; Huether, J.; Hoey, J. M.; Wagner, A.; Sandstrom, J.; Bunzow, D.; Swenson, O. F.; Akhatov, I. S.; Schulz, D. L. *J. Non. Cryst. Solids* **2008**, *354* (19-25), 2623.

(110) Kim, S.; Han, T.-H.; Jung, H.; Oh, Y.-S.; Pu, L.; Lee, P.-C.; Nam, J.-D. *J. Mater. Chem.* **2011**, *21* (9), 3025.

(111) Frisch, M. J.; Trucks, G. W.; Schlegel, H. B.; Scuseria, G. E.; Robb, M. A.; Cheeseman, J. R.; Montgomery Jr., J. A.; Vreven, T.; Kudin, K. N.; Burant, J. C.; Millam, J. M.; Iyengar, S. S.; Tomasi, J.; Barone, V.; Mennucci, B.; Cossi, M.; Scalmani, G.; Rega, N.; Petersson, G. A.; Nakatsuji, H.; Hada, M.; Ehara, M.; Toyota, K.; Fukuda, R.; Hasegawa, J.; Ishida, M.; Nakajima, T.; Honda, Y.; Kitao, O.; Nakai, H.; Klene, M.; Li, X.; Knox, J. E.; Hratchian, H. P.; Cross, J. B.; Bakken, V.; Adamo, C.; Jaramillo, J.; Gomperts, R.; Stratmann, R. E.; Yazyev, O.; Austin, A. J.; Cammi, R.; Pomelli, C.; Ochterski, J. W.; Ayala, P. Y.; Morokuma, K.; Voth, G. A.; Salvador, P.; Dannenberg, J. J.; Zakrzewski, V. G.; Dapprich, S.; Daniels, A. D.; Strain, M. C.; Farkas, O.; Malick, D. K.; Rabuck, A. D.; Raghavachari, K.; Foresman, J. B.; Ortiz, J. V.; Cui, Q.; Baboul, A. G.; Clifford, S.; Cioslowski, J.; Stefanov, B. B.; Liu, G.; Liashenko, A.; Piskorz, I.; Komaromi, P.; Martin, R. L.; Fox, D. J.; Keith, T.; Al-Laham, M. A.; Peng, C. Y.; Nanayakkara, A.; Challacombe, M.; Gill, P. M. W.; Johnson, B.; Chen, W.; Wong, M. W.; Gonzalez, C.; Pople, J. A. *Gaussian03*, Revision C.; Gaussian, Inc.: Wellingford, CT, 2004.

(112) Pitzer, K. S.; Gwinn, W. D. *J. Chem. Phys.* **1942**, *10* (7), 428.

(113) Mackay, K. M.; Sutton, K. J. *J. Chem. Soc. A Inorganic, Phys. Theor.* **1968**, No. 2312, 2312.

(114) Wistey, M. A.; Fang, Y.-Y.; Tolle, J.; Chizmeshya, A. V. G.; Kouvetakis, J. *Appl. Phys. Lett.* **2007**, *90* (8), 082108.

(115) Xu, C.; Gallagher, J. D.; Sims, P.; Smith, D. J.; Menéndez, J.; Kouvetakis, J. *Semicond. Sci. Technol.* **2015**, *30* (4), 045007.

(116) Spitzer, W. G.; Trumbore, F. A.; Logan, R. A. *J. Appl. Phys.* **1961**, *32* (10), 1822.

(117) Xu, C.; Gallagher, J. D.; Wallace, P. M.; Senaratne, C. L.; Sims, P.; Menéndez, J.; Kouvetakis, J. *Semicond. Sci. Technol.* **2015**, *30* (10), 105028.

(118) Kouvetakis, J.; Favaro, R.; Grzybowski, G. J.; Senaratne, C.; Menéndez, J.; Chizmeshya, A. V. G. *Chem. Mater.* **2014**, *26* (15), 4447.

(119) Claeys, C.; Simoen, E. *Germanium-based technologies: from materials to devices*; Elsevier, 2011.

(120) Vanhellemont, J.; Simoen, E. *Mater. Sci. Semicond. Process.* **2012**, *15* (6), 642.

(121) Chui, C. O.; Kulig, L.; Moran, J.; Tsai, W.; Saraswat, K. C. *Appl. Phys. Lett.* **2005**, *87* (9), 091909.

(122) Simoen, E.; Satta, A.; D'Amore, A.; Janssens, T.; Clarysse, T.; Martens, K.; De Jaeger, B.; Benedetti, A.; Hoflijk, I.; Brijs, B.; Meuris, M.; Vandervorst, W. *Mater. Sci. Semicond. Process.* **2006**, *9* (4-5 SPEC. ISS.), 634.

(123) Tsouroutas, P.; Tsoukalas, D.; Zergioti, I.; Cherkashin, N.; Claverie, A. *Mater. Sci. Semicond. Process.* **2008**, *11* (5), 372.

(124) Dilliway, G.; Van Den Boom, R.; Van Daele, B.; Leys, F. E.; Clarysse, T.; Parmentier, B.; Moussa, A.; Defranoux, C.; Benedetti, A.; Richard, O.; Bender, H.; Simoen, E.; Meuris, M. M. *ECS Trans.* **2006**, *3* (7), 599.

(125) Yamamoto, Y.; Kurps, R.; Mai, C.; Costina, I.; Murota, J.; Tillack, B. *Solid. State. Electron.* **2013**, *83*, 25.

(126) Yu, H.-Y.; Battal, E.; Okyay, A. K.; Shim, J.; Park, J.-H.; Baek, J. W.; Saraswat, K. C. *Curr. Appl. Phys.* **2013**, *13* (6), 1060.

(127) Poon, C. H.; Tan, L. S.; Cho, B. J.; Du, A. Y. *J. Electrochem. Soc.* **2005**, *152* (12), G895.

(128) Moriyama, Y.; Kamimuta, Y.; Kamata, Y.; Ikeda, K.; Sakai, A.; Tezuka, T. *Appl. Phys. Express* **2014**, *7* (10), 106501.

(129) Satta, A.; Simoen, E.; Duffy, R.; Janssens, T.; Clarysse, T.; Benedetti, A.; Meuris, M.; Vandervorst, W. *Appl. Phys. Lett.* **2006**, *88* (16), 5.

(130) Jang, S.-M.; Liao, K.; Reif, R. *J. Electrochem. Soc.* **1995**, *142* (10), 3520.

(131) Tutuc, E.; Chu, J. O.; Ott, J. A.; Guha, S. *Appl. Phys. Lett.* **2006**, *89* (26), 7.

(132) Hartmann, J. M.; Barnes, J. P.; Veillerot, M.; Fédéli, J. M.; Benoit A La Guillaume, Q.; Calvo, V. *J. Cryst. Growth* **2012**, *347* (1), 37.

(133) Scappucci, G.; Capellini, G.; Klesse, W. M.; Simmons, M. Y. *Nanoscale* **2013**, *5* (7), 2600.

(134) Scappucci, G.; Capellini, G.; Lee, W. C. T.; Simmons, M. Y. *Appl. Phys. Lett.* **2009**, *94* (16), 162106.

(135) Xu, C.; Senaratne, C. L.; Kouvetakis, J.; Menéndez, J. *Appl. Phys. Lett.* **2014**, *105* (23), 232103.

(136) Takenaka, M.; Morii, K.; Sugiyama, M.; Nakano, Y.; Takagi, S. *Jpn. J. Appl. Phys.* **2011**, *50* (1).

(137) Jakomin, R.; De Kersauson, M.; El Kurdi, M.; Largeau, L.; Mauguin, O.; Beaudoin, G.; Sauvage, S.; Ossikovski, R.; Ndong, G.; Chaigneau, M.; Sagnes, I.; Boucaud, P. *Appl. Phys. Lett.* **2011**, *98* (9), 2.

(138) Jakomin, R.; Beaudoin, G.; Gogneau, N.; Lamare, B.; Sagnes, I. *Proceeding XIII Eur. Work. pn Met. Vap. Phase Ep. Conf.* **2009**, *C.21*, 7.

(139) Xie, J.; Tolle, J.; D'Costa, V. R.; Weng, C.; Chizmeshya, A. V. G.; Menendez, J.; Kouvetakis, J. *Solid. State. Electron.* **2009**, *53* (8), 816.

(140) Isherwood, B. J.; Wallace, C. A. *J. Appl. Crystallogr.* **1970**, *3* (2), 66.

(141) Xu, C.; Senaratne, C. L.; Kouvetakis, J.; Menéndez, J. *Phys. Rev. B* **2016**, *93* (4), 041201.

(142) Dresselhaus, G.; Kip, A. F.; Kittel, C. *Phys. Rev.* **1955**, *98* (2), 368.

(143) Cardona, M.; Paul, W.; Brooks, H. *Helv. Phys. Acta* **1960**, 329.

(144) Hilsum, C. *Electron. Lett.* **1974**, *10* (13), 259.

(145) Cuttriss, D. B. *Bell Syst. Tech. J.* **1961**, *40* (2), 509.

(146) Ralph, H. I.; Simpson, G.; Elliott, R. J. *Phys. Rev. B* **1975**, *11* (8), 2948.

(147) Oehme, M.; Werner, J.; Kasper, E. *J. Cryst. Growth* **2008**, *310*, 4531.

(148) Thareja, G.; Chopra, S.; Adams, B.; Kim, Y.; Moffatt, S.; Saraswat, K.; Nishi, Y. *IEEE Electron Device Lett.* **2011**, *32* (7), 838.

(149) Thompson, P.; Silvestre, C.; Twigg, M.; Jernigan, G.; Simons, D. . *Thin Solid Films* **1998**, *321* (1-2), 120.

(150) Foord, J. .; Howard, F. .; McGrady, G. .; Davies, G. . *J. Cryst. Growth* **1998**, *188* (1-4), 144.

(151) Menna, R. J.; Capewell, D. R.; Martinelli, R. U.; Ayers, W.; Moulton, R.; Palmer, J.; Olsen, G. *J. Cryst. Growth* **1994**, *141* (1-2), 310.

(152) Cai, Y.; Thorpe, M. F. *Phys. Rev. B* **1992**, *46* (24), 15872.

(153) Martins, J. L.; Zunger, A. *Phys. Rev. B* **1984**, *30* (10), 6217.

(154) McSkimin, H. J.; Andreatch, P. *J. Appl. Phys.* **1964**, *35* (11), 3312.

(155) Van de Walle, C. G. *Phys. Rev. B* **1989**, *39* (3), 1871.

(156) Ahmad, C. N.; Adams, A. R. *Phys. Rev. B* **1986**, *34* (4), 2319.

(157) Teherani, J. T.; Chern, W.; Antoniadis, D. A.; Hoyt, J. L.; Ruiz, L.; Poweleit, C. D.; Menéndez, J. *Phys. Rev. B* **2012**, *85* (20), 205308.

(158) Ito, R. *J. Phys. Soc. Japan* **1963**, *18* (11), 1604.

(159) Furukawa, Y. *J. Phys. Soc. Japan* **1962**, *17* (4), 630.

(160) Chroneos, A. *J. Appl. Phys.* **2010**, *107* (7), 076102.

(161) Chroneos, A. *Mater. Sci. Semicond. Process.* **2012**, *15* (6), 691.

(162) Pan, S. H.; Recht, D.; Charnvanichborikarn, S.; Williams, J. S.; Aziz, M. J. *Appl. Phys. Lett.* **2011**, *98* (12), 14.

(163) Wu, C.; Crouch, C. H.; Zhao, L.; Carey, J. E.; Younkin, R.; Levinson, J. A.; Mazur, E.; Farrell, R. M.; Gothoskar, P.; Karger, A. *Appl. Phys. Lett.* **2001**, *78* (13), 1850.

(164) Baumann, A. L.; Guenther, K. M.; Saring, P.; Gimpel, T.; Kontermann, S.; Seibt, M.; Schade, W. *Energy Procedia* **2012**, *27*, 480.

(165) Bao, X.; Liu, F.; Zhou, X. *Optik (Stuttg).* **2012**, *123* (16), 1474.

(166) Guenther, K. M.; Baumann, A. L.; Gimpel, T.; Kontermann, S.; Schade, W. *Energy Procedia* **2012**, *27*, 555.

(167) Janzén, E.; Stedman, R.; Grossmann, G.; Grimmeiss, H. G. *Phys. Rev. B* **1984**, *29* (4), 1907.

(168) Kim, T. G.; Warrender, J. M.; Aziz, M. J. *Appl. Phys. Lett.* **2006**, *88* (24), 98.

(169) Liu, K.; Qu, S.; Zhang, X.; Tan, F.; Bi, Y.; Lu, S.; Wang, Z. *Appl. Phys. A Mater. Sci. Process.* **2014**, *114* (3), 765.

(170) Brotherton, S. D.; King, M. J.; Parker, G. J. *J. Appl. Phys.* **1981**, *52* (7), 4649.

(171) Astrov, Y. A.; Portsel, L. M.; Lodygin, A. N.; Shuman, V. B. *Semicond. Sci. Technol.* **2011**, *26* (5), 055021.

(172) Guenther, K. M.; Gimpel, T.; Kontermann, S.; Schade, W. *Appl. Phys. Lett.* **2013**, *102* (20), 16.

(173) Grimmeiss, H. G.; Montelius, L.; Larsson, K. *Phys. Rev. B* **1988**, *37* (12), 6916.

(174) Ikeda, K.; Yamashita, Y.; Sugiyama, N.; Taoka, N.; Takagi, S. I. *Appl. Phys. Lett.* **2006**, *88* (15), 16.

(175) Koike, M.; Kamimuta, Y.; Tezuka, T. *Appl. Phys. Express* **2011**, *4* (2), 2.

(176) Koike, M.; Kamimuta, Y.; Tezuka, T. *Appl. Phys. Lett.* **2013**, *102* (3).

(177) Tohyama, S. Protection Circuit for Semiconductor Device. US 5,684,323, 1997.

(178) Zhou, Z.; Li, C.; Lai, H.; Chen, S.; Yu, J. *J. Cryst. Growth* **2008**, *310* (10), 2508.

(179) Shin, K. W.; Kim, H. W.; Kim, J.; Yang, C.; Lee, S.; Yoon, E. *Thin Solid Films* **2010**, *518* (22), 6496.

(180) Yamamoto, Y.; Zaumseil, P.; Arguirov, T.; Kittler, M.; Tillack, B. *Solid. State. Electron.* **2011**, *60* (1), 2.

(181) Li, H.; Cui, Y. X.; Wu, K. Y.; Tseng, W. K.; Cheng, H. H.; Chen, H. *Appl. Phys. Lett.* **2013**, *102* (25), 251907.

(182) Gaubas, E.; Vanhellemont, J. *Appl. Phys. Lett.* **2006**, *89* (14), 14.

(183) Smirl, A. L.; Moss, S. C.; Lindle, J. R. *Phys. Rev. B* **1982**, *25* (4), 2645.

(184) Du, W.; Ghetmiri, S. A.; Conley, B. R.; Mosleh, A.; Nazzal, A.; Soref, R. A.; Sun, G.; Tolle, J.; Margetis, J.; Naseem, H. A.; Yu, S.-Q. *Appl. Phys. Lett.* **2014**, *105* (5), 051104.

(185) Moslehi, M. M. Low-temperature in-situ dry cleaning process for semiconductor wafer. US 5,403,434, April 4, 1995.

(186) Doolittle, L. R. *Nucl. Instruments Methods Phys. Res. B* **1985**, *9* (3), 344.

(187) Meyerson, B. S.; Uram, K. J.; LeGoues, F. K. *Appl. Phys. Lett.* **1988**, *53* (1988), 2555.

(188) Faleev, N.; Sustersic, N.; Bhargava, N.; Kolodzey, J.; Magonov, S.; Smith, D. J.; Honsberg, C. *J. Cryst. Growth* **2013**, *365*, 35.

(189) Ayers, J. E. E. *J. Cryst. Growth* **1994**, *135*, 71.

(190) Matthews, J. W.; Blakeslee, A. E. *J. Cryst. Growth* **1974**, *27*, 118.

(191) Houghton, D. C. *J. Appl. Phys.* **1991**, *70* (4), 2136.

(192) Menéndez, J. *J. Appl. Phys.* **2009**, *105* (6), 063519.

(193) Hirth, J. P.; Lothe, J. *Theory of Dislocations*; McGraw-Hill: New York, 1968.

(194) Toonder, J. M. J. den; Dommelen, J. A. W. van; Baaijens, F. P. T. *Model. Simul. Mater. Sci. Eng.* **1999**, *7* (6), 909.

(195) Price, D. L.; Rowe, J. M.; Nicklow, R. M. *Phys. Rev. B* **1971**, *3* (4), 1268.

(196) Bhargava, N.; Coppinger, M.; Prakash Gupta, J.; Wielunski, L.; Kolodzey, J. *Appl. Phys. Lett.* **2013**, *103* (4).

(197) Hull, R.; Bean, J. C.; Buescher, C. *J. Appl. Phys.* **1989**, *66* (12), 5837.

(198) Yonenaga, I.; Werner, M.; Bartsch, M.; Messerschmidt, U.; Werner, E. R. *Phys. Status Solidi* **1999**, *171* (1), 35.

(199) Gosling, T. J.; Jain, S. C.; Harker, A. H. *Phys. Status Solidi* **1994**, *146* (2), 713.

(200) Gencarelli, F. 2014, Private Communication, cited in Senaratne, C. L.; Gallagher, J. D.; Jiang, L.; Aoki, T.; Menéndez, J.; Kouvetakis, J. *J. Appl. Phys.* **2014**, *116* (13), 133509.

(201) Kouvetakis, J.; Menendez, J.; Chizmeshya, A. V. G. *Annu. Rev. Mater. Res.* **2006**, *36* (1), 497.

(202) Sun, G.; Soref, R. A.; Cheng, H. H. *J. Appl. Phys.* **2010**, *108* (3), 033107.

(203) Moontragoon, P.; Ikonić, Z.; Harrison, P. *Semicond. Sci. Technol.* **2007**, *22* (7), 742.

(204) Eckhardt, C.; Hummer, K.; Kresse, G. *Phys. Rev. B* **2014**, *89* (16), 165201.

(205) Trita, A.; Cristiani, I.; Degiorgio, V.; Chrastina, D.; Von Känel, H. *Appl. Phys. Lett.* **2007**, *91* (4), 1.

(206) Menéndez, J.; Kouvetakis, J. *Appl. Phys. Lett.* **2004**, *85* (7), 1175.

(207) Haynes, J. R. *Phys. Rev.* **1955**, *98* (6), 1866.

(208) Arguirov, T.; Kittler, M.; Abrosimov, N. V. *J. Phys. Conf. Ser.* **2011**, *281*, 012021.

(209) Grzybowski, G.; Roucka, R.; Mathews, J.; Jiang, L.; Beeler, R.; Kouvetakis, J.; Menéndez, J. *Phys. Rev. B* **2011**, *84*, 1.

(210) Gallagher, J. D.; Xu, C.; Jiang, L.; Kouvetakis, J.; Menéndez, J. *Appl. Phys. Lett.* **2013**, *103* (20), 202104.

(211) Jiang, L.; Gallagher, J. D.; Senaratne, C. L.; Aoki, T.; Mathews, J.; Kouvetakis, J.; Menéndez, J. *Semicond. Sci. Technol.* **2014**, *29* (11), 115028.

(212) Jiang, L.; Xu, C.; Gallagher, J. D.; Favaro, R.; Aoki, T.; Menéndez, J.; Kouvetakis, J. *Chem. Mater.* **2014**, *26* (8), 2522.

(213) Gallagher, J. D.; Senaratne, C. L.; Kouvetakis, J.; Menéndez, J. *Appl. Phys. Lett.* **2014**, *105*, 142102.

(214) Kim, J.; Bedell, S. W.; Sadana, D. K. *Appl. Phys. Lett.* **2011**, *98* (8), 082112.

(215) Dutt, B.; Lin, H.; Sukhdeo, D. S.; Vulovic, B. M.; Gupta, S.; Nam, D.; Saraswat, K. C.; Harris, J. S. *IEEE J. Sel. Top. Quantum Electron.* **2013**, *19* (5), 1502706.

(216) Senaratne, C. L.; Gallagher, J. D.; Aoki, T.; Kouvetakis, J.; Menéndez, J. *Chem. Mater.* **2014**, *26* (20), 6033.

(217) Geiger, R.; Frigerio, J.; Süess, M. J.; Chrastina, D.; Isella, G.; Spolenak, R.; Faist, J.; Sigg, H. *Appl. Phys. Lett.* **2014**, *104* (6), 062106.

(218) Chizmeshya, A. V. G.; Ritter, C. J.; Hu, C.; Tice, J. B.; Tolle, J.; Nieman, R. A.; Tsong, I. S. T.; Kouvetakis, J. *J. Am. Chem. Soc.* **2006**, *128* (21), 6919.

(219) Chynoweth, A. G.; Feldmann, W. L.; Logan, R. A. *Phys. Rev.* **1961**, *121* (3), 684.

APPENDIX A

EXPERIMENTAL PARAMETERS FOR DEPOSITION OF $GE_{1-Y}SN_Y$ ALLOYS ON GE/SI SUBSTRATES

Introduction

This appendix describes the detailed procedures used for the deposition of GeSn alloys described in chapters 5, 6 and 7. The first section describes the deposition of intrinsic alloys with 0%-6% Sn composition range using Ge_2H_6/SnD_4 precursor mixtures. The second section describes the deposition of samples with compositions 5%-11% using Ge_3H_8 and SnD_4. These alloys films used in the studies described in Chapter 5. The next section describes the growth of *n*-type doped GeSn alloys in the 4%-9% composition range described in Chapter 6. The fourth section describes the deposition of intrinsic GeSn layers on *n*-type doped Ge buffers in order to obtain the active components of *n*-Ge/*i*-$Ge_{1-y}Sn_y$/*p*-$Ge_{1-z}Sn_z$ diodes. Techniques for optimizing epilayer quality such as growth of Ge spacer layers using Ge_3H_8 and variable temperature growth are also described in this section. Next, the growth of thick *n*-type doped GeSn films which act as the bottom contact layers of *n*-$Ge_{1-y}Sn_y$/*p*-$Ge_{1-z}Sn_z$ diodes is described. In the fifth section, deposition of the *p*-type doped GeSn layers, which complete the device stacks outlined in the previous sections, is described. Finally, the synthesis methods for *n*-$Ge_{1-x}Sn_x$/*i*-$Ge_{1-y}Sn_y$/*p*-$Ge_{1-z}Sn_z$ diodes is described. Properties of all of the above diode structures were discussed in Chapter 7.

Growth of Intrinsic $Ge_{1-y}Sn_y$ Alloys in the Three-Zone Hot Wall UHV CVD Reactor

The first series of GeSn alloys on Ge buffered Si substrates, with compositions from 1-6% Sn, were produced using Ge_2H_6 and SnD_4 precursors in a UHV-CVD chamber heated using a three-zone clam shell resistance furnace which allows the pre-activation of the precursors before reaching the growth front. The precursor mixtures were made by mixing ~100 LTorr of Ge_2H_6 with varying amounts of SnD_4 from 1.3 – 6.1 LTorr in 3 L glass containers. The

amounts of Ge_2H_6 and SnD_4 used to produce representative samples in the given composition range are listed in Table A: 1, which also contains additional growth parameters, as discussed below. These precursor mixtures were also diluted with research grade H_2 such that the final concentration of Ge_2H_6 with respect to H_2 was 10% (i.e. the partial pressure of H_2 is nine times that of Ge_2H_6). Therefore the final pressure of H_2 in a mixture container is ~300 Torr.

Before the growth, the 4" virtual Ge substrates were cleaved into 45 mm × 45 mm quarter wafer segments to allow their placement in the wafer boat. Typically two wafers were used per growth. The wafers were subjected to a pre-epi clean by dipping in a 5% aqueous HF solution for 2 min in order to remove the native oxide. After the 2 min HF dip, the wafers were rinsed in de-ionized water for 5 min, and then blow dried using ultra high purity N_2.

Prior to introducing the wafers into the CVD chamber, it was passivated by a flow of SiH_4 lasting for 5 min with the chamber temperature at 700°C, 725°C and 725°C in the first, second and third zones respectively. The pressure used for passivation was 200 mTorr. For this procedure, the required amount of SiH_4 was collected in the gas manifold connected to the deposition chamber. A pressure of 300 Torr in the manifold, which has a volume of ~100 mL, was found to be sufficient for a single passivation.

The cleaned wafers were first placed in a quartz wafer boat in the load lock, with one wafer in the 4th slot (labelled A) and a second wafer in the 8th slot (labelled B). A schematic of the wafer boat, indicating the slots in the frame used for placing the wafers, is given

Table A: 1 – Growth temperatures and mixture compositions for intrinsic $Ge_{1-y}Sn_y$ alloy films deposited on Ge/Si substrates using the three-zone UHV-CVD.

Sample	Temperature (°C)			Amount of Ge_2H_6 (LTorr)	Amount of SnD_4 (LTorr)	Amount of H_2 (LTorr)	Growth Time (min)	Epilayer Sn content (%)	Epilayer Thickness (nm)
	Zone 1	Zone 2	Zone 3						
1	325	350	350	107.6	1.34	968	100	1	738
2	325	350	350	101.6	2.25	914	100	1.7	905
3	315	335	335	91.3	2.69	822	91	3	538
4	300	335	335	96.5	4.87	868	95	4	667
5	290	315	315	96.9	6.06	872	96	5.4	429

in Figure A: 1. The load lock was then pumped down to a pressure of 1.0×10^{-6} Torr. After this pressure was reached, the boat was moved into the growth chamber under flow of H_2. The temperature of the wafers was allowed to equilibrate for 2 min, then an *in-situ* cleaning step was performed by flowing Ge_2H_6 over the surface of the wafer. The Ge_2H_6 used had a concentration of 30% (in H_2) and flowed at a rate of 10% through a MFC with a maximum flow of 50 sccm calibrated for SiH_4 (MFC TZ-4). Together with the Ge_2H_6 flow, a flow of pure H_2 was maintained via a 200 sccm MFC calibrated for He operating at 10% flow (MFC TZ-2). The pressure inside the chamber was maintained at 50 mTorr during this 'digermane clean', which lasted 5 min. At the end of this period, the Ge_2H_6/SnD_4 mixture prepared earlier was introduced into the chamber via MFC TZ-4 with a flow rate of 30%, and the pressure was increased to 300 mTorr by controlling the gas flow out of the chamber using a throttle valve. The growths were typically conducted until the pressure in the

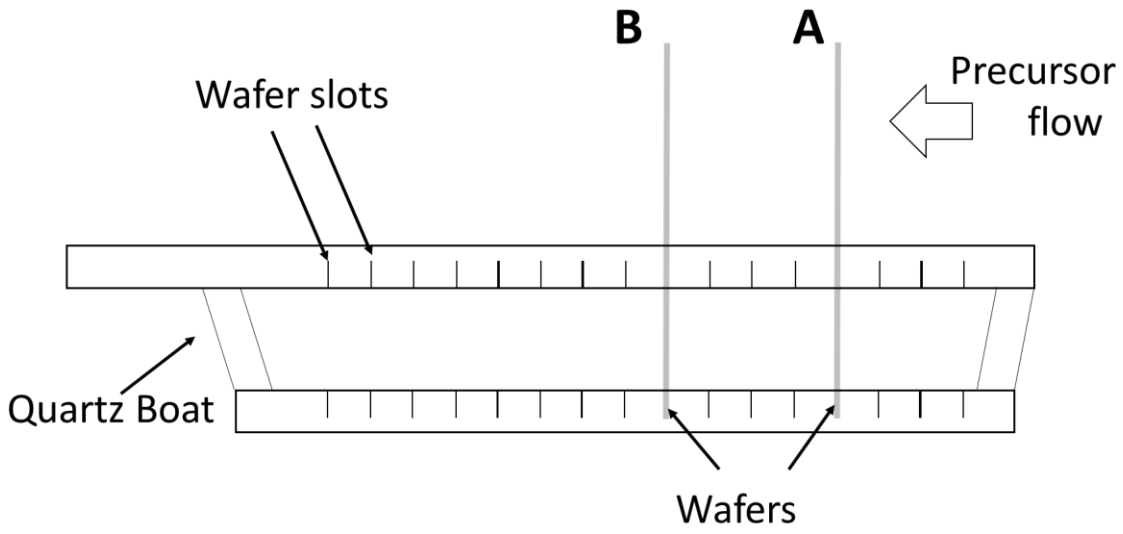

Figure A: 1 – Side-view schematic of quartz boat used to hold the wafers inside the UHV-CVD chamber during deposition. The relative positions of the wafers which are placed in slots #4 and #8 in this case is indicated, as is the direction of precursor flow during growth.

precursor mixture bulb dropped to 40 Torr, at which point the MFCs are no longer capable

of maintaining an even precursor flow. After this point is reached, the flow of the precursor mixture is turned off, and the boat containing the wafers is removed to the load lock under H_2 flow.

The growth time for each sample is given in column eight of Table A: 1, which lists growth parameters for representative samples deposited using techniques described above. The second, third and fourth columns of the table give the temperatures set in the zones of the furnace, with zone 1 being closest to the gas inlet. The next two columns give the amounts of Ge_2H_6 and SnD_4 precursors used for the respective growths. Column seven gives the amount of H_2 carrier gas used in each mixture. The final two columns give the Sn content of the GeSn epilayer formed on the 'A' wafer as a result of the deposition, and thickness of the film.

In order to get higher Sn contents, Ge_3H_8 was used for the growth of the next series of samples. These were grown in a second UHV-CVD reactor which is heated using a single zone clam shell furnace.

Growth of Intrinsic $Ge_{1-y}Sn_y$ Alloys in the Single-Zone Hot Wall UHV CVD Reactor

The substrate preparation method for this reactor is similar to the earlier procedure, with the Ge buffered Si wafers being cleaved into 45 mm × 45 mm quarters and then cleaned using a 2 min HF/H_2O dip. The wafers are then placed in the loading boat where they are positioned in the third and sixth slots of the quartz boat (see Figure A: 1). The wafers are labeled 'A' and 'B' respectively. After placing the wafers on the boat, the load lock is evacuated using a turbomolecular pump to a pressure of 1.0×10^{-6} Torr, and the boat is introduced into the chamber under hydrogen flow. The flow was conducted at a rate of

Table A: 2 – Growth temperatures and mixture compositions for intrinsic $Ge_{1-y}Sn_y$ alloy films deposited on Ge/Si substrates using the single-zone UHV-CVD.

Sample	Tempe-rature (°C)	Amount of Ge_3H_8 (LTorr)	Amount of SnD_4 (LTorr)	Amount of H_2 (LTorr)	Growth Time (min)	Epilayer Sn content (%)	Epilayer Thickness (nm)
6	320	43.3	5.4	1962	117	4.9	739
7	315	42.1	6.4	1916	113	6	682
8	310	33.9	5.5	1170	115	7	568
9	305	34.8	6.4	1201	116	7.8	463
10	295	34.2	7.8	2318	148	9	549
11	285	21.5	6.0	2296	142	10.5	260

20% via a MFC calibrated with N_2 which had a maximum flow of 90 sccm (MFC SZ-4). The CVD chamber was passivated prior to growth by SiH_4 at a temperature of 750°C and a pressure of 200 mTorr for 5 min.

After positioning the wafers in the growth chamber, the temperature was allowed to equilibrate for a period of 2 min. Thereafter, the wafers surfaces were subjected to further cleaning by flowing 10% Ge_2H_6 in H_2 mixture at a flow rate of 45% via a MFC calibrated for GeH_4 with a maximum flow of 20 sccm (MFC SZ-3). At the end of this step, the growth mixture (described for each sample in Table A: 2) was introduced into the chamber via MFC SZ-3, along with H_2 from MFC SZ-4. The precursor mixtures used for a series of representative samples are given in Table A: 2. The second column lists the temperature used for the growths, while the next three columns list the amounts of Ge_3H_8, SnD_4 and H_2 used in each case. The amounts are given in liter-Torr, and since the mixtures are made in 3 L glass containers, the final pressure of a mixture is 390 Torr – 770 Torr. The mixture flow was carried out using either MFC SZ-3 or a 100 sccm MFC calibrated for He (MFC SZ-1). A flow rate of 64% from the former (used for samples 6 to 9) is equivalent to a flow

rate of 28% from the latter (used for samples 9 and 10), and no difference was seen when using one MFC over the other. In both cases, a concomitant H_2 flow was maintained through MFC SZ-4 at a rate of 15.5%.

The above table also gives the growth times, layer thicknesses and Sn contents of the 'A' wafers in the final three columns. This data can be used as a guide for determining requisite precursor ratios for growth of intrinsic GeSn alloys with target Sn compositions using Ge_3H_8 and SnD_4.

Growth of *n*-type Doped $Ge_{1-y}Sn_y$ Alloys

The growth of *n*-doped $Ge_{1-y}Sn_y$ layers described in Chapter 6 was conducted in the single zone hot wall CVD system on intrinsic Ge buffered Si substrates. These were cleaned using HF/H_2O, and loaded into the chamber following the same procedures described above for growth of intrinsic $Ge_{1-y}Sn_y$ alloys. After introduction of wafers into the chamber, a further cleaning step was carried out using Ge_2H_6 as described earlier. Thereafter, the growth mixture was introduced into the chamber via MFC SZ-1 at a flow rate of 28%, together with H_2 via MFC SZ-4 at a flow rate of 15.5%. The depositions were conducted at a pressure of 200 mTorr.

Several different donor sources were used for the above depositions. The samples doped using $P(GeH_3)_3$ are listed in Table A: 3, which gives the growth temperatures, the amounts of Ge_3H_8 , SnD_4 and $P(GeH_3)_3$ precursors in the mixtures, the amount of H_2 used to dilute each mixture, and in the final column, the growth time. In addition to $P(GeH_3)_3$, the silyl compounds $P(SiH_3)_3$, $As(SiH_3)_3$, and $Sb(SiH_3)_3$ were all used as donor delivery agents. The corresponding growth temperature, mixture composition and growth time data for

Table A: 3 – Precursor mixtures, growth temperatures and times for $Ge_{1-y}Sn_y$ alloys *n*-type doped using $P(GeH_3)_3$.

Sample	Temperature (°C)	Amount of precursor (LTorr)				Growth time (min)
		Ge_3H_8	SnD_4	$P(GeH_3)_3$	H_2	
12	325	41.51	3.83	0.247	1939	130
13	320	41.51	4.70	0.200	1945	129
14	315	41.99	6.36	0.220	1936	123
15	295	25.15	5.06	0.148	2281	150

depositions using these compounds are given in Table A: 4. For all of the above growths, the mixtures were made in 3 L glass containers, resulting in final H_2 pressures of 500 – 760 Torr within.

Table A: 5 gives the thicknesses, carrier concentrations and Sn contents of the 'A' wafers of the growths listed in Tables A: 3 and A: 4. This data portrays the composition and doping ranges which can be obtained using the methods described above.

Table A: 4 - Precursor mixtures, growth temperatures and times for $Ge_{1-y}Sn_y$ alloys *n*-type doped using $M(SiH_3)_3$ (M = P, As, Sb).

Sample	Temperature (°C)	Amount of precursor (LTorr)				Growth time (min)
		Ge_3H_8	SnD_4	$M(SiH_3)_3$	H_2	
M=P						
16	325	33.03	3.06	0.196	1554	102
17	305	27.93	4.35	0.138	2183	130
18	300	25.15	4.68	0.157	2319	150
M=As						
19	325	33.03	3.08	0.202	1559	99
20	325	33.33	3.12	0.601	1578	101
M=Sb						
21	325	33.94	2.55	0.334	1580	101

Table A: 5 – Composition, thickness and active carrier concentrations of $Ge_{1-y}Sn_y$ alloys doped with P, As and Sb atoms.

Sample	Dopant atom	Thickness (nm)	Carrier concentration ($/cm^3$)	Composition (Sn %)
12	P	625	3.7×10^{19}	4.4
13	P	625	1.2×10^{19}	5.3
14	P	580	2.8×10^{19}	6.2
15	P	375	1.0×10^{19}	8.7
16	P	575	2.5×10^{19}	4.6
17	P	400	1.3×10^{19}	6.4
18	P	475	1.0×10^{19}	8
19	As	620	1.0×10^{19}	4.2
20	As	475	6.9×10^{19}	3.8
21	Sb	500	5.7×10^{18}	3.2

Growth of *pin* diodes with Ge bottom contact layers

The *n*-Ge/*i*-Ge_{1-y}Sny/*p*-$Ge_{1-z}Sn_z$ series of *pin* diode structures described in Chapter 7 were deposited on *n*-type doped virtual Ge substrates, which acted as the bottom contact layers. Prior to growth, these were subjected to surface cleaning using the same methods described earlier for intrinsic Ge buffers. All the intrinsic GeSn epilayers described here were deposited in the single zone hot wall CVD reactor described in the previous sections. The growth chamber was passivated either using SiH_4 at 750°C or Si_3H_8 at 650°C for a period of 5-10 min prior to the deposition, following procedures identical to those described earlier. For both passivations the chamber pressure was 200 mTorr.

The $Ge_{1-y}Sn_y$ diode with the lowest active layer Sn content of y=0.02 (sample 22) was deposited using a mixture of 55.6 LTorr Ge_2H_6 and 1.77 LTorr of SnD_4, diluted with H_2 so that the concentration of Ge_2H_6 was 10%. This precursor mixture was introduced into the chamber via MFC SZ-1 at flow rate of 13%, along with a concomitant H_2 flow via MFC

SZ-5 at a rate of 10%. The latter MFC was calibrated for N_2 with a maximum flow of 90 sccm. The deposition was conducted at a temperature of 335°C and a pressure of 200 mTorr. The A wafer obtained using these growth parameters was 530 nm thick, which corresponds to a growth rate of 4.8 nm/min.

The diode structures with higher Sn contents were deposited using Ge_3H_8/SnD_4 mixtures. For the samples 23 and 24, which have active layer compositions of 5.5% and 7% respectively, the growth procedures used were the same as for the deposition of intrinsic GeSn layers described earlier in the second part of this appendix. Flow rates of 28% and 20% through MFCs SZ-1 and SZ-5 were used for the precursor mixture and the concomitant H_2 flow respectively. The amounts of precursors used, growth temperatures and the resultant film properties are given in Table A: 6.

Table A: 6 – Mixture compositions, growth times, temperatures and resultant epilayer properties for 5.5% and 7% samples.

Sample	Tempe-rature (°C)	Amount of precursor (LTorr)			Growth time (min)	Thickness (nm)	Compo-sition (% Sn)
		Ge_3H_8	SnD_4	H_2			
23	315	33.9	4.3	1841	116	450	5.3
24	305	27.5	4.4	2104	130	400	6.9

For growths of higher Sn (8-11%) samples listed as 25-27 in Table A: 7, an additional *in-situ* surface cleaning procedure was employed. The quarter wafers were cleaned with HF/H_2O as before, and then introduced into the growth chamber while the chamber temperature was 340°C instead of the deposition temperature, as was the case for previous growths. After allowing the temperature to equilibrate for 5 min, a mixture containing 2% Ge_3H_8 in H_2 was introduced into the chamber via MFC #1 to conduct regrowth of the Ge surface. This was allowed to procced for a period of ~30 min, whereupon the temperature

control of the clam shell furnace was set to the growth temperature of the $Ge_{1-y}Sn_y$ layer and the chamber was allowed to cool down. The amount of material in the regrowth mixture must be adjusted to allow for the different cooling times which result from different growth temperatures for the $Ge_{1-y}Sn_y$ epilayers. These temperatures are given in column two of Table A: 7. After growth temperature was reached, the $Ge_{1-y}Sn_y$ precursor mixture was introduced into the chamber via MFC SZ-1 at a flow rate of 28%, together with H_2 flow via MFC SZ-5 at 20% as before. The precursor mixture compositions are listed in Table A: 7, where the amounts of G_3H_8, SnD_4 and H_2 for each mixture are given in liter-Torr. As in earlier growths, the mixtures were made in 3 L glass containers, leading to pressures of 650 – 770 Torr in the final mixtures. The growth time for each growth, and the thickness and Sn composition of the final GeSn epilayers, are given in the final three columns of the table.

For intrinsic layers with higher Sn contents (samples 28 – 29, 12-13.7%)), the sample cleaning procedure used was the same as above, including the regrowth of the Ge surface. Representative samples in this range are listed in Table A: 8. However, a temperature gradient was applied during growth in order to obtain thicker intrinsic alloy films. The

Table A: 7 - Mixture compositions, growth times and temperatures for samples deposited at a constant temperature with a Ge refreshing layer. The thickness and composition of the resultant 'A' wafers is also given, as a guide to the film properties achieved under a given set of conditions.

Sample	Tempe-rature (°C)	Precursor amount (LTorr)			Growth time (min)	Thickness (nm)	Composition (%)
		Ge_3H_8	SnD_4	H_2			
25	295	22.4	4.9	1903	118	375	8.6
26	287	26.9	7.2	2282	140	430	10.5
27	283	26.8	7.2	2292	140	400	11.1

Table A: 8 – Mixture composition, growth time and thickness for device stack intrinsic layers grown with the temperature ramp method. The thickness and composition of the 'A' wafers are given as a guide to the achievable film parameters.

Sample	Temperature (°C)		Precursor amount (LTorr)			Growth time	Thick-ness	Compo-sition
	Initial	Final	Ge_3H_8	SnD_4	H_2	(min)	(nm)	(%)
28	280	288	26.9	8.6	2330	143	360	12.0
29	270	280	26.4	10.0	2320	142	430	12.8
30	273	278	26.3	9.9	2326	142	335	13.7

growth of the intrinsic $Ge_{1-y}Sn_y$ layer was initiated as above by introducing the precursor mixture into the growth chamber at a suitable growth temperature. The growth was allowed to proceed at this temperature for 45-60 min, with the aim of creating a strain relaxed seed layer suitable for further growth. Thereafter, the chamber temperature was slowly increased by 5-10°C over a period of 10-30 min. The growth was then allowed to proceed to completion at the higher temperature. The chamber pressure during growth as maintained at 200 mTorr. The thickness and composition properties of the films obtained following this procedure are given in last two columns of Table A: 8. The second and third columns of the same table lists the initial and final temperatures used in each growth. Columns 4-6 give the amounts of germanium and tin precursors and H_2 carrier gas used in each mixture, which was made in a 3 L container. The final mixture pressure is ~770 Torr, and it was fed into the chamber via MFC SZ-1 at a flow rate of 28%. A concomitant H_2 flow was also maintained, as was the case in earlier growths.

In conclusion, this section outlines the growth parameters which can be used to synthesize intrinsic GeSn alloys on *n*-type doped Ge/Si substrates which can be used as active layers of *n*-Ge/*i*-Ge_{1-y}Sny/*p*-$Ge_{1-z}Sn_z$ diodes.

Growth of *n*-type doped layers for *pn* junction diodes

By following the temperature gradient growth method described above for samples 28-30, it was possible to obtain thick, strain relaxed films. Such films can be *n*-type doped as the first step in the fabrication of *pn* junction diodes with compositions above indirect-direct crossover. These films were deposited on intrinsic virtual Ge substrates which were quartered and subjected to a HF clean as described earlier. Thereafter the wafers were introduced into the single zone CVD reactor, where the Ge surface was subjected to regrowth. The growth of the *n*-type doped epilayer was initiated by introducing the precursor mixture consisting of Ge_3H_8, SnD_4, $P(SiH_3)_3$ and H_2 into the growth chamber via MFC SZ-1 at a flow rate of 28%. Concomitant H_2 flow was maintained at a rate of 20% via MFC SZ-5. The procedure for temperature variation during growth was similar to that describe earlier intrinsic $Ge_{1-y}Sn_y$ epilayers. The temperature ranges used for the representative samples is given in the second and third columns of Table A: 9, together with amounts of precursors used for growth mixtures listed in the next three columns. The final column of Table A: 9 gives the growth time for each epilayer.

The properties of the resultant films are listed in Table A: 10, which gives the film thickness, Sn content and active donor concentration for the various epilayers. This data

Table A: 9 – Growth temperatures, times and mixture compositions for *n*-type doped samples grown using the temperature gradient method.

Sample	Temperature (°C)		Mixture contents (LTorr)				Growth Time (min)
	Initial	Final	Ge_3H_8	SnD_4	$P(SiH_3)_3$	H_2	
31	287	295	27.12	7.26	0.31	2310	145
32	280	287	26.76	7.81	0.39	2297	145
33	280	287	26.80	8.82	0.14	2323	147
34	280	287	26.81	8.83	0.40	2316	142

provides a guide to the various types of films which can be obtained using the above procedures.

Table A: 10 – Thickness, composition and active carrier concentrations obtained in the 'A' wafers using the growth parameters listed in Table A: 9.

Sample	Thickness (nm)	Composition (% Sn)	Doping ($/cm^{-3}$)
31	525	9.3	4.8×10^{18}
32	325	11.2	2.7×10^{19}
33	535	12.0	5.7×10^{18}
34	480	11.9	2.0×10^{19}

Growth of *p*-type doped top contact layers

The *p*-type doped top contact layers required to complete the above device stacks were deposited in the three zone UHV-CVD reactor. The conditions used for depositing *p*-type layers for samples listed earlier in Tables A: 7, A: 8 and A: 10 are given in Table A: 11. Prior to deposition, the surface of the structures which consist of the *n*-type (for *pn* diodes) and intrinsic (for *pin* diodes) layers deposited using the methods described thus far were cleaned using aqueous HF. The wafer loading procedure was identical to the one used when depositing intrinsic $Ge_{1-y}Sn_y$ alloys using Ge_2H_6 in the three zone reactor, which was described earlier. After loading, the surfaces were subjected to an *in-situ* cleaning step using Ge_2H_6. The growth of the *p*-type layers was initiated after this cleaning step by introducing the mixtures consisting of Ge_2H_6 and SnD_4 in to the chamber via MFC TZ-4 at a flow rate of 30%. A flow of research grade H_2 was maintained throughout the growth, as well as a flow of B_2H_6 diluted with H_2 in order to achieve doping. The flow rate for the

former was 10% via MFC TZ-2. The amounts of precursors used for the Ge_2H_6/SnD_4 mixtures are given in the fifth and sixth and seventh columns of Table A: 11. The containers used for this purpose typically had a volume of 1 L. The B_2H_6 mixture flow rate via MFC-TZ1 (5 sccm / H_2 calibration) was varied between different growths, as given in column 8 of the table. The mixture compositions are listed in columns 9 and 10, and were typically made in 250 mL containers. The pressure used for all the depositions was 300 mTorr. The growth times are also given in the table. The resultant *p*-type film compositions, thicknesses and doping are described in Table A: 12. These layers are the final components which complete the *pn* and *pin* device structures whose initial components were described in previous sections.

Growth of diodes with *n*, *i* and *p* components consisting of GeSn

The first growth of a Si/Ge/*n*-$Ge_{1-x}Sn_x$/*i*-$Ge_{1-y}Sn_y$/*p*-$Ge_{1-z}Sn_z$ diode stack was conducted on an intrinsic virtual Ge substrate, which was prepared for epitaxy using the same cleaning procedures used earlier. After loading the wafers into the single zone UHV-CVD chamber a Ge spacer layer was deposited using Ge_3H_8 in order to regenerate the surface. Then, an *n*-type layer of suitable thickness to be used as the bottom contact was deposited using a mixture consisting of 28.0 LTorr of Ge_3H_8 and 3.7 LTorr of SnD_4. The dopant was introduced by including 0.3 LTorr of $P(SiH_3)_3$ in this precursor mixture, which was finally diluted with H_2. The mixture was made in a 3 L container, and the addition of 2160 LTorr of H_2 gave a final pressure of 720 Torr. The growth was started at 310°C in order to promote strain relaxation, and slowly cooled to 305°C, a temperature more suitable for the

Table A: 11 – Growth parameters for *p*-type layers.

Sample	Temperature (°C)			GeSn mixture contents (LTorr)			Diborane mixture flow rate (%)	Diborane mixture contents (LTorr)		Growth time (min)
	Zone 1	Zone 2	Zone 3	Ge_2H_6	SnD_4	H_2		B_2H_6	H_2	
22	315	345	345	17.03	0.62	153	8	2.63	20	20
23	310	330	330	18.71	1.41	168	8	2.50	18	21
24	310	330	330	18.48	1.42	166	8	3.82	18	24
25	305	330	330	18.02	1.43	162	8	3.60	19	20
26	305	325	325	18.15	1.78	163	8	3.76	19	25
27	273	293	293	34.16	4.51	307	25	3.71	19	46
28	273	293	293	34.16	4.51	307	25	3.71	19	46
29	260	280	280	40.52	3.31	365	25	3.55	19	56
30	270	290	290	33.76	4.68	304	21	3.60	19	45
31	270	290	290	32.37	3.73	291	20	3.63	19	45
32	265	285	285	31.88	3.74	287	20	3.57	19	39
33	275	295	295	33.26	2.40	299	20	2.19	20	44
34	265	285	285	31.94	4.00	287	25	3.78	19	30

Table A: 12 – Thickness, doping and Sn contents of *p*-type doped layers deposited using parameters listed in Table A: 11.

Sample	Thickness (nm)	Composition (% Sn)	Doping ($/cm^{-3}$)
22	150	1.9	1.4×10^{19}
23	150	4	7.9×10^{18}
24	200	4.1	2.7×10^{19}
25	150	5	9.1×10^{19}
26	135	4.4	1.6×10^{19}
27	250	4.8	8.9×10^{19}
28	275	6	6.6×10^{19}
29	140	10	3.4×10^{19}
30	140	8.4	4.0×10^{19}
31	300	8.6	2.4×10^{19}
32	150	10.4	3.1×10^{19}
33	100	7.7	3.0×10^{19}
34	120	11.9	1.8×10^{19}

growth of the target active layer composition of y=0.07. Upon completion of the *n*-layer deposition, the growth chamber was flushed with H_2 for a period of 5 min prior to the commencement of the intrinsic layer growth. For the growth of this second layer, a 27.7 LTorr Ge_3H_8 and 4.8 LTorr SnD_4 mixture diluted with H_2 was employed. The mixture container was again 3 L in volume, and therefore the final H_2 pressure was 700 Torr. The chamber pressure used for the deposition was 200 mTorr. After the growth of this *n-i* stack, the sample was removed from the CVD chamber and the top *p*-type contact layer was grown in the three zone UHV-CVD chamber using the same procedure used for previous *pin* diodes. By using a mixture of 18.7 LTorr of Ge_2H_6 and 1.8 LTorr of SnD_4 at a temperature of 315°C, it was possible to lattice match the final epilayer to the *n-i* stack. Characterization of the final *n-i-p* stack showed that the *n*-type layer has an active carrier concentration of 3×10^{19} cm^{-3}, a thickness of 410 nm and a Sn content of 6.0%. The intrinsic layer is thicker, with a thickness of 550 nm, and has a Sn incorporation of 7.0%. The top

layer has a Sn concentration of 6.0%, and the dopant level as measured by ellipsometry is 3×10^{19} cm^{-3}. The thickness of the layer is 120 nm.

It was possible to obtain diodes with higher active layer Sn contents by increasing the Sn composition of the *n*-type doped $Ge_{1-x}Sn_x$ layer. The samples which prove this concept were deposited on an *n*-type doped virtual Ge substrate, which was cleaned and loaded into the growth chamber following the same methods described earlier. After re-growing the Ge surface, the *n*-type doped $Ge_{1-x}Sn_x$ layer was deposited using a mixture of 26.9 LTorr of Ge_3H_8, 8.66 LTorr of SnD_4, 0.146 LTorr of $P(SiH_3)_3$ and 2308 LTorr of H_2. The growth temperature for this layer was initially 280°C, but was increased to 287°C during the growth. Resultant epilayers had thicknesses of 275 nm and 215 nm (A and B wafers respectively), and a composition of ≈11-12% Sn. The carrier concentration of the layers was 9×10^{18} cm^{-3}.

The wafers were then removed from the growth chamber for characterization. Prior to re-introducing them into the growth chamber, the surfaces were cleaned using HF/H_2O. The active layers were deposited starting at an initial temperature of 260°C. The temperature was increased to 265°C during the course of the deposition. After depositing the intrinsic layer for 115 min, B_2H_6 was introduced into the chamber via MFC SZ-4.1 (5 sccm / N_2) in order to dope the top layer *p*-type. The B_2H_6 mixture used for this purpose consisted of 4.1 LTorr of B_2H_6 and 20.9 LTorr of H_2. The growth time for the *p*-doped layer was 25 min. The intrinsic layer of the A wafer obtained from this procedure was 130 nm thick with a composition of 15.1% Sn, while the B wafer was 16% Sn with a thickness of 120 nm. The *p*-type layers were 60 nm and 55 nm respectively, while both films had the same

composition as the active layer. The active carrier concentrations were measured to be ~5×10^{19} cm^{-3}.

The properties of all the device stacks deposited using the above methods are given in Chapter 7.

APPENDIX B

PERMISSIONS FOR REPRINTED MATERIALS

This appendix contains licensing agreements and permissions for reprinted material used in this dissertation. For all papers which have been reprinted, permission has been obtained from all co-authors for use of the articles.

Fundamental experimental and theoretical aspects of high-order Ge-hydride chemistry for versatile low-temperature Ge-based materials fabrication

G. Grzybowski, A. V. G. Chizmeshya, C. Senaratne, J. Menendez and J. Kouvetakis, *J. Mater. Chem. C*, 2013, **1**, 5223
DOI: 10.1039/C3TC30865K

If you are the author of this article you do not need to formally request permission to reproduce figures, diagrams etc. contained in this article in third party publications or in a thesis or dissertation provided that the correct acknowledgement is given with the reproduced material.

Reproduced material should be attributed as follows:

- For reproduction of material from NJC:
  [Original citation] - Reproduced by permission of The Royal Society of Chemistry (RSC) on behalf of the Centre National de la Recherche Scientifique (CNRS) and the RSC
- For reproduction of material from PCCP:
  [Original citation] - Reproduced by permission of the PCCP Owner Societies
- For reproduction of material from PPS:
  [Original citation] - Reproduced by permission of The Royal Society of Chemistry (RSC) on behalf of the European Society for Photobiology, the European Photochemistry Association, and RSC
- For reproduction of material from all other RSC journals:
  [Original citation] - Reproduced by permission of The Royal Society of Chemistry

Xu, C.; Gallagher, J. D.; Wallace, P. M.; Senaratne, C. L.; Sims, P.; Menéndez, J.; Kouvetakis, J. *Semicond. Sci. Technol.* **2015**, *30* (10), 105028.

Dear Charutha Lasitha Senaratne,

Thank you for your email which has been forwarded to me as I deal with permissions here at IOP Publishing.

When you transferred the copyright in your article to IOP, we granted back to you certain rights, including the right to include the Accepted Manuscript of the article within any thesis or dissertation. Please note you may need to obtain separate permission for any third party content you included within your article.

Please include citation details, "© IOP Publishing. Reproduced with permission. All rights reserved" and for online use, a link to the Version of Record.

The only restriction is that if, at a later date, your thesis were to be published commercially, further permission would be required.

Please let me know if you have any further questions.

In the meantime, I wish you the best of luck with the completion of your dissertation.

Kind regards,

Kathryn Shaw

Copyright & Permissions Team
Gemma Alaway – Rights & Permissions Adviser
Kathryn Shaw - Editorial Assistant

Contact Details
E-mail: permissions@iop.org

For further information: http://iopscience.iop.org/page/copyright

Please note: We do not provide signed permission forms as a separate attachment. Please print this email and provide it to your institution as proof of permission.

Kouvetakis, J.; Favaro, R.; Grzybowski, G. J.; Senaratne, C.; Menéndez, J.; Chizmeshya, A. V. G. Molecular strategies for configurational sulfur doping of group IV semiconductors grown on Si (100) using S $(MH_3)_2$ (M= Si, Ge) delivery sources: An experimental and theoretical inquiry. *Chem. Mater.* **2014**, *26* (15), 4447.

PERMISSION/LICENSE IS GRANTED FOR YOUR ORDER AT NO CHARGE

This type of permission/license, instead of the standard Terms & Conditions, is sent to you because no fee is being charged for your order. Please note the following:

- Permission is granted for your request in both print and electronic formats, and translations.
- If figures and/or tables were requested, they may be adapted or used in part.
- Please print this page for your records and send a copy of it to your publisher/graduate school.
- Appropriate credit for the requested material should be given as follows: "Reprinted (adapted) with permission from (COMPLETE REFERENCE CITATION). Copyright (YEAR) American Chemical Society." Insert appropriate information in place of the capitalized words.
- One-time permission is granted only for the use specified in your request. No additional uses are granted (such as derivative works or other editions). For any other uses, please submit a new request.

Xu, C.; Senaratne, C. L.; Kouvetakis, J.; Menéndez, J. Experimental doping dependence of the lattice parameter in *n*-type Ge: Identifying the correct theoretical framework by comparison with Si. *Phys. Rev. B* **2016**, *93* (4), 041201.

November 2012

Terms and conditions associated with the American Physical Society Transfer of Copyright Agreement

Copyright to the [above-listed] unpublished and original article submitted by the [above] author(s), the abstract forming part thereof, and any subsequent errata (collectively, the "Article") is hereby transferred to the American Physical Society (APS) for the full term thereof throughout the world, subject to the Author Rights (as hereinafter defined) and to acceptance of the Article for publication in a journal of APS. This transfer of copyright includes all material to be published as part of the Article (in any medium), including but not limited to tables, figures, graphs, movies, other multimedia files, and all supplemental materials. APS shall have the right to register copyright to the Article in its name as claimant, whether separately or as part of the journal issue or other medium in which the Article is included.

The author(s), and in the case of a Work Made For Hire, as defined in the U.S. Copyright Act, 17 U.S.C. §101, the employer named [below], shall have the following rights (the "Author Rights"):

1. All proprietary rights other than copyright, such as patent rights.
2. The nonexclusive right, after publication by APS, to give permission to third parties to republish print versions of the Article or a translation thereof, or excerpts therefrom, without obtaining permission from APS, provided the APS-prepared version is not used for this purpose, the Article is not republished in another journal, and the third party does not charge a fee. If the APS version is used, or the third party republishes in a publication or product charging a fee for use, permission from APS must be obtained.
3. The right to use all or part of the Article, including the APS-prepared version without revision or modification, on the author(s)' web home page or employer's website and to make copies of all or part of the Article, including the APS-prepared version without revision or modification, for the author(s)' and/or the employer's use for educational or research purposes.
4. The right to post and update the Article on free-access e-print servers as long as files prepared and/or formatted by APS or its vendors are not used for that purpose. Any such posting made or updated after acceptance of the Article for publication shall include a link to the online abstract in the APS journal or to the entry page of the journal. If the author wishes the APS-prepared version to be used for an online posting other than on the author(s)' or employer's website, APS permission is required; if permission is granted, APS will provide the Article as it was published in the journal, and use will be subject to APS terms and conditions.
5. The right to make, and hold copyright in, works derived from the Article, as long as all of the following conditions are met: (a) at least one author of the derived work is an author of the Article; (b) the derived work includes at least ten (10) percent of new material not covered by APS's copyright in the Article; and (c) the derived work includes no more than fifty (50) percent of the text (including equations) of the Article. If these conditions are met, copyright in the derived work rests with the authors of that work, and APS (and its successors and assigns) will make no claim on that copyright. If these conditions are not met, explicit APS permission must be obtained. Nothing in this Section shall prevent APS (and its successors and assigns) from exercising its rights in the Article.
6. If the Article was prepared under a U.S. Government contract, the government shall have the rights under the copyright to the extent required by the contract.

All copies of part or all of the Article made under any of the Author Rights shall include the appropriate bibliographic citation and notice of the APS copyright.

By signing this Agreement, the author(s), and in the case of a Work Made For Hire, the employer, jointly and severally represent and warrant that the Article is original with the author(s) and does not infringe any copyright or violate any other right of any third parties, and that the Article has not been published elsewhere, and is not being considered for publication elsewhere in any form, except as provided herein. If each author's signature does not appear [below], the signing author(s) represent that they sign this Agreement as authorized agents for and on behalf of all authors who have the legal right to transfer copyright and that this Agreement and authorization is made on behalf of the same. The signing author(s) (and, in the case of a Work Made For Hire, the signing employer) also represent and warrant that they have the full power to enter into this Agreement and to make the grants contained herein.

As the author of an APS-published article, may I include my article or a portion of my article in my thesis or dissertation?

Yes, the author has the right to use the article or a portion of the article in a thesis or dissertation without requesting permission from APS, provided the bibliographic citation and the APS copyright credit line are given on the appropriate pages.

-https://journals.aps.org/copyrightFAQ.html#thesis

Senaratne, C. L.; Gallagher, J. D.; Jiang, L.; Aoki, T.; Menéndez, J.; Kouvetakis, J. $Ge_{1-y}Sn_y$ (y=0.01-0.10) alloys on Ge-buffered Si: Synthesis, microstructure, and optical properties. *J. Appl. Phys.* **2014**, *116* (13), 133509.

AIP PUBLISHING LLC LICENSE TERMS AND CONDITIONS

Mar 20, 2016

This Agreement between Charutha L Senaratne ("You") and AIP Publishing LLC ("AIP Publishing LLC") consists of your license details and the terms and conditions provided by AIP Publishing LLC and Copyright Clearance Center.

License Number	3832941327282
License date	Mar 20, 2016
Licensed Content Publisher	AIP Publishing LLC
Licensed Content Publication	Journal of Applied Physics
Licensed Content Title	Ge1-ySny (y = 0.01-0.10) alloys on Ge-buffered Si: Synthesis, microstructure, and optical properties
Licensed Content Author	C. L. Senaratne,J. D. Gallagher,Liying Jiang, et al.
Licensed Content Date	Oct 2, 2014
Licensed Content Volume Number	116
Licensed Content Issue Number	13
Type of Use	Thesis/Dissertation
Requestor type	Author (original article)
Format	Print and electronic
Portion	Excerpt (> 800 words)
Will you be translating?	No
Title of your thesis / dissertation	Chemical Vapor Deposition of Metastable Germanium Based Semiconductors for Optoelectronic Applications
Expected completion date	May 2016
Estimated size (number of pages)	200
Requestor Location	Charutha L Senaratne School of Molecular Sciences Box 871604 Arizona State University TEMPE, AZ 85287 United States Attn: Charutha L Senaratne
Billing Type	Invoice
Billing Address	Charutha L Senaratne School of Molecular Sciences Box 871604 Arizona State University TEMPE, AZ 85287 United States Attn: Charutha L Senaratne
Total	0.00 USD

Terms and Conditions

AIP Publishing LLC -- Terms and Conditions: Permissions Uses

AIP Publishing hereby grants to you the non-exclusive right and license to use and/or distribute the Material according to the use specified in your order, on a one-time basis, for the specified term, with a maximum distribution equal to the number that you have ordered. Any links or other content accompanying the Material are not the subject of this license.

1. You agree to include the following copyright and permission notice with the reproduction of the Material:"Reprinted from [FULL CITATION]. with the permission of AIP Publishing." For an article, the credit line and permission notice must be printed on the first page of the article or book chapter. For photographs, covers, or tables, the notice may appear with the Material, in a footnote, or in the reference list.
2. If you have licensed reuse of a figure, photograph, cover, or table, it is your responsibility to ensure that the material is original to AIP Publishing and does not contain the copyright of another entity, and that the copyright notice of the figure, photograph, cover, or table does not indicate that it was reprinted by AIP Publishing, with permission, from another source. Under no circumstances does AIP Publishing purport or intend to grant permission to reuse material to which it does not hold appropriate rights.
   You may not alter or modify the Material in any manner. You may translate the Material into another language only if you have licensed translation rights. You may not use the Material for promotional purposes.
3. The foregoing license shall not take effect unless and until AIP Publishing or its agent, Copyright Clearance Center, receives the Payment in accordance with Copyright Clearance Center Billing and Payment Terms and Conditions, which are incorporated herein by reference.
4. AIP Publishing or Copyright Clearance Center may, within two business days of granting this license, revoke the license for any reason whatsoever, with a full refund payable to you. Should you violate the terms of this license at any time, AIP Publishing, or Copyright Clearance Center may revoke the license with no refund to you. Notice of such revocation will be made using the contact information provided by you. Failure to receive such notice will not nullify the revocation.
5. AIP Publishing makes no representations or warranties with respect to the Material. You agree to indemnify and hold harmless AIP Publishing, and their officers, directors, employees or agents from and against any and all claims arising out of your use of the Material other than as specifically authorized herein.
6. The permission granted herein is personal to you and is not transferable or assignable without the prior written permission of AIP Publishing. This license may not be amended except in a writing signed by the party to be charged.
7. If purchase orders, acknowledgments or check endorsements are issued on any forms containing terms and conditions which are inconsistent with these provisions, such inconsistent terms and conditions shall be of no force and effect. This document, including the CCC Billing and Payment Terms and Conditions, shall be the entire agreement between the parties relating to the subject matter hereof.

This Agreement shall be governed by and construed in accordance with the laws of the State of New York. Both parties hereby submit to the jurisdiction of the courts of New York County for purposes of resolving any disputes that may arise hereunder.

V1.1

Questions? customercare@copyright.com or +1-855-239-3415 (toll free in the US) or +1-978-646-2777.

Senaratne, C. L.; Gallagher, J. D.; Aoki, T.; Kouvetakis, J.; Menéndez, J. Advances in light emission from group-IV alloys via lattice engineering and n-type doping based on custom-designed chemistries. *Chem. Mater.* **2014**, *26* (20), 6033.

Copyright Clearance Center RightsLink®

Home | Create Account | Help | Live Chat

ACS Publications Most Trusted. Most Cited. Most Read.

Title: Advances in Light Emission from Group-IV Alloys via Lattice Engineering and n-Type Doping Based on Custom-Designed Chemistries

Author: C. L. Senaratne, J. D. Gallagher, T. Aoki, et al

Publication: Chemistry of Materials

Publisher: American Chemical Society

Date: Oct 1, 2014

Copyright © 2014, American Chemical Society

LOGIN

If you're a copyright.com user, you can login to RightsLink using your copyright.com credentials. Already **a RightsLink user** or want to learn more?

PERMISSION/LICENSE IS GRANTED FOR YOUR ORDER AT NO CHARGE

This type of permission/license, instead of the standard Terms & Conditions, is sent to you because no fee is being charged for your order. Please note the following:

- Permission is granted for your request in both print and electronic formats, and translations.
- If figures and/or tables were requested, they may be adapted or used in part.
- Please print this page for your records and send a copy of it to your publisher/graduate school.
- Appropriate credit for the requested material should be given as follows: "Reprinted (adapted) with permission from (COMPLETE REFERENCE CITATION). Copyright (YEAR) American Chemical Society." Insert appropriate information in place of the capitalized words.
- One-time permission is granted only for the use specified in your request. No additional uses are granted (such as derivative works or other editions). For any other uses, please submit a new request.

BACK | CLOSE WINDOW

Copyright © 2016 Copyright Clearance Center, Inc. All Rights Reserved. Privacy statement. Terms and Conditions.
Comments? We would like to hear from you. E-mail us at customercare@copyright.com

Senaratne, C. L.; Gallagher, J. D.; Xu, C.; Sims, P.; Menendez, J.; Kouvetakis, J. Doping of Direct Gap $Ge_{1-y}Sn_y$ Alloys to Attain Electroluminescence and Enhanced Photoluminescence. *ECS Trans.* **2015**, *69* (14), 157. Copyright 2015, The Electrochemical Society.

ECS Copyright and Permissions

Guidelines for Use of ECS Material

Fees
How to Ask for Permission
Permission Request Form (PDF)
Credit Lines
Permission to Reproduce Full Articles

Permission Requests Key Points

- To request permission, please submit this form with full bibliographic information and figure/table numbers to copyright@electrochem.org.
- Our normal turnaround times for permission requests are 4–5 working days for figure and/or table requests, and 4–6 working days for full articles.
- ECS does not hold the copyright on the Open access articles published in its journals. Please follow reuse instructions that correspond with the Creative Commons license on the paper.
- Authors may use their own tables and figures in other scholarly research papers that they write, without writing to ECS for permission. Full credit to the original source should be given.

Guidelines for Use of Open Access Materials from ECS Publications

ECS does not hold the copyright on the Open Access articles published in its journals. The copyright is held by the author(s). Please follow reuse instructions given by Creative Commons for its various licenses. ECS articles are published using either CC BY or CC BY–NC–ND licenses, here are links for more information:

CC BY: http://creativecommons.org/licenses/by/4.0/

CC BY–NC–ND: http://creativecommons.org/licenses/by-nc-nd/4.0/

Best Practices for Citing CC Licensed Articles:
https://wiki.creativecommons.org/Best_practices_for_attribution

Guidelines for Use of Materials from ECS Publications

**Before submitting your request, please note our normal turnaround times are 4–5 working days for figure and/or table requests, and 4–6 working days for full article requests. We will try our best to meet your deadline; but please plan to submit your request with these times in mind.

Before using ECS material or requesting to reproduce ECS material, please see the ECS Transfer of Copyright Form for the rights retained by authors and employers. **For example, authors may use their own tables and figures in other scholarly research papers that they write, without writing to ECS for permission.** Full credit to the original source should be given, for example, "Reproduced with permission from *J. Electrochem. Soc.*, **150**, H205 (2003). Copyright 2003, The Electrochemical Society."

Permission is not needed if figures and/or tables from one ECS publication will be reused in another forthcoming ECS publication.

Gallagher, J. D.; Senaratne, C. L.; Sims, P.; Aoki, T.; Menéndez, J.; Kouvetakis, J. Electroluminescence from GeSn heterostructure pin diodes at the indirect to direct transition. *Appl. Phys. Lett.* **2015**, *106* (9), 091103.

AIP PUBLISHING LLC LICENSE TERMS AND CONDITIONS

Jun 18, 2016

This Agreement between Charutha L Senaratne ("You") and AIP Publishing LLC ("AIP Publishing LLC") consists of your license details and the terms and conditions provided by AIP Publishing LLC and Copyright Clearance Center.

License Number	3837461189850
License date	Mar 28, 2016
Licensed Content Publisher	AIP Publishing LLC
Licensed Content Publication	Applied Physics Letters
Licensed Content Title	Electroluminescence from GeSn heterostructure pin diodes at the indirect to direct transition
Licensed Content Author	J. D. Gallagher,C. L. Senaratne,P. Sims, et al.
Licensed Content Date	Mar 2, 2015
Licensed Content Volume Number	106
Licensed Content Issue Number	9
Type of Use	Thesis/Dissertation
Requestor type	Author (original article)
Format	Print and electronic
Portion	Photograph/Image
Title of your thesis / dissertation	Chemical Vapor Deposition of Metastable Germanium Based Semiconductors for Optoelectronic Applications
Expected completion date	May 2016
Estimated size (number of pages)	200
Requestor Location	Charutha L Senaratne School of Molecular Sciences Box 871604 Arizona State University TEMPE, AZ 85287 United States Attn: Charutha L Senaratne
Billing Type	Invoice
Billing Address	Charutha L Senaratne School of Molecular Sciences Box 871604 Arizona State University TEMPE, AZ 85287 United States Attn: Charutha L Senaratne
Total	**0.00 USD**

Gallagher, J. D.; Senaratne, C. L.; Xu, C.; Sims, P.; Aoki, T.; Smith, D. J.; Menéndez, J.; Kouvetakis, J. Non-radiative recombination in $Ge_{1-y}Sn_y$ light emitting diodes: The role of strain relaxation in tuned heterostructure designs. *J. Appl. Phys.* **2015**, *117* (24), 245704.

Copyright Clearance Center RightsLink®

Home | Account Info | Help

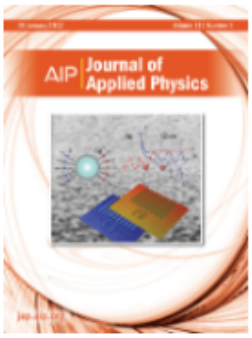

Title: Non-radiative recombination in Ge1−ySny light emitting diodes: The role of strain relaxation in tuned heterostructure designs
Author: J. D. Gallagher,C. L. Senaratne,C. Xu, et al.
Publication: Journal of Applied Physics
Volume/Issue 117/24
Publisher: AIP Publishing LLC
Date: Jun 30, 2015
Page Count: 10
Rights managed by AIP Publishing LLC.

Logged in as:
Charutha Senaratne
Account #:
3001008772
LOGOUT

Order Completed

Thank you for your order.

This Agreement between Charutha L Senaratne ("You") and AIP Publishing LLC ("AIP Publishing LLC") consists of your license details and the terms and conditions provided by AIP Publishing LLC and Copyright Clearance Center.

Your confirmation email will contain your order number for future reference.

Get the printable license.

License Number	3871710204320
License date	May 17, 2016
Licensed Content Publisher	AIP Publishing LLC
Licensed Content Publication	Journal of Applied Physics
Licensed Content Title	Non-radiative recombination in Ge1−ySny light emitting diodes: The role of strain relaxation in tuned heterostructure designs
Licensed Content Author	J. D. Gallagher,C. L. Senaratne,C. Xu, et al.
Licensed Content Date	Jun 30, 2015
Licensed Content Volume	117
Licensed Content Issue	24
Requestor type	Author (original article)
Format	Print and electronic
Portion	Figure/Table
Number of figures/tables	3
Requestor Location	Charutha L Senaratne School of Molecular Sciences Box 871604 Arizona State University TEMPE, AZ 85287 United States Attn: Charutha L Senaratne
Billing Type	Invoice
Billing address	Charutha L Senaratne School of Molecular Sciences Box 871604 Arizona State University TEMPE, AZ 85287 United States Attn: Charutha L Senaratne
Total	0.00 USD

AIP PUBLISHING LLC LICENSE
TERMS AND CONDITIONS

Jun 18, 2016

This Agreement between Charutha L Senaratne ("You") and AIP Publishing LLC ("AIP Publishing LLC") consists of your license details and the terms and conditions provided by AIP Publishing LLC and Copyright Clearance Center.

License Number	3892100821775
License date	Jun 18, 2016
Licensed Content Publisher	AIP Publishing LLC
Licensed Content Publication	Journal of Applied Physics
Licensed Content Title	Non-radiative recombination in Ge1−ySny light emitting diodes: The role of strain relaxation in tuned heterostructure designs
Licensed Content Author	J. D. Gallagher,C. L. Senaratne,C. Xu, et al.
Licensed Content Date	Jun 30, 2015
Licensed Content Volume Number	117
Licensed Content Issue Number	24
Type of Use	Thesis/Dissertation
Requestor type	Author (original article)
Format	Print and electronic
Portion	Excerpt (> 800 words)
Will you be translating?	No
Title of your thesis / dissertation	Chemical Vapor Deposition of Metastable Germanium Based Semiconductors for Optoelectronic Applications
Expected completion date	May 2016
Estimated size (number of pages)	200
Requestor Location	Charutha L Senaratne School of Molecular Sciences Box 871604 Arizona State University TEMPE, AZ 85287 United States Attn: Charutha L Senaratne
Billing Type	Invoice
Billing Address	Charutha L Senaratne School of Molecular Sciences Box 871604 Arizona State University TEMPE, AZ 85287 United States Attn: Charutha L Senaratne
Total	0.00 USD

Gallagher, J. D.; Senaratne, C. L.; Wallace, P. M.; Menéndez, J.; Kouvetakis, J. Electroluminescence from $Ge_{1-y}Sn_y$ diodes with degenerate *pn* junctions. *Appl. Phys. Lett.* **2015**, *107* (12), 123507.

AIP PUBLISHING LLC LICENSE TERMS AND CONDITIONS

Jun 18, 2016

This Agreement between Charutha L Senaratne ("You") and AIP Publishing LLC ("AIP Publishing LLC") consists of your license details and the terms and conditions provided by AIP Publishing LLC and Copyright Clearance Center.

License Number	3892101122493
License date	Jun 18, 2016
Licensed Content Publisher	AIP Publishing LLC
Licensed Content Publication	Applied Physics Letters
Licensed Content Title	Electroluminescence from Ge1−ySny diodes with degenerate pn junctions
Licensed Content Author	J. D. Gallagher,C. L. Senaratne,P. M. Wallace, et al.
Licensed Content Date	Sep 25, 2015
Licensed Content Volume Number	107
Licensed Content Issue Number	12
Type of Use	Thesis/Dissertation
Requestor type	Author (original article)
Format	Print and electronic
Portion	Photograph/Image
Title of your thesis / dissertation	Chemical Vapor Deposition of Metastable Germanium Based Semiconductors for Optoelectronic Applications
Expected completion date	May 2016
Estimated size (number of pages)	200
Requestor Location	Charutha L Senaratne School of Molecular Sciences Box 871604 Arizona State University TEMPE, AZ 85287 United States Attn: Charutha L Senaratne
Billing Type	Invoice
Billing Address	Charutha L Senaratne School of Molecular Sciences Box 871604 Arizona State University TEMPE, AZ 85287 United States Attn: Charutha L Senaratne
Total	0.00 USD